NMR Studies of Ruthenium and Rhodium Complexes. In-situ and Ex-situ Photochemistry

Sarah-Louise Henshaw

Doctor of Philosophy

University of York

Chemistry

December 2016

Abstract

Catalytic processes often involve organometallic complexes, the aims of this thesis were to study some specific ruthenium and rhodium complexes using photochemistry. This allowed their behaviour towards small molecules to be investigated since the coordination and activation of small molecules are fundamental parts of catalytic cycles. A further aim was to study suitable complexs with parahydrogen using time-resolved NMR methods with the intention of measuring *p*-H_2 addition and/or the evolution of the *p*-H_2-derived singlet state

The photochemistry of $CpRh(CH_2CHSiMe_3)_2$ (**2.1**), $CpRh(COE)_2$ (**2.2**) and CpRh(COD) (**2.3**) with DMSO PhSOMe, trimethylvinylsilane and triethylsilane was probed. The photoactivity of **2.3** proved minimal with the main products being associated with the loss of the COD ligand. By contrast, **2.1** and **2.2** undergo the substitution of one or both of the alkene ligands, depending on the nature of the reacting ligand. Complexes **2.1**, $CpRh(CH_2CHSiMe_3)(DMSO)$ (**2.4**) and $CpRh(P^*Ph)(C_2H_4)$ (**3.2**) were deemed suitable for time-resolved studies with *p*-H_2. **2.1** was found to form the expected dihydride (**3.1**) on a 50 ms timescale. **2.4** was also formed **3.1** but its PHIP enhancement was poor and whilst **3.1** did form the expected dihydride product PHIP was not observed.

$[Ru(H)_2(CO)(PPh_3)(Xantphos)]$ **5.1** was also synthesised and its reactivity towards a range of small molecules, which included DMSO, CO, ethene and Et_3SiH, investigated. These studies revealed that its H_2, CO and PPh_3 ligands could all be lost photochemically and that the xantphos ligand could switch between κ^2-PP and κ^3-POP coordination. Time-resolved NMR studies on **5.1**, with *p*-H_2, found the H_2 addition to the intermediate to occur with a rate of the order of 0.5 s^{-1}. *cis*-$[Ru(H)_2(dppp)_2]$ **6.1** was also studied using time-resolved NMR, in this case the rate of H_2 addition was faster than the NMR timescales. This allowed the evolution of the *p*-H_2 singlet state to be probed and shown to be as a function of the difference in scalar coupling between the hydrides and the equatorial ^{31}P nuclei.

Contents

Table of Figures

Table of Tables

Acknowledgements

Firstly, I would like to thank my supervisors Simon Duckett and Robin Perutz for the opportunity to work on this project and their guidance and support throughout this project.

I would also like to thank all the past and present members of the Duckett and Perutz research groups. In particular; Naser, Jon and Mike for their help with synthetic procedures, Olga and Chris for teaching me how to use the *in-situ* photochemistry setups and Meghan and Alexandra for their Matlab skills. Also thanks to my fellow *in-situ* photolysis colleagues Olga, Magnus, Barby, Meghan and Marta for their support. Sincerest thanks goes to those I have shared offices with during this time: Fran, Richard the First, Richard the Second, Ryan, Barby, Vicky, Wissam, Pete and Phil and last but certainly not least Alexandra and Marianna. Their steady supply of coffee, chocolate and mid-afternoon light entertainment made these last few years thoroughly enjoyable.

I would also like to thank the Centre for Magnetic Resonance for providing funding. Thank you to Heather for teaching me all there is to know about nitrogen and helium fills and for always providing a friendly ear. Additionally, I would like to thank Amanda, Emma, Julia, Richard and Lewis for help with fills and making them more entertaining. I will always look back fondly on my time with the NMR service and that is because of all of you.

I would like to thank the friends I have made in York; Clare, Dan, David, Dave, Eleanor, Hayley, Louise, Mike and Phil, for many interesting walks, pub trips and good food. I would like to thank my family for always being there for me. In particular my parents whose support has never wavered, my grandparents whose regular Skype calls are the highlight of my week and my wonderful niece who never fails to make me smile.

Finally, I would like to thank my partner Ryan who has provided love and support throughout and without whom this would not have been possible.

Declaration

I declare that the work presented in this thesis is, to the best of my knowledge, original, except where specified. This work has not previously been presented for an award at this, or any other, university. All sources are acknowledged as references.

Work within this thesis is included in publication in the Journal of Magnetic Resonance (Halse *et. al. J Magn Reson*, 2017, **278**, 25-28).

1 Introduction

1.1 General Introduction

Organometallic chemistry is widely used in catalytic processes where the ability of metal centres to coordinate and/or activate small molecules is invaluable. To understand the mechanisms behind the catalytic cycles, the detection and characterisation of reaction intermediates and any minor products or isomers is needed. Often the initial steps in such a process is ligand loss followed by the coordination or activation of a small molecules, therefore it is important to understand how metal complexes interact with small molecules.

The intention in this thesis was to study the reaction of rhodium and ruthenium complexes with small molecules such as DMSO, triethylsilane and H_2, or more specifically *p*-H_2. Complexes containing hydride ligand(s) are common features in catalytic processes[7] and therefore understanding how they form and what further reactivity they can undertake is crucial in developing and improving catalysts. In this work photochemistry was be used to promote the loss of a ligand leaving a free coordination site for a small molecule to coordinate. The photoactivity of the complexes was explored before studies using *in-situ* photolysis with parahydrogen were performed. The purpose of using parahydrogen was to take advantage of the signal enhancements that parahydrogen gives with the hope that this will allow reaction intermediates to be observed and the rate of dihydrogen addition to reactive intermediates measured. Furthermore, the idea that the parahydrogen protons could be transferred on to other ligands through rearrangement reactions or hydrogenation was an interesting prospect.

1.2 Hyperpolarisation and NMR

1.2.1 Overview of NMR

NMR spectroscopy is an immensely powerful and widely used analytical technique. One of its major advantages is its ability to give structural information across a wide variety of structural

motifs from small organic compounds,[8] to organometallic complexes,[9] to complex proteins.[10] This property would be valuable in the study of reaction mechanisms for the detection and characterisation of reaction intermediates. Unfortunately, NMR spectroscopy is an intrinsically insensitive technique. The intensity of signals in an NMR spectrum depends upon a number of variables which are described by Equation (1.1),[11, 12] where N is the number of spins, γ is the gyromagnetic ratio, $\hbar$ is the reduced Planck's constant, B_0 refers to the size of the applied magnetic field, k is the Boltzmann constant and finally T is the temperature.

$$Intensity \propto \left(\frac{N\gamma\hbar B_0}{2kT}\right) B_0 \qquad (1.1)$$

The terms of note in Equation (1.1) are the number of spins, N, and the gyromagnetic ratio, γ. The number of spins relates to the concentration of the sample and the relative abundance of the NMR active nuclei. The larger the abundance of the spin-½ nuclei the larger the proportion of the sample is visible by NMR. The gyromagnetic ratio is an intrinsic property of the nuclei and its magnitude is proportional to the NMR signal. These properties combined give an indication of the relative sensitivities of the different nuclei and therefore how much sample is required to give an appropriate number of observable spins. The nuclei which have the largest gyromagnetic ratio are protons. These nuclei also have essentially 100 % abundance and this is why ^{1}H NMR spectroscopy is associated with the greatest sensitivity. Carbon based NMR experiments, however, are hampered by the active nuclei, ^{13}C, having a natural abundance of just 1.07 % and a gyromagnetic ratio approximately four times smaller than ^{1}H. These two factors combine to make ^{13}C NMR much more insensitive than ^{1}H NMR.

The signal intensity can also be defined by Equation (1.2) where N_α and N_β refer to the number of α and β spins. To understand this relationship an appreciation of the principles behind NMR spectroscopy is required. NMR spectroscopy utilises the intrinsic angular momentum of the nuclei within a substance. Angular momentum refers to an object that is moving in a circular

path with a particular direction and magnitude. NMR spectroscopy concerns the use of spin angular momentum, which is given the quantum number I. This is a property of the nuclei and is also referred to as spin. Spin angular momentum is quantised; this means that there are discreet values it may take. The total spin angular momentum, L_{tot}, is given by Equation (1.3), where ħ is the reduced Planck's constant and there are 2I + 1 sublevels.[13] Outside of a magnetic field, these sublevels are degenerate and they only separate in energy once they reside inside a magnetic field, this is known as the Zeeman effect and now each arrangement is described by the quantum number m_I which is a vector quantity, and as such has a direction and magnitude. If applied magnetic field is placed along the z axis it is only the I_z component of the spin angular momentum which can interact with the applied magnetic field.

$$Intensity \propto (N_\alpha - N_\beta)B_0 \tag{1.2}$$

$$L_{tot} = [I(I+1)]^{1/2}\hbar \tag{1.3}$$

The most routinely used nuclei, in solution-based NMR spectroscopy, have a spin quantum number, I, equal to a ½ and therefore I_z is associated with the values m_I + ½ and – ½. Spins align with the applied field become lower in energy and those aligned in the opposite direction increasing in energy (Figure 1.1) and the size of the intrinsic magnetic vector. The energy difference between these two states depends on the size of the magnetic field. As you move from smaller to larger magnets the energy difference increases and in doing so the population difference between the α and β spin states increases and thus the size of the signals also increase. Using standard NMR methods the distribution of the spins across these two spin states is determined by the Boltzmann distribution. However, even with large magnets, the energy gap between the spin up and spin down energy levels is small and as a consequence there is only a small population difference between the two energy levels.

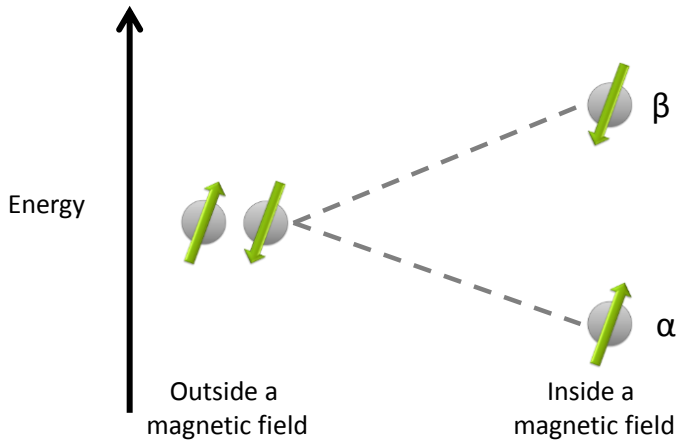

Figure 1.1: Pictorial representation of the behaviour of spins inside (right) and outside a magnetic field (left).

This can be quantified precisely, such that at a 9.4 T or 400 MHz for ^{1}H, there is a population difference of 1 in 31,000[14] between the two spins at 300 K. Increasing the size of the magnet to 600 MHz, or 14.1 T, causes this population difference to increase to 1 in 21,300.[15] An alternative way of viewing this effect is that on a 600 MHz spectrometer just 0.0047 % of the protons in a sample are observed rather than the 0.0032 % that is observed using a 400 MHz spectrometer. This is where the intrinsically low sensitivity of NMR spectroscopy lies.

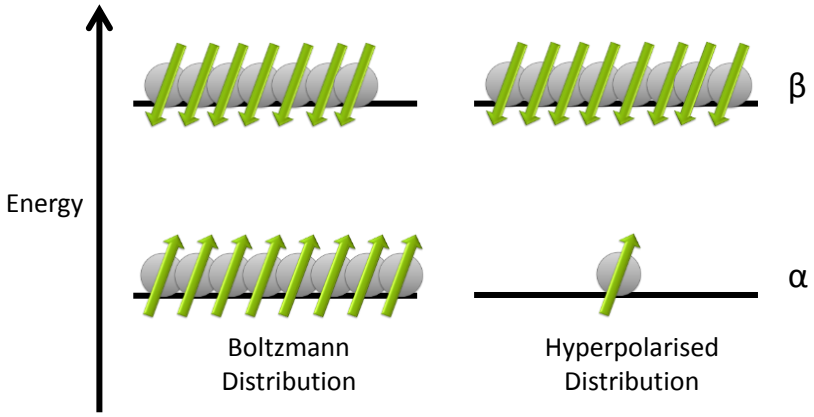

Figure 1.2: Schematic to show the relative population difference using the Boltzmann distribution of spins (left) and the distribution obtained with a hyperpolarisation method (right).

The intrinsic limitations of NMR spectroscopy may seem easily fixed by using larger concentrations of analyte but this is not always feasible, for instance, in the detection of reaction intermediates. These are typically only present in solution for a short period of time and are often in low concentration; therefore it is challenging to observe reaction

intermediates by NMR. This limits the number of reactions which can be studied by NMR. Whilst there are other analytical techniques which are far superior to NMR in terms of their limits of detection, both in terms of concentration and detection time, they do not offer the same level of structural information. For NMR studies the molecule must have particular characteristics, for example to comprise of atoms which have NMR active nuclei, e.g $I \neq 0$ and ideally $I = ½$. These nuclei also require appropriate natural abundance and gyromagnetic ratios that are larger enough to allow measurement to be made routinely. The substance also requires identifiable features in the NMR spectra to allow for confident assignments of its structure. A drawback of NMR spectroscopy is its insensitivity; improvements have been achieved in this field using hyperpolarisation methods. These create non-Boltzmann distributions of the spins, which give rise to considerably larger population differences. The result of this is NMR signals which can be enhanced, relative to the signals achieved by using the thermal equilibrium distribution of the spins, by several orders of magnitude.

1.2.2 Overview of hyperpolarisation methods

There are now a wide range of approaches for creating hyperpolarised NMR measurements available some of which will now be discussed. Optical pumping of noble gases utilises circularly polarised light and a glass cell containing a combination of a gaseous alkali metal and a noble gas. The polarised light is absorbed by the alkali metal and the spin angular momentum of the photons is transferred to the alkali metal's valence electrons. Like nuclei, photons of light may also have angular momentum, in this case the angular momentum has magnitude of $(2ħ)^{½}$ and the spin angular momentum of a specific photon is associated with a right or left handed helix, which relate to $+ħ$ or $–ħ$, which is where the plane polarised light terminology originates. This polarisation can then be transferred to the noble gas through collisions between the alkali metal and noble gas nuclei in a correlated way[16, 17] to create spin-polarised nuclei which have been used to make hyperpolarised MRI measurements.[18, 19]

Another hyperpolarisation method is dynamic nuclear polarisation (DNP). The signal intensity in NMR relates to the gyromagnetic ratios of the respective nuclei, which are many orders of magnitude smaller than the gyromagnetic ratio of an electron which has a much higher magnetic moment. DNP takes advantage of the gyromagnetic ratio of an electron to enhance NMR signals. It was initially developed by Abragam[20, 21] and Jeffries[22] in the 1950's. In more recent years, dissolution DNP has been developed.[23] Dissolution DNP works by doping a liquid sample of the analyte of interest with a free radical, the solution is frozen as a glass and placed in a polarising field at low temperatures, typically a 3.4 T field at 1-2 K. The sample is irradiated using low power microwaves. The high polarisation that comes from the single unpaired electron in the free radical is transferred to the analyte. To make the NMR or MRI measurements a dissolution step is required involving a hot liquid to rapidly dissolve the glass and the solution is transferred into the magnet for sample acquisition.[12]

Finally, parahydrogen can be used as a hyperpolarisation source. Parahydrogen is a nuclear spin isomer of H_2 which exist in a pure spin state (details discussed below). In 1986 Bowers and Weitekamp[24] proposed that the pure spin state of parahydrogen could be exploited to generate signals in NMR which are orders of magnitude larger than those generated from the equilibrium distribution. Parahydrogen has no nuclear angular momentum which means that it itself does not generate an NMR signal. It was proposed that the reaction between parahydrogen and an asymmetric substrate (Figure 1.3) would break the symmetry of the parahydrogen spin state and that this would convert the pure spin state of parahydrogen into observable magnetisation which has a population difference much greater than that achieved using standard methods. In addition to breaking the symmetry of the former parahydrogen protons, the other requirements for these enhancements were that the spin state in the product is a result of a chemical reaction and not a consequence of interaction with a magnetic field. This reaction must take place on a faster time scale than any relaxation.

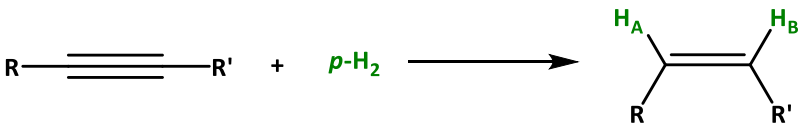

Figure 1.3: Proposed reaction which would give rise to parahydrogen enhanced products where H_A and H_B are the former *p*-H_2 protons.

1.2.3 Parahydrogen

The hyperpolarisation method utilised in this work is based on parahydrogen. The two isomeric forms of H_2 are para- and ortho-hydrogen, or *p*-H_2 and *o*-H_2 respectively, and were first proposed by Pauli in the 1920's. The difference between them can be identified by examining the respective components of their wavefunctions. Dihydrogen consists of two identical spin ½ nuclei and is classed as a fermion. The overall wavefunction of a fermion, such as in dihydrogen, has to be antisymmetric.[14] The wavefunction consists of electronic (ψ_E), vibrational (ψ_V), rotational (ψ_R), translational (ψ_T) and nuclear spin (ψ_S), components (Equation (1.4)). When these are combined, the electronic, vibrational and translational wavefunctions are always symmetric with respect to particle interchange. Hence, the antisymmetric nature of the overall wavefunction can be achieved by a suitable combination of the rotational and nuclear spin wavefunctions which can be either symmetric or antisymmetric. The rotational wavefunction is given the quantum number J. When J has an even value (e.g. J = 0, 2, 4 etc), the rotational wavefunction is symmetric, whereas when J has an odd value its wavefunction is antisymmetric. The nuclear spin of dihydrogen therefore determines whether the molecule is assigned as the ortho or para isomer, where orthohydrogen is the symmetric nuclear spin isomer and parahydrogen is the antisymmetric nuclear spin isomer (Figure 1.4). As dihydrogen is comprised of two I = ½ hydrogen atoms, each of which can have the values of either +½ or –½ these are combined in the nuclear wavefunction.

$$\Psi = \psi_E \psi_V \psi_R \psi_N \psi_S \qquad (1.4)$$

Ortho-Hydrogen Para-Hydrogen

Figure 1.4: Schematic representation of the spin Isomers of dihydrogen H_2, orthohydrogen is depicted on the left and parahydrogen on the right.

Using the α and β notations for spins aligned with and against the applied magnetic field respectively, there are four combinations of the two spins; αα, αβ, βα and ββ. However, since αβ and βα are identical, linear combinations are used to distinguish them. Now the four combinations are αα, ββ αβ + βα and αβ – βα. Three of these combinations are symmetric with respect to particle interchange (αα, ββ and αβ + βα) and thus form the triplet spin isomer orthohydrogen (Figure 1.4) and the fourth linear combination, αβ – βα, is antisymmetric. This singlet state corresponds to the parahydrogen spin isomer and therefore must occupy even rotational energy levels. The three other spins states are consigned to the odd values of J. This means that it is the parahydrogen isomer which populates the lowest energy rotational level (J = 0) and therefore is the most stable of the two isomers. The interconversion between the two isomers is forbidden as we need to changes two quantum numbers, J and α/β, simultaneously for interconversion. This means that it is feasible to isolate H_2 which is solely in the parahydrogen form.

For an equilibrating system, the relative proportions of *o*-H_2 and *p*-H_2 are temperature-dependent, as depicted in Figure 1.5.[14] The energy difference between the lowest energy rotational levels for *o*-H_2 and *p*-H_2 is small and at room temperature there is sufficient energy for odd and and even energy levels to be populated according to the Boltzmann distribution and the result of this is that as there is an almost equal number of odd and even energy levels populated. Since there are three spin states corresponding to orthohydrogen and just one for parahydrogen there is approximately 75 % o-H_2 and 25 % *p*-H_2. At lower temperatures there is no longer sufficient energy for these energy levels to be populated and there is a population

difference between J = 0 for *p*-H_2 and J = 1 for *o*-H_2.This is reflected in a difference in relative proportions of *o*-H_2 and *p*-H_2 seen with a decrease in temperature. At temperatures below 77 K, *p*-H_2 is now the major isomer and below 35 K, H_2 which is almost purely parahydrogen can be isolated.

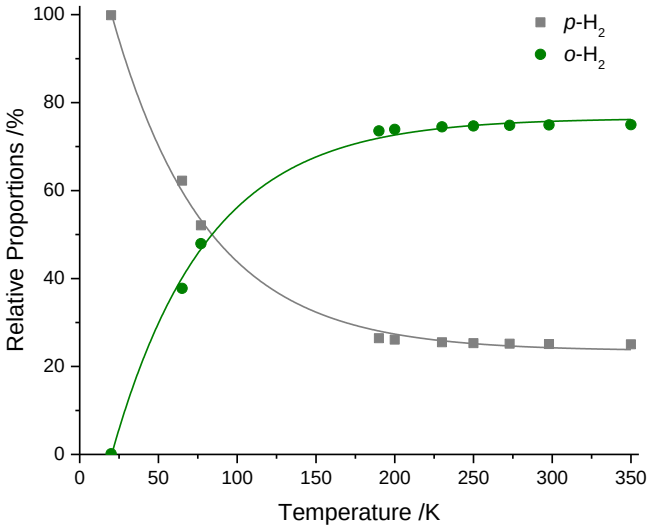

Figure 1.5: Variation of the percentage of para- and ortho-hydrogen as a function of temperature, using the relative proportions of ortho and para hydrogen tabulated in Green *et al.,* 2012.[14]

There are two approaches used to generate parahydrogen. The simplest is storing of a sample under an atmosphere of H_2 in liquid nitrogen, in the presence of a catalyst to generate samples with consisting of ~50% *p*-H_2. Alternatively, *p*-H_2 can be prepared using a closed-cycle cooler to drop the temperature of the H_2 to ~20 K where 100% *p*-H_2 can form. The H_2 is passed over a suitable catalyst at ~20K and this facilitates the interconversion between the two spin isomers. This is typically activated charcoal and iron oxide when the gas is removed from the catalyst and returned to room temperature it will retain its enriched parahydrogen state for a prolonged period, provided there is no paramagnetic material which may facilitate the conversion between the two spin isomers.

Parahydrogen itself is NMR silent, as it has no net spin angular momentum. Bowers and Weitekamp[24] proposed that the potential signal enhancements that result from parahydrogen being a singlet state could be unlocked through its addition to an unsymmetrical entity. They

suggested the hydrogenation of an unsymmetrical alkene (Figure 1.3). In the hydrogenation product the two former H_2 protons form an AX spin system, which means that the two protons are in chemically different environments and that they are coupled to one another. As in H_2, there are four combinations of these two spins, now, owing to them being distinct from another, linear combinations are not required. In the hydrogenation product which results from the use of naturally abundant H_2 all four of these states are approximately equally populated. Since it is population differences which give rise to NMR signals, the signals which result are small. The possible transitions from these states are governed by the selection rule $\Delta m_I = \pm 1$ i.e. either α goes to β or β goes to α but not both. This means there are four possible transitions which gives two doublets in the NMR spectrum (Figure 1.6). When *p*-H_2 is used instead, only the αβ and βα states are populated. This means there is a considerably larger population difference which equates to much larger signals in the NMR spectrum. There are also four allowed transitions, although since only the αβ and βα states are populated the transitions move from these states to the αα and ββ resulting in characteristic antiphase doublets in the NMR spectrum (Figure 1.6).

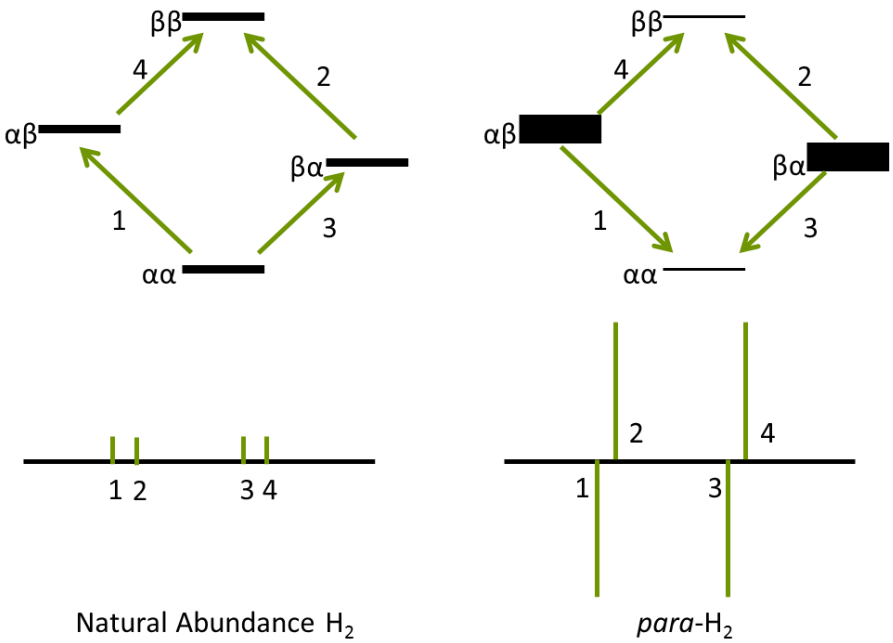

Figure 1.6: Schematic representation of an AX spin system in a hydrogenation product using natural abundant hydrogen (left) and parahydrogen (right). The relative populations are signified by thickness of the lines. The arrows represent allowed transitions and the bottom diagrams are the resultant NMR spectra from these transitions.

In 1987 Bowers and Weitekamp[25] followed up their theoretic paper with experimental observations of this phenomenon. Using the established hydrogenation catalyst, $RhCl(PPh_3)_3$ (Wilkinson's catalyst)[26] with H_2 enriched to 50% *p*-H_2 they studied the hydrogenation of acrylonitrile (Figure 1.7) inside an NMR spectrometer by bubbling the *p*-H_2 into the sample using a capillary. They observed signals corresponding to the hydrogenation product, proprionitrile, which were 100-200 times larger than the thermal equilibrium signals. The hydrogenation product, $RhH_2(PPh_3)_3Cl$, formed through the reaction of Wilkinson's catalyst with *p*-H_2 was also observed, where one hydride is trans to a chloride ligand and the other trans to a PPh_3 making the two hydrides chemically inequivalent (Figure 1.7B). They termed this phenomenon *p*arahydrogen *a*nd *s*ynthesis *a*llow *d*ramatic *e*nhanced *n*uclear *a*lignment (PASADENA). The use of parahydrogen also allowed the sign of the hydride coupling to be deduced as negative owing to the profile of the hydride resonances. This information cannot to be deduced from spectra obtained using equilibrium magnetisation.

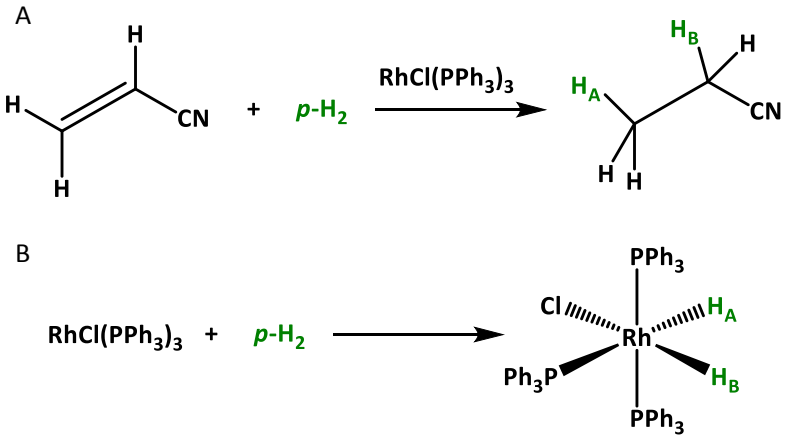

Figure 1.7: Reactions observed by Bowers and Weitekamp,[25] (A) the hydrogenation of acrylonitrile (B) the oxidative addition of *p*-H_2 by Wilkinson's complex. H_A and H_B refer to former *p*-H_2 protons.

Also in 1987, the Eisenberg group also demonstrated that parahydrogen could be used to created hyperpolarised signals in NMR.[27] The initial experiments utilised a rhodium trinuclear complex, $[Rh_3Cl_2H_2(CO)_2(Ph_2P(CH_2)_2PPh)_2]^+$, as the hydrogenation catalyst and phenyl acetylene as the substrate (Figure 1.8A). The sample was prepared and stored under H_2 in liquid nitrogen for at least 8 hours. This allows the H_2 to be enriched with approximately 50% *p*-H_2. After this

time a ^{1}H NMR spectrum was acquired at 50 °C and enhanced signals for the hydrogenation product styrene were observed. To confirm that these enhanced signals were due to parahydrogen two control experiments were performed. The first control involved storing the sample under vacuum for 8 hours in liquid nitrogen and only adding H_2 prior to the running the NMR experiment. As expected, this did not give any enhanced signals. The second control experiment did not store the sample in liquid nitrogen at all, instead parahydrogen prepared separately was added to the sample and the ^{1}H experiment performed. This sample did give enhancements comparable to the first. From this it can be concluded that the storing of H_2 in liquid nitrogen in the presence of the rhodium trinuclear complexes results in the enrichment of H_2 as the para isomer and that this can hydrogenate phenyl acetylene. This process breaks the symmetry of the former *p*-H_2 protons and allows enhanced signals in the phenyl acetylene product to be observed. They went on to study this rhodium trinuclear complex with the deuterated alkenes; d_8-styrene, d_6-propylene and d_4-ethylene.[27] In each of the products, they obtained enhanced signals, including the symmetrical ethylene substrate. This was explained by the concept of magnetic inequivalence due to H–D coupling meaning the product has an $AA'X_2X'_2$ spin system (Figure 1.8B).

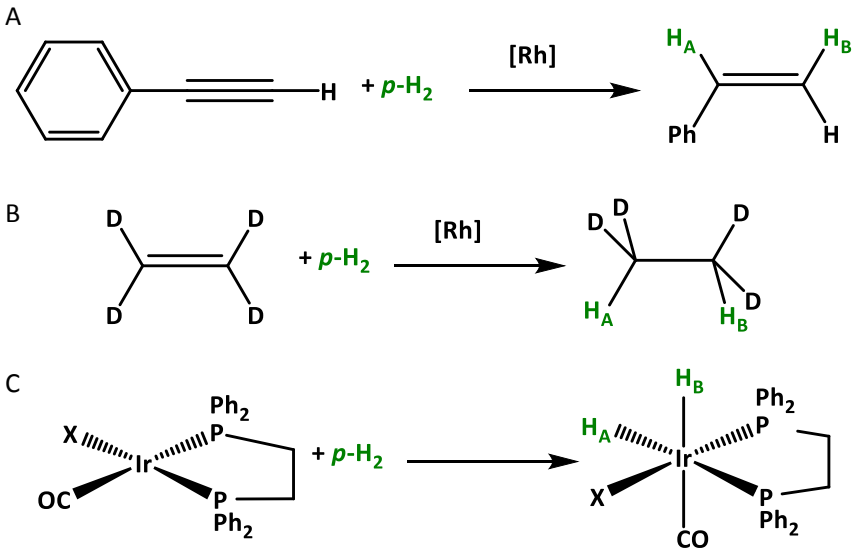

Figure 1.8: Summary of some of the reactions reported by the Eisenberg group. A) The hydrogenation of phenyl acetylene by $[Rh_3Cl_2H_2(CO)_2(Ph_2P(CH_2)_2\text{-}PPh)_2]^+$, [Rh], B) The hydrogenation of d_4-ethylene resulting in the magnetic inequivalent product with an $AA'X_2X'_2$ spin system. C) The oxidative addition of *p*-H_2 to the iridium complex IrXCl(dppe) where X = CN or Br. H_A and H_B refer to the former *p*-H_2 protons in each scheme.

The final reaction reported in the 1987 paper by Eisenberg,[27] involved the oxidative addition of *p*-H_2 to the iridium complex IrX(CO)(dppe), X = CN, Br. In this reaction, they observed the stereoselective H_2 oxidative addition forming a dihydride product where the two hydrides are cis to one another (Figure 1.8C). As with the earlier study by Weitekamp,[25] they were able to ascertain that the coupling between these hydrides has a negative sign as a consequence of the splitting pattern obtained in the parahydrogen enhanced spectrum. They proposed that the use of parahydrogen could be used to confirm whether a catalytic hydrogenation reaction proceeds via the pairwise transfer of protons as this is one of the requirements for parahydrogen enhancements to be observed. The Eisenberg group coined the abbreviation PHIP for this phenomenon where PHIP stands for *p*ara*h*ydrogen *i*nduced *p*olarisation. It is this abbreviation which will be used from here to refer to parahydrogen enhancements.

In the almost 30 years since these initial publications, there has been a great deal of research performed using parahydrogen as a hyperpolarisation source. In this work, the use of parahydrogen has been utilised in the study of hydrogenation reactions,[28] mechanistic organometallic chemistry[29, 30] and, more recently, as part of a non-hydrogenative process through the use of *s*ignal *a*mplification *b*y *r*eversible *e*xchange (SABRE).[31] In this method, the hyperpolarisation is passed from parahydrogen protons to a substrate via a transition metal complex.

1.2.4 NMR Theory for Boltzmann distribution model

The premise behind NMR spectroscopy is that each nucleus has a nuclear spin angular momentum which generates a magnetic moment. When inside a magnet they interact with the applied magnetic field and this ultimately gives rise to an NMR spectrum. To understand how a spectrum is obtained using a spectroscopic technique often requires an energy level approach; with NMR spectroscopy, however, this approach is insufficient. To understand the interactions between nuclear spin and the applied magnetic field and the implications of the

different pulse sequences within an NMR experiment a different approach is required. There are number of theories which can be used. One of the more basic and readily accessible models is the vector model. This is a geometric model which provides a non-mathematical approach to NMR spectroscopy; however, it is really only applicable to simple isolated spin systems and basic pulse sequences. Another model used to understand NMR theory utilises product operators. This model can be used to give a more complete description of NMR experiments and can be used on coupled spin-½ nuclei as well as multiple pulse experiments. There are other models which delve deeper into the quantum theory behind NMR spectroscopy but this level of rigour is beyond the scope of this thesis. The vector model has its limitations when used to describe NMR experiments but it can be used to introduce the ideas and terminology used by the more complex methods and as such provides a convenient starting point in discussing the theory behind NMR spectroscopy.

1.2.4.1 Vector Model

The vector model is often the first model used to introduce the concepts behind NMR spectroscopy. The limitations of the model, in terms of the examples it can be applied to, are offset by the advantage of it being a geometric approach. As such it provides pictorial representations of the underlying processes making it an accessible model to introduce the theory behind NMR spectroscopy.[32]

The vector model concerns the actions of the Bulk magnetisation; this is the average magnetic moment across all of the spins. This magnetisation which is aligned with the z axis, M_z, is not detectable. Radio frequency (RF) pulses are used to move this magnetisation from the z axis, into the x or y axes giving M_x and M_y magnetisation. This magnetisation is detected by wrapping a coil around either the x or y axis and when the precessing magnetisation cuts this coil it induces a current which is detectable. The rotating frame of reference is used to negate

the effect of the Larmor precession. In the rotating frame the axes are also rotating at the Larmor frequency and thus the magnetisation appears to be stationary.

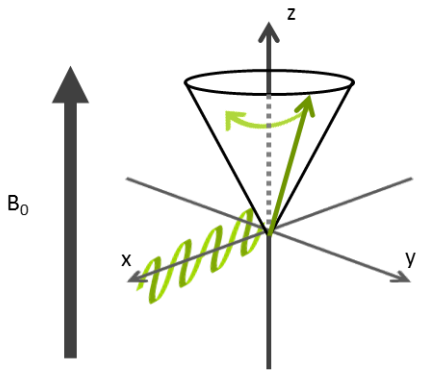

Figure 1.9: Schematic to show how once the magnetisation is moved away from the z axis it precesses around the z axis at the Larmor frequency. A signal can be detected by wrapping a coil along either the x or y axis (x in this example) and when this is crossed by the magnetisation a detectable current results. Adapted from Keeler.[32]

The most basic NMR experiment is the pulse-acquire experiment. This consists of a single pulse followed by the detection of the signal. For the maximum signal, the RF pulse is applied for a sufficient amount of time to tip all the magnetisation into the x or y axis. The signal intensity follows a sine function. Therefore, the maximum signals are seen when the magnetisation has been moved through 90° and 270° (or multiples thereof) and the minimum signals is seen when the magnetisation has been moved through 180° or 360°. To know how long to apply the RF pulse to achieve the maximum signal the pulse lengths need to be calibrated for the particular pulse power. This is done by varying the time that the pulse is applied for with a fixed pulse power and monitoring the changes in the on-resonance signal. Since the null point, where the minima are, are more distinctive than the maxima, pulse lengths that should approximately correspond to the 360° pulse length are used and once the null point is seen the pulse length is divided by 4 to give the value for a 90° pulse.

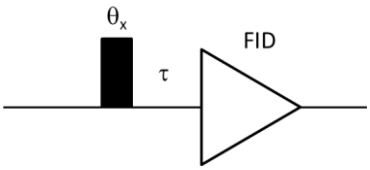

Figure 1.10: Pulse sequence for a pulse acquire experiment. A pulse, of angle θ, is applied either the x or y axis, in this example it is along x, followed by a delay, τ, and the signal is then observed by a free induction decay (FID).

1.2.4.2 Product Operators

The use of product operators can provide a more comprehensive description of NMR experiments than was possible using the vector model.[32] Unlike the vector model, the product operator approach can be used with systems containing more than one spin and systems where the spins are coupled, this coupling may be hetero- or homo-nuclear in origin. It may also be used on experiments which have a wider variety of pulses and delays than was demonstrated by the vector model.

The product operator analysis of a one spin system bears many hallmarks of the vector model. The one-spin system may be described by four operators; $\frac{1}{2}E$, I_x, I_y and I_z. E is the unity operator which does not generate observable magnetisation under the NMR experiment; it is included here for completeness and will not be discussed further. The remaining three operators describe magnetisation in each of the three axes and are analogous to the M_x, M_y and M_z of the vector model. As with the vector model, the applied magnetic field is assigned as the z axis and the right-handed coordinate system is used to assign the x and y axes, respectively. This means that I_z refers to the equilibrium magnetisation position making it unobservable and in experiments under Boltzmann distribution conditions it is the initial state.

The most basic NMR experiment is the pulse-acquire experiment (Figure 1.10). As covered in the vector model, the application of an RF pulse moves the magnetisation from aligned with the z axis (I_z) and into the xy plane where is can be observed as either I_x or I_y depending on which axis the pulse is applied along. How far the magnetisation moves into the xy plane depends on duration of the pulse. The evolution of starting operator varies as a function of cos(θ) where θ is the angle of the pulse applied and the new operator evolves as function of sin(θ) as can be seen by Figure 1.11A.

$$(\text{Original operator})\cos(\theta) + (\text{New operator})\sin(\theta)$$

This means that a 90° pulse results in all of the original operator being transformed into the new operator. This is why a 90° pulse results in the largest signal in a pulse-acquire experiment when the starting state is I_z. Once the magnetisation has moved away from the z axis it undergoes free precession around the z axis evolving under the resonance offset or chemical shift (Ω) and the time (τ). Note: whilst this is referred to as the chemical shift it is not the true chemical shift of the signal but rather it is the chemical shift frequency difference, in radians, between the signal and the transmitter frequency (where the pulse is applied). Although the free precession occurs from the moment the pulse is applied, it can be considered sequentially. Since this evolution occurs around the z axis any terms relating to I_z are unaffected by this evolution. The evolution of the I_x and I_y based terms follow a predictable pattern given by Figure 1.11C which equates to the magnetisation precessing anticlockwise around the xy plane. Using the pulse sequence in Figure 1.10 and starting with the equilibrium magnetisation I_z, the final collection of terms would be

$$-I_y \cos(\Omega\tau) + I_x \sin(\Omega\tau)$$

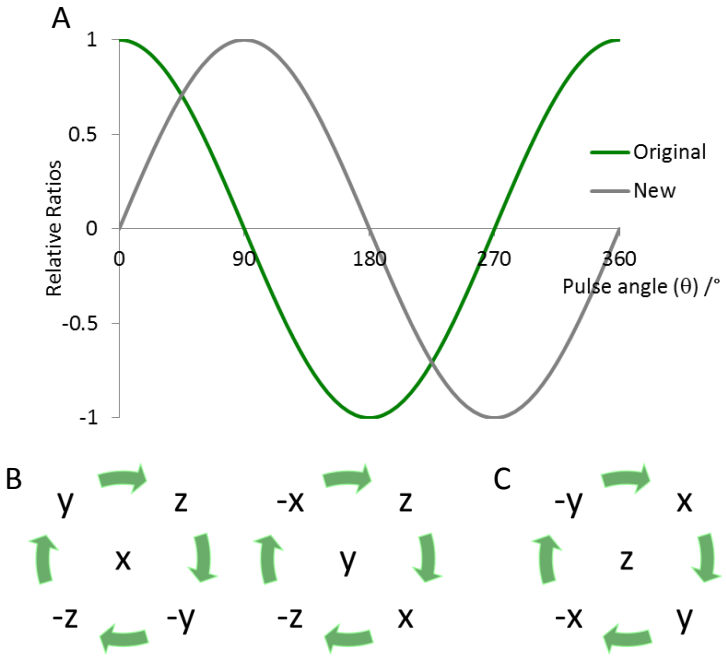

Figure 1.11: (A) Graphic representation of how the original and new operator vary as a function of the angle of the applied pulse. (B) The transformations with successive 90° pulses for pulse along the x axis (left) and along the y axis (right). (C) The evolution of x and y terms as a function of the chemical shift (Ω) and time (τ); (B) and (C) were adapted from Keeler.[32]

The results from the analysis of a one-spin system strongly resemble the results from the vector model and as such do not particularly demonstrate the need for the product operator approach over the vector model. One of the advantages of the product operator approach is that it is not restricted to spin systems with a single spin. To demonstrate this; a two-spin system, where the two spins are weakly coupled to one another, will be analysed. Weakly coupled spins are defined as spins which are coupled by a coupling constant which is smaller than the difference in chemical shift between the two spins. These spins may be homonuclear, for example two ^{1}H nuclei, or heteronuclear, for example one ^{1}H and one ^{13}C nuclei. Each of the spins can be described by the same four operators which described the single spin system, these combine to give a total of 16 operators (Table 1.1). These two spin can be labelled as I_1 and I_2, or as I and S, and the ½ and 2 on the various operators reflect normalisation constants for these terms. Some of the terms are familiar from the one spins system; I_x, I_y, I_z, S_x, S_y and S_z, which represent the in-phase operators for each of the two spins for the x, y and z axes. In addition to these terms there are four which represent multiple quantum coherences (shaded green in Table 1.1). Linear combinations of these operators give the zero and double quantum terms according to Equations (1.5)-(1.8). There are also five terms which are classed as antiphase operators (shaded grey in Table 1.1)

Table 1.1: Table of the 16 combinations of the four operators for the two spins *I* and *S*.

	½ E_2	S_x	S_y	S_z
½ E_1	½ E	S_x	S_y	S_z
I_x	I_x	$2I_xS_x$	$2I_xS_y$	$2I_xS_z$
I_y	I_y	$2I_yS_x$	$2I_yS_y$	$2I_yS_z$
I_z	$\hat{I}_z$	$2I_zS_x$	$2I_zS_y$	$2I_zS_z$

$$DQ_x = \frac{1}{2}(2I_xS_x - 2I_yS_y) \quad (1.5)$$

$$DQ_y = \frac{1}{2}(2I_xS_y + 2I_yS_x) \quad (1.6)$$

$$ZQ_x = \frac{1}{2}(2I_xS_x + 2I_yS_y) \quad (1.7)$$

$$ZQ_y = \frac{1}{2}(2I_xS_y - 2I_yS_x) \quad (1.8)$$

A two spin system allows the analysis of the spin echo sequence (Figure 1.12A). The spin echo is an essential building block for many more complex NMR experiments due to its ability to refocus chemical shift and/or scalar coupling. The spin echo follows a pulse, or collection of pulses in more complex experiments to generate observable magnetisation. The spin echo itself starts with a delay, τ, followed by a 180° pulse and a second delay, τ. For the refocussing to work, both of the delays have the same duration. This analysis will allow the behaviour of a two-spin system during RF irradiation and during periods of free precession to be demonstrated. Like the one-spin systems, the two spins systems evolve as a function of the chemical shift during free precession periods, in addition to this they evolve as a function of the scalar coupling, J, between the two spins, according to the schematic in Figure 1.12B. Both of these effects occur at the same time. However, they can be treated separately as the results are not linked and the same observations are made regardless of the order they are analysed.

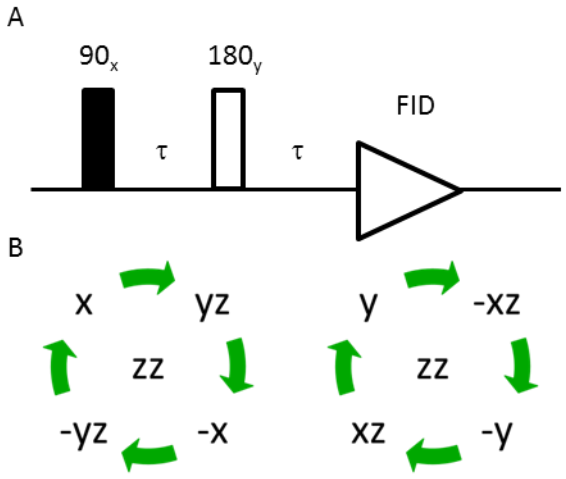

Figure 1.12: (A) Schematic of a basic spin echo pulse sequence. (B) Schematic representation of how I_x (left) and I_y (right) magnetisation evolves under J coupling (adapted from Keeler).[32]

In this example, the starting pulse is a pulse along x, the same as the pulse-acquire experiment which means we can use the result of the pulse-acquire experiment here. Starting from I_z, θ_x pulse generates the following terms

$$-I_y \cos(\Omega_I \tau) + I_x \sin(\Omega_I \tau)$$

Now the evolution as a function of the coupling needs to be considered. The $-I_y$ term evolves into $2I_xS_z$ and the I_y term evolves into $2I_yS_z$ both as a function of $\pi J_{IS}\tau$ there is a cosine relationship with the original operator and sine relationship with the new operator. Therefore, at the end of first delay, τ, the product operator description is as follows

$$-I_y\cos(\Omega_I\tau)\cos(\pi J_{IS}\tau) + 2I_xS_z\cos(\Omega_I\tau)\sin(\pi J_{IS}\tau) + I_x\sin(\Omega_I\tau)\cos(\pi J_{IS}\tau) + 2I_yS_z\sin(\Omega_I\tau)\sin(\pi J_{IS}\tau)$$

The next step is a 180° applied along the y axis. This changes the sign of each operator according to Figure 1.11B, since it is applied along the y axis the I_y terms do not change. The result of this is

$$-I_y\cos(\Omega_I\tau)\cos(\pi J_{IS}\tau) + 2I_xS_z\cos(\Omega_I\tau)\sin(\pi J_{IS}\tau) - I_x\sin(\Omega_I\tau)\cos(\pi J_{IS}\tau) - 2I_yS_z\sin(\Omega_I\tau)\sin(\pi J_{IS}\tau)$$

A second delay period follows the 180° pulse during which time the terms evolve again under the chemical shift and scalar coupling. First, the evolution under chemical shift will be examined, giving the following result

$$-I_y\cos^2(\Omega_I\tau)\cos(\pi J_{IS}\tau) + I_x\cos(\Omega_I\tau)\sin(\Omega_I\tau)\cos(\pi J_{IS}\tau) + 2I_xS_z\cos^2(\Omega_I\tau)\sin(\pi J_{IS}\tau)$$

$$+ 2I_yS_z\cos(\Omega_I\tau)\sin(\Omega_I\tau)\sin(\pi J_{IS}\tau) - I_x\cos(\Omega_I\tau)\sin(\Omega_I\tau)\cos(\pi J_{IS}\tau) - I_y\sin^2(\Omega_I\tau)\cos(\pi J_{IS}\tau)$$

$$-2I_yS_z\cos(\Omega_I\tau)\sin(\Omega_I\tau)\sin(\pi J_{IS}\tau) + 2I_xS_z\sin^2(\Omega_I\tau)\sin(\pi J_{IS}\tau)$$

Some of these terms cancel one another out and the trigonometric function in Equation (1.9) allows a simplification for the remaining terms and thereby the result from chemical shift evolution from the second delay τ is given below. The trigonometric function can only be used because the duration of the two delay periods are the same and the result of this is that the evolution as a function of the chemical shift is removed, it has been refocussed.

$$-I_y\cos(\pi J_{IS}\tau) + 2I_xS_z\sin(\pi J_{IS}\tau)$$

The evolution during the second delay period as a function of scalar coupling will now be considered using Figure 1.12B to give the terms below. Trigonometric functions may also be used here to provide further simplifications (Equations (1.10) and (1.11)).

$$- I_y \cos^2(\pi J_{IS}\tau) + 2(2I_xS_z \cos(\pi J_{IS}\tau)\sin(\pi J_{IS}\tau)) + - I_y \sin^2(\pi J_{IS}\tau)$$

$$= - I_y \cos(2\pi J_{IS}\tau) + 2I_xS_z \sin(2\pi J_{IS}\tau)$$

The same analysis can be performed on the other spin and thus the full result at the end of the spin echo sequence is

$$- (I_y + S_y) \cos(2\pi J_{IS}\tau) + (2I_xS_z + 2I_zS_x) \sin(2\pi J_{IS}\tau)$$

$$sin^2 A + cos^2 A \equiv 1 \quad (1.9)$$

$$cos^2 A - sin^2 A \equiv cos\, 2A \quad (1.10)$$

$$2\, sin\, A\, cos\, A \equiv sin\, 2A \quad (1.11)$$

The analysis of the spin echo sequence has allowed the behaviour of two coupled spins as consequence of RF pulses and free precession to be evaluated. Like the one-spin system, the two-spin systems evolve as a result of the RF pulse according to the diagrams in Figure 1.11B and as a function of the chemical shift during free precession according to Figure 1.11C. In addition to this, they evolve under their scalar coupling according to Figure 1.12B. This shows how by using the scalar coupling and appropriate delays magnetisation can be transferred from one spin to another. This concept is at the centre of many one and two dimensional NMR systems.

One class of operators not covered so far are the multiple quantum terms $2I_xS_x$, $2I_xS_y$, $2I_yS_x$ and $2I_yS_y$. Whilst these are not directly observable in an NMR experiment many pulse sequences make use of multiple quantum coherences. They are also important to describe some NMR experiments which utilise parahydrogen derived states, as will become apparent in Section 1.2.5. These can be created from antiphase terms using RF pulses; for example, a 90°_x pulse applied to both spins turns $2I_xS_z$ into $-2I_xS_y$. Multiple quantum terms evolve in the same way as the other terms under RF pulses and as a function of the chemical shift but they do not evolve as a function of scalar coupling between the two spins. The individual terms evolve using the

same rules described by Figure 1.11C, and combine in a known way according to Figure 1.13. The angle by which the terms evolves is dictated by the sum of the chemical shifts ($\Omega_I+\Omega_S$) for the double quantum terms and by the difference in the respective chemical shifts ($\Omega_I-\Omega_S$) for the zero quantum terms. This is because the transformation results in collections of terms which can be abbreviated by the trigonometric functions given in Equations (1.12) and (1.13). As with the previous transformations, the original operator varies with a cosine function and the new operator according to the sine function. A worked example of the evolution of ZQ_x into ZQ_y is shown below to demonstrate how the individual terms evolve to give this overall result.

$$cos\,A\,cos\,B \mp sin\,A\,sin\,B \equiv cos(A \pm B) \quad (1.12)$$
$$cos\,A\,sin\,B \pm sin\,B\,cos\,A \equiv sin(A \pm B) \quad (1.13)$$

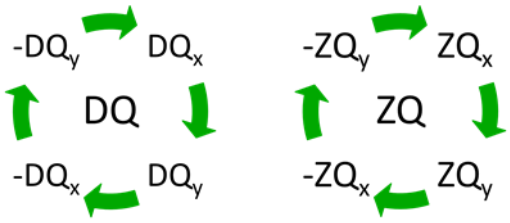

Figure 1.13: Schematic representation of the evolution of double quantum (*DQ*, left) and zero quantum (*ZQ*, right) operators evolved as a function of chemical shift. The *DQ* terms evolve as a function of the sum of the chemical shifts ($\Omega_I+\Omega_S$) and the *ZQ* terms evolve as a function of the difference in chemical shift ($\Omega_I-\Omega_S$).

Worked Example

The operators which are used to describe the ZQ_x term are $2I_xS_x$ and $2I_yS_y$ and these will evolve under $\Omega_I\tau$ and $\Omega_S\tau$, where Ω_I and Ω_S are the chemical shift offsets for the respective spins, using the rotations described in Figure 1.11C.

$$2I_xS_x + 2I_yS_y \xrightarrow{\Omega_I\tau I_z} 2I_xS_x\,cos\,\Omega_I\tau - 2I_yS_x\,sin\,\Omega_I\tau + 2I_yS_y\,cos\,\Omega_I\tau + 2I_xS_y\,sin\,\Omega_I\tau$$

$$\xrightarrow{\Omega_S\tau S_z} \begin{aligned} &2I_xS_x\,cos\,\Omega_I\tau\,cos\,\Omega_S\tau - 2I_xS_y\,cos\,\Omega_I\tau\,sin\,\Omega_S\tau \\ &-2I_yS_x\,sin\,\Omega_I\tau\,cos\,\Omega_S\tau + 2I_yS_y\,sin\,\Omega_I\tau\,sin\,\Omega_S\tau \\ &+2I_yS_y\,cos\,\Omega_I\tau\,cos\,\Omega_S\tau + 2I_yS_x\,cos\,\Omega_I\tau\,sin\,\Omega_S\tau \\ &+2I_xS_y\,sin\,\Omega_I\tau\,cos\,\Omega_S\tau + 2I_xS_x\,sin\,\Omega_I\tau\,sin\,\Omega_S\tau \end{aligned}$$

Grouping the terms based on their sine and cosine values and returning the normalisation constant ½ to the product operators gives the following result.

$$\begin{aligned} &½\,(2I_xS_x + 2\,I_yS_y)\,cos\,\Omega_I\tau\,cos\,\Omega_S\tau && + ½\,(2I_xS_x + 2I_yS_y)\,sin\,\Omega_I\tau\,sin\,\Omega_S\tau \\ &+ ½\,(2I_yS_x - 2I_xS_y)\,cos\,\Omega_I\tau\,sin\,\Omega_S\tau && - ½\,(2I_yS_x - 2I_xS_y)\,sin\,\Omega_I\tau\,cos\,\Omega_S\tau \end{aligned}$$

Using Equations (1.7)and (1.8) the operators can be substituted with ZQ_x and ZQ_y and grouping the ZQ_x and ZQ_y terms together generates the following terms.

$$ZQ_x(cos\,\Omega_I\tau\,cos\,\Omega_S\tau + sin\,\Omega_I\tau\,sin\,\Omega_S\tau) \qquad + ZQ_y(cos\,\Omega_I\tau\,sin\,\Omega_S\tau - sin\,\Omega_I\tau\,cos\,\Omega_S\tau)$$

These can be simplified using the trigonometric identities in Equations (1.12) and (1.13) to give the final result in Equation (1.14).

$$ZQ_x\,cos(\Omega_I - \Omega_S)\tau + ZQ_y\,sin(\Omega_I - \Omega_S)\tau \tag{1.14}$$

1.2.5 NMR Theory relating to parahydrogen

The description of NMR experiments in terms of product operators is different when parahydrogen in used as the starting state is not I_z but the same rules apply. NMR theory using the parahydrogen starting state will now be discussed.[13-15, 32]

Parahydrogen has a pure spin state denoted by αβ – βα, this is a singlet state and as such is described as $-½(2I_xS_x + 2I_yS_y + 2I_zS_z)$ in product operators. These are a combination of the longitudinal two spin order term $2I_zS_z$ and ZQ_x (Equation (1.7)). The evolution of the singlet state will now be analysed following the application of RF pulse along the x axis θ_x to demonstrate the differences between parahydrogen and Boltzmann or thermal situations. This will be applied to both spins sequentially and to each of the operators in turn, the –½ normalisation factor has been neglected from this and all subsequent analysis. Since the pulse chosen in this experiment is along the x axis the $2I_xS_x$ term is unchanged in this analysis. The resulting terms following the analysis of $2I_yS_y$ and $2I_zS_z$ are given below, where the observable terms, in green, are simplified using the trigonometric identity in Equation (1.11). The same

observable terms are generated from $2I_yS_y$ and $2I_zS_z$ only with the opposite sign to one another, and therefore cancel one another out and there is no NMR signal for parahydrogen.

$$2I_xS_x \xrightarrow{\theta I_x \theta S_x} 2I_xS_x$$

$$\begin{aligned} 2I_yS_y &\xrightarrow{\theta I_x \theta S_x} 2I_yS_y\cos^2\theta + 2I_yS_z\cos\theta\sin\theta + 2I_zS_y\sin\theta\cos\theta + 2I_zS_z\sin^2\theta \\ &= 2I_yS_y\cos^2\theta\sin\theta + 2I_zS_z\sin^2\theta + (I_yS_z + I_zS_y)\sin 2\theta \end{aligned}$$

$$\begin{aligned} 2I_zS_z &\xrightarrow{\theta I_x \theta S_x} 2I_zS_z\cos^2\theta - 2I_zS_y\cos\theta\sin\theta - 2I_yS_z\sin\theta\cos\theta + 2I_yS_y\sin^2\theta \\ &= 2I_zS_z\cos^2\theta + 2I_yS_y\sin^2\theta - (I_yS_z + I_zS_y)\sin 2\theta \end{aligned}$$

When parahydrogen adds to a metal complex further evolution is observed, provided the two former parahydrogen protons are now in chemically or magenetically inequivalent environments. This evolution occurs as a consequence of the chemical shift from between the two protons in the product. This evolution takes place around the z-axis and as such the $2I_zS_z$ does not evolve. The ZQ_x term does evolve, into ZQ_y based on the cycle described in Figure 1.13 giving Equation (1.14). In most parahydrogen experiments, the addition to the metal complexes does not occur synchronously. This means that the starting point for the evolution is different from one spin to the next, therefore decoherence of the ZQ_x term is observed and the amplitude of this term averages to zero, and only the $2I_zS_z$ terms remains. The observable operators are anti-phase in character and account for the characteristic anti-phase NMR signals observed in PHIP experiments. There is also a sin2θ relationship associated with these terms; this changes the pulse angle which is associated with the largest NMR signals. Now these are observed using a 45° pulse rather than a 90° pulse observed using standard NMR methods.

Parahydrogen may also add to the metal complex in a synchronous manner and this does not lead to the decoherence of the ZQ_x term and its evolution needs to be considered. This scenario is possible using a suitably photoactive metal complex with in situ photolysis, using the setup described in Section 8.3.2. This has been used with a ruthenium phosphine dihydride

complex $[Ru(H)_2(CO)(PPh_3)_3]$, the loss of H_2 from this complex occurs during the 10 ns laser pulse at 355 nm and the coordination of H_2 to the reactive intermediate occurs on an 1.4 μs timescale.[15] This means that the parahydrogen adds as one and the ZQ_x term evolves synchronously into ZQ_y at a frequency which relates to the chemical shift difference between the two former parahydrogen protons according to Equation (1.14). Hence, the amplitude of the ZQ_x terms change as a function of the chemical shift difference and now it is not always true that the ZQ_x and $2I_zS_z$ terms cancel one another out. The evolution of these terms as a function of time is depicted in Figure 1.14, at time $\tau = 0$ the amplitude of the observable terms from $2I_zS_z$ equal those from $-ZQ_x$. At time $\tau = t$, however, the amplitude of the observable terms, and thus signal, is given by $1-\cos(\Omega_1-\Omega_2)\tau$, provided there is time resolution between the addition of parahydrogen and the interrogation of the spin states after evolution.

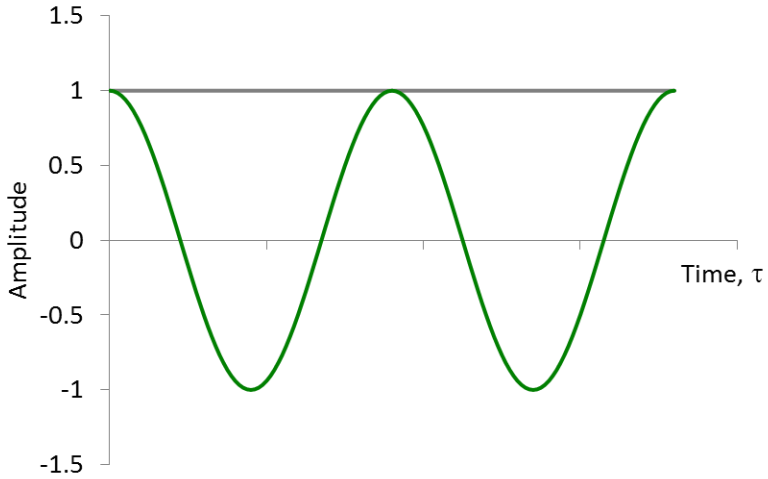

Figure 1.14: Graphical representation of the evolution of the $2I_zS_z$ and $-ZQ_x$ terms as a function of time. The amplitude of the $2I_zS_z$ does not vary time and $-ZQ_x$ evolves as a function of $\cos(\Omega_I-\Omega_S)\tau$.

The ZQ_y will also generate observable magnetisation following an RF pulse, and the states that this creates can be interrogated in the same manner as for the other starting states. As shown below in Equation (1.15), this results in the antiphase terms $2I_zS_x$ and $2I_xS_z$. This time, however, they evolve as a function of sinθ. This means that the maximum signal which results from this term is seen with a 90° pulse rather than a 45° pulse. These terms will evolve following the addition to a metal centre as a function of $\sin(\Omega_I-\Omega_S)\tau$ and this will result in the amplitudes of

the signals in the NMR spectrum varying by the same function. For $Ru(H)_2(CO)(PPh_3)_3$, the chemical shift difference between the two hydride ligands was 1098 Hz and an NMR signal oscillating as a sine function with a frequency of 1101 ± 3 Hz was observed when a 90° pulse was used after a single laser pulse and an incrementing pump-probe delay.[15]

$$2I_yS_x - 2I_xS_y \xrightarrow{\theta I_x \theta S_x} 2I_yS_x \cos\theta + 2I_zS_x \sin\theta + 2I_xS_y \cos\theta + 2I_xS_z \sin\theta \quad (1.15)$$

1.3 Activation of small molecules by metal complexes

To unlock the potential of parahydrogen it must add to a metal centre in a pairwise manner in a process known as bond activation. The process of H–H bond activation will now be discussed as well as the activation of Si–H bonds since triethylsilane will be utilised in this research as a test substrate to study the bond activation capabilities of the metal complexes.

1.3.1 H–H bond

Transition metal hydrides play important roles in many catalytic processes such as hydrogenation[33], hydroformylation[34] and hydrosilation[35] reactions. Catalytic hydrogenation reactions involve the transfer of two hydrogens to an unsaturated organic compound, such as those containing unsaturated carbon-carbon bonds, as well as other functional groups, such as ketone, imines and amide groups. The two protons maybe transferred from a suitable organic hydrogen donor, such as formic acid or isopropanol, through a method termed transfer hydrogenation[36] or via the addition and activation of molecular hydrogen, H_2, to the metal centre.[33]

The H–H bond of molecular hydrogen may add to a metal centre through many different pathways,[37] two of which are shown in Figure 1.15. The first is a σ bond metathesis pathway.[38-41] This method results in an uneven split of the H–H bond and gives an H^+ and an H^-. The second is a homolytic pathway during which the bond breaks evenly and both hydrogens add

to the metal centre and elicits a 2 point increase in the metal centre's oxidation state; this is why this route is also referred to as the oxidative addition pathway.

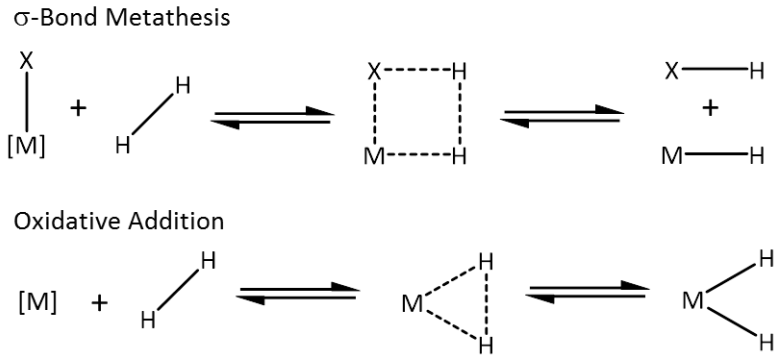

Figure 1.15: Schematic representation of the σ-bond metathesis (top) and oxidative addition (bottom) reaction pathways of H_2.[42, 43]

Both pathways involve the side on coordination of dihydrogen as a transition state. In 1984 Kubas[44] isolated for the first time a complex where dihydrogen has interacted with a metal centre and retained the H–H bond. Following this discovery it was determined that the possible products from the reaction of dihydrogen with a transition metal do not exist as either dihydrogen complex or dihydride complex but on a continuum between these two extremes and the complexes are grouped according to the distance between the two hydrides (Figure 1.16).[43, 45]

η^1-coordination	η^2-coordination Dihydrogen Complex	Elongated Dihydrogen	Compressed Dihydride Complex	Dihydride Complex
0.74 Å	0.8 – 1.0 Å	1.0 – 1.2 Å	1.2-1.6 Å	> 1.6 Å

Figure 1.16: Schematic representation of the continuum of metal dihydrogen and metal dihydride complexes, adapted from Crabtree[43] and Devarajan *et al.* [42]

This process can be rationalised by considering the molecular orbitals that are involved in the interaction between the metal centre and the dihydrogen ligand.[46] This approach is analogous to the Dewar-Chatt-Duncanson model[47, 48] used to rationalise the coordination of double

bonds to a metal centre. The bonding has two synergic components. Firstly, the σ orbital of the H–H bond donates electron density into an empty d orbital with the appropriate symmetry. Secondly, there is back-donation from filled d orbitals of the metal centre into the empty anti-bonding σ^* orbitals on the H_2 ligand. Both components act to weaken the H–H bond. It is thought that the donation from the metal into the antibonding σ^* orbital is the dominant force behind whether the H–H bond is retained in the product. With an increase in back donation the H–H bond begins to elongate and eventually breaks to give the dihydride complex. The factors that affect this are the electron density of the metal centre and the properties of the other ligands within the system. When these ligand are strong π acceptors, for example the CO ligands in $[(PPr^i_3)_2(CO)_3W(\eta^2\text{-}H_2)]$, the degree of back donation is less and the H–H bond is not cleaved. With electron rich metal such as $[(PPh_3)_3RhCl]$ the dihydride complex is observed. This bond activation process is also observed with X–H bonds where X can be carbon,[49] silicon[50] and boron.[51]

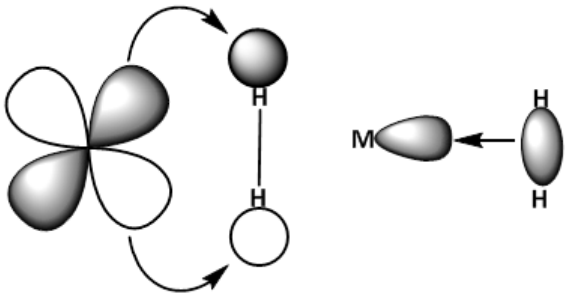

Figure 1.17: Schematic representation of the bonding interactions between a metal centre and dihydrogen.

The spectroscopic characteristics of metal-hydrides and metal-dihydrogen complexes are distinctive and allow for their characterisation. The ^1H NMR chemical shifts of metal-hydrides are, falling in the chemical shift range of δ 0 to –30 outside of the range of most other proton environments. Unfortunately, metal-dihydrogen species also fall in this range. There are, however, other NMR observations that can be used to distinguish between these two types of ligands. The first method involves substituting H_2 with HD and measuring their scalar coupling. In free HD, J_{HD} is 43.5 Hz; in a dihydrogen complex this coupling is only moderately smaller,

typically ~25 Hz since the H–D bond retains intact.[52] In a dihydride complex, however, this coupling is less than 5 Hz since the bond between H and D has been broken and this coupling now reflects nuclei separated by two bonds. The second method which can be used utilises the difference in relaxation parameter, T_1 in NMR. T_1 refers to the spin-lattice relaxation mechanism and this effect is dominated by the dipole-dipole interactions between adjacent NMR active nuclei. The magnitude of these interactions is proportional to distance between the two nuclei, r_{HH}^{-6}. For a dihydrogen complex, the distance between the two protons is shorter than in a dihydride complex and thus the dihydrogen complex has the shorter T_1 value. Typical T_1 values are less than 160 ms for a dihydrogen complex and greater than 350 ms for a dihydride.[53, 54] The specific relationship between bond length and T_1 is given by Equation (1.16) where $r_{H...H}$ refers to the distance between the two hydrogen atoms and ν is the magnetic frequency of the spectrometer.

$$r_{H...H}/\text{Å} = 5.815(T_1/\nu)^{1/6} \quad (1.16)$$

Infrared spectroscopy can also be used to identify metal-hydride complexes, with the M–H stretching vibrations appearing between 1400 –2300 cm^{-1} with deformation modes observed between 700 and 900 cm^{-1}.[55] It is for this reason, that Infrared spectroscopy has been widely used in the study of transition metal hydride complexes, this research has recently been reviewed by Procacci and Perutz.[55] By contrast, metal-dihydrogen complexes are associated with H–H stretching modes between 2400 and 3200 cm^{-1} and MH_2 stretching in the region of 1300 and 1600 cm^{-1} for the symmetric stretching modes and 850 and 1000 cm^{-1} for the antisymmetric.[52]

1.3.2 Si–H bond

The oxidative addition and η^2-coordination of Si–H bonds are also observed, through the same mechanism as the activation of H_2 bonds. The Si–H bond is typically weaker than a H–H bond

and therefore is more likely to form oxidative addition products. This observation can be rationalised by the σ^* orbital of the silyl bond being larger and more diffuse which makes them more accessible to the metals filled orbitals increase the degree of back donation possible weakening the bond. As with dihydrogen, the coupling between the two nuclei is indicative of the binding mode. Since silicon is also a spin-½ nucleus, this can be measured directly from the complex without the need for deuteration. Uncoordinated, or free, silanes typically exhibit have a J_{HSi} of 200 Hz, this shrinks to ~100 Hz in a M-η^2-(Si–H) interaction and is less than 20 Hz when oxidative addition has occurred.

1.4 Photochemistry

1.4.1 Overview

There are several routes through which a small molecule may react with a metal complex, these include: a reaction with a stable coordinatively unsaturated complex, or a metal complex which contains a coordinated alkene ligand which can become hydrogenated creating a reactive species. Alternatively, they can be formed using a metal complex that contains a suitable thermally or photochemically labile ligand which forms a coordinatively unsaturated intermediate *in-situ* which may then go on to react with the small molecule This work involves the use of photochemistry to prepare suitable intermediates which may undergo reactions with parahydrogen or other ligands.

The study of photochemistry concerns reactions initiated by light. The absorption of a photon of light allows electronically excited states to be accessed. The excited state may have different geometries and orbitals of different symmetries which provide routes to different reactivity to the thermal options. The use of light circumvents the requirement to heat a compound to prompt reactivity and therefore the reactions may be performed at lower

temperatures allowing the study of reactions involving thermally unstable intermediates or products.

This work involves the study of organometallic complexes where the use of light can be used to prompt the loss of a coordinated ligand and can provide routes for isomerisation, ligand substitution and bond activation reactions. There are a range of different photolabile ligands which can be used allowing for contrasting reactivity which include alkenes,[56, 57] CO[58, 59] and hydride(s)[55] ligands.

1.4.2 Time-Resolved methods

Time-resolved methods have been developed to allow the study and detection of reaction intermediates giving insight into the reaction mechanism. These measurements are possible through the coupling of a light source, typically a laser, and an analytical probe. The time resolution for the method depends on the timing of both the irradiation and detection steps. The development of lasers with ultra-short pulses has greatly improved the time resolution with pico- to femto-second (10^{-12} – 10^{-15} s^{-1}) reactions now being observable. There are a wide range of spectroscopic methods which can be used as the analytical probe which include UV-visible absorption[60] and infrared spectroscopy.[61, 62] Both these methods have high sensitivity and fast detection steps and as a consequence these methods have been used to study reactive intermediates with a short lifetimes on the order of pico- or femtoseconds. These are vastly shorter timescales than can be routinely used with NMR where the detection step at best is on the order of seconds or minutes if signal averaging is required.

1.4.3 In-situ NMR

1.4.3.1 Photolysis methods

The use of NMR in time-resolved methods is limited owing to the poor sensitivity and slow detection times. *In-situ* NMR methods have been developed providing much greater structural

information on reaction intermediates than other analytical methods used in time-resolved studies. *In-situ* NMR methods require a light source to be incorporated with the NMR spectrometer to allow for irradiation within the probe head where the NMR experiments take place. This can be achieved by directing the light down into the probe head from the top of the spectrometer ("top down") or by directing the light underneath the spectrometer and up to the sample ("down top"), (Figure 1.18).[63] The "top down" approach has been used by the Ball group, using 100 W Hg arc lamp with fibre optic cable as the light source.[64] The advantage of the "top down" approach is that it only requires modification to the NMR tube and therefore is not restricted to one spectrometer.[65]

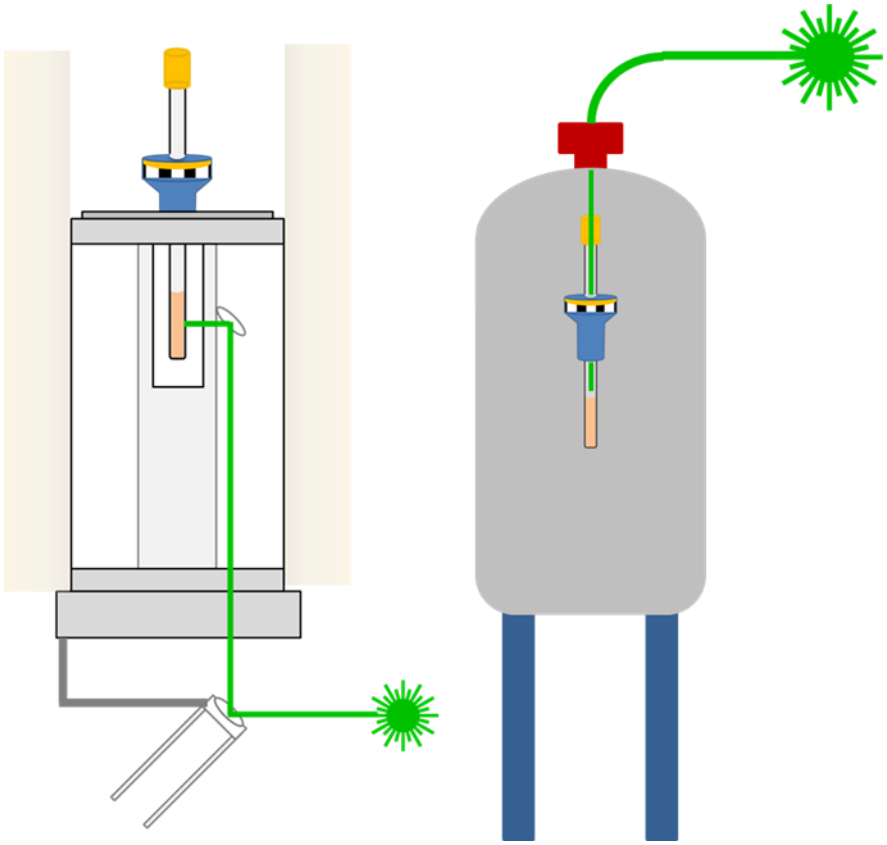

Figure 1.18: Schematic representation of the two *in-situ* NMR photolysis methods (left) bottom-up (adapted from Calladine *et al.*[66]) and (right) top-bottom.

The "top-down" approach to *in-situ* photochemistry has been used by a number of groups in vastly varied fields. These have included the photoisomerisation of azo dyes where *trans*/*cis* isomerisation is prompted following continuous irradiation from a argon-krypton mixed gas

laser.[67] Distinctive chemical shift differences between the *cis* and *trans* isomers were observed and it was proposed that this could be used in predicting the isomer assignment in more complex azo dyes.[67] Subsequent work combined the NMR measurements with DFT calculations allowing the *cis* isomers of commercial dyes to be observed and the structural characteristics of the two isomers to be identified.[68] More recently this technique has permitted the kinetics of these systems to be explored in more depth.[69] The photoinduced isomerisation of azobenzene has also been utilised in the field of molecular switches using macromolecules containing a number of different azobenzene linkers.[70] *In-situ* photolysis using a 150 W Xenon high stability lamp with a monochromator selecting 470 nm light coupled to a 700 MHz spectrometer allowed the isomerisation of a tetraazo macromolecule system to be studied.[71] The sequential isomerisation of the azobenzene linkers was observed and each of the isomeric forms were observed and characterised by 2D NMR methods. Through the combination of the *in-situ* NMR spectra observations and DFT calculations the relative stability of each of the isomers were analysed. The (*E*, *Z*, *E*, *Z*) isomer was found to have the highest free energy of activation which was attributed to the ring strain associated with this isomer. Other research fields using *in-situ* photochemistry with NMR spectroscopy have included: using titania coated NMR tubes to study the semiconductor photocatalysed oxidation of toluene where a Xe-arc lamp was used as the irradiation source.[65] Platinum azide complexes have also been studied as potential photochemotherapeutic agents[72] and the photooxidation of benzyl alcohols into the corresponding aldehydes used as a test reaction for an LED based *in-situ* NMR procedure.[73]

In York, however, the bottom up approach is being used, where modified NMR probes are used in conjunction with mirrors and appropriate light sources to direct the light on to the side of the NMR sample within the probe head. Early work used a He:Cd cw laser with a 400 MHz spectrometer[74] although this setup has since been superseded by a Nd:YAG laser coupled to a 600 MHz spectrometer.[66] The disadvantage of using this approach is that it requires holes to be drilled into the probe head to allow the light to be directed on to the side of the sample.

This is potentially risky and restricts the measurements to a single NMR probe but once the modifications have been made any NMR sample maybe used including Young's tapped NMR tubes to allow the study of air sensitive materials and reactions involving gases such as *p*-H_2.

1.4.3.2 Low temperature photolysis and characterisation

Low temperature *in-situ* irradiation and NMR spectroscopy has proved particularly fruitful in the study of alkane complexes. A number of half sandwich rhenium complexes have been studied (Figure 1.20). When $CpRe(CO)_2(PF_3)$ (Figure 1.20A) was irradiated at 185 K in cyclopentane three new species formed.[75] Two were consistent with alkane complexes and were characterised as $CpRe(CO)_2$(alkane) and $CpRe(CO)(PF_3)$(alkane) demonstrating that there are two competing photochemical processes in this system where either the CO or phosphine ligands may be lost. The third product formed corresponded to the C–H activation of the alkane to give the corresponding alkyl hydride complex. In $CpRe(CO)_2(N_2)$ (Figure 1.20B), however, *in-situ* photolysis only resulted in the loss of N_2 was observed giving $CpRe(CO)_2$(alkane) as the sole product.[66] These observations were supported by time-resolved IR measurements.[66, 76]

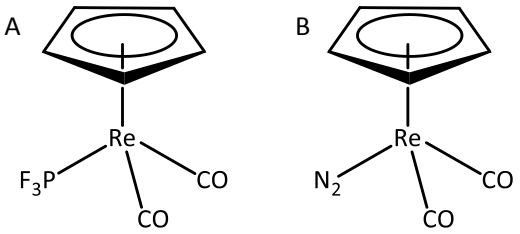

Figure 1.19: Starting complexes for the study between rhenium biscarbonyl complexes and alkanes.[66, 75]

Similar systems, which differ in the identity of the top ligand, have been studied. Recently $[(HEB)Re(CO)_3]^+$ (Figure 1.20A), where HEB refers to an η^6-hexaethylbenzene ligand, has been studied with alkane ligands and highly fluorinated solvents, such as $CF_3CH_2CF_3$.[77] Irradiation in the presence of cyclopentane at 193 K resulted in the loss of a CO ligand and the coordination of cyclopentane in preference over the fluorinated solvent indicating a preference for C–H

over C–F coordination. A third rhenium complex has also been studied (Figure 1.20B) where the half sandwich ligand has been replaced by a half sandwich cobalt complex with three diethylphosphito ligands which coordinate to the tricarbonyl rhenium centre also.[78] This too was studied using low temperature irradiation, at 178 K, which resulted in the loss of a CO ligand and coordination of the alkane using cyclopentane, cyclohexane and pentane.

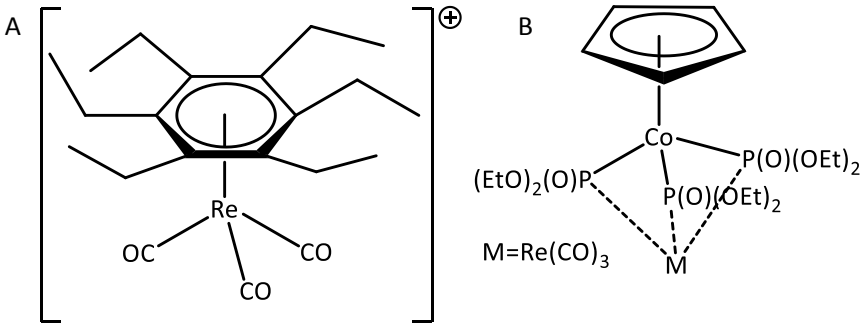

Figure 1.20: Rhenium complexes used to study the formation of alkane complexes.[75, 77, 78]

The reactivity between metal carbonyl complexes and coordinated alkane ligands has not been restricted to rhenium metal centres, manganese complexes have also been investigated. $CpMn(CO)_3$ has been found to undergo CO loss when photolysed at 355 nm at 133 – 136 K using liquid propane or butane as the solvent.[79] The same complex has been studied towards ethane and isopropane.[80]

1.4.3.3 Coupling of *in-situ* NMR and parahydrogen enhancements

In York, these *in-situ* photolysis methods have also been used to study reactions between metal complexes and parahydrogen providing improvements in the detection of intermediates and minor products or isomers in these systems.[29, 30] The reactivity of the tungsten dinitrogen complex, $[W(N_2)_2(dppe)_2]$ (Figure 1.21A), was studied with H_2.[81] The two dinitrogen ligands were demonstrated to be thermally labile at 328 K forming the tetrahydride complex, $[W(H)_4(dppe)_2]$ (Figure 1.21C). When the reactivity of this complex was studied using low temperature *in-situ* photolysis a trihydride species was identified, corresponding to the activation of H_2 and the *ortho*-metalation of a C–H bond of the dppe ligand (Figure 1.21B) and

was proposed to be an intermediate in the formation of the tetrahydride complex. A further product was also identified as $W(H)_3(OH)(dppe)_2$ (Figure 1.21D) which arose through the reaction with water impurity in the NMR solvent. PHIP enhanced signals were observed in each of these products.

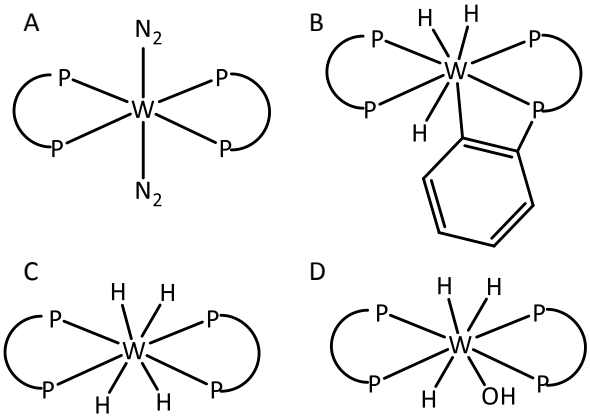

Figure 1.21: (A) Starting tungsten complex (B)-(D) Products formed following irradiation of (A) with *p*-H_2.[81]

The reactivity of a range of ruthenium complexes have also been studied with parahydrogen. The irradiation of $Ru(CO)_3$(dpae) and $Ru(CO)_3$(dppe) resulted in the loss of a carbonyl ligand followed by *p*-H_2 addition to give the corresponding $Ru(H)_2(CO)_2$(dpre) species where the two hydride ligands are PHIP enhanced (Figure 1.22).[82, 83] When this was performed with the arsine analogue, in the resulting dihydride complex, 100 % conversion of the *p*-H_2 encoded spin state was observed giving a signal enhancement of 31,000.[82] When this study was repeated with $Fe(CO)_3$(dppe), however, whilst the corresponding dihydride formed, it did not exhibit any PHIP enhancements.[84] This observation was attributed to the electronic state of the intermediate of the iron complex being a triplet and therefore this can facilitate the conversion of parahydrogen into orthohydrogen returning the encoded spin state back to its Boltzmann distribution. The ruthenium derivatives, however, have an intermediate with a singlet electronic state and hence the spin-encoded state has been retained and the enhancements are observable.

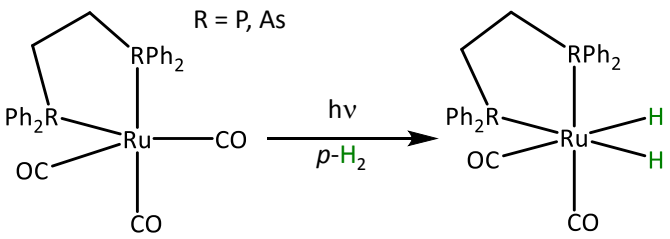

Figure 1.22: Reaction scheme for the photochemical reaction of $Ru(drpe)(CO)_3$ with *p*-H_2 where R is phosphine or arsine.[82, 83]

Using a related system, $Ru(CO)_2(dppe)(PPh_3)$ (Figure 1.23A), where one CO ligand has been replaced with a PPh_3 ligand its thermal and photochemical activity were investigated.[85] When the complex was heated in the presence of parahydrogen the dihydride $Ru(H)_2(CO)_2(dppe)$ formed, the same product was obtained using $Ru(CO)_3(dppe)$ as the starting complex and therefore it was concluded that heating resulted in the loss of a PPh_3 ligand. When $Ru(CO)_2(dppe)(PPh_3)$ was irradiated in the presence of parahydrogen, however, a second product was also detected. This corresponded to the loss of a CO ligand to give $Ru(H)_2(CO)(dppe)(PPh_3)$ as two isomers (Figure 1.23B and C) previously only complex B has been detected. The simultaneous loss of both a CO and PPh_3 was observed photochemically when $Ru(CO)_2(dppe)(PPh_3)$ was irradiated in the presence of pyridine to give complex D (Figure 1.23). This observation has also been observed in studies where the dppe ligand has been replaced by two monodentate phosphine ligands.[86]

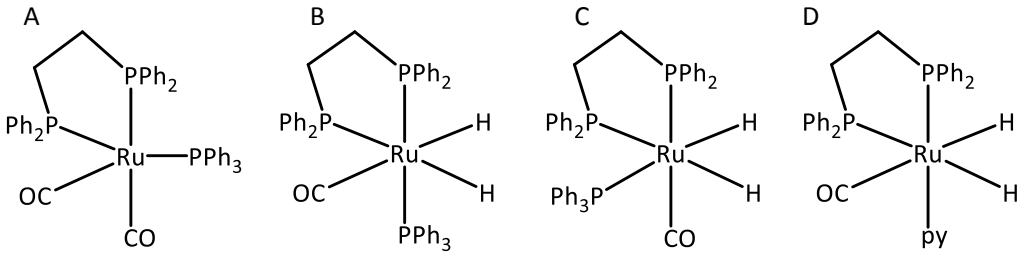

Figure 1.23: (A) $Ru(CO)_2(dppe)(PPh_3)$, (B) and (C) $Ru(H)_2(CO)(dppe)(PPh_3)$ and (D) $Ru(H)_2(CO)(dppe)(pyridine)$.[85]

Most recently, the combination of *in-situ* irradiation and parahydrogen has been used to study $Ir(H)_2(CO)(I)(PPh_3)$.[87] The dihydride complex was prepared thermally by the hydrogenation of the iodide analogue of Vaska's complex, $[Ir(CO)(I)(PPh_3)]$. Upon irradiation the complex was

found to undergo the reductive elimination of H_2 to revert back to this complex. When this occurs in the presence of *p*-H_2 with a single laser pulse and a precise variable time delay PHIP-enhanced signals were observed. The growth of these signals allowed the rate constant associated with H_2 addition to the unsaturated species to be measured as (3.06 ± 0.40) x10^2 mol^{-1} dm^3 s^{-1}, consistent with the literature values, validating the method.[88, 89]

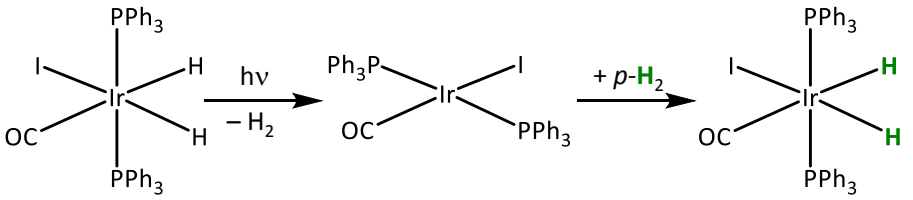

Figure 1.24: Reaction scheme for the photochemical reaction between $Ir(H)_2(CO)(I)(PPh_3)$ and *p*-H_2.[87]

1.5 Photochemistry of ruthenium phosphine dihydride complexes

1.5.1 *cis*-$[Ru(H)_2(PP)_2]$ complexes

Ruthenium phosphine dihydride complexes have been demonstrated to be suitable photochemical precursors through the reductive elimination of H_2 and the formation of a reactive intermediate which may undergo further reactivity.[55] The behaviour of complexes of the type *cis*-$[RuH_2(PP)_2]$, where PP refers to a bischelating phosphine, have been extensively studied.[90-94] Following the reductive elimination of H_2, a square planar $Ru(PP)_2$ intermediate forms which is capable of activating X–H bonds for a range of substrates, including HBpin and Et_3SiH, or coordinating other ligands such as CO or ethene (Figure 1.25). These studies have been performed with a range of different bidentate phosphines (Figure 1.26). The activity of different ethyl-bridged phosphines was studied towards H_2, CO and ethene.[90] The resultant reactivity was found to adhere to the following trends dfepe < dppe < depe < dmpe for the different phosphines and ethene < CO < H_2 for the different substrates. This preference for substrates was also observed when dmpm was used as the chelating phosphine.[91] These studies have also extended to monodentate and tetradentate phosphine ligands.

$Ru(H)_2(PMe_3)_4$ was found lose a PMe_3 ligand in addition to H_2 forming both $Ru(H)_2(PMe_3)$ and $Ru(PMe_3)_4$ intermediates which underwent reactions with CO and Et_3SiH.[95] $Ru(H)_2(PP_3)$, where PP_3 is $P(CH_2CH_2PPh_2)_3$, was found to undergo substitution reactions with N_2, CO and ethene as well as bond activation of C–H bonds of benzene and PP_3 as well as the Si–H bond of Et_3SiH.[96]

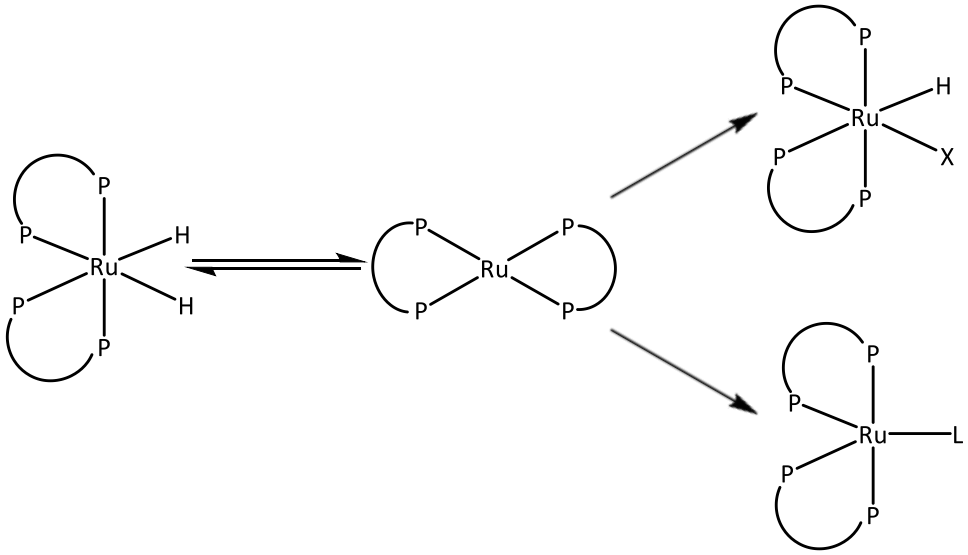

Figure 1.25: Reaction scheme for $Ru(H)_2(PP)_2$.[90-94]

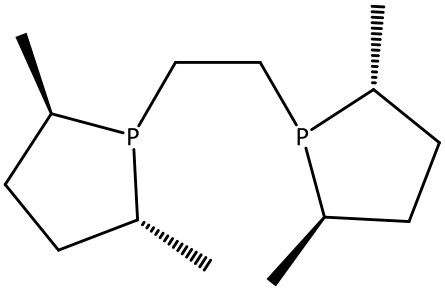

(R,R)-Me-BPE

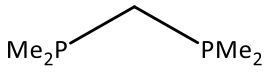

dmpm

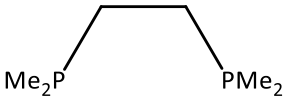

dmpe

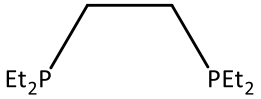

depe

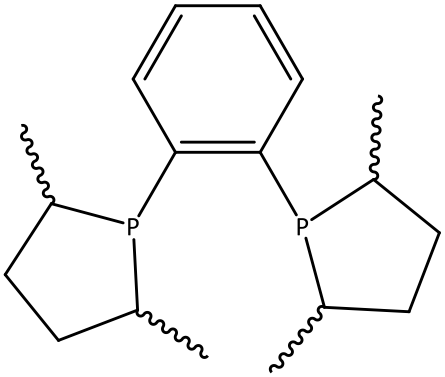

(R,R)-Me-DuPHOS
(S,S)-Me-DuPHOS

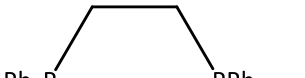

dppe

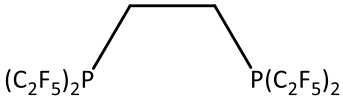

depe

Figure 1.26: Examples of bidentate (PP) ligands studied.[90-94]

1.5.2 Ruthenium phosphine carbonyl dihydride complexes

Complexes of the type $Ru(H)_2(CO)(P)_3$ have also been studied extensively, where $(P)_3$ may refer to three monodentate phosphine ligands, a combination of a mono- and bidentate ligands or a tridentate phosphine (Figure 1.27). The replacement of a phosphine ligand with a CO ligand offers the opportunity to follow the reactivity by infrared spectroscopy using the CO-stretching vibration. Time-resolved infrared spectroscopy was used to follow the reductive elimination of H_2 from $Ru(H)_2(CO)(PPh_3)_3$ and found that the process was complete within 6 ps of the laser pulse.[97]

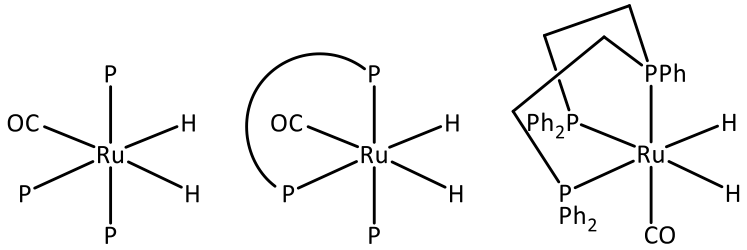

Figure 1.27: Structural motifs for ruthenium carbonyl dihydride complexes containing (A) three monodentate phosphine ligands,[95] (B) a monodentate and bidentate phosphine ligand and (C) a tridentate phosphine ligand.[96]

The use of CO potentially provides a second photolabile ligand which could result in competing reaction pathways with $Ru(H)_2(CO)(PPh_3)_3$ and $Ru(H)_2(CO)(etp)$, however, only H_2 loss was observed photochemically.[97, 98] $Ru(H)_2(CO)(etp)$ was studied in the presence of CO, ethene and triethylsilane to form the respective substitution or bond activation products.[96] The rates of these reactions were determined and the activity of the different ligands obeyed the following order H_2 > ethene > CO > Et_3SiH. The magnitude of these rates suggested that the reaction does not proceed via a solvent-stabilised intermediate nor an intermediate with a triplet ground state since both of these situations would have resulted in a slower reaction rate.

Further studies were performed where one of the phosphine ligands has been swapped for the N-heterocyclic carbene (NHC) IEt_2Me_2.[99] Low temperature *in-situ* irradiation revealed two further isomers of this complex as well as a cyclometallated product (Figure 1.28). With prolonged irradiation times the photochemical loss of PPh_3 was proposed resulting in a

$Ru(H_2)(H)_2$ species when performed under an atmosphere of H_2 and $Ru(H)_2(CO)(IEt_2Me_2)(PPh_3)(py)$ when performed with an excess of pyridine (py). It was subsequently determined that phosphine loss plays a role in the isomerisation process also.

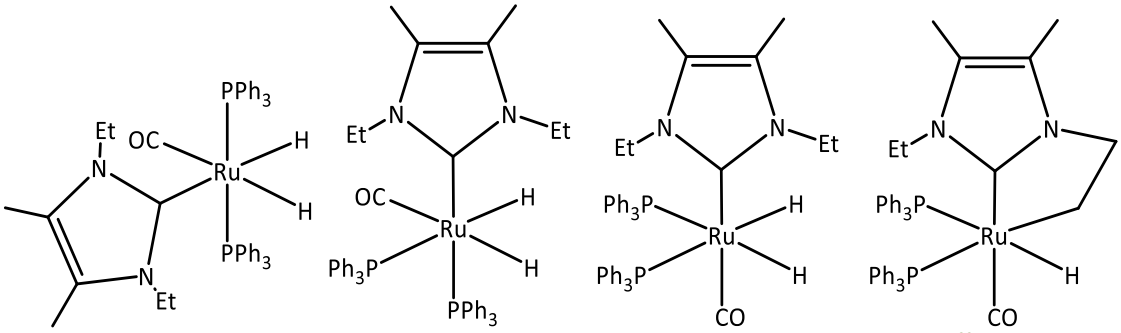

Figure 1.28: $Ru(H)_2(CO)(IEt_2Me_2)(PPh_3)_3$ isomers and cyclometallated NHC product.[99]

1.6 Aims and studies described in this thesis

The aims of this work were to investigate the photochemical activity of different ruthenium and rhodium-based organometallic complexes towards small ligands such as DMSO and triethylsilane. Once their photoactivity had been demonstrated, appropriate complexes were then studied with parahydrogen with the intention of making time-resolved NMR measurements. Suitable complexes were those where the resulting dihydride products contained chemically and/or magnetically distinct hydride ligands. This was induced through the inclusion of an asymmetric or chiral ligand or as a consequence of the arrangement of the ligands in the metal complex. When these reactions occurred on a suitable timescale, the coherent retention of the zero quantum coherence of the parahydrogen singlet state may occur providing an opportunity to observe the evolution of this singlet state.

An outline of the studies described in this thesis is provided below:

Chapter Two: The photochemistry of three half sandwich rhodium alkene complexes, $CpRh(CH_2{=}CHSiMe_3)_2$ **2.1**, $CpRh(COE)_2$ **2.2** and CpRh(COD) **2.3** was studied using *ex-situ* irradiation and their reactivity towards trimethylvinylsilane, DMSO and triethylsilane

investigated. The starting complexes and photoproduct are characterised by NMR spectroscopy and the reaction kinetics studied using relaxation kinetics (Appendix).

Chapter Three: The reactivity of **2.1** and $CpRh(CH_2=CHSiMe_3)(DMSO)$ **2.4** towards *p*-H_2 was studied using the laser based *in-situ* irradiation NMR method thereby providing two routes to the same rhodium dihydride species $CpRh(H)_2(CH_2=CHSiMe_3)$. The reactivity of a third rhodium complex, $CpRh(P^*Ph)(C_2H_4)$ **3.2**, was studied with H_2 initially using the broadband UV light *in-situ* NMR approach to establish activity towards H_2. It was then studied towards *p*-H_2 using laser initiation.

Chapter Four: The photochemical reactivity of **2.1** and **2.2** towards phenyl methyl sulfoxide (PhSOMe) was studied. The products were characterised by NMR spectroscopy and the reaction kinetics analysed using relaxation kinetics.

Chapter Five: The ruthenium complex $[Ru(H)_2(CO)(PPh_3)(Xantphos)]$ **5.1** was synthesised and its photochemical activity towards ethene, 4-methyl-pyridine, 4-tert-butylpyridine, ^{15}N-pyridine, CO, benzyl alcohol, DMSO and triethylsilane studied. Once the photoactivity of $[Ru(H)_2(CO)(PPh_3)(Xantphos)]$ had been established its reactivity towards these ligands in the presence of *p*-H_2 was studied using broadband UV irradiation. Subsequently it was studied using time-resolved NMR methods with parahydrogen enhancements.

Chapter Six: *cis*-$[Ru(H)_2(dppp)_2]$ **6.1** was synthesised and was used to study the evolution of the parahydrogen singlet state under a difference in scalar coupling. This was studied using a standard ^1H NMR experiment with a 90° pulse and a 45° pulse and with an OPSY pulse sequence which removes the thermal background. A related complex *cis*-$[Ru(H)_2(dppe)_2]$ **6.2** was studied to look at polarisation transfer to ^{31}P followed by evolution under the difference in scalar coupling.

Chapter Seven: Details of the experimental methods used in earlier chapters

2 Synthesis, Characterisation and Photochemistry of $[(\eta^5\text{-}C_5H_5)Rh(alkene)_2]$

2.1 Introduction

This chapter reports the study of three 18-electron $[(\eta^5\text{-}C_5H_5)Rh(alkene)_2]$ complexes. The reactivity of these types of complexes has been shown to involve the loss of one or both of the coordinated alkene ligands and that this may be achieved thermally or photochemically. This generates a co-ordinately unsaturated intermediate which may undergo further reactivity and complexes of this nature have been known to undergo a great number of useful transformations some of which is outlined below. The intent in this research is to establish the photochemical reactivity of the three rhodium complexes using ligands which are known to coordinate to similar systems.[56, 57, 100]

One of the most studied half sandwich rhodium bis-alkene complexes is $[(\eta^5\text{-}C_5H_5)Rh(\eta^2\text{-}C_2H_4)_2]$[101] (Figure 2.1). In 1964 Cramer *et al.,* demonstrated that the thermal displacement of its ethylene ligands occurs at temperatures in excess of 115 °C.[101] They subsequently showed that substitution by nucleophiles, such as phosphines, pyridines and other alkenes was possible.[102] The thermal reactivity of pentamethylcyclopentadienyl (Cp*) analogues of these systems have been studied by Brookhart, most commonly with trimethylvinylsilane as the coordinated alkene (Figure 2.1). When these displacement reactions were studied in different deuterated solvents H/D exchange was observed with the solvent and it was concluded that the system is capable of activating the C–D bonds of benzene, toluene, chlorobenzene and acetone.[103] In addition, when d_6-benzene was used as the solvent, deuterium incorporation into a series of co-substrates such as aniline, cyclopropene, ferrocene and methyl ethers was observed.

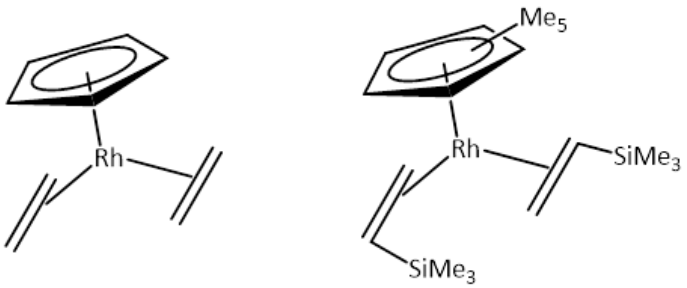

Figure 2.1: Structures of $[(\eta^5\text{-}C_5H_5)Rh(\eta^2\text{-}C_2H_4)_2]$[101] (left) and $[(\eta^5\text{-}C_5Me_5)Rh(\eta^2\text{-}CH_2CHSiMe_3)_2]$[103] (right)

These reactions could be followed by the changes in the ^{1}H NMR spectra. The deuterium exchange study in benzene showed significant deuteration of the vinyl resonances after 17 minutes at 78 °C and with longer reaction times additional deuteration of the $Si(CH_3)_3$ and Cp* groups was noted.[103] Contrasting with $Cp^*Rh(C_2H_4)_2$ reactivity where only 25% deuteration was observed after 2 hours at 78 °C.[104] The difference was attributed to the vinylsilane ligand being more labile than ethylene and thus providing a more efficient route to the reactive 16 electron intermediate Cp*Rh(alkene) proposed to be responsible for the C–H bond activation properties of these complexes. These observations highlighted the possibility of using the displacement of vinylsilane ligands to achieve access to the unsaturated metal centres under relatively mild conditions.

Since these initial studies, many reports have focussed on improving our understanding of transfer hydrogenation reactions.[105, 106] Some of the reported reactions are shown in Figure 2.3. These are all intramolecular transfer hydrogenation reactions where H_2 is transferred from the functional groups of the silane to the alkene. Using this procedure, silyl enolates,[103] silyl enamines[103] and 1,2-diheteroatom-substituted alkenes[106] have been prepared using the appropriated precursors. This complex was also used in a carbon-carbon bond forming reaction where the addition of an alkene to an aromatic aldehyde or ketone proved possible and mechanistic studies were performed.[105, 107]

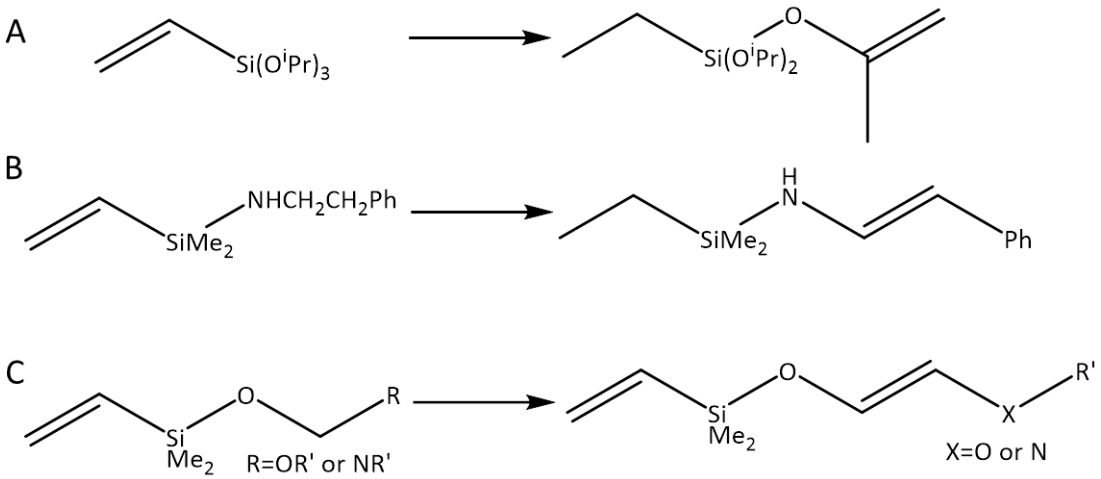

Figure 2.2: Examples of the transformations using Cp*Rh($CH_2CHSiMe_3$)$_2$ (A) vinylalkoxysilanes into silyl enolates;[103] (B) vinylaminosilanes into silyl enamines[103] and (C) the formation of 1,2 diheteroatom-substituted alkenes.[106]

Most recently this complex has been used to study intramolecular hydrogen transfer reactions using the alkoxyvinylsilane ligand (Figure 2.3A) to form the internal alkene product (Figure 2.3B).[108] In the active catalyst there is a bound alkoxyvinylsilane ligand and the ethoxy linker is in close proximity to the metal centre (Figure 2.3C). This allows the oxidative addition of its C–H bonds which facilitates hydrogen transfer into the vinylsilane giving the new internal alkene. Bolig *et al.* proposed two pathways for this process, which differ according to whether the first C –H activation occurs as position α or β. Use of deuterium labelling resulted in a highly regioselective product which allowed them to associate the reaction with a 5-membered metallacycle intermediate (Figure 2.3D).

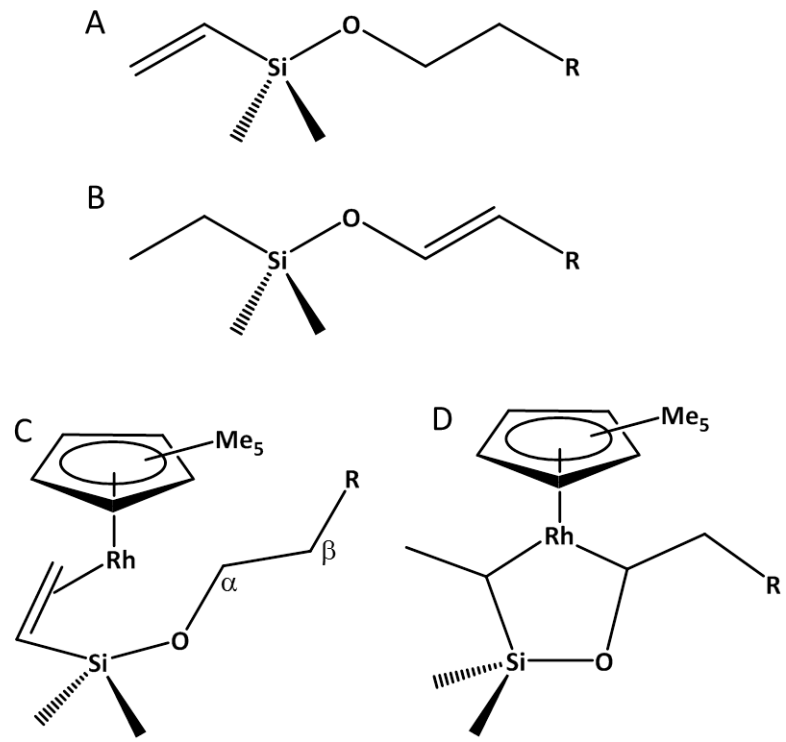

Figure 2.3: (A) Alkoxyvinylsilane starting ligand (B) Internal alkene product (C) Structure of the rhodium complexes with ligand (A) coordinated and (D) Structure of the 5-membered metallacycle intermediate. Structures adapted from Bolig *et al.*[108]

The work in this chapter focusses on studies of the photochemical activity of related half-sandwich rhodium-alkene complexes containing a cyclopentadienyl ligand. Their photochemical properties were originally studied using matrix isolation[79, 100] and in solution.[56, 57, 74, 100, 109, 110] Early work showed that one of the coordinated alkenes is readily lost photochemically. The reactive intermediate CpRh(alkene) is formed which is capable of coordinating a number of different substrates; infrared,[56, 100, 109] UV-Visible spectroscopy[100, 109] and NMR spectroscopy[56, 57, 74, 100, 111, 112] have been used to characterise this process. The most studied system is that of $[(\eta^5\text{-}C_5H_5)Rh(\eta^2\text{-}C_2H_4)_2]$. When the incoming ligand is DMSO[57, 100] or acetonitrile[57] only monosubstitution is observed (Figure 2.4A), whereas with PPh_3,[57, 100] CO[57, 100] and ^{t}BuNC[57] the sequential substitution of both of the original alkene ligands is possible (Figure 2.4A-B). When CO and ^{t}BuNC were used as the substrate, dinuclear species were also observed with the respective ligands bridging the two metal centres (Figure 2.4C).[57] The ethylene ligands were also substituted by trialkylvinylsilanes, butadiene and cyclohexene.[57] Additionally, the 16-

electron intermediate, $CpRh(C_2H_4)$, was found to be capable of the oxidative addition of Me_3SiH,[56] Et_3SiH[56] and H_2 bonds (Figure 2.4D-E).[57] The photochemical oxidative addition of trialkylsilanes was used to develop a silyl-based migration pathway in hydrosilation reactions.[113]

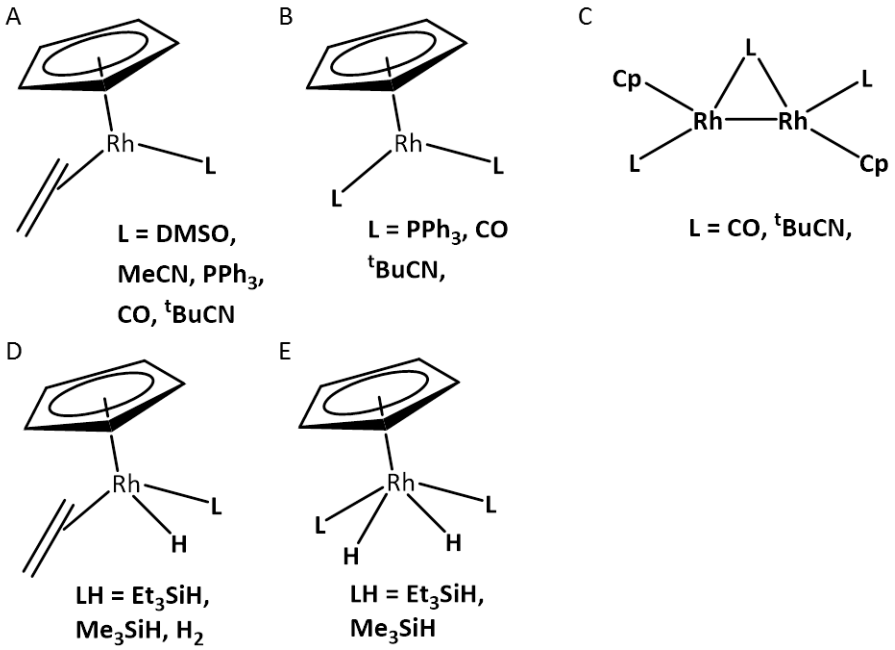

Figure 2.4: Summary of the different products from through the photochemical study of $CpRh(C_2H_4)_2$ (Figure 2.1) with different ligands, L, labelled. Adapted from Perutz *et al.*[56, 57, 113]

Subsequent research has moved towards studying complexes with different alkene ligands. Photolysing $[(\eta^5\text{-}C_5H_5)Rh(\eta^2\text{-}CH_2CHSi(CH_3)_3)_2]$ at low temperatures in toluene allowed the detection of the unstable solvent complex (Figure 2.5A),[74] where one alkene is substituted by an η^2-toluene group. This was not seen for $[(\eta^5\text{-}C_5H_5)Rh(\eta^2\text{-}CH_2CHCH_3)_2]$, where low-temperature photolysis in toluene only gave rise to the allyl hydride complex $[(\eta^5\text{-}C_5H_5)Rh(H)(\eta^3\text{-}CH_2CHCH_2)]$ (Figure 2.5B).[112] The expected η^2-arene complex was, however, observed when toluene was replaced with naphthalene (Figure 2.5C).[112] This stems from naphthalene retaining an element of aromatic stabilisation energy in the product, due to the second aromatic ring. The propensity of these complexes to undergo oxidative addition reactions has also been investigated with $[(\eta^5\text{-}C_5(CH_3)_5)Rh(\eta^2\text{-}CH_2CHCH_3)_2]$ and triethylsilane at room temperature.[112] The product, $[(\eta^5\text{-}C_5H_5)Rh(H)(Si(CH_2CH_3)_3)(\eta^2\text{-}CH_2CHCH_3)]$ (Figure 2.5D),

was found to exist in three isomeric forms which interconvert on the NMR timescale through the rotation of the bound alkene ligand and through the rotation of an η^2-(Si–H) bond. This type of behaviour was also observed when $[(\eta^5\text{-}C_5(CH_3)_5)Rh(\eta^2\text{-}CH_2CHCO_2{}^tBu)_2]$ was photolysed in the presence triethylsilane, diethylsilane and trimethoxysilane (Figure 2.5D).[111]

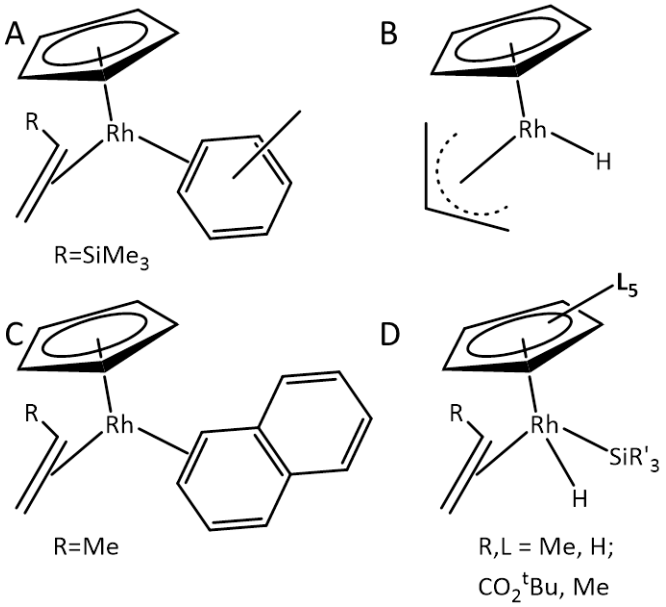

Figure 2.5: Summary of the product structures, only a single isomer is displayed for each of the structures. Adapted from Duckett and Perutz *et al.*[74, 111, 112]

This chapter extends these studies by reference to the three alkenes, trimethylvinylsilane, cyclooctene and cyclooctadiene. The parent complexes, $[(\eta^5\text{-}C_5H_5)Rh(\eta^2\text{-}CH_2CHSi(CH_3)_3)_2]$ **2.1**, $[(\eta^5\text{-}C_5H_5)Rh(\eta^2\text{-}C_8H_{14})_2]$ **2.2** and $[(\eta^5\text{-}C_5H_5)Rh(\eta^4\text{-}C_8H_{12})]$ **2.3**, shown in Figure 2.6, were synthesised and their NMR characterisation is detailed. This ligand choice will allow the difference in mono- and bi-dentate alkene ligands to be investigated, as well as structural isomerisation to be observed through the presence of a symmetry-breaking trimethylsilyl substituent. The intention of this research was to establish the photochemical activity of these complexes through their irradiation *ex-situ* in the presence of small molecules known to coordinate to similar complexes. The small molecules of interest were trimethylvinylsilane, DMSO and triethylsilane. Trimethylvinylsilane was chosen as a ligand it allowed the isomeristaion of **2.1** to be studied as well as and the substitution of COE and COD in **2.2** and

2.2, respectively. In so doing it established whether their alkene ligands are photochemically labile under the experimental conditions used here. It has been reported that when (η^5-C_5H_5)Rh(C_2H_4)$_2$ was photolysed in the presence of trimethylvinylsilane the predominant species which formed was (η^5-C_5H_5)Rh(C_2H_4)($CH_2CHSiMe_3$) and only through the removal of C_2H_4 by degassing was CpRh($CH_2CHSiMe_3$)$_2$ formed.[57] Cyclooctene and cyclooctadiene are both liquids, with boiling points of 145 °C and 150 °C, respectively, and therefore the removal of the liberated alkene is not as simple as for C_2H_4 which may impact on the distribution of the products. The relative activity of the monodentate and bidentate ligands was also of interest. Whilst DMSO and triethylsilane are common ligands used to demonstrate that a free coordination site has been generate via the detection of products containing coordinated DMSO or triethylsilane in place of a labile ligand.

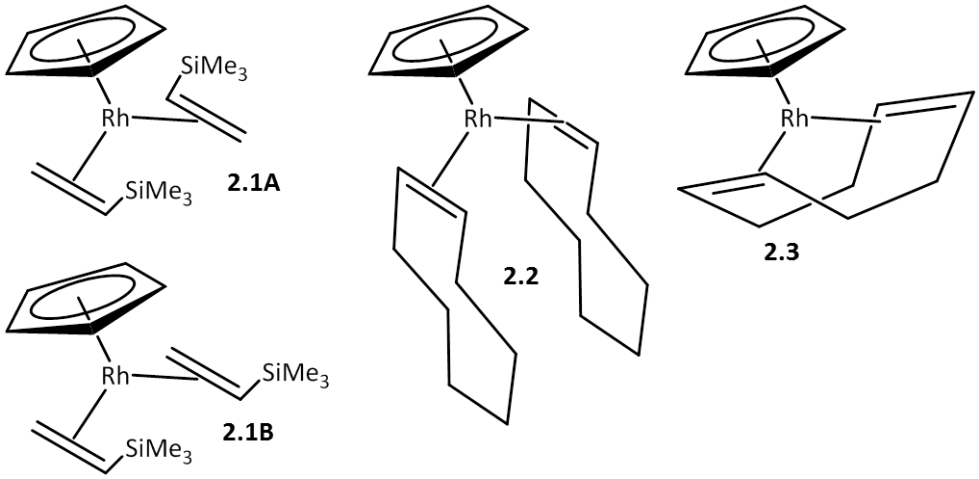

Figure 2.6: Structures of the three complexes to be studied in this chapter.

2.2 Synthesis

2.2.1 [(η^5-C_5H_5)Rh(η^2-$CH_2CHSi(CH_3)_3$)$_2$] **2.1**

The synthetic route to [(η^5-C_5H_5)Rh(η^2-$CH_2CHSi(CH_3)_3$)$_2$] **2.1** is shown in Figure 2.7, full details of the synthesis can be found in the Experimental Section 8.2. The first step involves the formation of Cramer's complex, [Rh(C_2H_4)$_2$(μ-Cl)]$_2$.[114] The coordinated ethylene ligands were then substituted for the desired trimethylvinylsilane ligands following the literature procedure

reported by Marciniec group in 2003.[115] The reaction time was increased from 3 hours to 21 hours to ensure complete substitution. **2.1** was then formed by reacting the trimethylvinylsilane dimer with cyclopentadienyl lithium[5] in a 31% isolated yield.

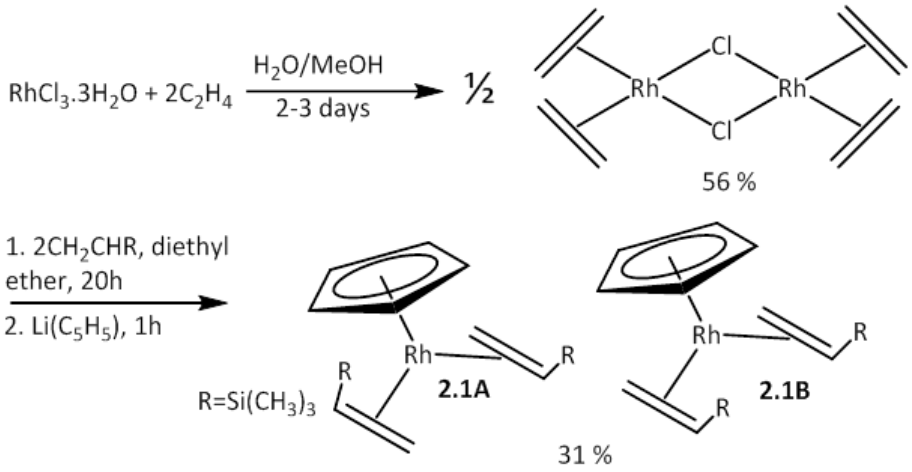

Figure 2.7: Synthetic route used to prepare $[(\eta^5\text{-}C_5H_5)Rh(\eta^2\text{-}CH_2CHSi(CH_3)_3)_2]$ **2.1**

In complexes of the type $[(\eta^5\text{-}C_5R_5)M(\eta^2\text{-}CH_2CHR)_2]$ there are 6 possible stereoisomers[116] which differ according to the orientation of the alkenes. These isomers can be grouped into two sets of three (Figure 2.8), according to whether they can interconvert by alkene rotation. Interconversion between the two sets of isomers however requires the loss and re-coordination of the alkene in a different orientation. The use of low temperature NMR with *in-situ* photolysis has allowed the detection of four of these isomers.[74] At room temperature only two are detected.[57] NMR characterisation was performed on these products (Section 2.3.1) and determined that the two isomers correspond to *trans-up-up* (**2.1A**) and *cis-up-up* (**2.1B**) with the *trans-up-up* isomer being the major of the two.

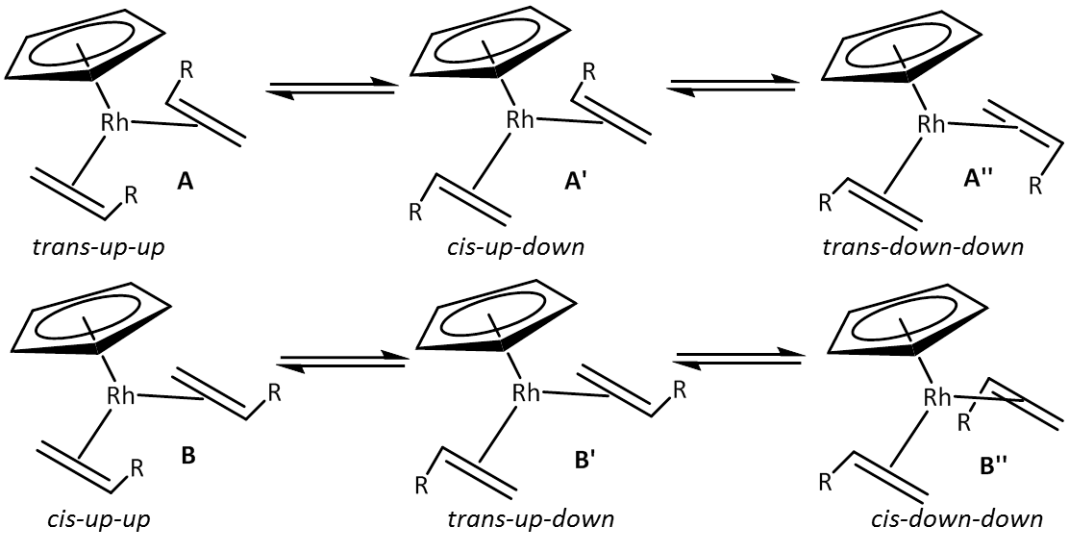

Figure 2.8: Possible isomers of half sandwich complexes with two monosubstituted bound alkene ligands, adapted from Hauptman *et al.*[116]

2.2.2 $[(\eta^5\text{-}C_5H_5)Rh(\eta^2\text{-}C_8H_{14})_2]$ **2.2** and $[(\eta^5\text{-}C_5H_5)Rh(\eta^4\text{-}C_8H_{12})]$ **2.3**

The synthetic route to form $[(\eta^5\text{-}C_5H_5)Rh(\eta^2\text{-}C_8H_{14})_2$ **2.2** and $[(\eta^5\text{-}C_5H_5)Rh(\eta^4\text{-}C_8H_{12})]$ **2.3** are shown in Figure 2.9. The first step in each synthesis is the formation of the rhodium alkene chloride dimer from $RhCl_3.3H_2O$. The literature methods[117, 118] for these steps were modified to allow the synthesis to be performed in a microwave oven. The use of the microwave oven allows shorter reaction times and less solvent to be used. The half sandwich complexes were then formed by reacting these dimers using cyclopentadienyl lithium.[5] The products were then isolated in a 69% yield for **2.2** and 60% yield for **2.3,** full experimental details can be found in the Experimental, Section 8.2.

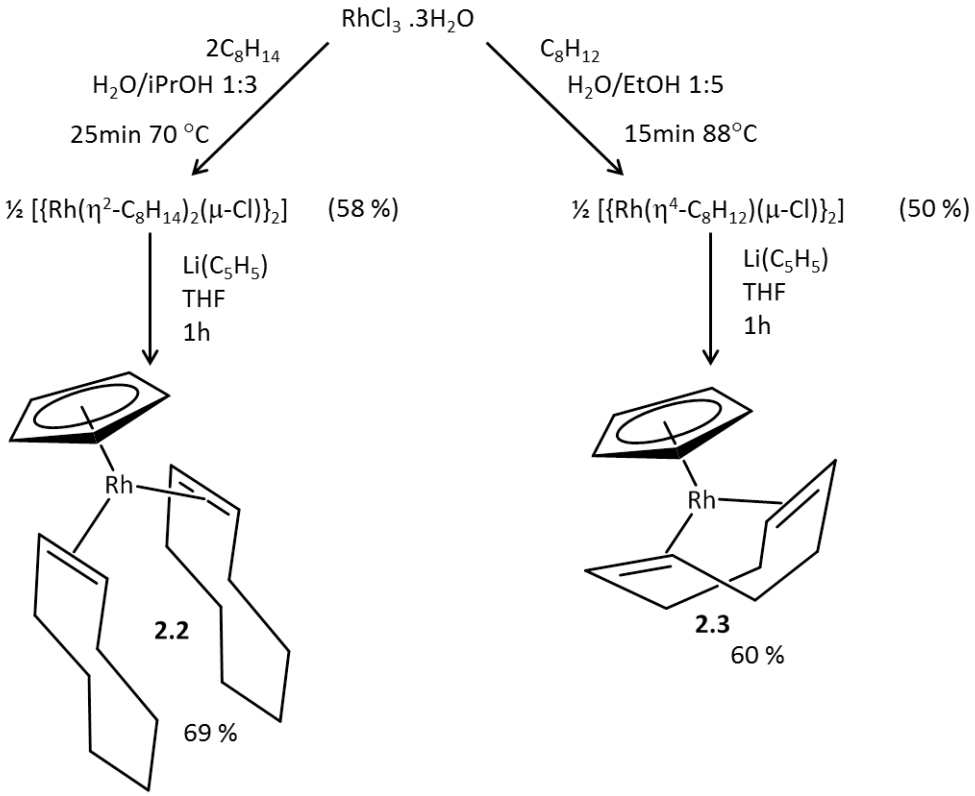

Figure 2.9: Synthetic route used to prepare $[(\eta^5\text{-}C_5H_5)Rh(\eta^2\text{-}C_8H_{14})_2$ **2.2** and $[(\eta^5\text{-}C_5H_5)Rh(\eta^4\text{-}C_8H_{12})]$ **2.3**

2.3 NMR Characterisation

2.3.1 $[(\eta^5\text{-}C_5H_5)Rh(\eta^2\text{-}CH_2CHSi(CH_3)_3)_2]$ **2.1**

The chemical shifts of cyclopentadienyl ligands in complexes of the form $CpML_n$ typically occur between δ 4 and 5.5.[57] They can be used to determine the number of half-sandwich species present in solution since each should be a singlet (or a doublet with small coupling to rhodium depending on the resolution). In the ^{1}H NMR spectrum of **2.1** (Figure 2.10) there are two peaks in this region at δ 5.00 and 5.04 indicating that, as expected, there are two isomers present (Figure 2.10). These have been characterised previously,[57, 74] and the details of the characterisation will be outlined to exemplify the methods used to characterise the products which form through the reaction with **2.1**.

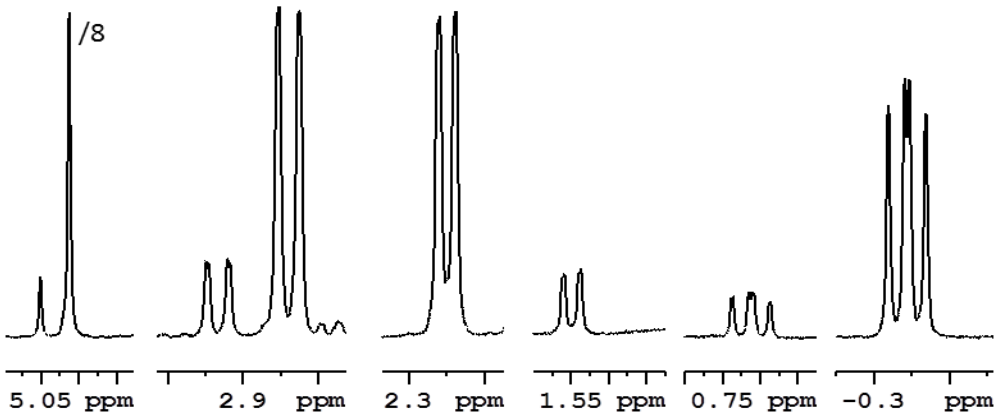

Figure 2.10: ^{1}H NMR Spectrum of **2.1** in C_6D_6 at 298 K

The major isomer yields three alkene signals at δ 2.84; 2.26 and –0.34. The distinctive δ –0.34 peak is diagnostic of the *trans-up-up* isomer. The couplings observed in these three peaks can be used to assign the relative alkene proton orientations (Figure 2.11). The peak at δ 2.84 is a broad doublet with a coupling of 13.5 Hz. A large proton-proton coupling links protons which are on the opposite side of the double bond, *trans,* to one another, as would be the case for H_A and H_C (Figure 2.11). Whilst the coupling in the peak at δ 2.26 is 11.0 Hz indicating the coupled protons are on the same side of the alkene, H_A and H_B, and therefore *cis* to one another. A smaller coupling of 1.5 Hz is also observed corresponding a geminal coupling between the terminal protons H_B and H_C; this splitting is obscured by the broadness of the peak at δ 2.84. A 2D ^{1}H-^{13}C HMQC NMR spectrum was used to correlate these peaks to their directly bound carbon centres and a 1D ^{13}C{^{1}H} NMR spectrum was used to measure the carbon-rhodium coupling for each of these carbon resonances. The CH group was assigned as δ 52.8 (d, J_{CRh} 14.1 Hz) and the CH_2 group was assigned as δ 39.0 (d, J_{CRh} 13.0 Hz).

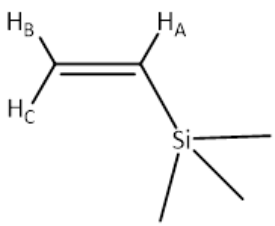

Figure 2.11: Assignment of the proton environments of the coordinated trimethylvinylsilane ligand

In the corresponding 2D ^{1}H-^{1}H NOESY NMR spectrum, the observation of an nOe connection between the methyl signals of the silyl group and the Cp peak at δ 5.00 indicates that the vinyl ligand's silyl substituent points up towards the ring. An nOe interaction between H_A and H_C, suggests that the silyl substituents on the two alkene ligands are not aligned with one another. Figure 2.12 shows the arrangements of the two ligands in each of the isomers, the cyclopentadienyl rings have been omitted for clarity. In the *cis-up-up* isomer the two ligands are arranged in the same orientation. This means that H_A (labelled orange) is never in close enough proximity to H_C (labelled green) for there to be an nOe interaction between them. In the *trans-up-up* isomer the two ligands are out of sync with one another meaning that H_A of one of the ligand can be in sufficiently close proximity to H_C on the second ligand to give an nOe correlation and therefore the presence of this nOe confirms that the major species is the *trans-up-up* isomer (Figure 2.78). This is consistent with the literature.[57, 74] The full details of NMR characterisation can be found in Table 2.14.

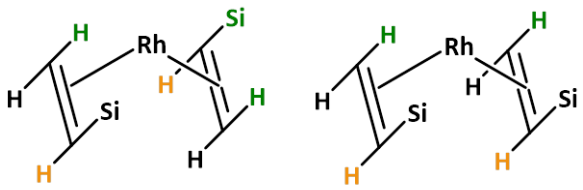

Figure 2.12: Schematic representation of the spatial arrangement of the two trimethylvinylsilane ligands *in trans-up-up* and *cis-up-up* isomers of **2.1**, Cp rings have been omitted for clarity.

The minor isomer was characterised using the same approach. This identified this product as the *cis-up-up* isomer. This is consistent with the literature[74] and the results of this analysis is summarised in Table 2.15.

2.3.2 $[(\eta^5\text{-}C_5H_5)Rh(\eta^2\text{-}C_8H_{14})_2]$ **2.2**

The ^{1}H NMR spectrum of **2.2** in C_6D_6 shows a singlet at δ 4.85, which correlates to a carbon resonance at δ 91.1 in the 2D ^{1}H-^{13}C HMQC data set. These values are consistent with a coordinated cyclopentadienyl ligand. There are two pseudo doublets with one measureable

coupling each, one at δ 2.32 (d, J_{HH} 13 Hz) and one at δ 1.76 (d, J_{HH} 9 Hz), each accounting for four protons, there are additional, unmeasurable smaller couplings hidden in the broadness of these resonances. This complex has previously been characterised by ^{1}H NMR spectroscopy[119] where the downfield doublet was reported to correspond to the vinylic protons of the coordinated double bond, labelled H_1 in Figure 2.14. However, it is the proton resonance at δ 1.76 which shows a correlation to a carbon resonance typical of a coordinated double bond, δ 65.1. Whereas the doublet at δ 2.32 correlates to a carbon resonance with a chemical shift of δ 33.5, more in keeping with a saturated carbon environment. The ^{13}C{^{1}H} NMR spectrum supports these assignment since the resonance at δ 65.1 exhibits a coupling to rhodium of 14.4 Hz. The resonance at δ 33.5, however, exhibits a much smaller coupling to rhodium of 1.3 Hz indicating that it is not directly bound to the metal centre. Furthermore, a second proton at δ 1.52 also shows a correlation to this carbon, confirming that the peak at δ 2.32 is one-half of a pair of inequivalent CH_2 protons. Both of these protons signals also couple to the CH resonance at δ 1.76 in the corresponding 2D ^{1}H-^{1}H COSY spectrum thereby suggesting that they correspond to the two methylene groups that are located at position 2 in Figure 2.14. The 13 Hz coupling observed in the proton resonance at δ 2.32 corresponds, therefore, to the geminal coupling between H_2 and $H_{2'}$.The 9 Hz coupling observed in proton peak at δ 1.76 is between this proton and H_2 (δ 1.52), which is *cis* relative to H_1.[120]

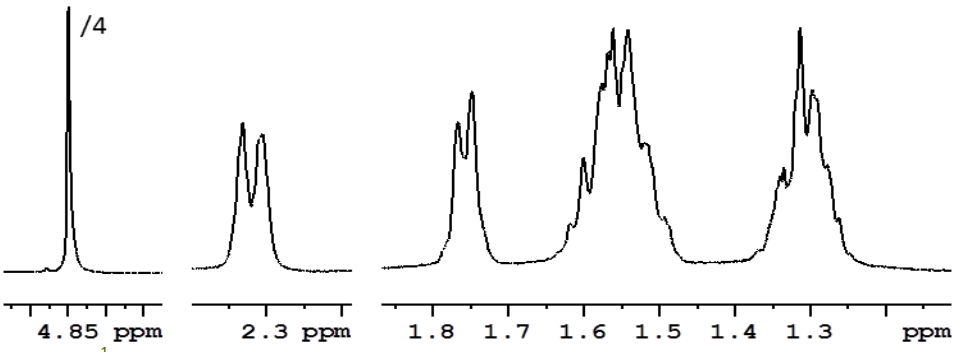

Figure 2.13: ^{1}H Spectrum of **2.2** in C_6D_6.at 298 K, insert shows resonances for this complex (integrated)

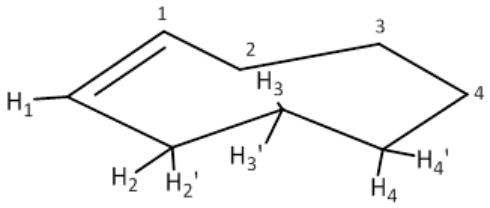

Figure 2.14: Assignments of cyclooctene ligand proton environments

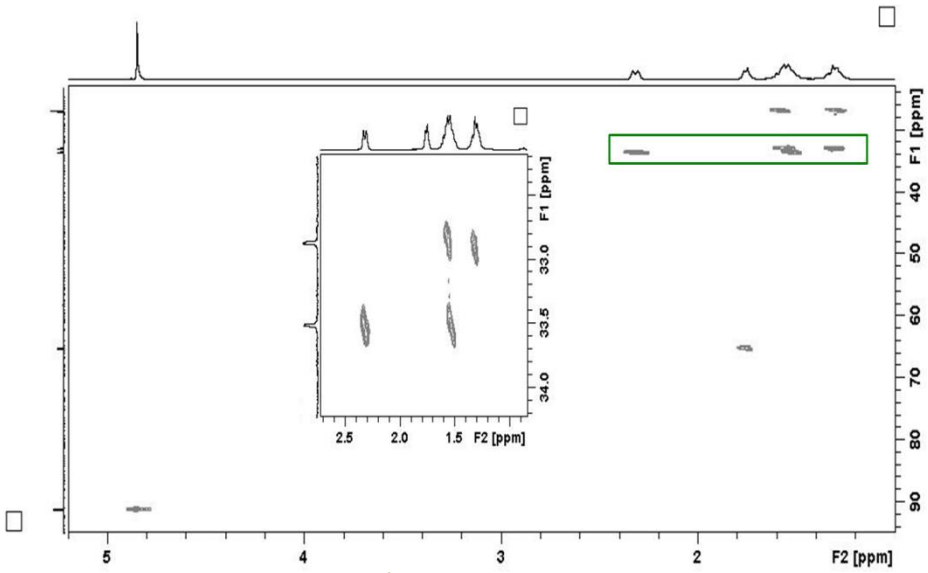

Figure 2.15: ^{1}H-^{13}C HMQC of **2.2**, in C_6D_6 at 298 K.

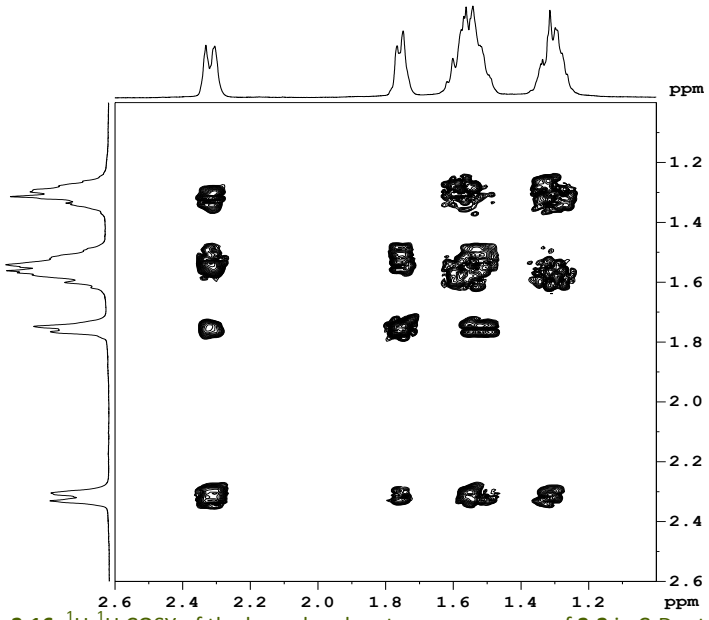

Figure 2.16: ^{1}H-^{1}H COSY of the bound cyclooctene resonances of **2.2** in C_6D_6 at 298 K

The remaining peaks in the proton spectrum appear as multiplets at δ 1.58 and 1.32. The highly overlapped peak at δ 1.58 corresponds to 12 protons, 4 of which have already been assigned to protons on carbon 2, leaving 8 protons to be accounted for. The peak at δ 1.32

corresponds to 8 protons. The ^{1}H-^{13}C HMQC data shows that both of these peaks correlate to carbon environments with chemical shifts of δ 32.9 and 26.8 respectively (positions 3 and 4 of Figure 2.14) and confirm that the remaining CH_2 groups are diastereotopic. This supports the structure depicted in Figure 2.79. Details of the NMR characterisation are summarised in Table 2.16.

2.3.3 $[(\eta^5\text{-}C_5H_5)Rh(\eta^4\text{-}C_8H_{12})]$ **2.3**

An NMR sample of **2.3** in d_8-toluene was used for characterisation. Its ^{1}H NMR spectrum contains four peaks (Figure 2.17). A singlet at δ 4.93 corresponding to the 5 protons of the cyclopentadienyl ligand, a broad singlet at δ 3.94 corresponding to the 4 alkene protons of the COD ligand (position 1, Figure 2.18) and two signals at δ 2.20 and 1.94 for the alkyl backbone (positions 2 and 2') of the COD ligand. The corresponding carbon chemical shifts were identified using 2D ^{1}H-^{13}C HMQC methods. The CH=CH signals (C_1) of the COD ligand have a carbon chemical shift of δ 62.5 (d, J_{CRh} 14.0 Hz), while the CH_2 groups of the COD's alkyl backbone (C_2) yield a carbon signal at δ 32.5. This characterisation is consistent with the structure drawn in Figure 2.80. This NMR data is summarised in Table 2.17.

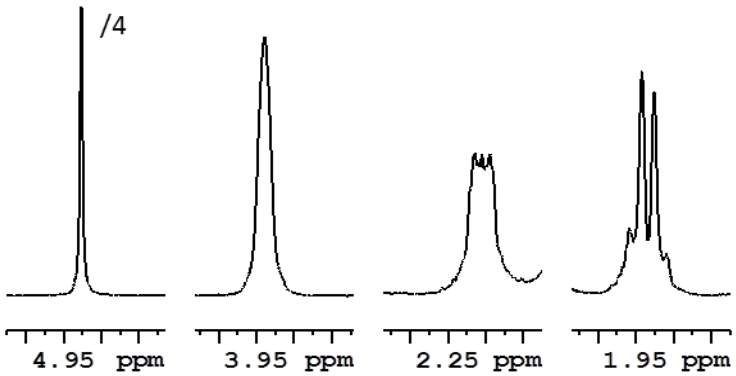

Figure 2.17: ^{1}H spectrum of **2.3** in d_8-toluene at 298 K.

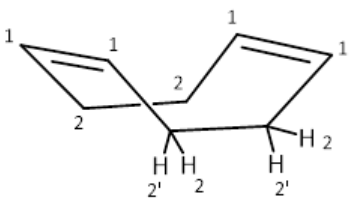

Figure 2.18: Unique proton and carbon environments on the coordinated COD ligand.

2.4 Photochemistry of $[(\eta^5\text{-}C_5H_5)Rh(\eta^2\text{-}CH_2CHSi(CH_3)_3)_2]$ **2.1**

There are six possible geometric isomers of **2.1**[116] (Figure 2.8) which can be grouped into two sets as described earlier. The synthetic route used gave two isomers of **2.1**; the *trans-up-up* (**2.1A**) and *cis-up-up* (**2.1B**) isomers. These belong in the different sets and as such their isomerisation can only occur via the loss of an alkene ligand and therefore, can be used to demonstrate the photolability of the alkene ligand. This known process [11] therefore can be used as proof of the photochemical loss of a trimethylvinylsilane ligand and thus allow the photochemical reactivity of **2.1** towards other ligands to be studied.

To investigate this, a sample containing 1.3 mg of $[(\eta^5\text{-}C_5H_5)Rh(\eta^2\text{-}CH_2CHSi(CH_3)_3)_2]$ **2.1** was prepared in C_6D_6 and 10 µL of trimethylvinylsilane added, this reflects a 20 fold excess relative to rhodium. The sample was then irradiated with broadband UV light and monitored periodically by ^1H NMR spectroscopy (Experimental 8.3.1) and the UV-visible spectrum of **2.1** is shown in Figure 2.19. After 15 minutes irradiation the ratio of the two isomers had changed from 18.3:1 to 1.3:1 (**2.1A**: **2.1B**) (Figure 2.20) demonstrating the photolability of the vinylsilane ligand.

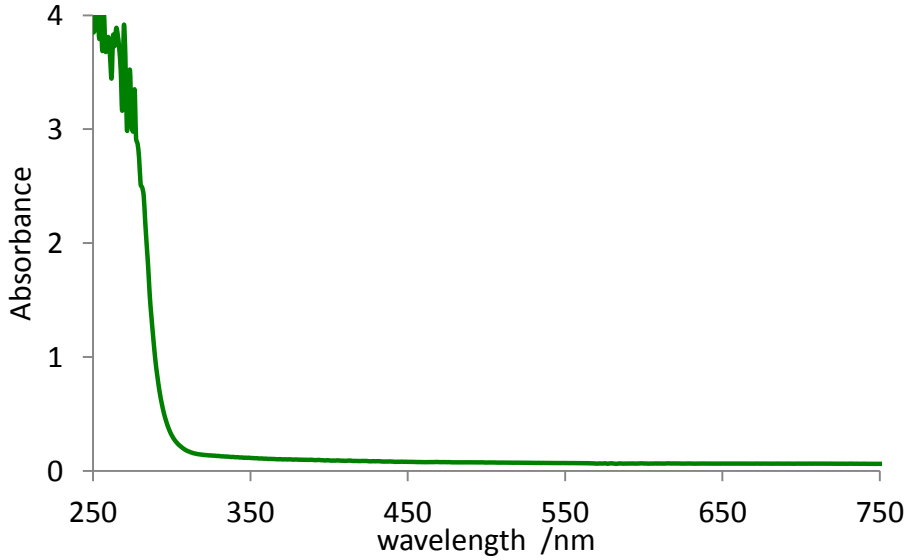

Figure 2.19: UV-Visible spectrum of **2.1** in C_6H_6

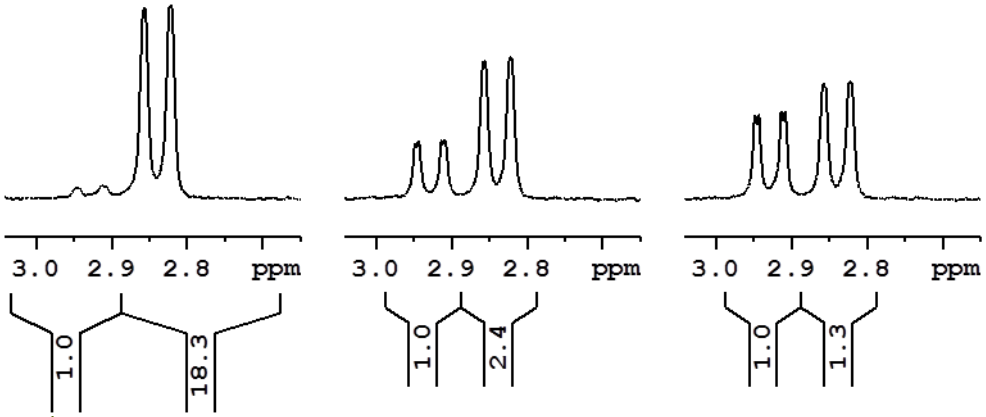

Figure 2.20: ^{1}H Spectrum in C_6D_6 at 298 K showing peaks for proton-H_A in **2.1A** (δ 2.84) and **2.1B** (δ 2.93).(A) prior to photolysis; (B) after 1 minute and (C) after 15 minutes. Integrals show relative ratios of the two isomers

The series of proton spectra recorded during the irradiation process were integrated to measure the concentrations of **2.1A** to **2.1B**, relative to the total amount of **2.1** present prior to irradiation. The relative concentrations are plotted against irradiation time, in seconds, in Figure 2.21; the full procedure is outlined in the Experimental Section 8.4. Figure 2.21 shows an initial period where the proportions of **2.1A** and **2.1B** change after this a photostationary state is established, indicating that both **2.1A** and **2.1B** are photoactive. At this point, there is approximately 53% **2.1A** and 39% **2.1B**. A small amount of decomposition occurs, which corresponds to 8% of the initial rhodium species and is not included in these data. The source of the decomposition was not identified. There was no discernible precipitate observed in the NMR tube and the total integral of the Cp region of the NMR spectrum was also consistent with this degree of decomposition, suggesting that the loss of the Cp ligand has occurred. The formation of a new equilibrium demonstrates that, in this system, UV light may be use to perturb the initial equilibrium and a second equilibrium is established. These types of process can be modelled using relaxation kinetics. The principles behind this are detailed in the Appendix Section 9.2.

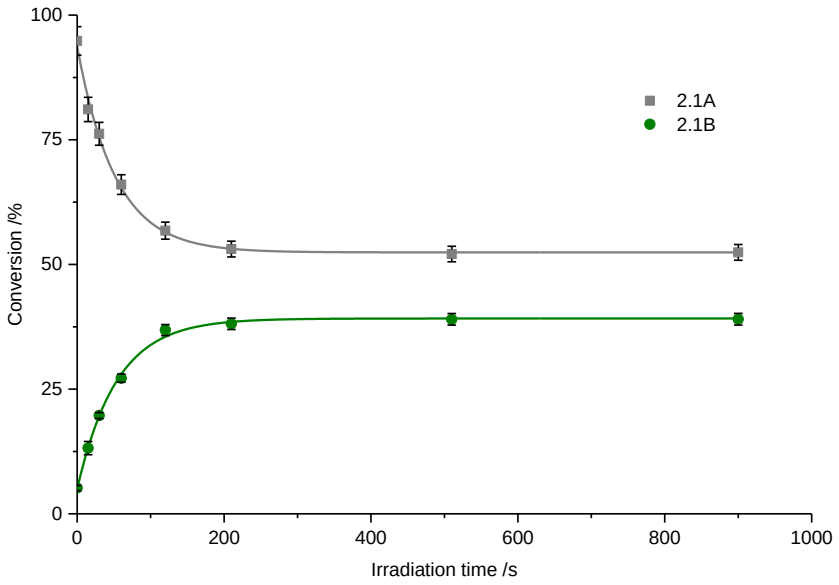

Figure 2.21: Time-profile showing the isomerisation of **2.1** between the *trans-up-up* (**2.1A**) and *cis-up-up* (**2.1B**) isomers, these were fitted to Equation (2.1) the results of which are given in Table 2.1

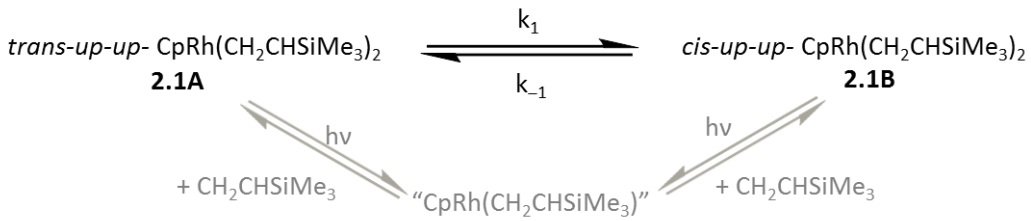

Figure 2.22: Kinetic model for the transformation of **2.1A** into **2.1B** under photochemical control, the net reaction is given in black and the process is given in grey

The kinetic model for this system is a first order equilibrium between two species (Figure 2.22). The integrated rate expression for this process is given by Equation (2.1)[121] and values of *a*, *b* and k_{obs} obtained accordingly (Table 2.1) where *a d*enotes the equilibrium concentrations ($[A]_{eq}$ where A is **2.1A** or **2.1B**), *b* the difference between the initial and equilibrium concentrations ($[A]_0 - [A]_{eq}$) and k_{obs} the sum of the rate constants and equate to the time it takes for the equilibrium to be established. There are a number of conditions necessary for this approach to be valid. Firstly that the sample was optically dilute and secondly that the thermal reaction is slow.

$$y = a + be^{-k_{obs}t} \qquad (2.1)$$

Where

a= $[A]_{eq}$

b= $[A]_0 - [A]_{eq}$

k_{obs}= $k_1 + k_{-1}$

Table 2.1: Fitting results for the changes of **2.1A** and **2.1B** as a function of irradiation using Equation (2.1)

	a /%	b /%	k_{obs} /s^{-1}
2.1A	52.4 ± 0.7	41.3 ± 1.2	(1.79 ± 0.33) x10^{-2}
2.1B	39.2 ± 0.4	-34.2 ± 0.7	(1.86 ± 0.19) x10^{-2}

There two descriptions of the equilibrium constant (Equation (2.2)),[122, 123] the first is in terms of the concentrations of **2.1A** and **2.1B** which gives a value of K_{eq} of 0.74 ± 0.02 under these conditions. It may also be described as the ratio k_1 to k_{-1} which also feature in the integrated rate expression (Equation (1)). These equations can be combined to allow the values of k_1 and k_{-1} to be calculated as (0.76 ± 0.15) x10^{-2} and (1.03 ± 0.20) x10^{-2} s^{-1} respectively via Equations (2.3) and (2.4).[124]

$$K_{eq} = \frac{k_1}{k_{-1}} = \frac{[2.1B]_{eq}}{[2.1A]_{eq}} \qquad (2.2)$$

$$k_1 = \frac{k_{obs}K_{eq}}{1 + K_{eq}} \qquad (2.3)$$

$$k_{-1} = \frac{k_{obs}}{1 + K_{eq}} \qquad (2.4)$$

In the Appendix, analysis of the rate equations for thermal and photochemical reactions was performed. The rates of the forward and back reactions in the photochemical process link to the Beer Lambert law. It was demonstrated that k_1 and k_{-1} of the thermal model relate to the photochemical model according to Equations (2.5) and (2.6) where $\Phi_{2.1A}$ and $\Phi_{2.1B}$ are the quantum yields of **2.1A** and **2.1B**, ε is the molar absorption coefficient of **2.1**, I_0 is the light intensity and l is the path length. The equilibrium constant, therefore, corresponds to the ratio of the quantum yields according to Equation (2.7).[122, 125] From the values of k_1, k_{-1} and thus, K_{eq}, it can be concluded that the quantum yield of **2.1A** is smaller than that of **2.1B**. This means

that **2.1B** is more efficient at forming the intermediate as a result its concentration relative to **2.1A** is reduced. Thermal isomerisation was not considered in this analysis as when a sample was left at room temperature in the absence of light for 13 weeks there was just 79% **2.1A** to 21% **2.1B**. Hence thermal isomerisation occurs on a much longer timeframe than the isomerisation observed here. This thermal isomerisation suggests that the photostationary state reflects the kinetic stability of the two isomers and in the absence of light the system moves towards the thermodynamic preference. The steric effect associated with trimethylsilyl substituent is a dominating influence on the thermodynamically preferred isomer.

$$k_1 = \Phi_{2.1A} I_0 \varepsilon l \tag{2.5}$$

$$k_{-1} = \Phi_{2.1B} I_0 \varepsilon l \tag{2.6}$$

$$K_{eq} = \frac{[2.1B]_{eq}}{[2.1A]_{eq}} = \frac{\Phi_{2.1A}}{\Phi_{2.1B}} \tag{2.7}$$

There is an alternate method for studying the relaxation kinetics of a system which is derived from a differential model. This will be of benefit with more complicated systems where deriving the integrated rate expression is challenging. The kinetic parameters for this system were determined using a simulation within Excel as outlined in the Experimental 8.4.3 When this was performed, values of k_1 and k_{-1} were determined to be (0.83 ± 0.06) x10^{-2} and (1.10 ± 0.07) x10^{-2} s^{-1} respectively which give an equilibrium constant, K_{eq}, of 0.77 ± 0.10 demonstrating that both approaches generate the same result, within experimental error.

2.5 Photochemistry of $[(\eta^5\text{-}C_5H_5)Rh(\eta^2\text{-}CH_2CHSi(CH_3)_3)_2]$ **2.1** with DMSO to form **2.4**

There are many rhodium DMSO complexes in the literature[126, 127] where coordination through oxygen[128] or sulfur[129] is possible. In some cases, the DMSO ligand is seen to bridge two metal centres by coordinating through both of these sites.[130] It is hypothesised that if **2.1** was photolysed in the presence of DMSO one or both of the trimethylvinylsilane ligands will be

C

replaced with DMSO. To investigate this an NMR sample containing 0.5 mg of [(η^5-C_5H_5)Rh(η^2-$CH_2CHSi(CH_3)_3)_2$] **2.1** was prepared in d_8-toluene and 2 µL of DMSO added to give a 20 fold excess of DMSO relative to **2.1**. The sample was then irradiated for a total of 20 minutes with periodic monitoring of the reaction being made by the acquisition of appropriate ^{1}H NMR spectra. Signals associated with a new rhodium species were observed. These included a new cyclopentadienyl resonance at δ 4.95 and two singlets where the methyls of the bound DMSO are expected (δ 2.41 and 2.42) as shown in Figure 2.23. This species was then characterised by NMR spectroscopy as **2.4**.

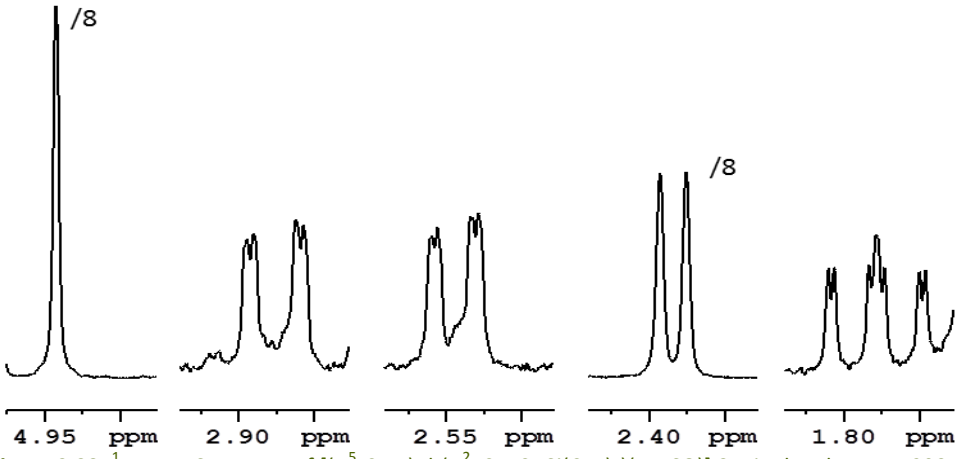

Figure 2.23: ^{1}H NMR Spectrum of [(η^5-C_5H_5)Rh(η^2-$CH_2CHSi(CH_3)_3$)(DMSO)] **2.4** in d_8-toluene at 298 K.

The proton spectrum (Figure 2.23) has a single peak, at δ 4.95, in the cyclopentadienyl region indicating that a single product has formed. There are two protons, at δ 2.88 (dd, 14 and 2.5 Hz) and 2.55 (dd, 11 and 2.5 Hz), where protons on coordinated alkenes are expected. Both of these protons integrate as 1 proton, relative to δ 4.95 as 5 protons. In the 2D ^{1}H-^{1}H COSY NMR spectrum these signals couple to one another and a third peak at δ 1.78 (ddd, 14, 11 and 1.5 Hz) where the 1.5 Hz is coupling to the rhodium centre. This observation is consistent with a bound trimethylvinylsilane ligand. The corresponding HMQC data showed that the signals at δ 2.88 and 2.55 correspond to proton resonances that share a common carbon partner, which appears at δ 37.5, while the peak at δ 1.78 connects to a carbon signal at δ 42.6. Both of these carbon resonances are doublets in the ^{13}C{^{1}H} NMR spectrum due to coupling to rhodium of

15.8 and 16.6 Hz respectively, consistent with a coordinated alkene. The proton resonances were assigned to each of the different proton environments based on their coupling network and this is summarised in Figure 2.24.

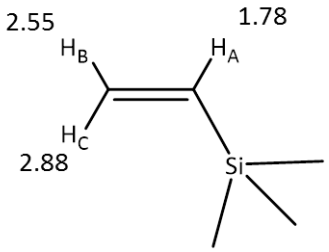

Figure 2.24: Assignments of the trimethylvinylsilane protons chemical shifts.

The silane substituent on the bound alkene introduces a degree of asymmetry within the complex and the consequence of this is the two methyl groups on the coordinated DMSO ligand are chemically inequivalent. This is demonstrated in Figure 2.25, where the structure is viewed from below it shows that the methyl group labelled A is on the same side as the CH_2 group of the vinyl silane and the methyl group labelled B on the same side as the CH group of the vinylsilane. For the two methyl groups to become equivalent either; the DMSO ligand rotates about the S=O axis highlighted, this would result in the breaking of the rhodium–DMSO bond or alternatively the alkene could rotate and this too would result in the rupture of the ligand rhodium bond.

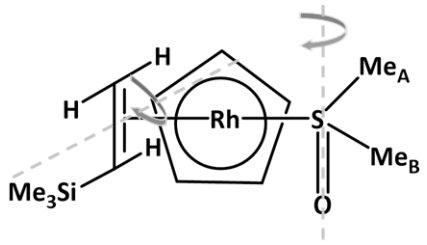

Figure 2.25: Schematic representation of **2.4**, as if looking up towards the Cp ring, to demonstrate the relative orientation of the two ligands relative to one another.

The chemical shifts of the methyl groups can be indicative of the DMSO binding mode. Firstly, the magnitude of the downfield shift of the proton resonance relative to free DMSO suggests sulfur binding if the shift is large and oxygen binding if it is smaller.[131] In **2.4** there is a 0.7 ppm

downfield shift in the proton chemical shift of the bound which is suggestive of binding through the sulfur. Alternatively, the carbon chemical shift of the methyl group can be used. This is a more distinctive approach since an upfield shift is observed for oxygen binding and a downfield shift for sulfur binding, relative to the free ligand.[57, 132] In **2.4** the methyl resonances have carbon chemical shifts of δ 54.9 and 55.1 and are downfield shifted when compared to free DMSO which has a chemical shift of δ 40.6. These observations confirm coordination through the sulfur.

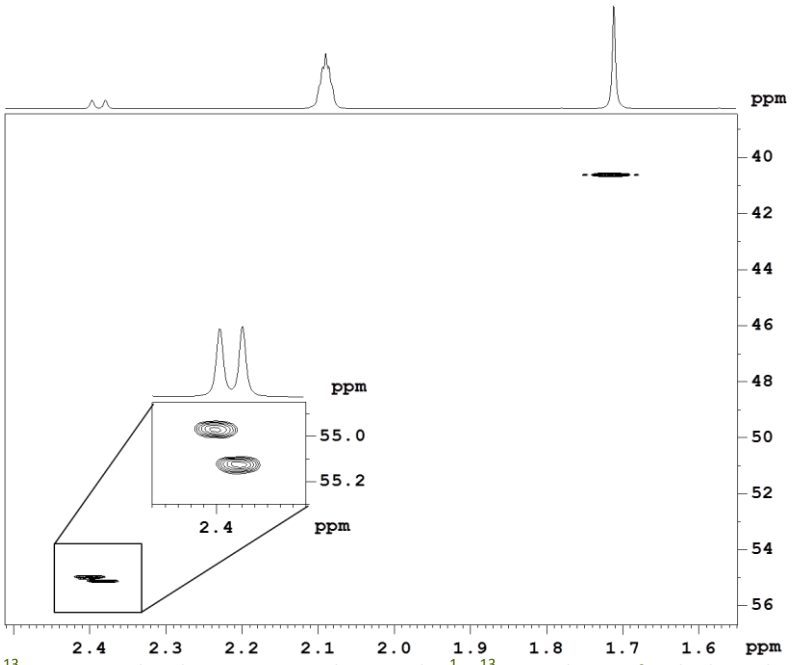

Figure 2.26: ^{1}H-^{13}C HMQC in d_8-toluene at 298 K showing the ^{1}H-^{13}C correlations for the bound DMSO in **2.4** and free DMSO in solution. Insert is an expansion of the bound DMSO methyl group.

All of this evidence points to the photoproduct being a half sandwich complex with a single trimethylvinylsilane ligand and one DMSO ligand coordinated as depicted in Figure 2.81. The NMR results are summarised in Table 2.18. This is consistent with the literature reactions between these types of rhodium complexes and DMSO.[57, 133] This was the only product observed and there was no evidence in the ^{1}H NMR spectrum of the bis-DMSO product $CpRh(DMSO)_2$.

The proton spectra acquired during irradiation period were analysed using the method outlined in the Experimental to determine the changes in concentration of the starting complexes, using H_A in both isomers, and the product, using the bound DMSO resonances, as a function of irradiation time. The contribution of both isomers of **2.1** will be combined so that isomerisation between the two isomers is not considered. The relative concentrations of **2.1** and **2.4** against irradiation time (Figure 2.27) reveal that this reaction also results in a photostationary state and therefore, this reaction may also be studied by relaxation kinetics. The photostationary state comprises of 94% **2.4** and 4% **2.1**, approximately 2% decomposition is observed over the course of the reaction. The identity of this decomposition was not identified and no precipitation was observed in the solution.

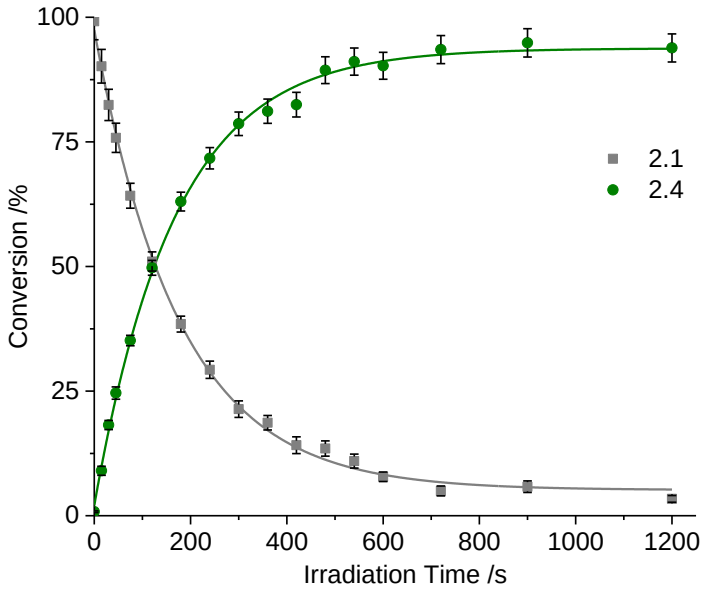

Figure 2.27: Time profile plot showing the conversion of **2.1** into **2.4** as a function of irradiation time. These were fitted to Equation (2.8) as per Table 2.2.

The proposed kinetic model for this system is a bimolecular second order equilibrium (Figure 2.28) and the kinetics associated with such a process are outlined in the Appendix. The formation of an equilibrium between **2.1** and **2.4** would suggest that both are complexes are photoactive and thus this is a photostationary state. Both **2.1** and **2.4**, therefore, may undergo ligand loss to form the reactive intermediate "$CpRh(CH_2CHSiMe_3)$". This intermediate may

react with either DMSO or vinylsilane to form **2.4** or **2.1** respectively. Since the bis-DMSO product was not observed, it is assumed that if trimethylvinylsilane may be lost from **2.4** to form the fragment "CpRh(DMSO)" it or the resulting product is not stable and thus this pathway does not significantly contribute towards the reactivity observed. The sample was optically dilute and it is assumed that any thermal reactivity is negligible compared with the photochemical reaction.

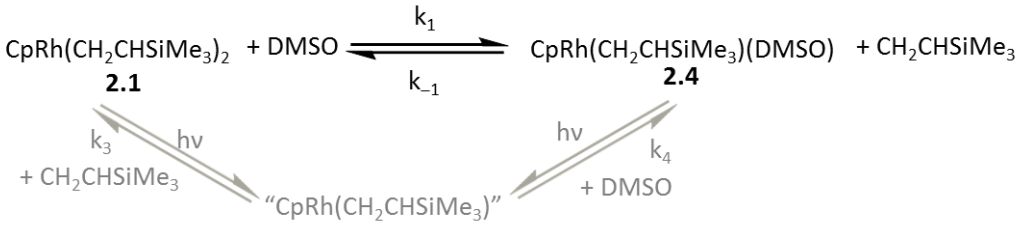

Figure 2.28: Proposed kinetic model for the reaction between **2.1** and **2.4**. The full process is described in grey and the net reaction in black.

The integrated rate equation for this model is given by Equation (2.8),[121, 123] where *a* reflects the equilibrium concentrations, $[A]_{eq}$, and *b* describes the difference in the initial and equilibrium concentrations, $[A]_0 - [A]_{eq}$, where A refers to either **2.1** or **2.4** in both cases. Whilst k_{obs} is observed rate constant and reflects the time it takes for the equilibrium to be achieved. It is a combination of the forward and back rate constants for the equilibrium based on Equation (2.9).[37, 124] The changes in **2.1** and **2.4** were fitted to Equation (2.8) and the values obtained are summarised in Table 2.2.

$$y = a + be^{-k_{obs}t} \qquad (2.8)$$

Where

$a = [A]_{eq}$

$b = [A]_0 - [A]_{eq}$

$$k_{obs} = k_1([DMSO]_{eq} + [2.1]_{eq}) + k_{-1}([CH_2CHSiMe_3]_{eq} + [2.4]_{eq}) \qquad (2.9)$$

Table 2.2: Fitting results for the changes of **2.1** and **2.4** as a function of irradiation using Equation (2.8)

	a /%	b /%	k_{obs} /mol^{-1} dm^3 s^{-1}
[**2.1**]	5.2 ± 0.7	92.3 ± 0.9	$(5.67 \pm 0.57)\ x10^{-3}$
[**2.4**]	93.8 ± 0.7	-91.7 ± 1.0	$(5.95 \pm 0.60)\ x10^{-3}$

The equilibrium constant, K_{eq}, for this photostationary state maybe defined either in terms of the concentrations of each of the species in the equilibrium or in terms of the rate constants for the forward and back reactions Equation (2.10).[122] Using the concentrations a K_{eq} of 0.92 $\pm$ 0.08 was calculated. The expression for the equilibrium constant includes the concentration of the free ligands in addition to the rhodium complexes. This would suggest that as the amount of the free ligands changes the ratio of **2.4** and **2.1** should also. Using a smaller excess of DMSO could result in less **2.4** forming, whilst higher concentrations of DMSO could push the reaction towards completion, with no **2.1** remaining. To investigate this, a stock solution of **2.1** was prepared in 1.35 mL of d_8-toluene and 8 mg of ferrocene was added as an internal standard. This was divided equally into three NMR tubes and the following amounts of DMSO were added, with the excess of ligand relative to **2.1** given in brackets: 1.5 µL (5.5), 3.5 µL (12.8) and 5 µL (18.2). The samples were wrapped in foil sheaths to protect them from ambient light before irradiating each in turn for 45 minutes with periodic reaction monitoring using ^{1}H NMR spectroscopy and the growth in signals associated with **2.4** were observed.

$$K_{eq} = \frac{[2.4]_{eq}[CH_2CHSiMe_3]_{eq}}{[2.1]_{eq}[DMSO]_{eq}} = \frac{k_1}{k_{-1}} \qquad (2.10)$$

The formation of a photostationary state suggests that **2.4** loses DMSO and thus can reform **2.1** following the grey pathway in Figure 2.28. To test this hypothesis 9.5 µL of trimethylvinylsilane was added to the sample containing 5 µL of DMSO after its irradiation time. This sample now contains a 17.2 fold excess of both DMSO and trimethylvinylsilane and was irradiated for a further 35 minutes. During this time the growth in the NMR signals associated with both isomers of **2.1** were observed.

The proton spectra acquired during each sample irradiation period were analysed using the same approach as the first sample and as detailed in the Experimental. The concentrations of **2.1** and **2.4** were plotted against the irradiation time in Figure 2.29-Figure 2.32. In each case,

the establishment of a photostationary state is observed after an initial growth period, and only modest differences in the equilibrium concentrations of **2.1** and **2.4** were observed in the three samples with only DMSO as the ligand in excess. The sample with the smallest excess (5.5 fold) contained 11% of **2.1** and 88% of **2.4** whereas the samples with 12.8 and 18.2 fold excess contained 7 and 6% of **2.1** and 89% and 90% **2.4** respectively, a small amount of decomposition was observed in each of the samples (<5%). No decomposition products were identified or characterised, nor was any precipitate observed in the NMR tubes. The total integral of the Cp region of the NMR spectrum also reflected this drop in rhodium containing species which would suggest that the Cp ligand has been lost as part of the decomposition process. When there is an excess of both trimethylvinylsilane and DMSO a difference in the product distribution was observed with a photostationary state consisting of 51% **2.4** and 25% **2.1**, confirming the photolability of the DMSO ligand and showing a preference for **2.4** over **2.1**. A greater amount of decomposition is now observed, after a total of 80 minutes irradiation, and is reflected in the total amount of rhodium species being ~85% of the original rhodium content prior to any irradiation, as with the previous decomposition the identity of the decomposition product was not identified or characterised.

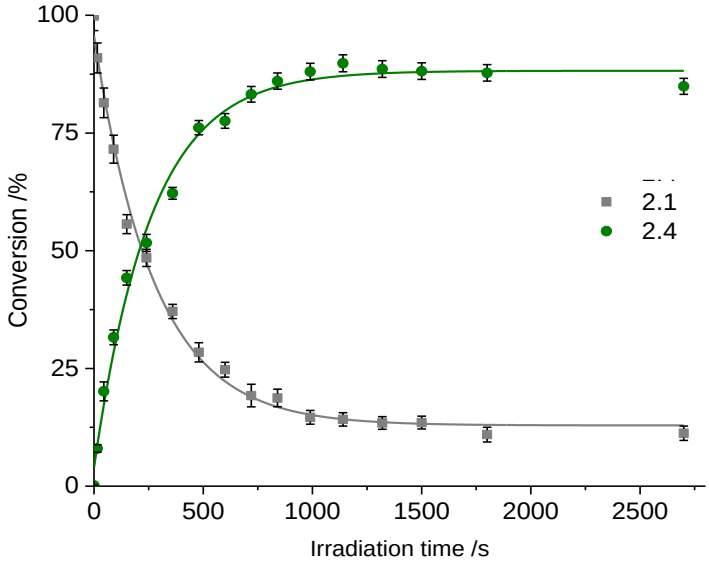

Figure 2.29 A plot showing the photochemical conversion of **2.1** into **2.4** as a function of irradiation time, with a 5.5 fold excess of DMSO, this was fitted to Equation (2.8) and the results are shown in Table **2.3** entry 1

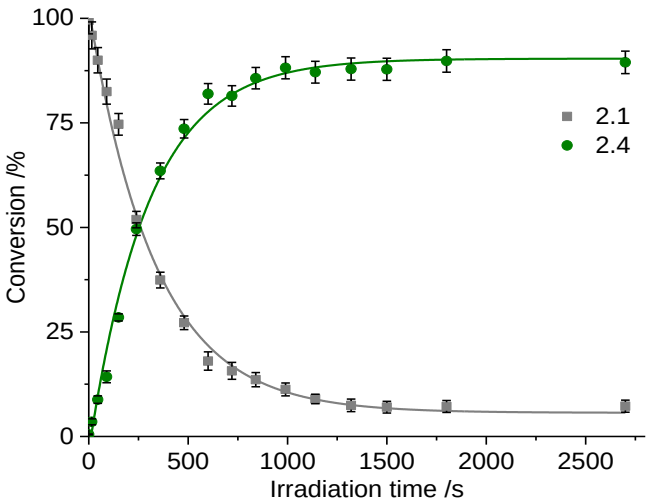

Figure 2.30 A plot showing the photochemical conversion of **2.1** into **2.4** as a function of irradiation time, with a 12.8 fold excess of DMSO, this was fitted to Equation (2.8) and the results are shown in Table **2.3** entry 2

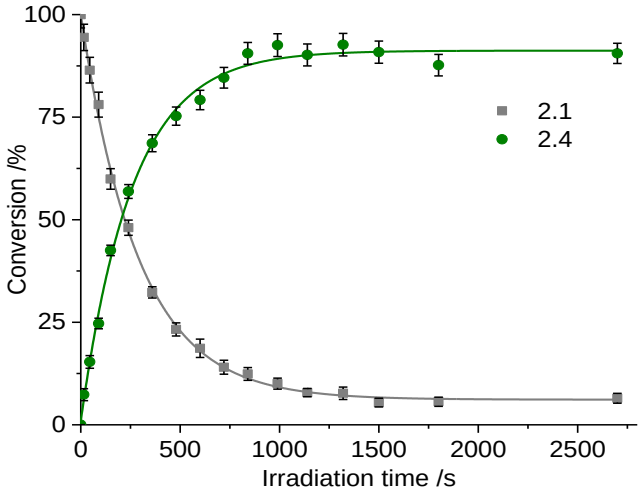

Figure 2.31 A plot showing the photochemical conversion of **2.1** into **2.4** as a function of irradiation time, with a 18.2 fold excess of DMSO**,** this was fitted to Equation (2.8) and the results are shown in Table **2.3** entry 3

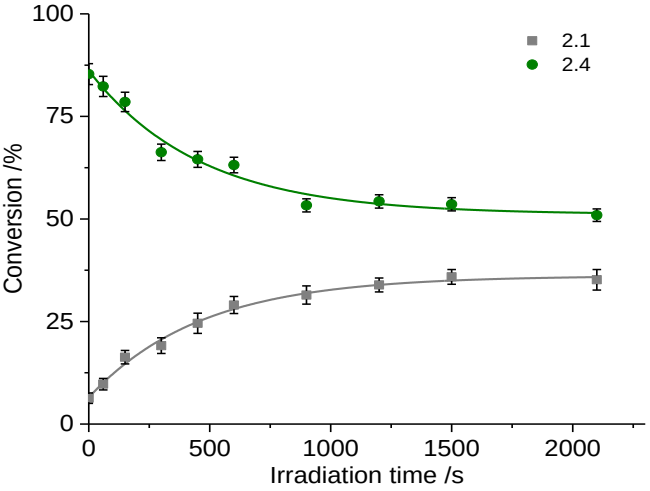

Figure 2.32: Time Plot showing the photochemical activity of **2.1** and **2.4** as a function of irradiation time when there is an excess of both DMSO and trimethylvinylsilane, this was fitted to Equation (2.8) and the results are shown in Table **2.3** entry 4

The relative compositions of each of these samples would suggest that the kinetic model proposed in Figure 2.28 is not correct and that the concentration of DMSO does not influence the reactivity. The concentration of trimethylvinylsilane, however, does appear to influence the reactivity. A new kinetic model is proposed (Figure 2.33). The associated integrated rate equation for this model is shown in Equation (2.11) where a is $[A]_{eq}$, b is $[A]_0 - [A]_{eq}$ and A can be **2.1** or **2.4** accordingly and k_{obs} is the observed rate constant defined by Equation (2.12). It is therefore expected that the three samples from the stock solution which only differ in the concentration of free DMSO should all have the same k_{obs} value whilst the k_{obs} for the sample containing an excess of trimethylvinylsilane as well as DMSO would be different. To confirm this, for each sample the changes in concentrations were fitted to Equation (2.11) and the results of this analysis are given Table 2.3. As expected, the values of k_{obs} for Entries 1-3 are within experimental error of one another and k_{obs} for Entry 4 is different confirming that the reaction rate is zero order with respect to DMSO indicating that the revised kinetic model in Figure 2.33 is correct.

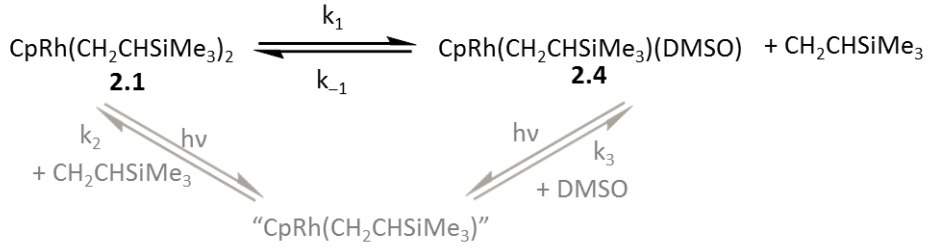

Figure 2.33: Revised kinetic model for the reaction between **2.1** and **2.4**. The full process is described in grey and the net reaction in black.

$$y = a + be^{-k_{obs}t} \qquad (2.11)$$

Where

a= $[A]_{eq}$

b= $[A]_0 - [A]_{eq}$

k_{obs}= $k_1 + k_{-1}([CH_2CHSiMe_3]_{eq}+[2.4]_{eq})$ (2.12)

Table 2.3: Fitting results for the changes of **2.1** and **2.4** as a function of irradiation using Equation (2.8) for each of the samples.

Entry	Molar Excess DMSO	Complex	a /%	b /%	k_{obs} /mol^{-1} dm^3 s^{-1}
1	5.5	[**2.1**]	12.9 ± 1.0	82.8 ± 1.6	(3.63 ± 0.55) x10^{-3}
		[**2.4**]	88.2 ± 1.1	-84.3 ± 1.9	(3.83 ± 0.62) x10^{-3}
2	12.8	[**2.1**]	5.7 ± 1.3	96.6 ± 1.8	(2.99 ± 0.46) x10^{-3}
		[**2.4**]	90.4 ± 1.6	-98.3 ± 2.5	(3.39 ± 0.54) x10^{-3}
3	18.2	[**2.1**]	6.1 ± 0.5	93.9 ± 0.9	(3.44 ± 0.43) x10^{-3}
		[**2.4**]	91.2 ± 0.9	-90.3 ± 1.5	(3.85 ± 0.57) x10^{-3}
4	17.2*	[**2.1**]	36.1 ± 0.8	-29.7 ± 1.0	(2.16 ± 0.42) x10^{-3}
		[**2.4**]	51.1 ± 1.6	35.0 ± 2.0	(2.18 ± 0.56) x10^{-3}

*Also contains 17.2 molar excess of trimethylvinylsilane

The expression of the equilibrium constant will change with the change in the kinetic model. A revised description of the equilibrium constant is given by Equation (2.14) and now does not include the concentration of DMSO. The equilibrium constant for each of the reactions, including the first sample (Entry 5) previously processed with Equation (2.10), were calculated using the equilibrium concentrations of the appropriate species and are given in Table 2.5. Whilst there is small variation between the equilibrium constants they are broadly within error experimental error of one another. The equilibrium constant for the sample with an excess of both DMSO and trimethylvinylsilane is notably higher than the other samples.

$$K_{eq} = \frac{[2.4]_{eq}[CH_2CHSiMe_3]_{eq}}{[2.1]_{eq}} = \frac{k_1}{k_{-1}} \qquad (2.13)$$

Table 2.4: Equilibrium constants for each of the samples

Entry	Molar Excess DMSO	K_{eq}
1	5.5	(4.7 ± 0.3) x10^{-2}
2	12.8	(9.8 ± 0.7) x10^{-2}
3	18.2	(1.2 ± 0.3) x10^{-1}
4	17.8*	(1.9 ± 0.1) x10^{-1}
5	20	(6.4 ± 0.2) x10^{-2}
6	17.8*	

*Also contains 17.8 molar excess of trimethylvinylsilane

Since k_{obs} and K_{eq} can be defined in terms of k_1 and k_{-1}, these expressions can be combined in order to calculate values of k_1 and k_{-1} using Equations (2.14) and (2.15). These were used calculate k_1 and k_{-1} for each of the samples (Table 2.5). For the three samples from the stock solution with only an excess of DMSO show k_1 values which are all within error of one another however this is not true across all samples for k_{-1}. The values of K_{eq} indicate that at the photostationary state there is a preference for **2.1** over **2.4**. This does not, however, explain **2.4** being the dominant species at the photostationary state when there is an equal excess of DMSO and trimethylvinylsilane suggesting that at higher concentrations the reaction is zero order with respect to trimethylvinylsilane. If this was the case, the equilibrium constant would simply be the ratio of two complexes and gives a K_{eq} of 1.51 $\pm$ 0.08. This is now over one indicating a preference for **2.4** over **2.1** and that k_1 must be greater than k_{-1}. In this scenario, k_1 and k_{-1} for a photochemical system are defined according to Equations (2.16) and (2.17). These expressions suggest that for an equilibrium favouring **2.4**, either the quantum yield of **2.1** is greater than that of **2.4** and therefore is more efficient at forming the reactive intermediate. Alternatively the coordination of DMSO is favoured over the coordination of trimethylvinylsilane.

$$k_1 = \frac{k_{obs}K_{eq}}{K_{eq} + [2.4]_{eq} + [CH_2CHSiMe_3]_{eq}} \quad (2.14)$$

$$k_{-1} = \frac{k_{obs}}{K_{eq} + [2.4]_{eq} + [CH_2CHSiMe_3]_{eq}} \quad (2.15)$$

Table 2.5: Rate constants determined using Equations (2.14) and (2.15)

Entry	Molar Excess DMSO	k_1 /mol^{-1} dm^3 s^{-1}	k_{-1} /mol^{-1} dm^3 s^{-1}
1	5.5	(3.0 $\pm$ 0.7) x10^{-3}	(6.1 $\pm$ 1.2) x10^{-2}
2	12.8	(2.8 $\pm$ 0.9) x10^{-3}	(2.8 $\pm$ 0.7) x10^{-2}
3	18.2	(3.4 $\pm$ 2.4) x10^{-3}	(2.6 $\pm$ 1.5) x10^{-2}
4	17.8*	(1.3 $\pm$ 0.5) x10^{-3}	(6.8 $\pm$ 1.9) x10^{-3}

*Also contains 17.8 molar excess of trimethylvinylsilane

$$k_1 = \frac{\Phi_{2.1} I_0 l \varepsilon_{2.1} k_3}{k_2 + k_3} \quad (2.16)$$

$$k_{-1} = \frac{\Phi_{2.4} I_0 l \varepsilon_{2.4} k_2}{k_2 + k_3} \quad (2.17)$$

2.6 Photochemistry of $[(\eta^5\text{-}C_5H_5)Rh(\eta^2\text{-}CH_2CHSi(CH_3)_3)_2]$ **2.1** with Et_3SiH to form **2.5** and **2.6**

To investigate the other properties of the reactive intermediate formed from **2.1** was studied with triethylsilane, which contains a Si–H bond that may undergo oxidative addition reactions with similar rhodium complexes.[111, 133] An NMR sample containing 0.5 mg $[(\eta^5\text{-}C_5H_5)Rh(\eta^2\text{-}CH_2CHSi(CH_3)_3)_2]$ **2.1** and 4 µL of triethylsilane was prepared in d_8-toluene, giving a 17 fold excess of triethylsilane compared to the rhodium complex. The sample was then irradiated *ex-situ* using a broadband UV lamp for a total of 2 hours and the reaction followed by ^{1}H NMR spectroscopy. Over the course of the irradiation two species were observed (Figure 2.34) although only one of these remained at the end of the 2 hours. After this time 4 µL of trimethylvinylsilane was added to the NMR sample and the sample was irradiated for a further hour to investigate whether the intermediate or the starting material could be reformed from the final product. No changes were evident in the ^{1}H NMR spectrum after this irradiation, suggesting that the final product is not photochemically active.

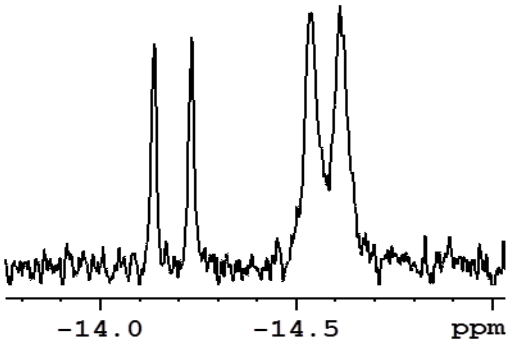

Figure 2.34: Hydride region of the ^{1}H NMR Spectrum following photolysis of **2.1** in the presence of triethylsilane in d_8-toluene at 298 K.

The distinguishing features of the final product are a hydride resonance at δ –14.2 with a coupling to rhodium of 38.0 Hz (Figure 2.34), these features are consistent with the known compound $[(\eta^5\text{-}C_5H_5)Rh(H)_2(Si(CH_2CH_3)_3)_2]$ **2.6.**[56, 134] The magnitude of the coupling constant is indicative of a Rh^V species, which arises via the oxidative addition of two Si–H bonds following the loss both alkene ligands. The other product formed also contains a metal hydride moiety, a doublet at δ –14.6 (J_{HRh} 31.5 Hz) (Figure 2.34). This smaller coupling is now consistent with a Rh^{III} species and fits with a stepwise reaction between **2.1** and Et_3SiH and thus the intermediate species observed is likely to correspond to a complex that containing a vinylsilane ligand as well as a hydride and silyl ligand.

In order to characterise the intermediate in this process this study was repeated with a fresh sample with a smaller excess of triethylsilane and a shorter irradiation time of 10 minutes to limit the formation of the second product. Many of the resonances associated with the intermediate are broad in the ^1H NMR spectrum (bottom spectrum Figure 2.36) indicating that there is a fluxional process within the system. Broadness in NMR resonances is often associated with movement on the NMR timescale and that can be reduced by lowering the temperature. At 283 K the resonances sharpened sufficiently to allow their multiplicity to be resolved and 2D NMR measurements to be made. Two of the broad resonances at δ 2.71 and 2.00 resolve as doublets with 14 Hz and 11 Hz couplings respectively and the third resonance, at δ 1.84, resolves to be a doublet of doublets with 14 and 11 Hz couplings. These three resonances are shown to couple to one another in a 2D ^1H-^1H COSY spectrum; this and their observed couplings would suggest that they belong to a coordinated trimethylvinylsilane ligand. The signals at δ 2.00 and 2.71 are consistent with the geminal protons H_B and H_C on the vinylsilane ligand, which is confirmed by their correlation to the same carbon environment at δ 38.2 in a 2D ^1H-^{13}C HMQC NMR spectrum. The third signal is consistent with H_A, these assignments are summarised in Figure 2.35. The hydride resonance at δ –14.6 shows an nOe

correlation to a triplet at δ 1.05 and a quartet at δ 0.66 which are consistent with the ethyl groups of the silane. It also shows an nOe connection to H_B at δ 2.00 and a weaker nOe connections to δ 1.84 (H_A) and 2.71 (H_C). These data are fully consistent with the structure in Figure 2.82 and the NMR data is summarised in Table 2.19.

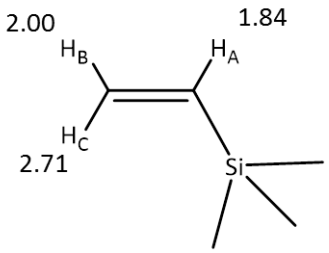

Figure 2.35: Assignments of the trimethylvinylsilane proton chemical shifts

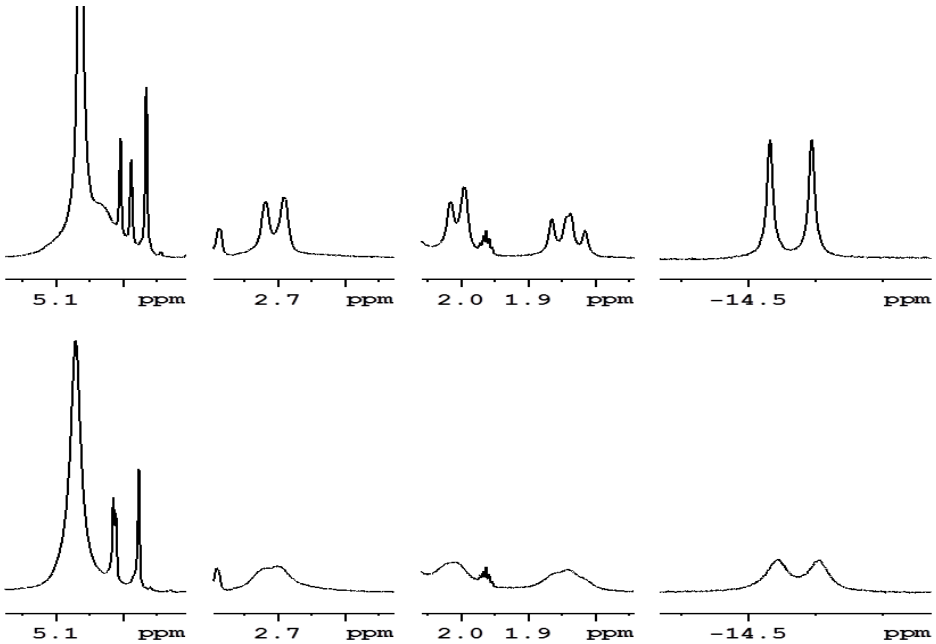

Figure 2.36: ^{1}H NMR spectrum of photoproduct following the photolysis of **2.1** in the presence of triethylsilane in d_8-toluene, the hydride region is magnified 4x relative to the rest of the spectrum. The top spectrum was recorded at 283 K and the bottom at 298 K

In **2.5** the substituent of the alkene could give rise to different isomers **2.5A** and **2.5B** (Figure 2.37), in the same way that it broke the symmetry of the two methyl groups of the bound DMSO ligand in **2.4**. If interconversion between these two isomers is possible it could be the source of the observed fluxionality. This has been observed with other substituted alkenes for example $[(\eta^5\text{-}C_5H_5)Rh(\eta^2\text{-}CH_2CHCO_2{}^tBu)_2]$[111] where the route to isomerisation between these two isomers was also studied. There are a number of possible pathways which include;

reversible hydride and/or silyl migration, reductive elimination of the Si–H bond or rotation via an intermediate. These isomers themselves do not interconvert through the rotation of the bound alkene, although further isomers are accessible through this rotation resulting in a product containing the trimethylsilyl group pointing down as illustrated in **2.5C** (Figure 2.37). It should be noted that the specific stereochemistry has been omitted and either orientation of the hydride and silyl group is feasible.

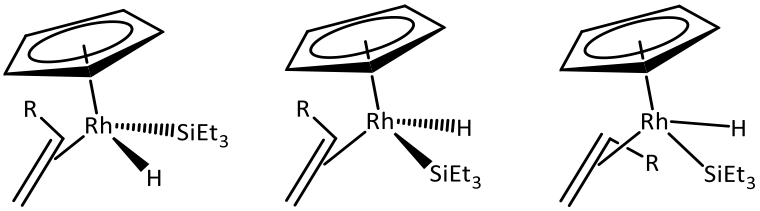

2.5A **2.5B** **2.5C**

Figure 2.37: Possible isomers of **2.5**; where R = $Si(CH_3)_3$

Previous work in the group utilised exchange spectroscopy (EXSY)[111, 112] to distinguish between the possible isomerisation routes and was able to conclude that the process was intramolecular based on the absence of exchange between the bound and free ligands, which applied to both the silane and the alkene. Therefore, it was deduced that the isomerisation was achieved through an intermediate or transition state and that this must involve the silyl and hydride ligands as the observed isomerisation cannot be achieved through the rotation of the bound alkene ligand, it must involve the silyl and hydride groups. As discussed in the Introduction, Si–H bonds can be considered as coordinating to a metal centre either in an η^2 fashion, to give an M-(η^2-H-Si) species, or alternatively it may undergo oxidative addition, resulting in the cleavage of the Si–H bond forming a M(H)(Si) complex. In reality any position between these two extremes is possible and the degree of cleavage is not static within a system. This is the basis of the proposed isomerisation mechanism between **2.5A** and **2.5B** where a Rh-(η^2-H-Si) intermediate or transition state forms from either **2.5A** or **2.5B**, rotation about this bond may then occur and generate the opposite isomer (Figure 2.38). Exchange cross peaks were observed between the trimethylvinylsilane resonances in a ^{1}H-^{1}H EXSY

experiment at 283 K and no exchange was observed between the coordinated and free triethylsilane. Both of these observations support the proposed route for interconversion

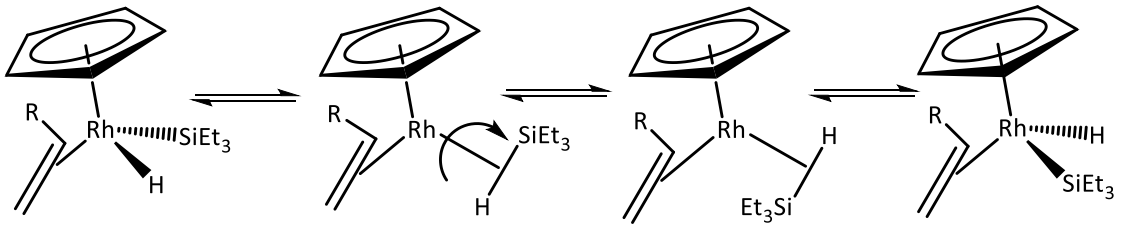

Figure 2.38: Proposed pathway for the interconversion between **2.5A** and **2.5B**, R = $Si(CH_3)_3$, adapted from Duckett *et al.*[111, 112]

Further variable temperature measurements were therefore performed in order to confirm the presence of other isomers of **2.5**. ^{1}H NMR spectra were acquired at temperatures between 243 and 298 K (Figure 2.39) and revealed the presence of two further resonances at δ –14.9 and –17.0, both doublets with a coupling to rhodium of 33 Hz. At this time, the relative proportion of the three isomers was 74: 14: 10 in order by chemical shift (from low field to high field) indicating these isomers form only a small proportion of the product.

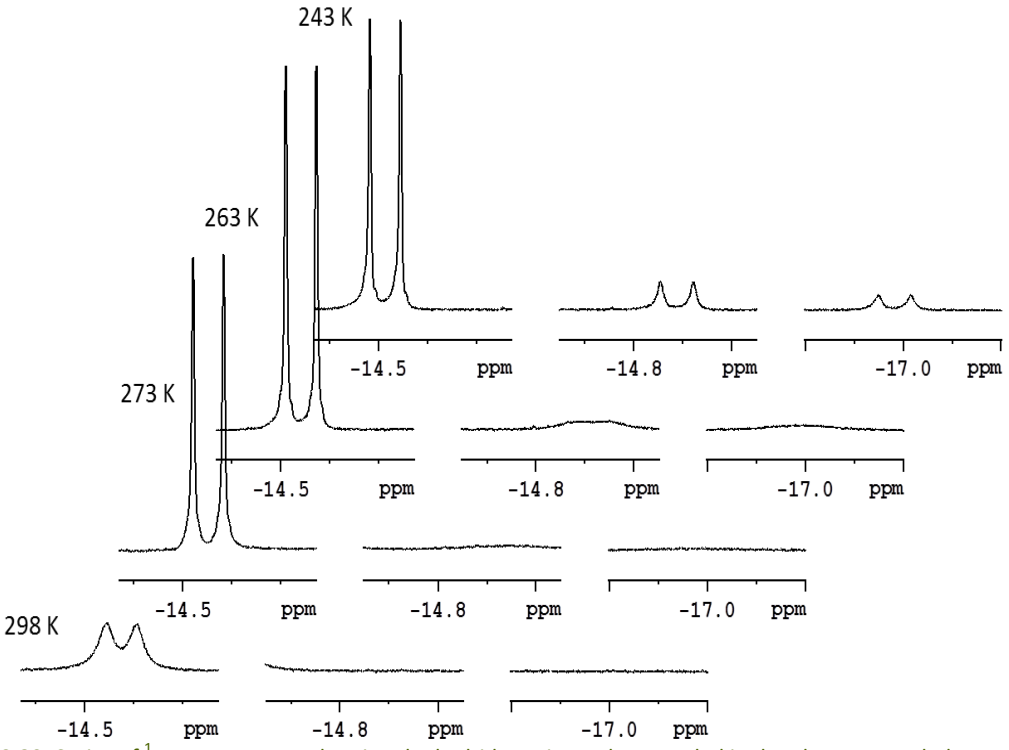

Figure 2.39: Series of ^{1}H NMR spectra, showing the hydride region only, recorded in d_8-toluene recorded at variable temperatures (as labelled).

The ^{1}H NMR spectra recorded during the first 2 hours of irradiation were analysed using the approach outlined in the Experimental 8.4. The two hydride resonances were used for the respective products and CH group of the vinylsilane in **2.1A** and **2.1B** were used to follow the starting material, for simplicity the contributions of the two isomers of **2.1** were combined. The concentrations of **2.1**, **2.5** and **2.6** relative to the initial concentration of **2.1** were plotted against irradiation time in seconds (Figure 2.40) revealing a two-step process with the second step, the formation of **2.6**, occurring on a notably slower timescale than the first. Over the course of the reaction there was a notable drop in the total rhodium content with there being 40% of rhodium content being unaccounted for by the end of the irradiation time and suggests that there is a route to decomposition for at least one of the complexes observed. The nature of the decomposition was not determined, no obvious precipitate was observed in solution. The total integral for the Cp region of the NMR spectrum was consistent with a 40% drop in half sandwich rhodium species which would suggest that the Cp ligand is lost during decomposition but beyond this no further information is known.

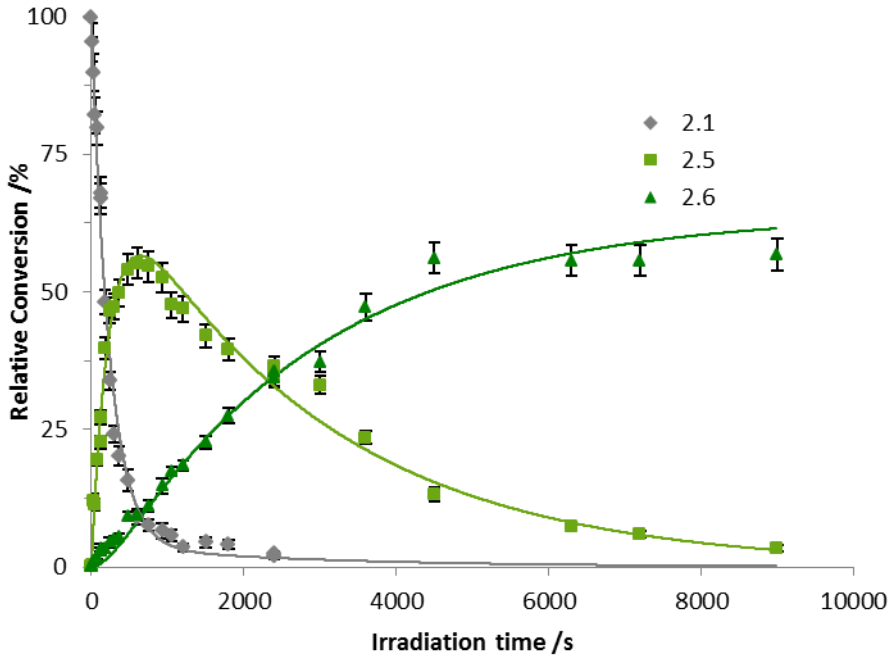

Figure 2.40: Time profile showing the conversion of **2.1** into **2.5** which then forms **2.6**.

The proposed kinetic model for this reaction is outlined in Figure 2.41. The first step involves an equilibrium between **2.1** and **2.5** and is followed by a second step corresponding to the irreversible formation of **2.6**. This was modelled using the differential approach detailed in Experimental 8.4.3, through a chemical exchange model within Excel coupled with the Solver function, allowing values of k_1, k_{-1} and k_2 to be obtained (Table 2.6).

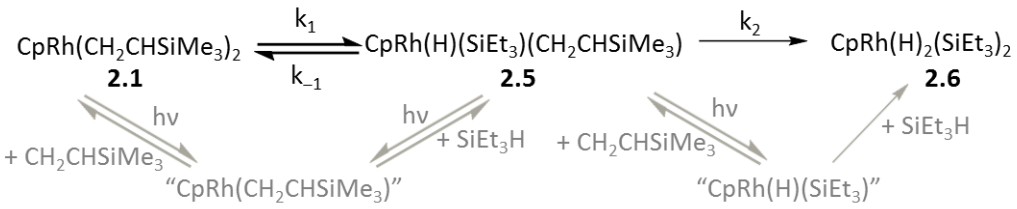

Figure 2.41: Kinetic model for the reaction of **2.1** with triethylsilane to form **2.5** and **2.6**; the observable reaction is given in black and in grey is the route to these species.

Table 2.6: Relaxation constants for each step in the kinetic model for the reaction between 2.1 and triethylsilane and the calculated equilibrium constant

k_1 /mol^{-1} dm^3 s^{-1}	k_{-1} /mol^{-1} dm^3 s^{-11}	k_2 /mol^{-1} dm^3 s^{-1}	K_{eq}
(6.22 ± 0.54) x10^{-2}	(8.9 ± 1.1) x10^{-2}	(6.63 ± 0.62) x10^{-3}	0.71 ± 0.14

The values of k_1 and k_{-1} may be used to give the equilibrium constant for the equilibrium between **2.1** and **2.5** giving a K_{eq} of 0.71 ± 0.14 using Equation (2.18).[122] If it is assumed that the sample has low absorbance (Appendix), the equilibrium constant relates to the molar absorbance and quantum yield of **2.1** and **2.5** and the rate of the ligand addition to the intermediate (Equation (2.19)).[122, 125] An equilibrium constant of 0.71 suggests that either the quantum yield of **2.1** is smaller than that of **2.5**, and therefore the triethylsilane ligand is more photolabile than trimethylvinylsilane, or that trimethylvinylsilane coordination to the intermediate occurs at a faster rate than the oxidative addition of triethylsilane. Both of these situations would result in less of the photoproduct **2.5** than **2.1** in the equilibrium.

$$K_{eq} = \frac{k_1}{k_{-1}} \tag{2.18}$$

$$K_{eq} = \frac{\Phi_{2.1}\varepsilon_{2.1}k_1}{\Phi_{2.5}\varepsilon_{2.5}k_{-1}} = \frac{[2.5][CH_2CHSiMe_3]}{[2.1][Et_3SiH]} \tag{2.19}$$

The value for k_2 approximately 10 times smaller than that of k_{-1}. This would suggest that the reductive elimination of the silane to give "$CpRh(CH_2CHSiMe_3)$" occurs more readily than the loss of vinylsilane to give "$CpRh(H)(SiEt_3)$". Alternatively this could demonstrate that "$CpRh(H)(SiEt_3)$" is more active towards vinylsilane to reform **2.5** than it is a second molecule of triethylsilane.

2.7 Photochemistry of $[(\eta^5\text{-}C_5H_5)Rh(\eta^2\text{-}CH_2CHSi(CH_3)_3)(DMSO)]$ **2.4** with Et_3SiH to form **2.5**, **2.6** and **2.7**

In Section 2.5 it was demonstrated that DMSO is photolabile in $[(\eta^5\text{-}C_5H_5)Rh(\eta^2\text{-}CH_2CHSi(CH_3)_3)(DMSO)]$ **2.4** by the formation of **2.1** when **2.4** was irradiated with an excess of trimethylvinylsilane. This reactivity could only be accounted for by the photochemical loss of DMSO from **2.4**. What is unknown is whether **2.4** may also lose its trimethylvinylsilane ligand as $CpRh(DMSO)_2$ was not observed, this could also be due to thermal instability in the product, and coordination of the vinylsilane to "CpRh(DMSO)" would reform **2.4**. To investigate the photochemical properties of **2.4** further, 3.5 µL of Et_3SiH was added a sample of **2.4** to result in a 20 fold excess of the Et_3SiH relative to **2.4**, in addition to 1 equivalent of $CH_2CHSiMe_3$ and a 19 fold excess of DMSO still present from the reaction to form **2.4**. The sample was then photolysed for 15 minutes after which time NMR spectroscopy indicated the formation of three new rhodium hydride products (Figure 2.34). The hydride signal at δ –14.6 has already been shown to belong to $[(\eta^5\text{-}C_5H_5)Rh(H)(Si(CH_2CH_3)_3)(\eta^2\text{-}CH_2CHSi(CH_3)_3)]$ **2.5** confirming the photolability of DMSO. The hydride signal at δ –14.2 is consistent with the formation of the double oxidative addition product $[(\eta^5\text{-}C_5H_5)Rh(H)_2(Si(CH_2CH_3)_3)_2]$ **2.6**. Accordingly, the third rhodium hydride species must contain a coordinated DMSO ligand indicating that $[(\eta^5\text{-}C_5H_5)Rh(H)(Si(CH_2CH_3)_3)(DMSO)]$ **2.7** has been formed and is associated with the hydride resonance at δ –13.45, exhibiting a 33.7 Hz rhodium coupling (Figure 2.42), which is consistent a Rh^{III} product. The chemical shift of this hydride matches the literature value, however the

rhodium coupling was reported as 35.3 Hz.[110] The coordinated DMSO ligands yielded resonances δ 2.45 and δ 2.55 consistent with the reported values.

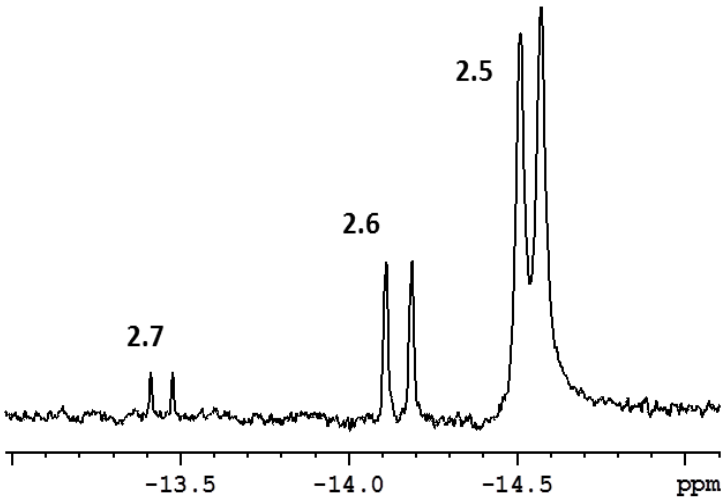

Figure 2.42: Hydride region of an ^{1}H NMR spectrum at 298 K following the 15 min photolysis of **2.4** and Et_3SiH in d_8-toluene showing the hydride resonances for **2.5**, **2.6** and **2.7** as labelled.

To investigate this further, triethylsilane was added to two samples containing different concentrations of DMSO. Sample 1 contained an 11.8 fold excess of DMSO relative to the total rhodium content and 1 equivalent of trimethylvinylsilane and sample 2 contained a sub-stoichiometric amount of DMSO (0.3 equivalents) and no trimethylvinylsilane, both samples contained 3 µL of Et_3SiH providing a 5 fold excess relative to the rhodium content. Sample 1 was irradiated for 1.5 hours and during this time proton spectra were acquired. The spectra, which were recorded using parameters that would allow them to be used quantitatively, did not yield the required information to study this reaction in the same manner as the other reactions in this chapter, owing to resonance overlap. Signals in clear regions of the ^{1}H NMR spectrum had insufficient signal-to-noise ratios for the reliable integration necessary for quantification. ^{1}H NMR spectra were also recorded with more scans (NS 128 vs 8) but with a shorter interscan delay (d1 = 3 s) and may be used qualitatively (Figure 2.43). The irradiation of **2.4** first yields **2.5** and only after 20 minutes irradiation does **2.7** form, **2.6** is not observed until the sample has been irradiated for 1.5 hours. At this time the sample contains 53% of **2.4**. Looking only at the hydride-containing species the sample consists of 78% **2.5**, 4% **2.6** and 18%

2.7. After the sample was then left for 15 days at room temperature, and protected from ambient light, it consisted of 71% **2.5**, 5% **2.6** and 24% **2.7**.

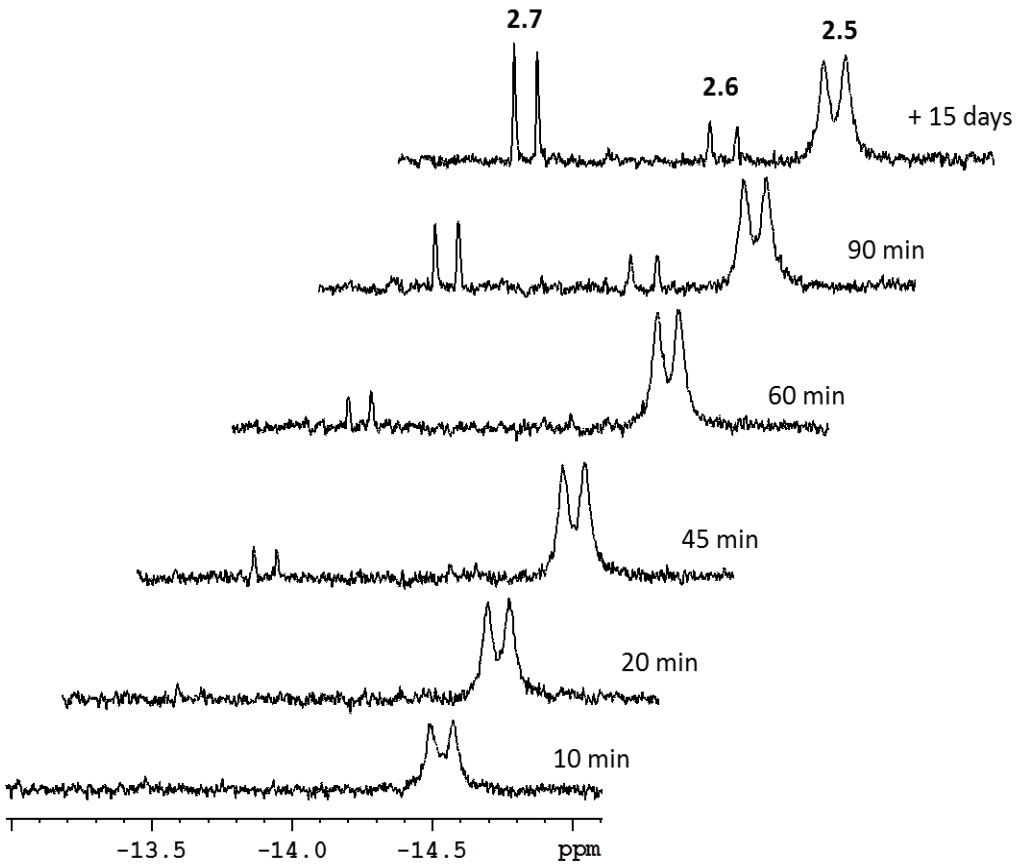

Figure 2.43: Hydride region of the ^{1}H NMR spectrum for sample 1 recorded in d_8-toluene at 298 K. Spectra labelled with the associated irradiation time and the top-most spectrum was recorded 15 days later showing the thermal activity

Sample 2 was then irradiated for 1 hour and the reaction followed by ^{1}H NMR spectroscopy (Figure 2.44). Now **2.6** is observed, in addition to **2.4**, after 10 minutes irradiation and only after 45 minutes irradiation is **2.7** observed. After 1 hour irradiation just 24% of the initial amount of **2.4** remains. The relative amounts of the hydride species at this time were 85% **2.5**, 11% **2.6** and 4% **2.7** and after 15 days at room temperature protected from ambient light there was now 82% **2.5**, 13% **2.6** and 5% **2.7**.

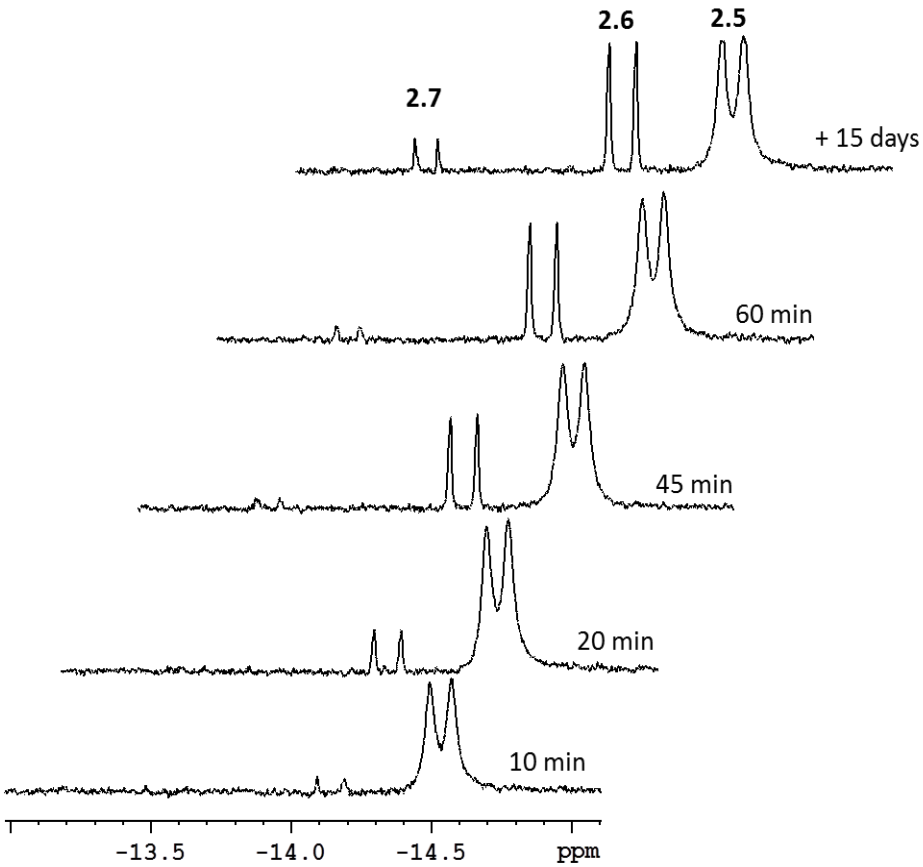

Figure 2.44: Hydride region of the ^{1}H NMR spectrum for sample 2 recorded in d_8-toluene at 298 K. Spectra labelled with the associated irradiation time and the top-most spectrum was recorded 15 days later showing the thermal activity

The potential routes to the formation of these three rhodium hydrides species are presented in Figure 2.45. $CpRh(CH_2CHSiMe_3)(DMSO)$, **2.4**, may lose either DMSO or vinylsilane which, following Et_3SiH addition, gives either **2.5** or **2.7** respectively. Both **2.5** and **2.7** may lose a ligand to generate the intermediate "$CpRh(H)(SiEt_3)$" which provides a route to the formation of all three hydride species.

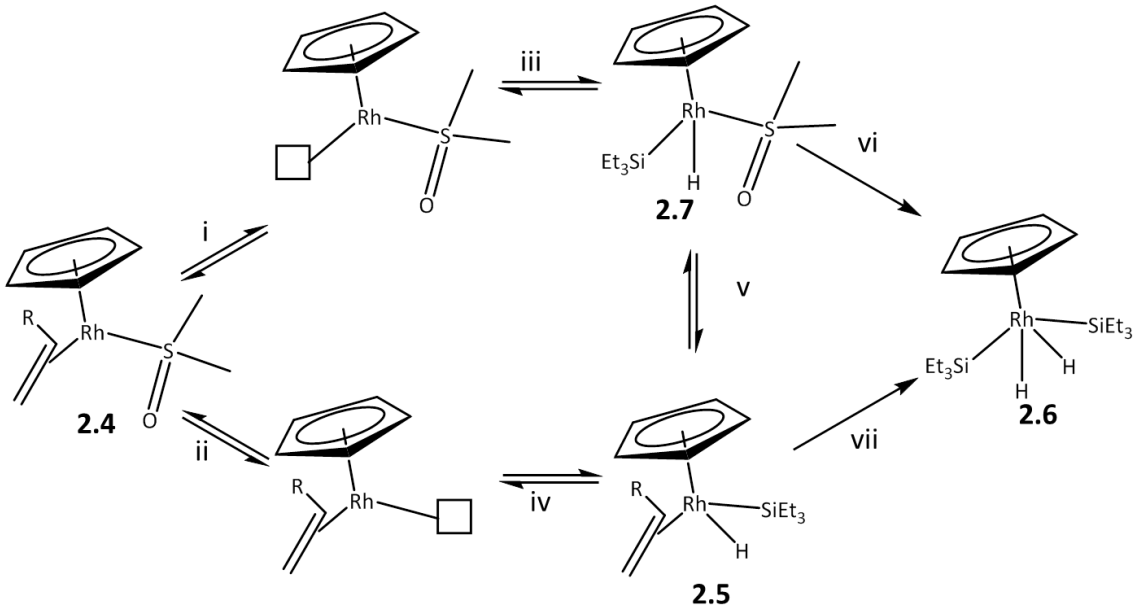

Figure 2.45: Possible pathway for the formation of the three rhodium-hydride species

In summary, the irradiation of the two samples yielded the following observations

- **2.5** always forms first
- With sub-stoichiometric amounts of DMSO and no free trimethylvinylsilane **2.6** forms in the first 10 minutes of irradiation but not until after 1.5 hours when free DMSO and vinylsilane are present
- **2.7** forms on a slower timescale than **2.5** and can form thermally from **2.5**, over the course of 15 days.

From these observation it can be concluded that **2.7** is more likely to form through the loss of trimethylvinylsilane from **2.5** than from **2.4** and that the kinetic model associated with the reactivity observed between **2.4** and Et_3SiH is consistent with Figure 2.46. An equilibrium is formed between **2.4** and **2.5.** In the sample with an excess of DMSO after 1.5 hours irradiation there is still 53% of **2.4** suggesting that DMSO coordination is favoured over Et_3SiH, or that Et_3SiH is more photolabile than DMSO in this equilibrium. A second equilibrium is proposed between **2.5** and **2.7**. When there was a larger excess of DMSO than Et_3SiH, **2.5** still dominated

over **2.7** indicating **2.5** is more stable than **2.7** or DMSO is more photolabile or coordination of vinylsilane to "CpRh(H)(SiE_3)" is favoured.

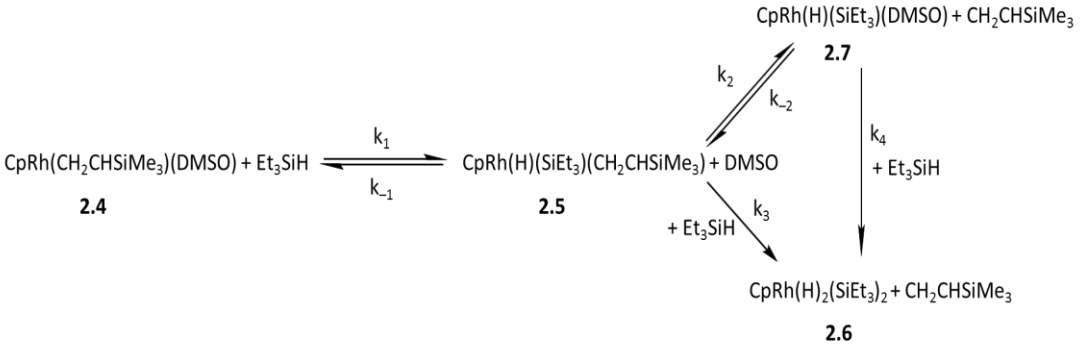

Figure 2.46: Proposed kinetic model for the reaction of **2.4** with triethylsilane.

2.8 Photochemistry of **2.2** and **2.3** with $CH_2CHSi(CH_3)_3$ – to form **2.8**, and **2.1**

The photoreactivities of complexes **2.2** and **2.3** were studied in order to provide new insights into the reactivity of these systems, their UV-Vis spectra are shown in Figure 2.47 and Figure 2.48. First, the photosubstitution of the respective alkenes with a trimethylvinylsilane ligand was investigated. The product distribution will reveal whether one or both of the alkene moieties can be lost. The difference between the monodentate cyclooctene to the bidentate cyclooctadiene is expected to impact on this chemistry. To study this process two samples were prepared and irradiated in turn as detailed in Table 2.7. These reactions were monitored by ^{1}H NMR spectroscopy and are now discussed.

Table 2.7: Sample preparation details

Complex	Rh /mg	$CH_2CHSiMe_3$ /µL	Molar Excess	Irradiation time
2.2	1.0	4.5	12	1h
2.3	1.8	7.5	8	5h20

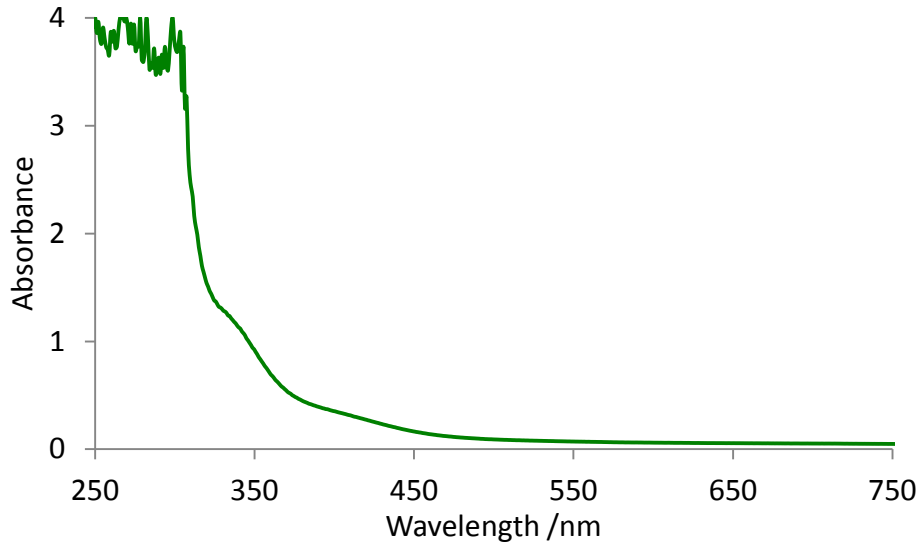

Figure 2.47: UV-Visble spectrum of **2.2** in C_6H_6

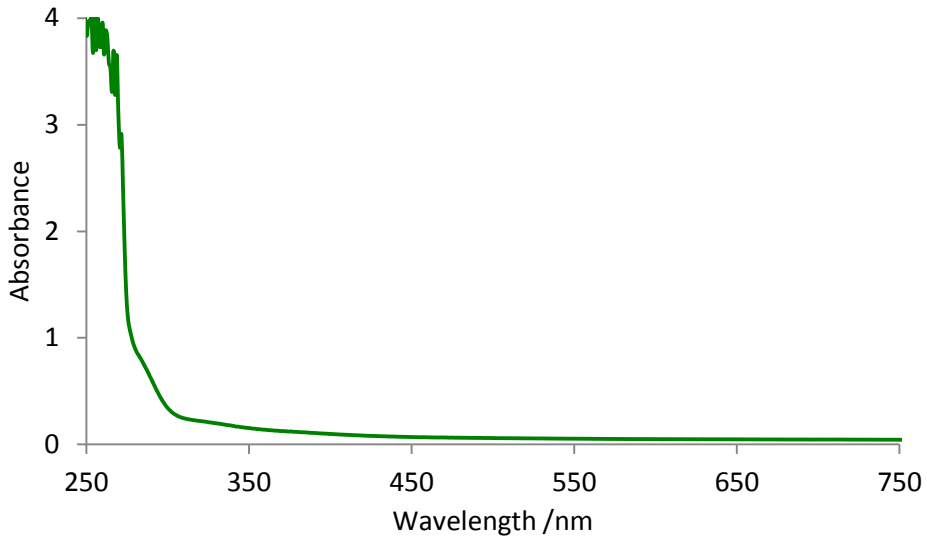

Figure 2.48: UV-Visible spectrum of **2.3** in C_6H_6

2.8.1 $[(\eta^5\text{-}C_5H_5)Rh(\eta^2\text{-}C_8H_{14})_2]$ **2.2**

The irradiation of **2.2** in the presence of trimethylvinylsilane resulted in new signals which can be attributed to three rhodium half sandwich products (Figure 2.49). Plotting the change in speciation with irradiation reveals that **2.2** converts first into a new photoreactive product before evolving further into two stable species which are still observable at the end of photolysis (Figure 2.52). These correspond to two isomers of **2.1** which result from substitution of both of the cyclooctene ligands. The intermediate, therefore, is likely to correspond to a complex with one cyclooctene ligand and one trimethylvinylsilane ligand.

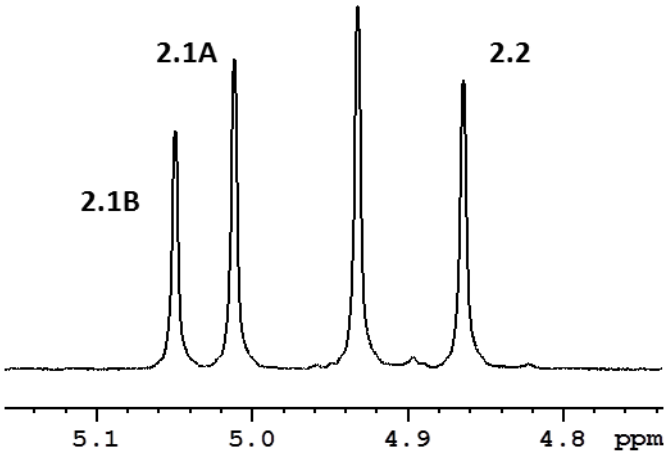

Figure 2.49: ^{1}H NMR spectrum at 298 K of **2.2** after photolysis in the presence of trimethylvinylsilane (in d_8-toluene), the peaks associated with already characterised species are labelled as **2.1A**, **2.1B** and **2.2**.

In order to characterise the intermediate this study was repeated with a fresh sample and the irradiation halted prior to complete conversion into the bis-substituted products. The proton spectrum now exhibits four peaks in the cyclopentadienyl region. Three of these peaks have already been assigned to complexes **2.1A** (δ_H 4.98, δ_C 87.1), **2.1B** (δ_H 5.01, δ_C 87.2) and **2.2** (δ_H 4.83, δ_C 90.8), by elimination, the peak at δ 4.90 must correspond to the **2.8** (Figure 2.49).

In the ^{1}H-^{1}H COSY NMR spectrum there are three sets of signals for bound trimethylvinylsilane ligands, two sets can be attributed to the isomers of **2.1**.The third set comprises three doublets of doublets at δ -0.16 (J_{HH} 11, 14 Hz), δ 2.10 (J_{HH} 1.5 Hz) and δ 2.97 (J_{HH} 14, 1.5 Hz) and arises from the intermediate. Due to overlap with a solvent signal the δ 2.10 resonance is poorly resolved however, examination of the COSY NMR spectrum reveals an 11 and 1.5 Hz coupling. The small coupling of 1.5 Hz is consistent with the geminal coupling between H_B and H_C assigning these protons as the CH_2 group and is corroborated by both of these resonances showing correlations to a carbon signal at δ 40.9 in a ^{1}H-^{13}C HMQC experiment. The third proton, δ –0.16, showed a correlation to a separate carbon resonance at δ 50.8 consistent with the CH group of the vinylsilane ligand. Both carbon signals exhibited a coupling to rhodium of 14 Hz, indicative of a rhodium coordinated alkene ligand. The respective proton environments were assigned based on their proton-proton couplings (Figure 2.50) and the arrangement of

this ligand was confirmed by observations in the ^{1}H-^{1}H NOESY 2D NMR spectrum. The proton at δ 2.97 shows an nOe to the Cp peak at δ 4.90 and to the trimethyl group of the silane substituent. This would suggest that the silane substituent is on the same side of the alkene as the proton at δ 2.97 and that they are pointing up towards the Cp ring.

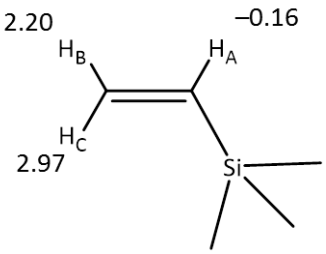

Figure 2.50: Assignments of the trimethylvinylsilane protons

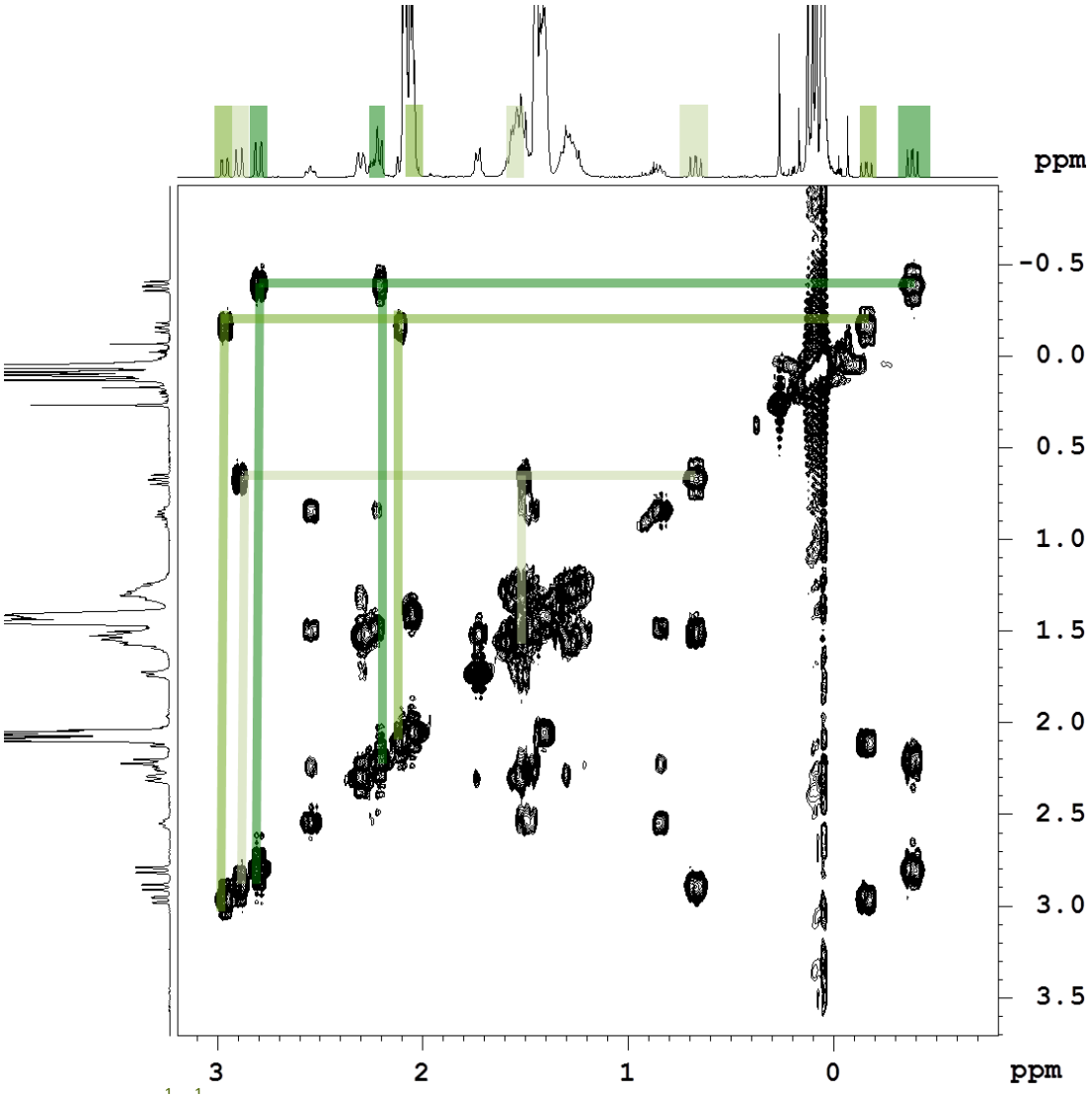

Figure 2.51: ^{1}H-^{1}H COSY NMR spectrum in d_8-toluene of photoproducts form through the reaction of **2.2** with trimethylvinylsilane showing the three products with bound trimethylvinylsilane ligands.**2.1A** is highlighted in ■; **2.1B** in ■ and **2.8** in ■.

The resonances of note from the COE ligand are the vinylic protons at δ 2.55 and 0.80 which correlate to carbon resonances in the ^{1}H-^{13}C HMQC NMR spectrum at δ 61.6 and 68.4 respectively. In the $^{13}C\{^{1}H\}$ NMR spectrum both of these resonances exhibited a coupling to rhodium of ~14 which corresponds to a rhodium coordinated alkene. In a ^{1}H-^{1}H NOESY spectrum the proton resonances show an nOe correlation with the δ –0.16 proton on the vinylsilane ligand confirming the assumption that the product contains both a cyclooctene and trimethylvinylsilane ligand. The proposed structure of this product is depicted in Figure 2.85 and the details of the NMR characterisation are summarised in Table 2.22.

Having fully assigned the proton spectrum, the series of spectra recorded during photolysis were reanalysed to extract more information. The percent of each species relative to the initial concentration of **2.2** were calculated and then plotted against the irradiation time (Figure 2.52). The profiles of the different rhodium complexes as a function of irradiation time suggest that the loss of COE ligands occurs in a step-wise fashion since the intermediate peaks in intensity prior to significant growth of the final products and that the loss of the second ligand occurs on a similar timescale to the first. After 4 minutes irradiation, **2.8** reached a maximum concentration of 27%, relative to the initial concentration of rhodium whilst a photostationary state was achieved after 20 minutes there is 10% **2.8** remaining in addition to 48% of **2.1A** and 41% of **2.1B**. Further irradiation did not improve these conversions.

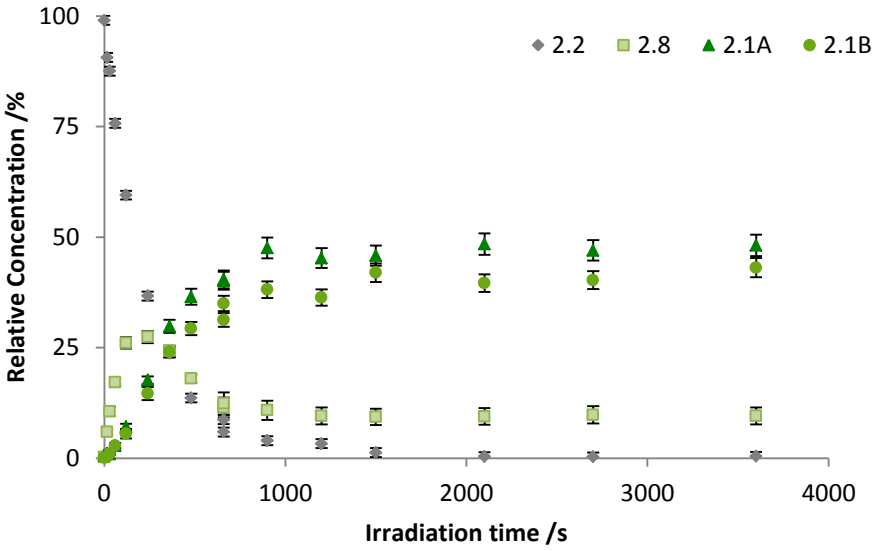

Figure 2.52: Time profile showing the change in concentration of **2.2, 2.8, 2.1A** and **2.1B** as a function of irradiation time.

The kinetic model which describes the reaction of **2.2** with trimethylvinylsilane is shown in Figure 2.53. Firstly the product, **2.8**, is formed reversibly from **2.2**. These two species share the common reactive intermediate "CpRh(COE)" and **2.2** or **2.8** forms depending on whether the COE or vinylsilane coordinates. The product **2.8** may also lose COE to form "CpRh($CH_2CHSiMe_3$" which also may coordinate COE or vinylsilane to either reform **2.8** or form one of the two isomers of **2.1**. There are four reversible steps connecting **2.2**, **2.8**, **2.1A** and **2.1B**. To fit each of these would be challenging. The equilibrium between **2.1A** and **2.1B** has already been analysed in Section 2.4. The ratio of **2.1B** to **2.1A** at the photostationary state is 0.86 ± 0.08,[122] consistent with the K_{eq} value obtained in Section 2.4. Combining the contributions of these two isomers offers a simplification to the complex kinetic model for this system. The new model (Figure 2.54) now just contains two reversible steps which are described by the rate constants k_1, k_{-1}, k_2 and k_{-2}.

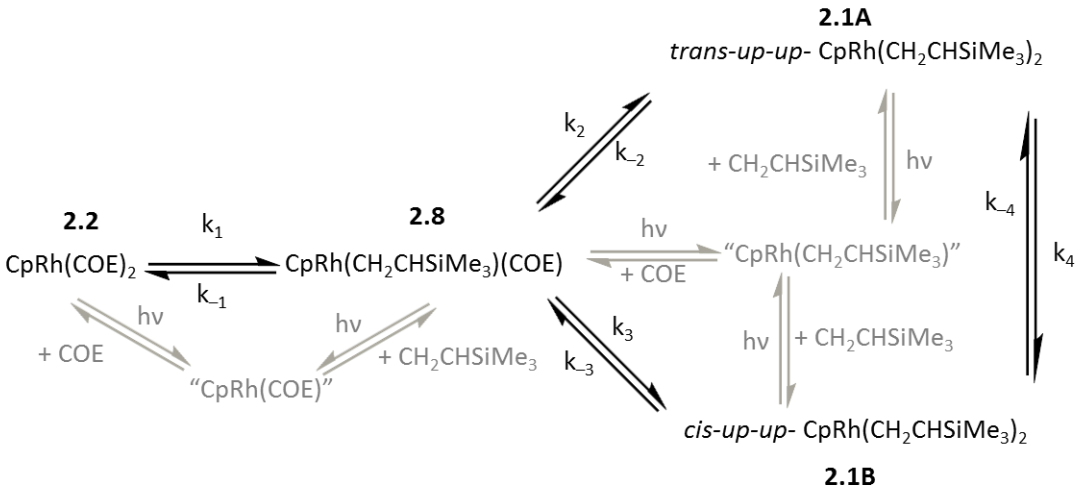

Figure 2.53: Kinetic Model to describe the reaction of **2.2** with trimethylvinylsilane; the observable species are in black and the intermediates through which they are formed are shown in grey

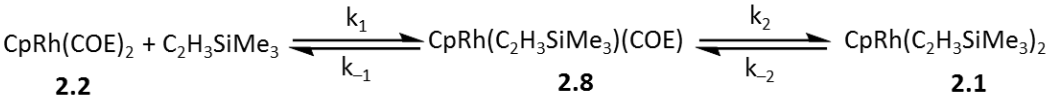

Figure 2.54: Simplified kinetic model to describe the formation of **2.1** from **2.2** via **2.8**

A differential approach was used to model the relaxation kinetics for the simplified kinetic model (Experimental 8.4.3). Values for each of the rate constants were obtained (Table 2.8) and the corresponding equilibrium constants, K_i, were calculated using Equation (2.21).[122] K_1 is approximately 1 showing little difference in the activity of **2.2** and **2.8**, whereas K_2 is 1.56 $\pm$ 0.14, reflecting a difference in activity between **2.1** and **2.8**. If it is assumed that this sample was suitably optically dilute (Appendix), the equilibrium constant can be considered as a combination of the quantum yields and molar absorption coefficients of **2.8** and **2.1** in addition to the energetics associated with ligand coordination. A value of K_{eq} greater than one would indicate that the quantum yield of **2.8** is greater than that of **2.1** and thus **2.8** is more efficient at forming the intermediate. Alternatively it might suggest that there is a preference for the coordination of trimethylvinylsilane to the intermediate, over the coordination of cyclooctene.

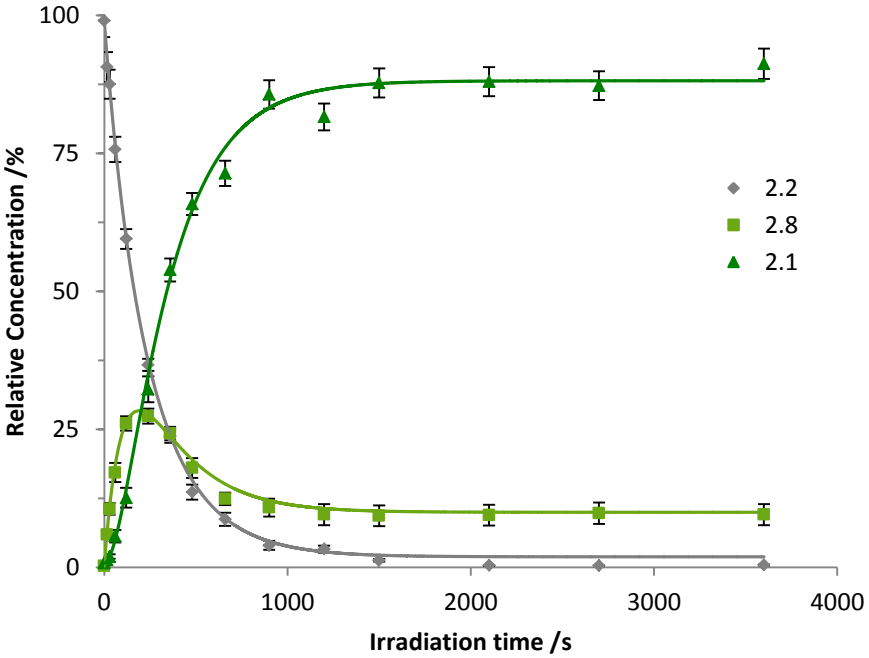

Figure 2.55: Time profile showing the change in concentration **of 2.2, 2.8** and **2.1** as a function of irradiation time. The lines show the results of the fitting in Excel.

Table 2.8: Relaxation constants for each step of the simplified kinetic model for the reaction between 2.2 and trimethylvinylsilane and the calculated equilibrium constant

i	k_i /mol^{-1} dm^3 s^{-1}	k_{-i} /mol^{-1} dm^3 s^{-1}	K_i
1	$(7.70 \pm 0.53)\ x10^{-2}$	$(7.94 \pm 1.37)\ x10^{-2}$	0.98 ± 0.12
2	$(1.21 \pm 0.09)\ x10^{-1}$	$(7.79 \pm 0.80)\ x10^{-2}$	1.56 ± 0.14

$$K_i = \frac{k_i}{k_{-i}} \tag{2.20}$$

$$K_{eq} = \frac{[2.1][\text{Vinylsilane}]}{[2.8][\text{COE}]} = \frac{\varepsilon_{2.8}\Phi_{2.8}k_1}{\varepsilon_{2.1}\Phi_{2.1}k_2} \tag{2.21}$$

2.8.2 $[(\eta^5\text{-}C_5H_5)Rh(\eta^4\text{-}C_8H_{12})]$ **2.3**

A much longer irradiation time was required for **2.3** compared with **2.2** and **2.1** reflecting lower photoactivity of this system. During this time, two products formed, identified as **2.1A** and **2.1B** based on their ^{1}H NMR characteristics (Figure 2.56). However, despite the much

longer irradiation time, the major component was still **2.3** which accounts for 74% of the initial rhodium content.

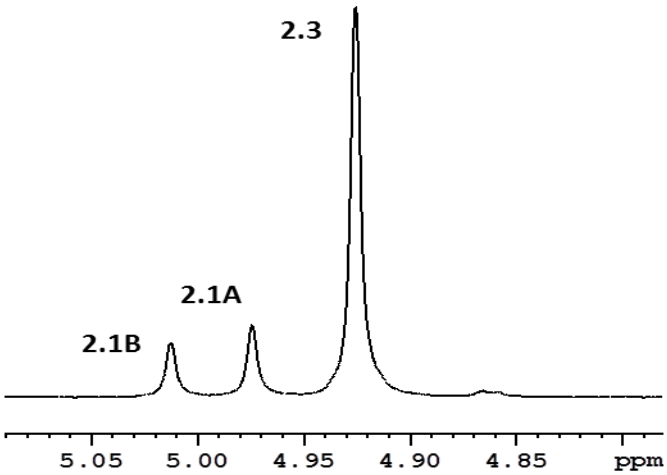

Figure 2.56: Cp Region of proton spectrum following 4.5 hours photolysis, labelled with known complexes

The relative concentrations for each species were calculated and then plotted against irradiation time; showing much slower changes in the speciation than previously seen (Figure 2.57). The final ratio of **2.1B** to **2.1A** was 0.83: 1, which is consistent with the ratio of these two isomers when they were prepared from **2.1** and **2.2** via a photochemical process. The kinetic model for this reaction is depicted in Figure 2.58. Through the loss of the COD ligand **2.1A** or **2.1B** can be formed and these two complexes may interconvert between each other. It is likely that the loss of COD occurs stepwise via the breakage of one of the rhodium-COD alkene bond resulting in a "CpRh(η^2-COD)" species. This may recoordinate the COD's second alkene moiety or trimethylvinylsilane resulting in the intermediate CpRh(η^2-COD)($CH_2CHSiMe_3$). It is likely that this this due to the bidentate nature of the COD ligand which means that the C=C bond remains close to the metal centre following the breaking of the metal-alkene bond. As a consequence of this the recoordination of the second COD alkene is favoured over coordination of a vinylsilane solution. Since the intermediate is not observed, it would suggest that it is only present in solution for short periods of time and in low concentration. This result could also be rationalised by the trimethylvinylsilane ligand being more photolabile than the COD ligand driving the back reaction towards reform the starting material in preference over

the formation of **2.1** based on the assumption of low absorbance as outlined in the Appendix but this is unlikely given the earlier studies

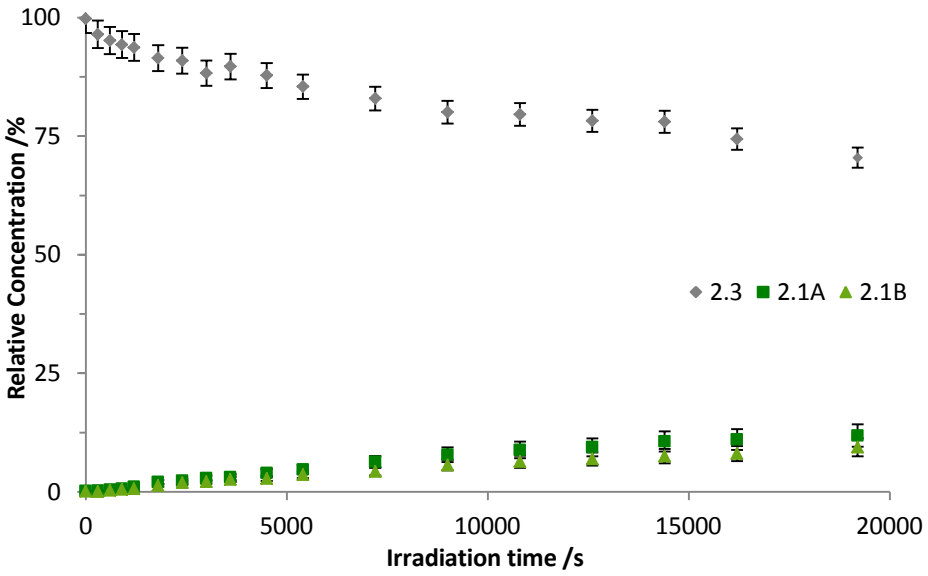

Figure 2.57: Time profile showing the change in concentration **of 2.3, 2.1A** and **2.1B** as a function of irradiation time.

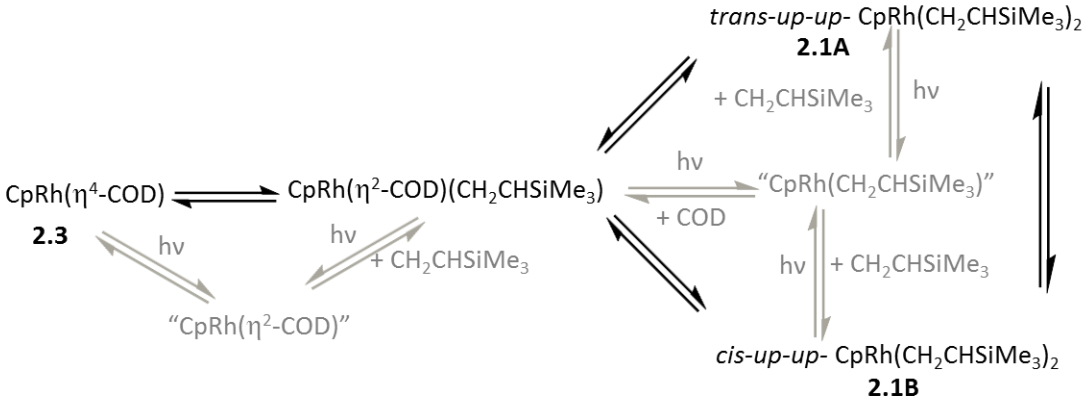

Figure 2.58: Kinetic Model for the reaction of 2.3 with trimethylvinylsilane to 2.1A and 2.1B; the intermediate CpRh(η^2-COD)($CH_2CHSiMe_3$) was not observed. The net process is given in black and the route is shown in grey.

A simplified model was used to fit the relaxation kinetics of this system; this is shown in Figure 2.59. The two isomers of **2.1** are combined, this means that the isomerisation between them does not need to be considered, and the proposed intermediate has not been included in this model. Figure 2.57 shows that the equilibrium position has not been fully reached which means that the concentrations of the species in equilibrium at this equilibrium are not known. The relaxation kinetics were therefore obtained using the differential method described in the

Experimental and the results of this are shown in Table 2.9. The calculated equilibrium constant from this fitting is 0.11 ± 0.02 mol dm^{-3} using Equation (2.22),[122] this shows that at the equilibrium position **2.3** is considerably more favoured than **2.1**. This contrasts with the behaviour seen by in **2.2** and reflects the need for a much longer irradiation time with **2.3** when compared to **2.2**. The equilibrium constant may be considered in terms of the ratio of quantum yields. A value for the equilibrium constant of 0.1 mol dm^{-3} reflects the quantum yield for the **2.3** being smaller than that of **2.1**. It also indicates that there is an energetic preference for COD coordination over trimethylvinylsilane.

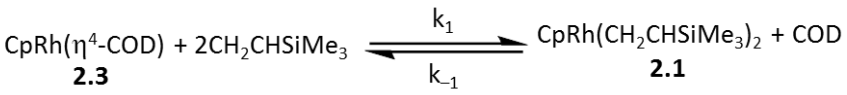

Figure 2.59: Simplified kinetic model of reaction between **2.3** and trimethylvinylsilane.

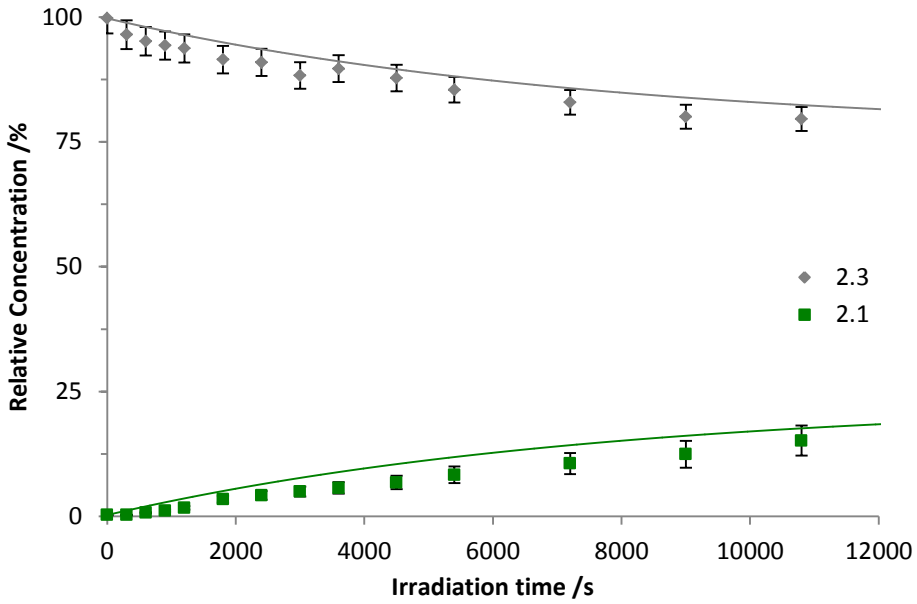

Figure 2.60: Time profile showing the change in concentration **of 2.3** and **2.1** as a function of irradiation time. The lines show the results of the fitting in Excel.

$$K_{eq} = \frac{[2.1]_{eq}[COD]_{eq}}{[2.3]_{eq}[CH_2CHSiMe_3]^2_{eq}} = \frac{k_1}{k_{-1}} \qquad (2.22)$$

Table 2.9: Relaxation constants for the simplified kinetic model and calculated equilibrium constant, K_{eq}

k_1/mol^{-2} dm^6 s^{-1}	k_{-1}/mol^{-1} dm^3 s^{-1}	K_{eq} /mol dm^{-3}.
(3.14 ± 0.14)x10^{-3}	(2.95 ± 0.42)x10^{-2}	0.11 ± 0.02

2.9 Photochemistry of **2.2** and **2.3** with DMSO – to form **2.9**

Having determined that the alkene ligands in **2.2** and **2.3** are photolabile; their reactivity towards DMSO was investigated. Since $CD_3S(O)CD_3$ is readily available, a neat solvent reaction can be undertaken to probe the behaviour of the COD ligand in **2.3**. Additionally the potential to form the bis-DMSO complex $[(\eta^5\text{-}C_5H_5)Rh(DMSO)_2]$, which has not previously been observed, reflects an interesting prospect. To study this process the following samples were prepared in d_8-toluene, unless otherwise stated, and then irradiated for the given amount of time (

Table 2.11). The reactions were monitored by ^{1}H NMR spectroscopy and the observations during this process will now be discussed.

Table 2.10: Sample preparation details

Entry	Complex	Rh /mg	DMSO /µL	Excess	Irradiation time
1	**2.2**	0.5	5	59	15m
2	**2.2**	1.6	1.4	4.7	30m
3	**2.3**	0.3	3.5	42	3.5h
4	**2.3***	0.4	7	70	5h
5	**2.3**	1.4	5	14	42h
6	**2.3**†	~0.5	500		42h

*3 bar H_2 added; † in d_6-DMSO

2.9.1 $[(\eta^5\text{-}C_5H_5)Rh(\eta^2\text{-}C_8H_{14})_2]$ **2.2**

The proton NMR spectra showed the growth of peaks indicative of free cyclooctene and a rhodium containing photoproduct **2.9**. This product yields a new cyclopentadienyl peak at δ 4.84. There is also a singlet at δ 2.49, which integrates to six protons if the cyclopentadienyl peak is five suggesting that this belongs to the bound DMSO peak. The two methyls group are equivalent in this product due to the symmetrical alkene, in contrast to the observations in **2.4**. This resonance correlates to a carbon signal at δ 55.8 suggesting that the DMSO is coordinated through the sulfur in the same way as in complex **2.4**.[57, 132] A doublet at δ 3.00 correlates to a carbon resonance at δ 59.5 which indicates that this resonance corresponds to a coordinated alkene, confirmed through the detection of a 16 Hz rhodium-carbon coupling in the $^{13}C\{^{1}H\}$ NMR spectrum. The ^{1}H-^{1}H COSY NMR spectrum correlated this resonance to its adjacent methylene group at δ 2.46 and 1.65 (δ_C 33.2). The resonance at δ 2.46 is a doublet of quartets with just one large coupling (J_{HH} 13.5 Hz) corresponding to the geminal coupling to its partner at δ 1.65, therefore it must be *trans* relative to the alkene proton at δ 3.00 as this arrangement is more in keeping with the 3.5 Hz coupling of the quartet, this is quartet owing coupling to H_3 and $H_{3'}$ also with ~3.5 Hz coupling constants. The proton at δ 3.00 is a pseudo doublet with a large coupling of J_{HH} 9.5 Hz between H_1 and H_2 in a *cis* arrangement, its smaller

coupling to $H_{2'}$ is hidden in the broadness of the resonance. The remaining positions on the cyclooctene ring overlap with one another and free COE at between δ 1.50 and 1.65.

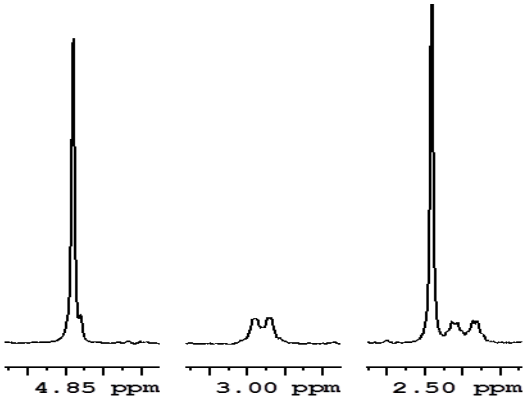

Figure 2.61: ^{1}H NMR Spectrum of **2.2** with DMSO in d_8-toluene at 298 K after 15 minutes irradiation

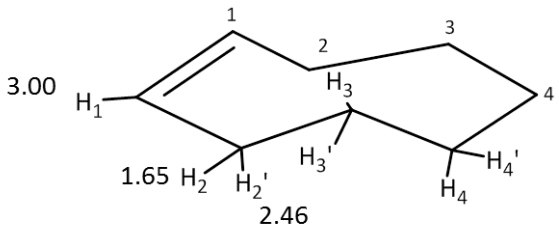

Figure 2.62: Summary of the ^{1}H assignments of the coordinated cyclooctene ligand.

Using the signal at δ 2.98, proton 2' in **2.2**, and the singlet at δ 2.49, for the bound DMSO in **2.9,** the change in concentrations of **2.2** and **2.9** during the irradiation period and these were plotted against the irradiation time (Figure 2.63). Revealing that the formation of a photostationary state after an initial growth period. This equilibrium comprised of 90% of **2.9** and 4% of **2.2**, decomposition amounting to 6% was also observed. There was no evidence of the bis-DMSO product, $CpRh(DMSO)_2$. The identity of the decomposition was not identified and no precipitate was observed in solution, the total integral for the Cp region of the NMR spectrum before and after irradiation was consistent with this observation and therefore the loss of the Cp ligand could be responsible for the decomposition. If $CpRh(DMSO)_2$ does not form due to the instability of the CpRh(DMSO) fragment this could provide a route for decomposition.

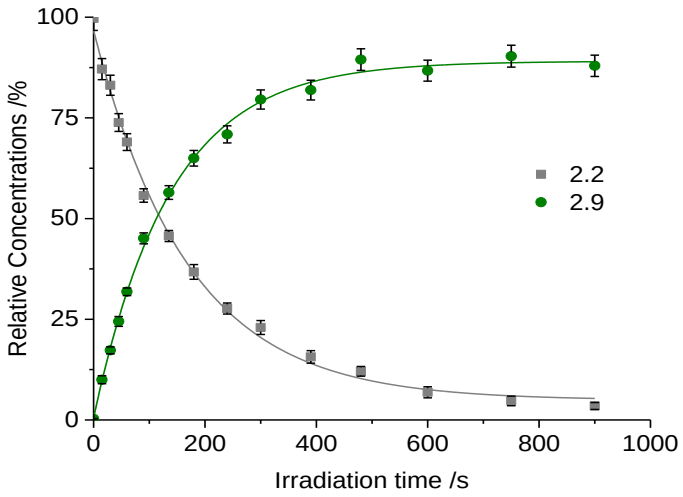

Figure 2.63: Time profile; showing growth of **2.9** and decay of **2.2** using the sample from entry 1 in Table 2.10. The lines reflect the fitting described in

Table 2.11 (entry 1)

One kinetic model which can be used to describe this system is a simple one step, bimolecular equilibrium (Figure 2.64) whose kinetics obey the principles outlined in the Appendix. In this model **2.2** and **2.9** undergo photochemical ligand loss to give a common intermediate "CpRh(COE)". The absence of the bis-DMSO complex suggests that the loss of COE from **2.9** to give "CpRh(DMSO)" does not significantly impact on the reactivity of **2.9**. The equilibrium constant, K_{eq}, for this reaction is given by Equation (2.23)[122] which gives a K_{eq} value for this sample as 0.25 ± 0.06.

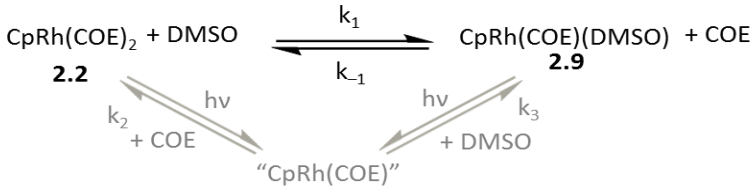

Figure 2.64: Kinetic Model for the transformation of **2.2** into **2.9**

$$K_{eq} = \frac{k_1}{k_{-1}} = \frac{[2.9]_{eq}\,[COE]}{[2.2]_{eq}[DMSO]} \qquad (2.23)$$

In Section 2.5, it was observed that the reaction between **2.1** and DMSO was independent of DMSO concentration. To investigate whether this was the case with **2.2** also, a second sample was prepared (entry 2, Table 2.10) containing a smaller excess of DMSO. This sample was prepared in same manner as the first. The change in concentration of the two rhodium species as a function of irradiation time is depicted in Figure 2.65. In this sample at the equilibrium position there is now 25% of the starting complex, compared with 4% in the first sample. The equilibrium constant was calculated to be 0.19 ± 0.01. This would suggest that in this reaction the concentration of DMSO does influence the reaction rate, however, this needs to be treated with caution considering the two samples were prepared separately and with different concentrations of **2.2**.

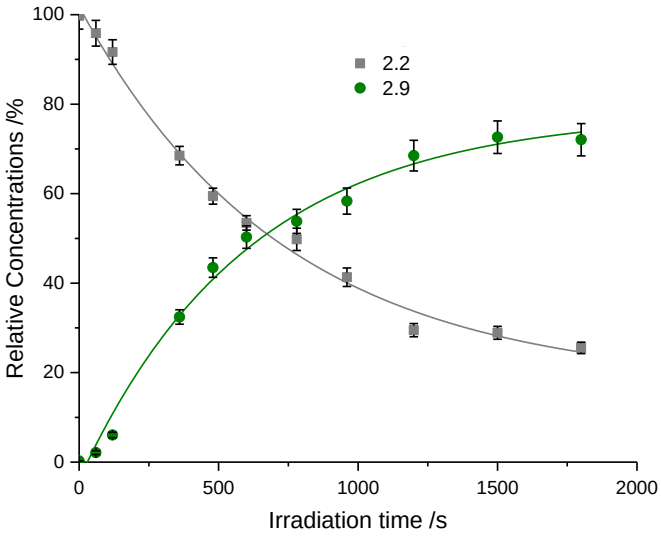

Figure 2.65: Time profile; showing growth of complex **2.9** and decay of complex **2.2** using the sample from entry 2 in Table 2.10. The lines reflect the fitting described in

Table 2.11 (entry 2)

The change in the concentrations of the rhodium complexes during the irradiation were fitted to exponential curves according to Equation (2.24)[121, 123], where a is the equilibrium concentration, b is the change in concentration and k_{obs} is the time for the equilibrium to be reached. This equation was derived using relaxation kinetics for the model described in Figure 2.64. The result of this fitting, for both samples, is given in

Table 2.11. Since the observed rate constant, k_{obs}, and the equilibrium constant, K_{eq} relates to the rates of the two steps in this process the values of k_1 and k_{-1} can be calculated (

Table 2.12) [124] Assuming the sample is optically dilute and has low absorbance, the equilibrium constant relates to the ratio of the quantum yields, and molar absorption coefficient, as well as the energetics associated with coordination of the ligands to the intermediate (Equation (2.25)).[122, 125] The values of k_1 and k_{-1} can also be expressed in terms of the photochemical properties (Equation (8.1) and (8.2)) showing that k_1 relates to the quantum yield of **2.1** and the rate of DMSO addition to the intermediate and k_{-1} the quantum yield and addition of COE to the intermediate. The values of k_1, k_{-1} and K_{eq} suggest that either the quantum yield of **2.2** is notably smaller than that of **2.9** or cyclooctene preferentially coordinates to the intermediate or a combination of the two effects.

$$y = a + be^{-k_{obs}t} \tag{2.24}$$

where

a= $[A]_{eq}$

b= $[A]_0 - [A]_{eq}$

k_{obs}= $k_1([DMSO]_{eq}+[2.2]_{eq}) + k_2([COE]_{eq}+[2.9]_{eq})$

$$K_{eq} = \frac{[2.9][COE]}{[2.2][DMSO]} = \frac{\varepsilon_{2.2}\Phi_{2.2}k_3}{\varepsilon_{2.9}\Phi_{2.9}k_2} \tag{2.25}$$

$$k_1 = \frac{\Phi_{2.2}I_0 l\varepsilon_{2.2}k_3}{k_2[COE] + k_3[DMSO]} \tag{2.26}$$

$$k_2 = \frac{\Phi_{2.9}I_0 l\varepsilon_{2.9}k_3}{k_2[COE] + k_3[DMSO]} \tag{2.27}$$

Table 2.11 Fitting results for the changes of **2.2** and **2.9** as a function of irradiation using Equation (2.24) for each of the samples.

Entry	Molar excess DMSO		a /%	b /%	k_{obs} /mol^{-1} dm^3 s^{-1}
1	60	[**2.2**]	4.9 ± 1.1	91.8 ± 1.4	(5.91 ± 0.44) x10^{-3}
		[**2.9**]	89.1 ± 0.9	−88.5 ± 1.2	(7.25 ± 0.49) x10^{-3}
2	5	[**2.2**]	17.3 ± 3.6	84.5 ± 3.4	(1.37 ± 0.18) x10^{-3}
		[**2.9**]	77.9 ± 3.5	−81.8 ± 3.5	(1.65 ± 0.24) x10^{-3}

Table 2.12: Rate constants and calculated equilibrium constant, K_{eq}

Entry	Molar excess DMSO	k_1/mol^{-1} dm^3 s^{-1}	k_{-1} /mol^{-1} dm^3 s^{-1}	K_{eq}
1	60	(4.48 ± 0.76) x10^{-2}	0.189 ± 0.068	0.25 ± 0.06
2	5	(1.87 ± 0.43) x10^{-2}	0.101 ± 0.024	0.19 ± 0.01

2.9.2 $[(\eta^5\text{-}C_5H_5)Rh(\eta^4\text{-}C_8H_{12})]$ **2.3**

An NMR sample was prepared and irradiated according to Entry 3 in Table 2.10. After 3.5 hours irradiation there were very few changes to the proton spectrum; two very small signals at δ 4.80 and δ 2.45 were observed. These are in the right parts of the spectrum for coordinated Cp and DMSO ligands in these types of complexes (Figure 2.66), however due to their weak intensity it is difficult to assign these peaks with any confidence. The other change to the proton spectrum is seen in the δ 5.5 to 6.5 region where uncoordinated alkene resonances are typically seen. In the spectra following the photolysis two peaks were present in this area; a doublet at δ 5.81 (J_{HH} 9 Hz) and a broad resonance at δ 5.54 (Figure 2.66). These were also seen following the photolysis of this complex with trimethylvinylsilane which would be consistent with them being due to the free COD in solution but only one peak in this region would be expected owing to the symmetry of COD. The second resonance could be an uncoordinated alkene resonance of a CpRh(η^2-COD) type species.

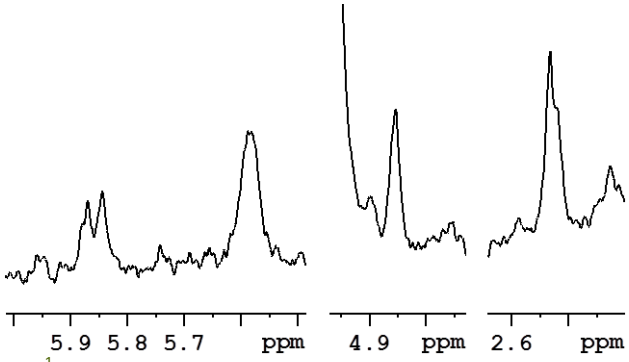

Figure 2.66: ^{1}H NMR spectrum of **2.3** in d_8-toluene at 298 K, following irradiation

To investigate this reaction further, a sample was prepared and 3 bar H_2 was added (Entry 4 Table 2.10) on the basis that this could hydrogenate the COD ligand to COE, allowing it to coordinate in an η^2 fashion leaving a vacant site for DMSO to bind, and/or hydrogenate the COD ligand to cyclooctane which could potentially provide a route to the formation of [(η^5-C_5H_5)Rh(DMSO)$_2$]. Despite 5 hours of irradiation, there was only minimal conversion to the new species seen with the first sample. There was also only the two previously observed resonances in the alkene region of the spectrum suggesting that COE did not form, however there was a singlet at δ 1.44 in keeping with a cycloalkane such as cyclooctane suggesting some COD was hydrogenated.[135]

The study of **2.3** with trimethylvinylsilane occurred at a slower pace than with **2.2**, taking this into account this reaction was then studied over a longer timescale (42 hours). Two samples were prepared, one of which was prepared in neat d_6-DMSO and the other in d_8-toluene with a 14 fold excess of DMSO (Entries 5 and 6 Table 2.10). During the irradiation time, degradation of the starting material was observed, as was free cyclooctadiene, however, no clear product formed in either sample. This suggests that the complex is photoactive but any products which might have formed are not stable. The degradation product(s) were not identified, some brown precipitate was observed in the NMR tube and a notable drop in the intensity of the Cp containing species seen. This would indicate the degradation resulted from the loss of the Cp ligand.

2.10 Photochemistry of **2.2** and **2.3** with Et_3SiH – to form **2.10**, and **2.6**

Many important reactions involving organometallic complexes with small organic compounds relates to their ability to activate seemingly inert bonds such as C–H,[49] B–H[51] or Si–H.[50] Triethylsilane was chosen as a test substrate to determine whether these complexes can activate such bonds. To investigate this process, NMR samples of **2.2** and **2.3** were prepared in d_8-toluene according to Table 2.13.

Table 2.13: Sample preparation details

Entry	Complex	Rh /mg	Silane /µL	Excess	Irradiation time
1	**2.2**	0.6	5	19	20m
2	**2.3**	0.75	10	23	2h

2.10.1 $[(\eta^5\text{-}C_5H_5)Rh(\eta^2\text{-}C_8H_{14})_2]$ **2.2**

^{1}H NMR spectra recorded during irradiation of **2.2** with Et_3SiH showed the growth of two Rh–H species (Figure 2.67). The first species to form corresponded to a hydride at δ –15.02 (J_{HRh} 33 Hz) this is consistent with a Rh^{III} species, **2.10**. The second species which forms and is consistent with the known $[(\eta^5\text{-}C_5H_5)Rh(H)_2(Si(CH_2CH_3)_3)_2]$ **2.6**.

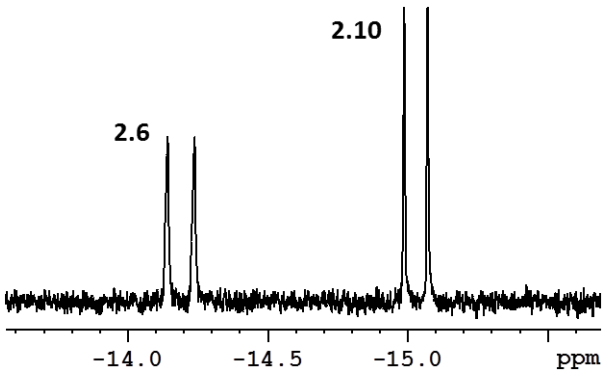

Figure 2.67: Hydride Region of the ^{1}H Spectrum at 298 K after 32.5 minute irradiation of **2.3** in the presence of triethylsilane in d_8-toluene.

Like **2.5**, many resonances associated with **2.10** are broad (Figure 2.68). Cooling the sample to 270 K allowed the multiplicities of these resonances to be resolved and 2D NMR experiments were acquired to allow for **2.10** to be characterised. The key features of this characterisation

are two resonances at δ 2.91 and 2.44. At room temperature these peaks are broad with no distinguishing features, cooling resolves both of these peaks as triplets with 9 Hz couplings. In a 2D ^{1}H-^{1}H NOESY spectrum these two resonances exhibit exchange cross peaks between one another in addition to nOe connections to the rhodium hydride and the triethylsilane ligand. The source of the fluxionality is due to the chemical exchange, this could be through the same mechanism as was seen in **2.5** (Figure 2.69). Unlike **2.5**, in **2.10** this exchange would not give rise to different isomers due to the symmetry of the alkene. The two extremes are chemically the same but the two halves of the COE ligand are magnetically inequivalent and therefore the CH labelled * is different to the CH labelled ‡ and the rotation of the Si–H bond results in these two position being different in the two extremes and gives rise to the fluxionality in **2.10**. In **2.10**, rotation of the COE ligand would also give the same exchange. The proposed structure and the associated NMR characterisation data are found in Figure 2.87 and Table 2.24.

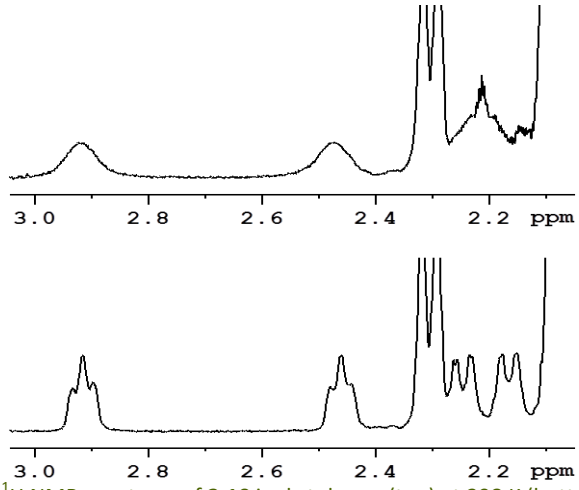

Figure 2.68: ^{1}H NMR spectrum of **2.10** in d_8-toluene (top) at 298 K (bottom) at 270 K.

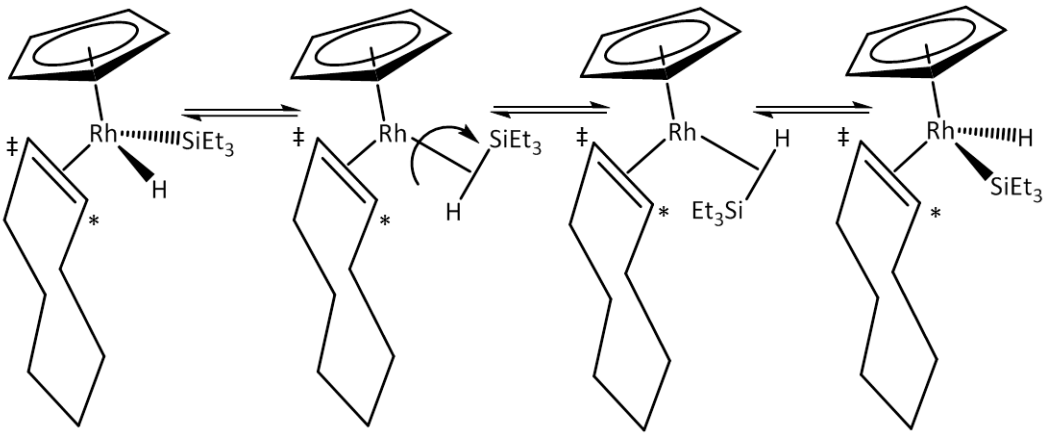

Figure 2.69: Proposed route to chemical exchange in the COE protons in the product **2.10**

The series of proton spectra acquired during the photolysis were analysed and used to measure the conversion of the **2.2** into the two products, these were then plotted against the photolysis time (Figure 2.70). This plot shows that the first product forms quickly during the initial 10 minutes of irradiation reaching a maximum concentration of 84% of the initial rhodium content after 11 minutes photolysis. After this time its concentration starts to fall as the second product begins to form. This second product appears to form on a slower timescale than the first.

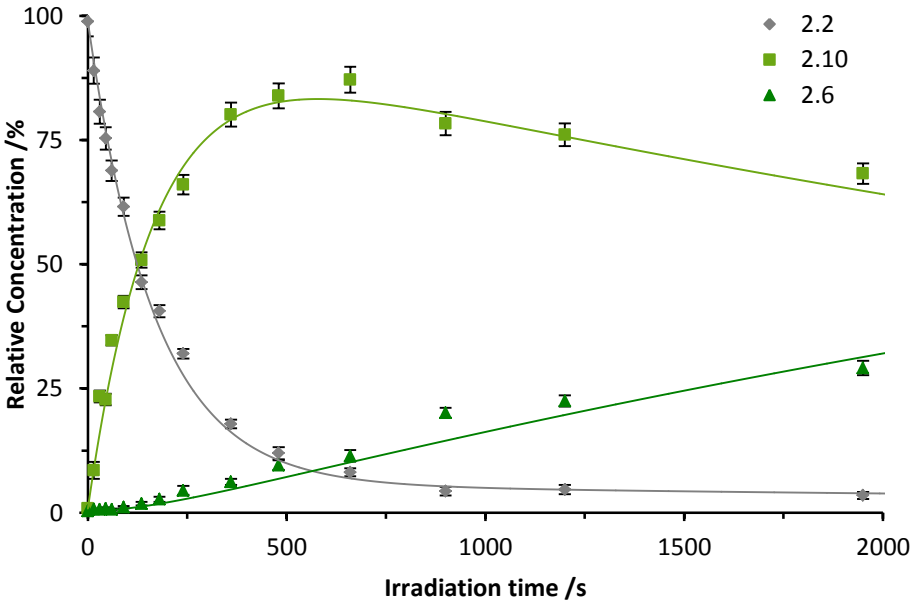

Figure 2.70: Time profile following the reaction of **2.2** with triethylsilane

The kinetic model which describes this reaction is given in Figure 2.71, starting with the reversible formation of **2.10** from **2.2**, where the formation of **2.6** from **2.10** indicates that this product is photoactive. The third step involves the reaction of **2.10** with a second triethylsilane to form **2.6** which has been demonstrated not to be photoactive and thus forms irreversibly. Using a relaxation kinetics approach the kinetics of this reaction can be evaluated. To calculate the equilibrium constant for this step the relative relaxation constants for each of the steps in the kinetic model with fitted using the process described in the Experimental. Once the concentrations of the ligands were taken into account, this resulted in values of k_1 and k_{-1} of $(9.63 \pm 0.42)\ x10^{-2}$ and $(8.31 \pm 0.72)\ x10^{-2}\ mol^{-1}\ dm^3\ s^{-1}$which gives an equilibrium constant of 1.17 ± 0.15 using Equation (2.18).[122] The value of k_2 calculated was $(3.78 \pm 0.22)\ x10^{-3}\ mol^{-1}\ dm^3\ s^{-1}$.

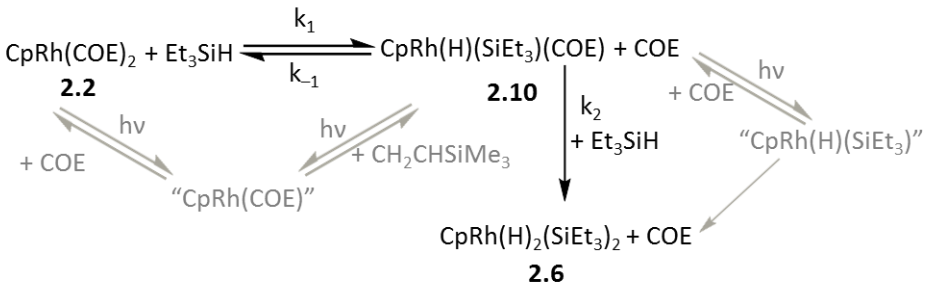

Figure 2.71: Kinetic Model for the reaction between **2.2** and triethylsilane

In this kinetic model **2.10** and **2.2** share a common reactive fragment, "CpRh(COE)" which is formed by the photochemical loss of COE from **2.2** and the reductive elimination of triethylsilane from **2.10**. An equilibrium constant of 1 would suggest that there is an equal preference for this fragment to coordinate COE or oxidatively add the silane and/or the fragment is formed at comparable rate from either **2.2** or **2.10**. As predicted the value of k_2 is smaller than that of k_1 and k_{-1}, in fact it more than 20 times smaller than them. The reactive fragment that is formed in order to generate **2.6** is "CpRh(H)($SiEt_3$)" which is formed by the loss of COE from **2.10**. Since k_2 is much smaller than k_{-1} it would suggest that the COE is less photolabile from **2.10** than silane is.

2.10.2 $[(\eta^5\text{-}C_5H_5)Rh(\eta^4\text{-}C_8H_{12})]$ **2.3**

The photolysis of **2.3** with Et_3SiH resulted in two hydride resonances in the ^1H NMR spectra at δ –14.19 and –15.06 (Figure 2.72), both of these resonances display coupling to one rhodium centre. The coupling seen in the δ –14.19 peak was 38 Hz; this is consistent with the Rh^V species **2.6**. Whereas the other hydride, at δ –15.06 has a 33 Hz which is more consistent with a Rh^{III} species, such as $[(\eta^5\text{-}C_5H_5)Rh(H)(Si(CH_2CH_3)(\eta^2\text{-}C_8H_{12})]$. This would be the first time in this research that a stable product which has the COD ligand coordinated in an η^2 fashion has been detected, however, this can only be postulated since this species is only ever present in very low concentrations, limiting its characterisation.

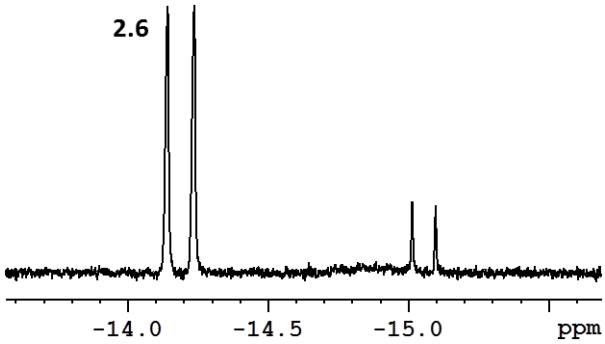

Figure 2.72: Hydride region at 298 K following the reaction of **2.3** with triethylsilane in d_8-toluene.

The proton spectra were analysed and the results of this are shown in Figure 2.73. This shows a slow growth of the double oxidation product and a steady very low level (1-2% only) of the other product. After 2 hours irradiation there was 17.3% of **2.6** and 1.3% of **2.11** in addition to 81.4% starting material. This reaction was modelled using a chemical exchange mechanism based on the kinetic model in Figure 2.74 this gave values of k_1, k_{-1} and k_2 of (5.61 $\pm$ 0.56) $x10^{-4}$, (1.43 $\pm$ 0.21) $x10^{-3}$ and (7.19 $\pm$ 0.45) $x10^{-3}$ respectively. Unlike **2.1** and **2.2**, the rate of the first oxidative addition is comparable to that of the second, to give **2.6**. The overall activity is notably reduced when compared to **2.1** and **2.2**, since the starting material is the major species after 2 hours irradiation.

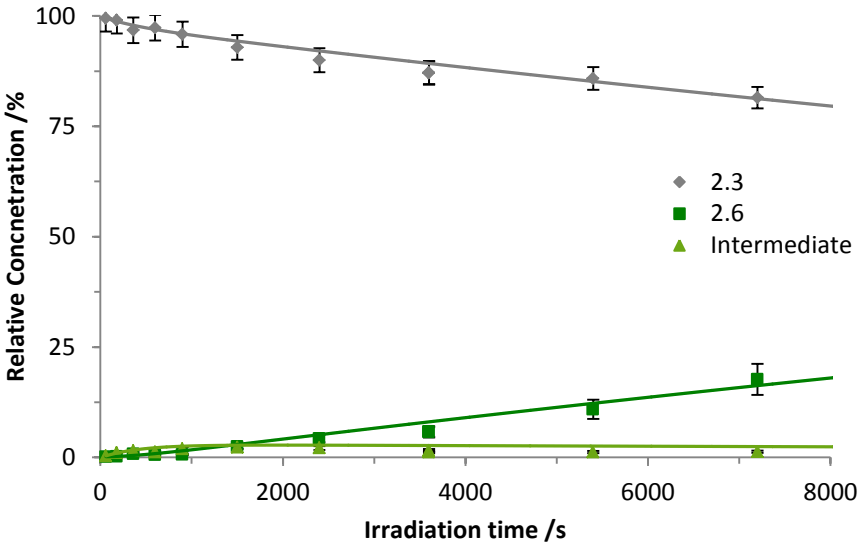

Figure 2.73: Time profile following the reaction of **2.3** with triethylsilane.

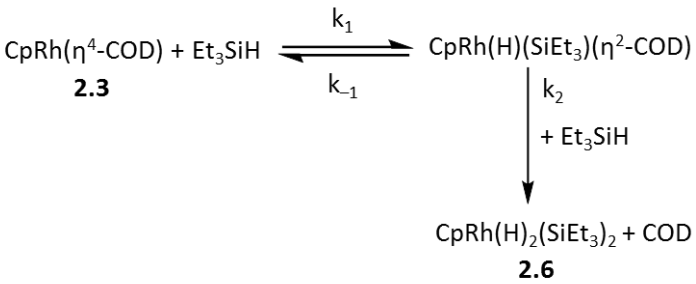

Figure 2.74: Kinetic Model for the reaction of CpRh(COD) with triethylsilane.

2.11 Conclusions

$CpRh(CH_2CHSiMe_3)_2$ **2.1**, $CpRh(COE)_2$ **2.2** and CpRh(COD) **2.3** have been synthesised via the reaction of the analogous rhodium chloride dimers with cyclopentadienyl lithium. Complex **2.1** was synthesised as two isomers; *trans-up-up* (**2.1A**) and *cis-up-up* (**2.1B**) which differ in the relative orientation of the trimethylvinylsilane. All four complexes were characterised by NMR spectroscopy before their reactions with the substrates; trimethylvinylsilane, DMSO and triethylsilane were studied.

Irradiation of **2.1** in the presence of trimethylvinylsilane revealed that isomerisation between **2.1A** and **2.1B** could be achieved photochemically. Irradiation resulted in the formation of a photostationary state which was analysed by relaxation kinetics and associated with a K_{eq} value of 0.74 ± 0.02 indicating that there is a preference for the *trans-up-up* isomer, **2.1A** over

CL

the *cis-up-up* isomer **2.1B**. This was rationalised to reflect the difference in the quantum yields of the two isomers. From this study it could be concluded that, under these reaction conditions, a trimethylvinylsilane ligand could be lost photochemically. This spurred further studies with DMSO and triethylsilane.

The reaction between **2.1** and DMSO gave rise to a single product identified as being $CpRh(CH_2CHSiMe_3)(DMSO)$ **2.4** where the DMSO ligand coordinates via its sulfur atom. This reaction also formed a photostationary state. The initial sample contained 94% **2.4** and 4% **2.1**, to investigate the whether changing the concentration of DMSO would influence the distribution of products a three samples were prepared from a stock solution and different amounts of DMSO were added. Analysis of these samples revealed that the reaction is independent of DMSO concentration and a K_{eq} value of ~0.1 were measured. An excess of trimethylvinylsilane was added to a sample of **2.4** and DMSO and following irradiation there was a growth in signal associated with **2.1**. At the end of the irradiation period **2.4** was still the dominant species indicating that it is favoured in the equilibrium and can be rationalised as a combination of the photochemical and thermodynamic properties of **2.1** and **2.4**.

The photoreactivity of **2.1** and **2.4** towards triethylsilane was then investigated, resulting in the formation of $CpRh(H)(SiEt_3)(CH_2CHSiMe_3)$ **2.5**, $CpRh(H)_2(SiEt_3)_2$ **2.6** and $CpRh(H)(SiEt_3)(DMSO)$ **2.7**. From the reaction between **2.1** and Et_3SiH it was determined that **2.5** forms on route to the formation of **2.6** and that the formation of **2.6** occurs on a slower time scale. Its formation was associated with a rate constant that was a factor of 10 slower than the corresponding value for the formation of **2.5**. To investigate the formation of **2.5**, **2.6** and **2.7** from **2.4** two samples were prepared with different excesses of DMSO. These studies revealed that **2.7** forms slower than **2.5** and on a similar timescale to the formation of **2.6** when an excess of DMSO was used and slower still without an excess of the ligand. From this it was concluded

that **2.7** formed through the loss of trimethylvinylsilane from **2.5** and subsequent coordination of DMSO rather than from **2.4** directly.

The reactivity of **2.2** and **2.3** towards trimethylvinylsilane was also studied to determine whether the COE or COD ligands are photochemically labile. With **2.2**, three products were observed, **2.1A**, **2.1B** and **2.8**, which was identified as CpRh(COE)($CH_2CHSiMe_3$). This process was analysed using relaxation kinetics which determined the equilibrium constant for the first equilibrium to be 0.98 ± 0.12 and the second equilibrium 1.56 ± 0.14 which demonstrates that either the intermediate "CpRh(COE)" has no preference for COE or trimethylvinylsilane coordination or that the quantum yields of **2.2** and **2.8** are similar. In contrast, "CpRh($CH_2CHSiMe_3$)" does have a preference for the vinylsilane over COE or the quantum yield for **2.8** is greater than that of **2.1**. The reaction between **2.3** and trimethylvinylsilane, however, only resulted in the formation of **2.1A** and **2.1B** and these formed on a much slower timescale. This was rationalised as being a consequence of the bichelating ligand keeping the liberated alkene ligand close to the metal centre making its recoordination favoured over the coordination of different ligand.

Having demonstrated photoactivity of **2.2** and **2.3**, they were next studied with DMSO and triethylsilane. The reaction between **2.2** and DMSO resulted in the product CpRh(COE)(DMSO) **2.9**. Its formation was studied using relaxation kinetics giving an equilibrium constant of 0.25 ± 0.06 and 0.19 ± 0.01 for samples containing 60 and 5 fold excesses of DMSO respectively. This would suggest that either the quantum yield of **2.9** is greater than that of **2.2** or that there is an energetic preference for COE coordination. The reaction between **2.2** and Et_3SiH resulted in the stepwise substitution of the COE ligands with silyl hydride ligands to give CpRhH($SiEt_3$)(COE) **2.10** and **2.6**, with the second step occurring on a slower timescale than the first. No reaction between **2.3** and DMSO was observed, even with long irradiation times and using neat d_6-DMSO, and only limited activity towards Et_3SiH was observed. The major species

after two hours irradiation was **2.3** and approximately 17% of **2.6** and trace amounts (<2%) of a Rh^{III} species were detected hypothesised as being $CpRhH(SiEt_3)(\eta^2\text{-COD})$.

It can therefore be concluded that the presence of a bidentate alkene in **2.3** heavily influences its activity. This is thought to be due to the close proximity of the liberated alkene to the metal centre following its loss from **2.3**, making its recoordination favoured over substitution with another ligand. Only products which corresponded to the loss of the COD ligand formed in any appreciable concentration. The reactivity of **2.1** and **2.2** is similar; both may lose their alkene ligands in a stepwise manner to give mono- and bis- substitution products. Their reactions with DMSO revealed some differences in their activity, however, with **2.1** exhibit a concentration dependence in its K_{eq} which was not seen in **2.2.** The reactivity of these starting complexes are summarised in Figure 2.75-Figure 2.77.

In conclusion, this work has extended the previous studies to complexes containing trimethylvinylsilane, cyclooctene and cyclooctadiene ligands. The observations were broadly consistent with the literature with a mix of mono- and bis-substitution of the alkenes observed depending on the substrate. The cyclooctene and cyclooctadiene dimers were both synthesised using a microwave preparation allowing reduced reaction times and lower volumes of solvent. This preparation is notable simpler than the corresponding method used to synthesis Cramer's complex $[Rh(C_2H_4)_2(\mu\text{-Cl})]_2$. **2.2** has been shown to react in a similar way to $CpRh(C_2H_4)_2$, COE could therefore be a viable alternative to ethylene in other complexes also. This research has also demonstrated that DMSO is a photolabilie ligand, further investigations into this as a photolabile ligand would be of interest.

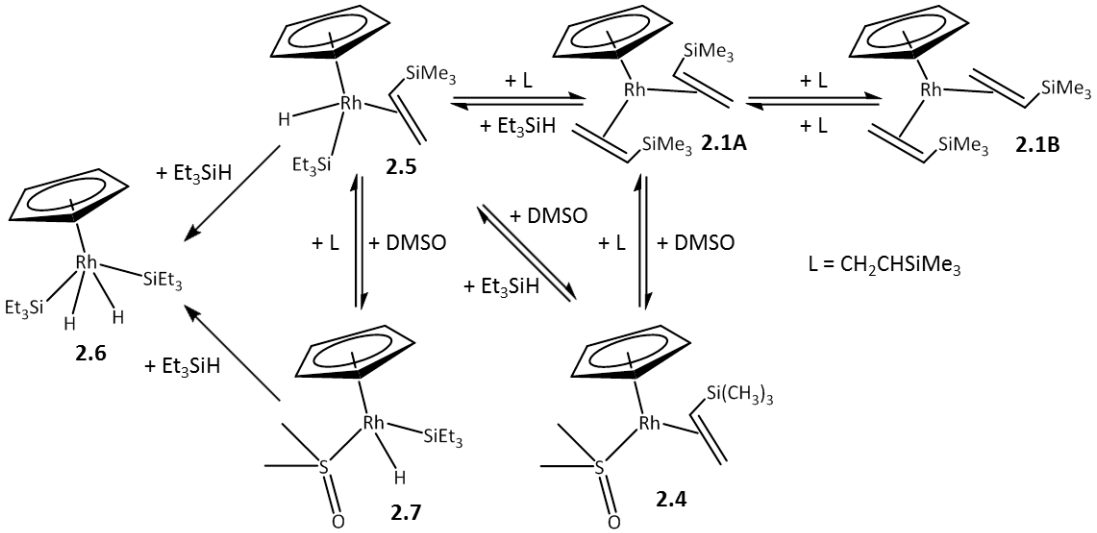

Figure 2.75: Summary of the observed reactivity of **2.1** and its photoproducts.

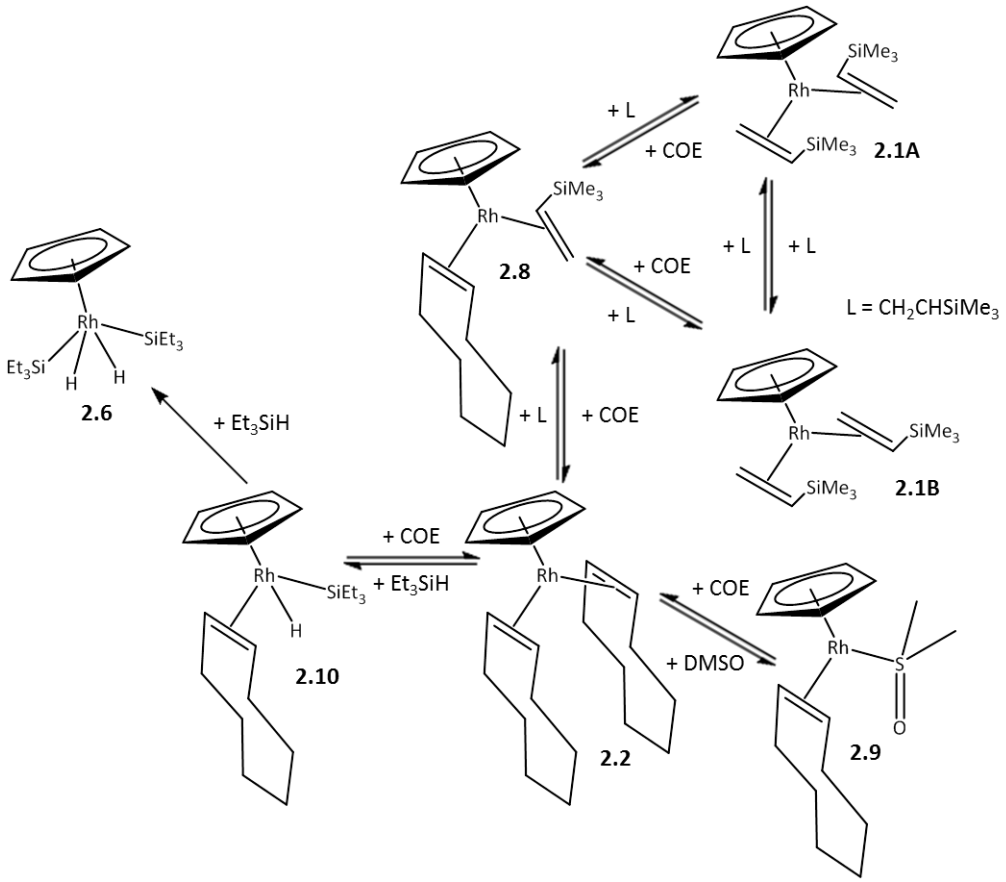

Figure 2.76: Summary of the reactivity of **2.2** with DMSO, vinylsilane and Et_3SiH.

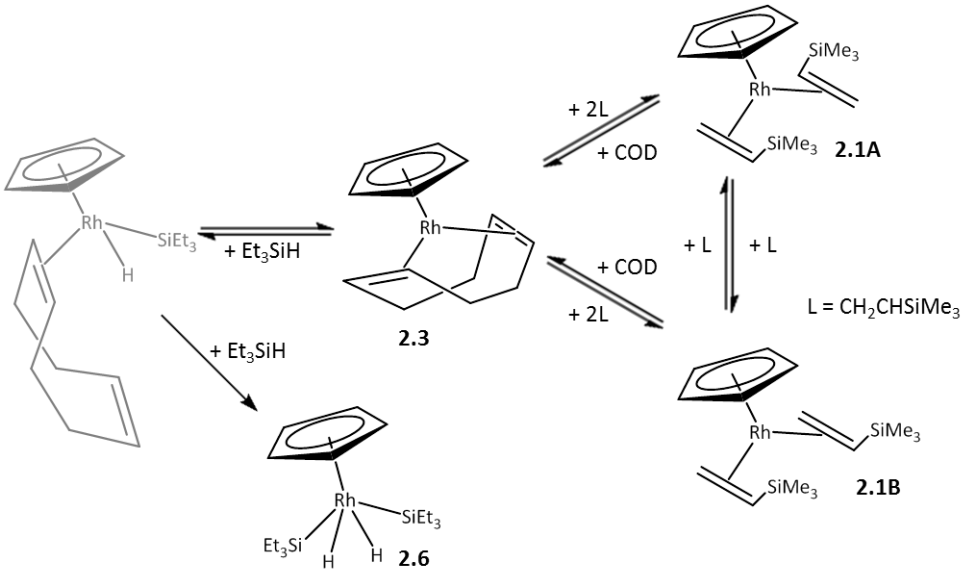

Figure 2.77: Summary of the observed reactivity of **2.3** with Et_3SiH and vinylsilane, it was not possible to characterise the grey structure.

2.12 Structures and NMR data

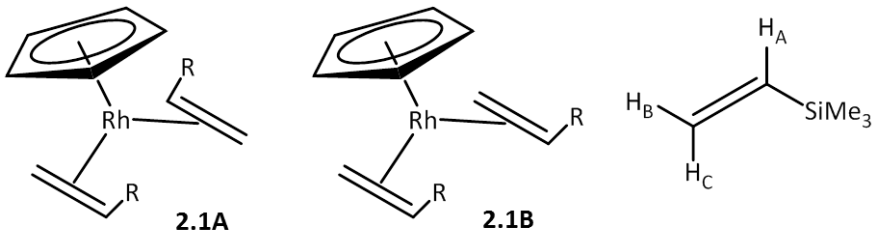

Figure 2.78: Structure of *trans-up-up*-[(η^5-C_5H_5)Rh(η^2-$CH_2CHSi(CH_3)_3)_2$] **2.1A** (left) and *cis-up-up*-[(η^5-C_5H_5)Rh(η^2-$CH_2CHSi(CH_3)_3)_2$] **2.1B** (middle), labelled positions on vinylsilane ligand (right).

Table 2.14: NMR Characterisation for the major isomer *trans-up-up*-[(η^5-C_5H_5)Rh(η^2-$CH_2CHSi(CH_3)_3)_2$] **2.1A**

	δ/ppm (multiplicity, integration)	Coupling constant/Hz	Assignment	Group
^{1}**H**	5.00 (d, 5H)	J_{HRh} 0.6	$C_5\underline{H}_5$	C_5H_5
	2.84 (br.d, 2H)	J_{HH} 13.5	$\underline{H}_C$	CH_2=$CHSi(CH_3)_3$
	2.26 (dd, 2H)	J_{HH} 11.0, 1.5	$\underline{H}_B$	CH_2=$CHSi(CH_3)_3$
	– 0.34 (dd 2H)	J_{HH} 13., 11.0	$\underline{H}_A$	CH_2=$CHSi(CH_3)_3$
	0.07 (s, 18H)		$(C\underline{H}_3)_3$	CH_2=$CHSi(CH_3)_3$
^{13}**C**	87.3 (d)	J_{CRh} 4.0	$\underline{C}_5H_5$	C_5H_5
	39.0 (d)	J_{CRh} 13.0	$\underline{C}H_2$	CH_2=$CHSi(CH_3)_3$
	52.8 (d)	J_{CRh} 14.1	$\underline{C}H$	CH_2=$CHSi(CH_3)_3$
	0.41 (s)		$(\underline{C}H_3)_3$	CH_2=$CHSi(CH_3)_3$

Table 2.15: NMR Characterisation for the minor isomer *cis-up-up*-[(η^5-C_5H_5)Rh(η^2-$CH_2CHSi(CH_3)_3)_2$] **2.1B**

	δ/ppm (multiplicity, integration)	Coupling constant/Hz	Assignment	Group
^{1}**H**	5.04 (d, 5H)	J_{HRh} 0.6	$C_5\underline{H}_5$	C_5H_5
	2.93 (dd, 2H)	J_{HH} 14.0, 2.5	$\underline{H}_C$	CH_2=$CHSi(CH_3)_3$
	1.55 (dd, 2H)	J_{HH} 11.0, 2.0	$\underline{H}_B$	CH_2=$CHSi(CH_3)_3$
	0.71 (dd 2H)	J_{HH} 14.0, 11.0	$\underline{H}_A$	CH_2=$CHSi(CH_3)_3$
	0.10 (s, 18H)		$Si(C\underline{H}_3)_3$	CH_2=$CHSi(CH_3)_3$
^{13}**C**	87.5 (d)	J_{CRh} 3.9	$\underline{C}_5H_5$	C_5H_5
	43.0 (d)	J_{CRh} 13.1	$\underline{C}H_2$	CH_2=$CHSi(CH_3)_3$
	49.4 (d)	J_{CRh} 14.0	$\underline{C}H$	CH_2=$CHSi(CH_3)_3$
	0.49 (s)		$Si(\underline{C}H_3)_3$	CH_2=$CHSi(CH_3)_3$

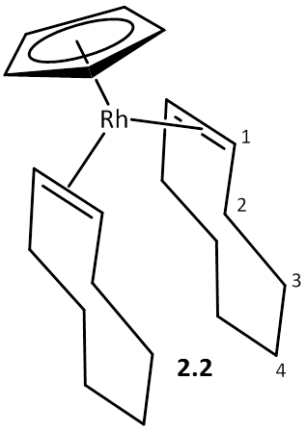

2.2

Figure 2.79: Structure of $[(\eta^5\text{-}C_5H_5)Rh(\eta^2\text{-}C_8H_{14})_2]$ **2.2.**

Table 2.16 NMR Characterisation of $[(\eta^5\text{-}C_5H_5)Rh(\eta^2\text{-}C_8H_{14})_2]$ **2.2**

	δ/ppm (multiplicity, integration)	Coupling constant/Hz	Assignment	Group
^{1}**H**	4.85 (s, 5H)		$C_5\underline{H}_5$	C_5H_5
	2.32 (d, 4H)	J_{HH} 13	H^2	COE
	1.76 (d, 4H)	J_{HH} 9	H^1	COE
	1.58 (m 12H total)		H^3 & H^4	COE
	1.52 (m 12H total)		$H^{2'}$	COE
	1.32 (m 8H)		$H^{3'}$ & $H^{4'}$	COE
^{13}**C**	91.1 (d)	J_{CRh} 3.7	$C_5\underline{H}_5$	C_5H_5
	65.1 (d)	J_{CRh} 14.4	C^1	COE
	33.5 (d)	J_{CRh} 1.3	C^2	COE
	32.9 (d)	J_{CRh} 1.3	C^3	COE
	26.8 (s)		C^4	COE

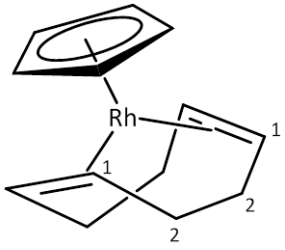

2.3

Figure 2.80: Structure of $[(\eta^5\text{-}C_5H_5)Rh(\eta^4\text{-}C_8H_{12})]$ **2.3.**

Table 2.17: NMR Characterisation of $[(\eta^5\text{-}C_5H_5)Rh(\eta^4\text{-}C_8H_{12})]$ **2.3**

	δ/ppm (multiplicity, integration)	Coupling constant/Hz	Assignment	Group
^{1}**H**	4.93 (s, 5H)		$C_5\underline{H}_5$	C_5H_5
	3.94 (s, 4H)		$C\underline{H}^1$	COD
	2.20 (m, 4H)		$(C\underline{H}_2)^2$	COD
	1.94 (dd, 4H)	J_{HH} 8.5, 16.0	$(C\underline{H}_2)^{2'}$	COD
^{13}**C**	86.7 (d)	J_{CRh} 3.7	$C_5\underline{H}_5$	C_5H_5
	62.5 (d)	J_{CRh} 14.0	$\underline{C}^1H$	COD
	32.5 (s)		$\underline{C}^2H_2$	COD

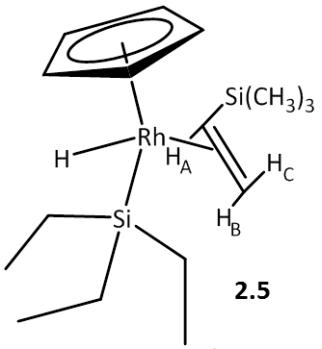

2.5

Figure 2.81: Photoproduct $[(\eta^5\text{-}C_5H_5)Rh(\eta^2\text{-}CH_2CHSi(CH_3)_3)(SO(CH_3)_2)]$ **2.4**

Table 2.18: NMR Characterisation for the $[(\eta^5\text{-}C_5H_5)Rh(\eta^2\text{-}CH_2CHSi(CH_3)_3)(SO(CH_3)_2)]$ **2.4**

	δ/ppm (multiplicity, integration)	Coupling constant/Hz	Assignment	Group
^{1}H	4.95 (s, 5H)		$C_5\underline{H}_5$	C_5H_5
	2.88 (dd, 1H)	J_{HH} 2.5, 14.0	$\underline{H}_C$	CH_2=$CHSi(CH_3)_3$
	2.55 (dd, 1H)	J_{HH} 2.5, 11.0	$\underline{H}_B$	CH_2=$CHSi(CH_3)_3$
	2.42 (s, 3H)		$(C\underline{H}_3)^D$	DMSO
	2.41 (s, 3H)		$(C\underline{H}_3)^E$	DMSO
	1.78 (ddd, 1H)	J_{HH} 11.0, 14.0 J_{HRh} 1.5	$\underline{H}_A$	CH_2=$CHSi(CH_3)_3$
	0.16 (s, 9H)		$Si(C\underline{H}_3)_3$	CH_2=$CHSi(CH_3)_3$
^{13}C	86.2 (d)	J_{CRh} 4.2	$\underline{C}_5H_5$	C_5H_5
	55.1 (d)	J_{CRh} 3.0	$(\underline{C}H_3)^D$	DMSO
	54.9 (d)	J_{CRh} 3.0	$(\underline{C}H_3)^E$	DMSO
	42.6 (d)	J_{CRh} 16.6	$\underline{C}H$	CH_2=$CHSi(CH_3)_3$
	37.5 (d)	J_{CRh} 15.8	$\underline{C}H_2$	CH_2=$CHSi(CH_3)_3$
	0.54		$Si(\underline{C}H_3)_3$	CH_2=$CHSi(CH_3)_3$

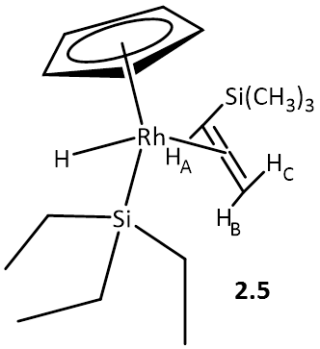

2.5

Figure 2.82: Photoproduct [(η^5-C_5H_5)Rh(H)(Si(CH_2CH_3)$_3$)(η^2-$CH_2CHSi(CH_3)_3$)] **2.5**

Table 2.19: NMR Characterisation for the [(η^5-C_5H_5)Rh(H)(Si(CH_2CH_3)$_3$)(η^2-$CH_2CHSi(CH_3)_3$)] **2.5** at 283 K

	δ/ppm (multiplicity, integration)	Coupling constant/Hz	Assignment	Group
^{1}**H**	5.06 (s, 5H)		$C_5\underline{H}_5$	C_5H_5
	2.71 (d, 1H)	J_{HH} 14.0	$\underline{H}_C$	CH_2=$CHSi(CH_3)_3$
	2.00 (d, 1H)	J_{HH} 11.0	$\underline{H}_B$	CH_2=$CHSi(CH_3)_3$
	1.84 (dd, 1H)	J_{HH} 11, 14	$\underline{H}_A$	CH_2=$CHSi(CH_3)_3$
	1.05 (t, 9H)	J_{HH} 7.5	$C\underline{H}_3$	$Si(CH_2CH_3)_3$
	0.66 (q, 6H)	J_{HH} 7.5	$C\underline{H}_2$	$Si(CH_2CH_3)_3$
	0.07 (s, 9H)		$Si(C\underline{H}_3)_3$	CH_2=$CHSi(CH_3)_3$
	-14.6 (d, 1H)	J_{RhH} 31.5	$\underline{H}$	Rh–H
^{13}**C**	88.6		$\underline{C}_5H_5$	C_5H_5
	41.7		$\underline{C}^1H$	CH_2=$CHSi(CH_3)_3$
	38.2		$\underline{C}^2H_2$	CH_2=$CHSi(CH_3)_3$
	10.6		$\underline{C}H_2$	$Si(CH_2CH_3)_3$
	9.4		$\underline{C}H_3$	$Si(CH_2CH_3)_3$
	0.1		$Si(\underline{C}H_3)_3$	CH_2=$CHSi(CH_3)_3$

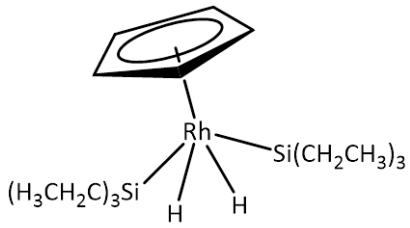

2.6

Figure 2.83: Photoproduct $[(\eta^5\text{-}C_5H_5)Rh(H)_2(Si(CH_2CH_3)_3)_2]$ **2.6**

Table 2.20: NMR Characterisation for the $[(\eta^5\text{-}C_5H_5)Rh(H)_2(Si(CH_2CH_3)_3)_2]$ **2.6**

	δ/ppm (multiplicity, integration)	Coupling constant/Hz	Assignment	Group
^{1}**H**	5.01 (d, 5H)	J_{RhH} 0.6	$C_5\underline{H}_5$	C_5H_5
	1.04 (overlap)		CH_2	$Si(CH_2CH_3)_3$
	0.77 (q, 4H)	J_{HH} 8.9	CH_3	$Si(CH_2CH_3)_3$
	–14.2 (d, 2H)	J_{HRh} 38	H	Rh–H
^{13}**C**	87.0		$\underline{C}_5H_5$	C_5H_5
	13.7		CH_2	$Si(CH_2CH_3)_3$
	8.9		CH_3	$Si(CH_2CH_3)_3$

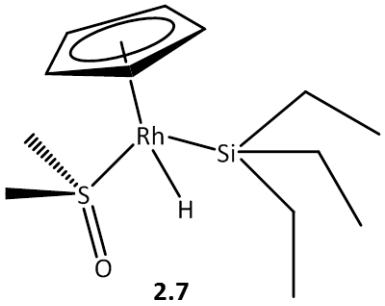

2.7

Figure 2.84: Photoproduct $[(\eta^5\text{-}C_5H_5)Rh(H)(Si(CH_2CH_3)_3)(SO(CH_3)_2)]$ **2.7**

Table 2.21: NMR Characterisation for the $[(\eta^5\text{-}C_5H_5)Rh(H)(Si(CH_2CH_3)_3)(DMSO)]$ **2.7**

	δ/ppm (multiplicity, integration)	Coupling constant/Hz	Assignment	Group
^{1}**H**	4.97 (s, 5H)		$C_5\underline{H}_5$	C_5H_5
	2.55 (s, 3H)		$(C\underline{H}_3)_A$	DMSO
	2.45 (s, 3H)		$(C\underline{H}_3)_B$	DMSO
	1.30 (overlap)		$C\underline{H}_3$	$SiEt_3$
	0.94 (overlap)		$C\underline{H}_2$	$SiEt_3$
	–13.45 (d, 1H)	33.7	Rh–H	Rh–H
^{13}**C**	87.7		$\underline{C}_5H_5$	C_5H_5
	58.4		$(\underline{C}H_3)_A$	DMSO
	58.1		$(\underline{C}H_3)_B$	DMSO

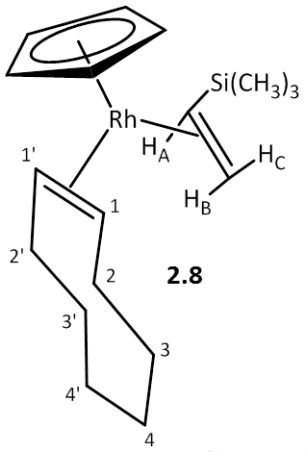

Figure 2.85: Photoproduct [(η^5-C_5H_5)Rh(η^2-C_8H_{14})(η^2-$CH_2CHSi(CH_3)_3$)] **2.8**

Table 2.22: NMR Characterisation for the [(η^5-C_5H_5)Rh(η^2-C_8H_{14})(η^2-$CH_2CHSi(CH_3)_3$)] **2.8**

	δ/ppm (multiplicity, integration)	Coupling constant/Hz	Assignment	Group
	4.90 (s, 5H)		$C_5\underline{H}_5$	C_5H_5
	2.97 (dd, 2H)	J_{HH} 1.5, 14	$\underline{H}^C$	CH_2=$CHSi(CH_3)_3$
	2.55 (t 1H)	J_{HH} 10	$C\underline{H}^1$	COE
	2.20 (overlap)	J_{HH} 1.5, 11	$\underline{H}^B$	CH_2=$CHSi(CH_3)_3$
^{1}H	2.10 (overlap)		$C\underline{H}_2$	COE
	1.50 (overlap)		$C\underline{H}_2$	COE
	0.80 (overlap)		$C\underline{H}^{1'}$	COE
	0.17 (s, 9H)		$(C\underline{H}_3)_3$	CH_2=$CHSi(CH_3)_3$
	–0.16 (dd 2H)	J_{HH} 11, 14	$\underline{H}^A$	CH_2=$CHSi(CH_3)_3$
	89.4 (d)	J_{RhC} 4.0	$\underline{C}_5H_5$	C_5H_5
	68.4 (d)	J_{RhC} 14.0	$\underline{C}H^1$	COE
	61.6 (d)	J_{RhC} 13.5	$\underline{C}H^{1'}$	COE
	50.8 (d)	J_{RhC} 14.0	$\underline{C}H$	CH_2=$CHSi(CH_3)_3$
^{13}C	40.9 (d)	J_{RhC} 14.0	$\underline{C}H_2$	CH_2=$CHSi(CH_3)_3$
	33.4 (s)		$\underline{C}H_2$	COE
	32.9 (s)		$\underline{C}H_2$	COE
	32.7 (s)		$\underline{C}H_2$	COE
	32.6 (s)		$\underline{C}H_2$	COE
	0.15 (s)		$(\underline{C}H_3)_3$	CH_2=$CHSi(CH_3)_3$

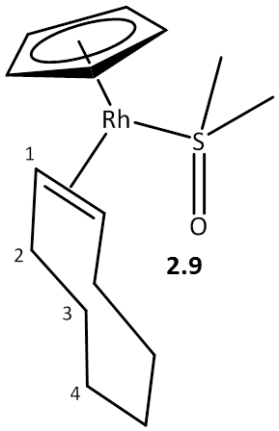

2.9

Figure 2.86: Photoproduct $[(\eta^5\text{-}C_5H_5)Rh(\eta^2\text{-}C_8H_{14})(SO(CH_3)_2)]$ **2.9**

Table 2.23: NMR Characterisation for $[(\eta^5\text{-}C_5H_5)Rh(\eta^2\text{-}C_8H_{14})(SO(CH_3)_2)]$ **2.9**

	δ/ppm (multiplicity, integration)	Coupling constant/Hz	Assignment	Group
^{1}H	4.84 (s, 5H)		$C_5\underline{H}_5$	C_5H_5
	3.00 (dm, 2H)	J_{HH} 9.5	H^1	COE
	2.49 (s, 6H)		$C\underline{H}_3$	DMSO
	2.46 (dq, 2H)	J_{HH} 13.5, 3.5	$H^{2'}$	COE
	1.65 (overlap)		H^2	COE
	1.50 (overlap)		H^3 /H^4	COE
13C	87.2	J_{CRh} 3.7	$\underline{C}_5H_5$	C_5H_5
	59.5	J_{CRh} 16.0	C^1	COE
	55.8		$\underline{C}H_3$	DMSO
	33.2		C^2	COE
	26.0		C^3/C^4	COE

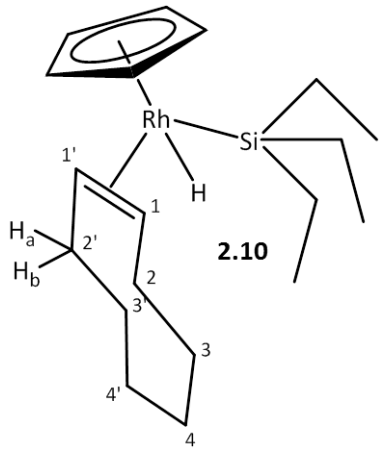

Figure 2.87: Photoproduct [(η^5-C_5H_5)Rh(H)(Si(CH_2CH_3)$_3$)(η^2-C_8H_{14})] **2.10**

Table 2.24: NMR Characterisation for the [(η^5-C_5H_5)Rh(H)(Si(CH_2CH_3)$_3$)(η^2-C_8H_{14})] **2.10** at 270 K

	δ/ppm (multiplicity, integration)	Coupling constant/Hz	Assignment	Group
^{1}H	4.99 (s, 5H)		$C_5\underline{H}_5$	C_5H_5
	2.91 (br t, 1H)	J_{HH} 9.5	$C\underline{H}^1$	COE
	2.45 (br t, 1H)	J_{HH} 9.5	$C\underline{H}^{1'}$	COE
	2.24 (dd, 1H)	J_{HH} 13.8, 2	$C\underline{H}_2^{2a}$	COE
	2.16 (br d, 1H)	J_{HH} 13.8	$C\underline{H}_2^{2a'}$	COE
	1.56 (overlap)		$C\underline{H}_2^{2b}$	COE
	1.47 (overlap		$C\underline{H}_2^{2b'}$	COE
	1.10 (t, 9H)	J_{HH} 8	Si($CH_2C\underline{H}_3$)$_3$	Silane
	0.74 (q, 6H)	J_{HH}	Si($C\underline{H}_2CH_3$)$_3$	Silane
	–15.00 (d, ^{1}H)	J_{RhH} 33.5	H	Rh – H
^{13}C	90.1		$\underline{C}_5H_5$	C_5H_5
	61.7		$\underline{C}^{1'}H$	COE
	58.4		$\underline{C}^1H$	COE
	33.6		$\underline{C}^2H_2$	COE
	33.1		$\underline{C}^{2'}H_2$	COE
	10.7		Si($\underline{C}H_2CH_3$)$_3$	Silane
	9.4		Si($CH_2\underline{C}H_3$)$_3$	Silane

3 Photochemistry of [(η^5-C_5H_5)RhLL'] with H_2

3.1 Introduction

This chapter concerns the reactivity of half sandwich rhodium complexes with H_2. The reaction of Cp'Rh(alkene)$_2$, where Cp' refers to a cyclopentadienyl ligand and its derivatives, with H_2 has been studied using complexes with a range of different coordinated alkene ligands. In York, a number of these systems have been studied previously using low temperature *in-situ* irradiation.[74, 112, 136] One of the complexes studied was CpRh(C_2H_4)$_2$ and when it was irradiated in d_8-toluene at 203 K, in the presence of H_2, the solvent complex CpRh(C_2H_4)(η^2-toluene) was detected (Figure 3.1A). However, when the related dinuclear species $CH_2[(C_5H_4)Rh(C_2H_4)_2]_2$ was used instead, in addition to the solvent complex, a hydride bridged species was observed (Figure 3.1B). When this reaction was repeated using CpRh($CH_2CHSiMe_3$)$_2$ (**2.1**), with extended irradiation the analogue bridged hydride product was detected. With short irradiation times, using the para-spin isomer of H_2 (*p*-H_2), a PHIP enhanced dihydride species, CpRh(H)$_2$($CH_2CHSiMe_3$) (Figure 3.1) was detected, providing the first NMR spectrum of a CpRh(H)$_2$(alkene) moiety.[74] A number of similar dihydride species have been detected since this time.[136]

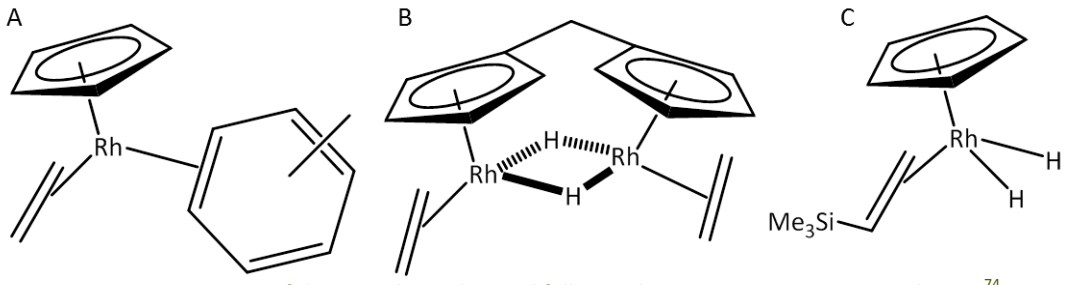

Figure 3.1: Structures of three products observed following low temperature *in-situ* irradiation.[74]

The specific complexes described in this chapter are shown in Figure 3.2. They include [(η^5-C_5H_5)Rh(η^2-$CH_2CHSi(CH_3)_3$)$_2$] **2.1** and [(η^5-C_5H_5)Rh(η^2-$CH_2CHSi(CH_3)_3$)(DMSO)] **2.4** which provide two routes to the same intermediate "(η^5-C_5H_5)Rh(η^2-$CH_2CHSi(CH_3)_3$)".[74] This intermediate was expected to activate the H–H bond of *p*-H_2 giving a dihydride complex with chemically

inequivalent hydride ligands due to the trimethylsilane substituent on the bound alkene. The rationale behind studying **2.1** with parahydrogen was primarily to determine whether the use of parahydrogen and laser irradiation would allow the rate of H_2 addition to the 16-electron intermediate to be measured. A second motivation was to investigate whether the parahydrogen protons could be transferred to the coordinated alkene or provide further insights into the reactivity of $CpRh(H)_2(CH_2CHSiMe_3)$.[74] The analogous $CpRh(H)(SiEt_3)$(alkene) was found to be involved in a hydrosilation pathway and it was found to undergo reactivity with a range of ligands including ethene, DMSO and silanes.[110] It would be interesting to see if this similar activity was replicated in the dihydride analogue. Furthermore, Brookhart *et. al.* observed that following prolonged heating at 140 °C of $Cp^*Rh(CH_2CHSiMe_3)_2$ in cyclohexane resulted in products consistent with the C–Si activation of the trimethylvinylsilane ligand and the subsequent formation of *trans* 1,2-bis(trimethylsilane)ethene and 1,1-bis(trimethylsilane)ethene.[103] It would be interesting to determine if these products could formed photochemically and whether their formation be probed through the use of parahydrogen. **2.4** was included in this study as the DMSO ligand was also found to be photolabile and how readily this ligand is lost, in comparison to the vinylsilane in **2.1**, was of interest.

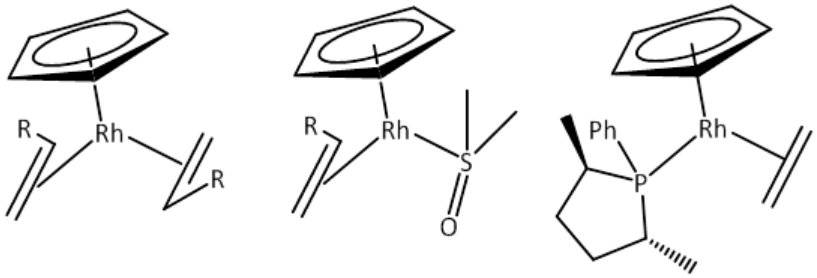

Figure 3.2: Structures of **2.1**, **2.4** and **3.2**.

The reported photoactivity of half sandwich rhodium complexes is not restricted to bis-alkenes as complexes of the type CpRh(L)(alkene) also undergo loss of the bound alkene. The resulting 16 electron intermediate "CpRh(L)" may again undergo further reaction with 2-electron donor

ligands and the oxidative addition of an X–Y bond. The thermal and photochemical reactivity of $CpRh(PR_3)(C_2H_4)$ complexes (Figure 3.3) have been studied extensively using different coordinating phosphines and with a range of substrates. The third complex studied in the chapter is $[(\eta^5\text{-}C_5H_5)Rh(P^*Ph)(C_2H_4)]$ **3.2** (Figure 3.2). As in **2.1** it contains a coordinated photolabile alkene and a second ligand which breaks the symmetry of the hydrides in any potential dihydride product. In **2.1** it is the asymmetry of the coordinated alkene which breaks the symmetry in the resultant hydride ligands. In contrast in **3.2** it is the chirality of phosphine, P*Ph, where P*Ph refers to (2R, 5R) 2,5 dimethyl, 1-phenyl phospholane, which makes the two hydrides distinct from one another. One of the reasons behind selecting this complex is the 0.76 ppm chemical shift difference between the two hydride ligands in its corresponding dihydride complex.[6] Having ^1H signals which are well resolved from one another is an advantage in NMR spectroscopy. This chemical shift difference also raises the possibility of studying the evolution of the parahydrogen singlet state as a function of this chemical shift difference according to the theory outlined in Introduction Section 1.2.5.

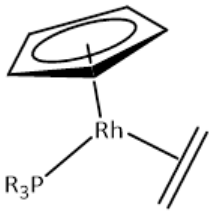

R = Me[1-3]
Ph[4, 5]
PR_3 = P*Ph[6]

Figure 3.3: Structure of $CpRh(PR_3)(C_2H_4)$, the starting complex in many of these studies.

The early work by the Perutz group used the PMe_3 analogues of this complex and followed its reactivity using matrix isolation and solution-based product studies.[2] They discovered in a matrix that there were two competing photochemical processes; photosubstitution and C–H bond activation of the liberated alkene (Figure 3.4A).[2] In CO and N_2 matrices the loss of the ethylene ligand was observed and the coordination of either CO and N_2 respectively was observed (Figure 3.4B).[2] These products were characterised by IR spectroscopy. The complex was next studied in a toluene glass.[2] The sample was irradiated at 77 K for 8 hours before

being warmed to 203 K for characterisation by ^{1}H and $^{31}P\{^{1}H\}$ NMR spectroscopy. The distinguishing features were a phosphorus signal at δ 13.9 which has a coupling to rhodium of 156.1 Hz.[2] A coupling constant of this magnitude is consistent with a Rh^{III} species indicating that an oxidative addition process has occurred. A hydride resonance at δ –13.52 (dd, J_{HP} 41.6, J_{HRh} 31.5 Hz) supports this observation. Full characterisation revealed this product to be the vinyl hydride complex (Figure 3.4A). Warming this sample to 253 K results in the complete conversion back to the starting material suggesting the vinyl hydride product is not thermally stable.[2]

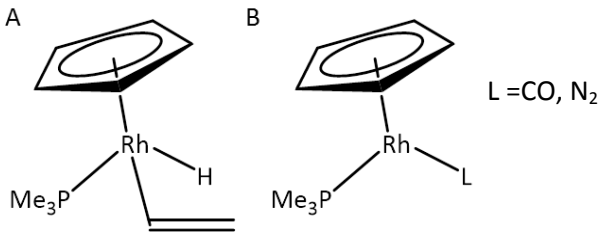

Figure 3.4: Structures of the photoproducts formed when $CpRh(PMe_3)(C_2H_4)$ is irradiated in a matrix, adapted from Bell *et al*.[2]

The activity of $CpRh(PMe_3)(C_2H_4)$ has also been studied in different aromatic solvents. In benzene, the loss of ethylene and activation of a C–H bond of benzene to give the phenyl hydride product in Figure 3.5A occurs.[3] In hexafluorobenzene, however, coordination of the arene via an η^2 interaction resulted (Figure 3.5B).[3] They proposed that this corresponds to an intermediate on the pathway to oxidative addition, a similar observation has been made with the analogous Cp* rhodium complexes.[137] Further studies were performed with using toluene, this time at room temperature. A rhodium hydride complex was formed which was determined to be the tolyl hydride complex (Figure 3.5C) formed by the C–H activation of one of the methyl protons of toluene.[2] Irradiation at 213 K gave a mixture of the tolyl, vinyl and benzyl hydride complexes.

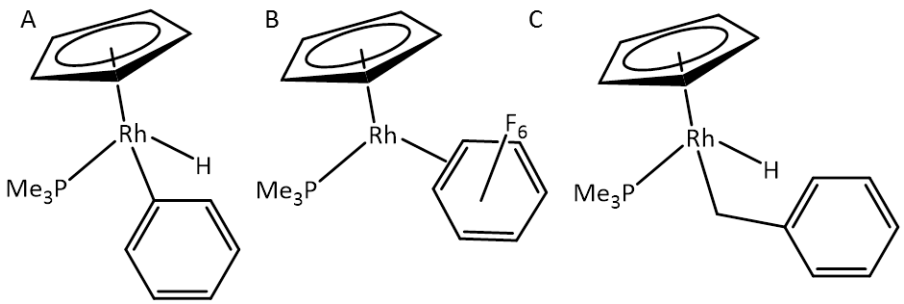

Figure 3.5: Products formed after UV irradiation of $CpRh(PMe_3)(C_2H_4)$ in the indicated arene, adapted from[2, 3].

The photochemistry of the PPh_3 analogue, $CpRh(PPh_3)(C_2H_4)$, has also been studied. In hexafluorobenzene, like with the PMe_3 complexes,[2] the resulting product contained an η^2-C_6F_6 ligand in place of the ethylene (Figure 3.6A).[138] This was not the case, however, when partially fluorinated aryl ligands were used, with pentafluorobenzene yielding the C–H bond activation product $CpRh(PPh_3)(C_6F_5)H$ (Figure 3.6B). The NMR defining features of this product being a hydride resonance in the ^1H spectrum at δ –11.50 (dd, J_{HRh} 21.6, J_{HP} 43.9 Hz), and three separate fluorine resonances consistent with the *ortho*, *meta* and *para* positions of a coordinated arene. A similar observation was made with 1,3-difluorobenzene (Figure 3.6C).

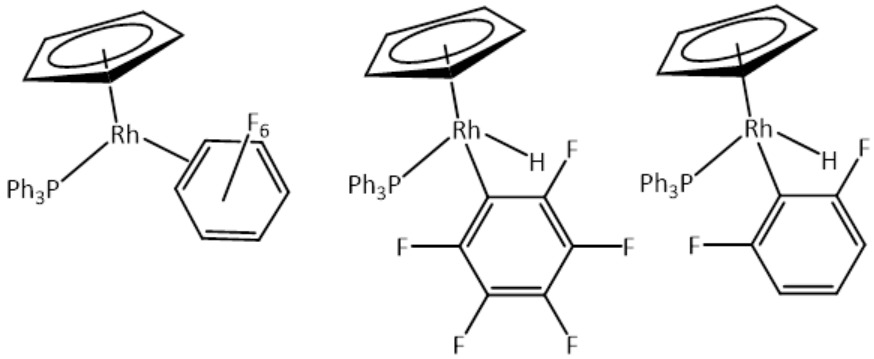

Figure 3.6: Typical products formed after the the reaction of $CpRh(PPh_3)(C_2H_4)$ with a fluorinated arene, adapted from Heaton *et al.*[138]

More recently, the reaction of **3.2** with pinacolborane (HBpin) has been studied.[6] A chiral phosphine was chosen in this study as in introduces a second chiral element to the oxidative addition product resulting in products that are diastereomers of one another, enabling their detection by ^1H NMR spectroscopy and thus allowing the stereoselectivity of the reaction to be investigated. The resulting diastereomers (A and B) of the product are shown in Figure 3.7. The

most noted differences in the NMR spectra of these two isomers were observed in the chemical shifts of the respected hydrides. Isomer A was associated with a resonance at δ –13.6 and B with a hydride resonance at δ –14.3 both appear as doublets of doublets with J_{HP} of 30 Hz and J_{HRh} of 35 Hz. These hydride resonances were shown to interconvert on the NMR timescale. The use of $^{31}P\{^{1}H\}$ EXSY measurements and doping with triphenylphosphine demonstrated that exchange occurred without the loss of the phosphine and therefore a mechanism incorporating a η^2-(B–H) containing intermediate was proposed.

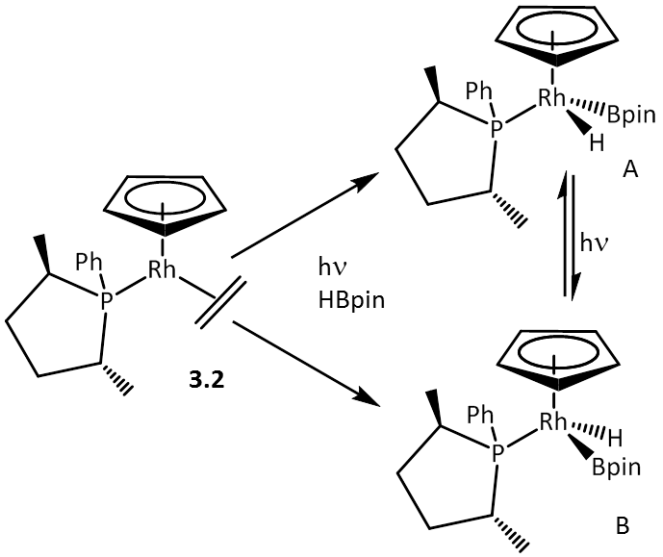

Figure 3.7: Reaction schematic for the photoinitiated reaction of CpRh(P*Ph)(C_2H_4) with HBpin. (Adapted from Câmpian et al[5]).

In addition to studying the activity of these Bpin products they separately synthesised the dihydride complex [CpRh(H)$_2$(P*Ph)] **3.3** from **3.2** using $NaBH_4$ in toluene/ethanol. The two hydride ligands were observed at δ –13.71 (dd, J_{HRh} 36.1, J_{HP} 27.8 Hz) and δ –14.47 (dd, J_{HRh} 37.9, J_{HP} 28.0 Hz). They too were found to interconvert on the NMR timescale, via a proposed dihydrogen intermediate.

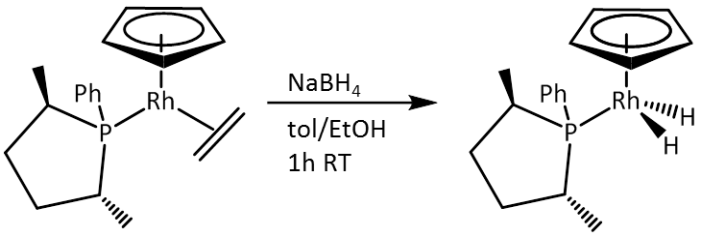

Figure 3.8: Synthesis of [CpRh(H)$_2$(P*Ph)] **3.3**.

3.2 Photochemistry of **2.1** with *p*-H_2 – to form **3.1**

Previous work in York on [(η^5-C_5H_5)Rh(η^2-$CH_2CHSiMe_3$)$_2$] **2.1** has shown that when it is photolysed in the presence of *p*-H_2 the replacement of one of the trimethylvinylsilane ligands by H_2 is possible[74] (Figure 3.9). The Rh^{III} product has two chemically inequivalent hydride resonances at δ –13.43 and –13.37 ppm, both of which exhibit a coupling to rhodium of 25.3 Hz (Figure 3.10b). This study was performed at 213 K with continuous irradiation *in-situ*, using a 325 nm 25 mW He-Cd cw laser as the radiation source in conjunction with to a 400 MHz spectrometer.[74] Since this time the *in-situ* photochemistry set-up at York has changed to use a Nd:YAG laser coupled with a 600 MHz spectrometer.[66] Synchronisation between the light source and NMR spectrometer has allowed for precise time delays between the irradiation and detection steps. Additionally, it has permitted control over the number and frequency of the laser pulses. The PHIP enhanced hydride obtained with the cw laser reflects a PHIP/PASADENA experiment and it is the longitudinal two-spin order term ($2I_zS_z$) which is detected. The synchronicity in the newer approach offers the possibility of coherently retaining the *ZQ* coherence also as detailed in Introduction Section 1.2.5 and Chapter 6.

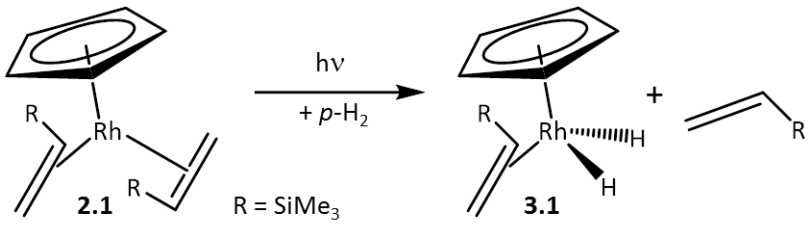

Figure 3.9: Reaction scheme for the photochemical addition of *p*-H_2 to **2.1**.

An optically dilute NMR sample of **2.1** was therefore prepared in d_8-toluene and 20 µL of trimethylvinylsilane added. An excess of the alkene ligand is used because during the reaction the trimethylvinylsilane may become hydrogenated. When this occurs, the ligand is no longer able to coordinate to the metal centre with the same degree of stabilisation compared to the alkene. This provides a route for the decomposition of the starting material. The sample was degassed and backfilled with 3 bar of *p*-H_2. The sample was then irradiated *in-situ* at 263 K as

described in the Experimental Section 8.3.2. Initially the OPSY protocol was employed in conjunction with a single laser pulse and a series of pump-probe delays. This approach would be predicted to allow the initial ZQ_x terms evolution to be monitored (see Chapter 6) if sufficient signal-to-noise was available. No signal was seen.

When the number of laser pulses prior to the NMR experiment was increased a PHIP-enhanced signal was seen at δ –13.5 (Figure 3.10A labelled as 263 K). These laser pulses were separated by 0.2 seconds. Surprisingly, the profile of the hydride peak does not resemble that reported in the literature.[74] Analysis revealed that a combination of the size of magnet, 400 vs 600 MHz, and temperature effects operated. The experiment was repeated at 298, 240 and 220 K and the resulting hydrides resonances are shown in Figure 3.10A.

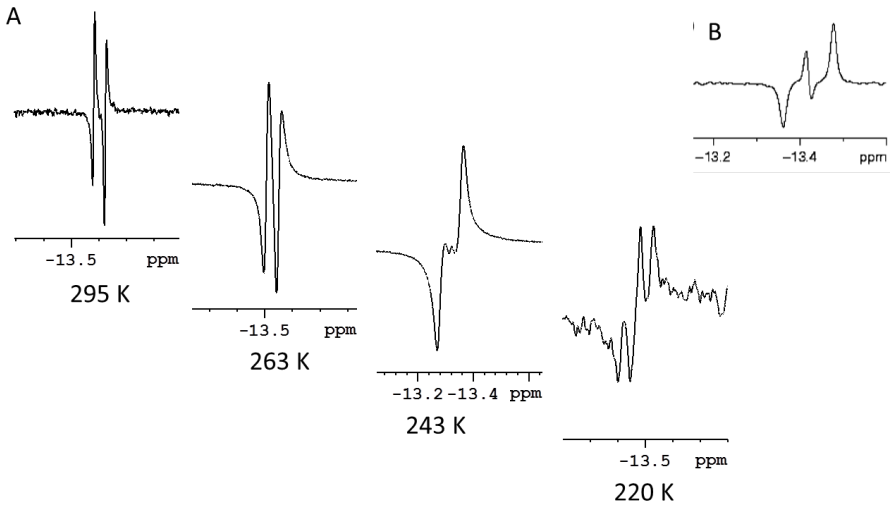

Figure 3.10: Hydride resonance of **3.1** as a function of temperature. a) hydride resonance recorded on a 600 MHz spectrometer in d_8-toluene at the temperatures labelled b) hydride resonance in Godard *et. al.*[74] recorded on a 400 MHz spectrometer in d_8-toluene at 213 K.

Both hydrides couple to the Rh^{III} centre as well as one another forming an ABX spin system. Typical values of J_{HRh} in a Rh^{III} spin system lie in the region of 25-30 Hz, whilst the splitting between A and B, is 2-6 Hz. Simulations of the chemical shift differences of the two hydrides and the respective couplings were simulated for each of the different temperatures using the manual iteration mode in g-NMR. The results of this fitting are shown in Figure 3.11. Due to the broadness of the experimental signal, a large amount of line broadening had to be applied

in the simulated spectra and this distorted the baseline in the fitted spectra as demonstrated by comparing the simulations with and without line broadening applied (Figure 3.11). Aside from the discrepancy in the baseline, there is a good match in the profile of the peaks. The fitted chemical shift difference and the coupling constants are summarised in Table 3.1 and show that the chemical shift difference increases from 0.01 ppm at 298 K to 0.10 ppm at 220 K and that J_{HRh} is approximately 26 Hz and J_{HH} is approximately 3 Hz.

Table 3.1: Fitted chemical shift differences and coupling constants for the PHIP enhanced hydrides of **3.1** at variable temperatures.

Temperature /K	$\Delta\delta$ /ppm	J_{HRh} /Hz	J_{HH} /Hz
298	0.01	26.7	2.9
263	0.02	26.5	2.8
243	0.07	26.1	2.9
220	0.10	26.8	2.8

.

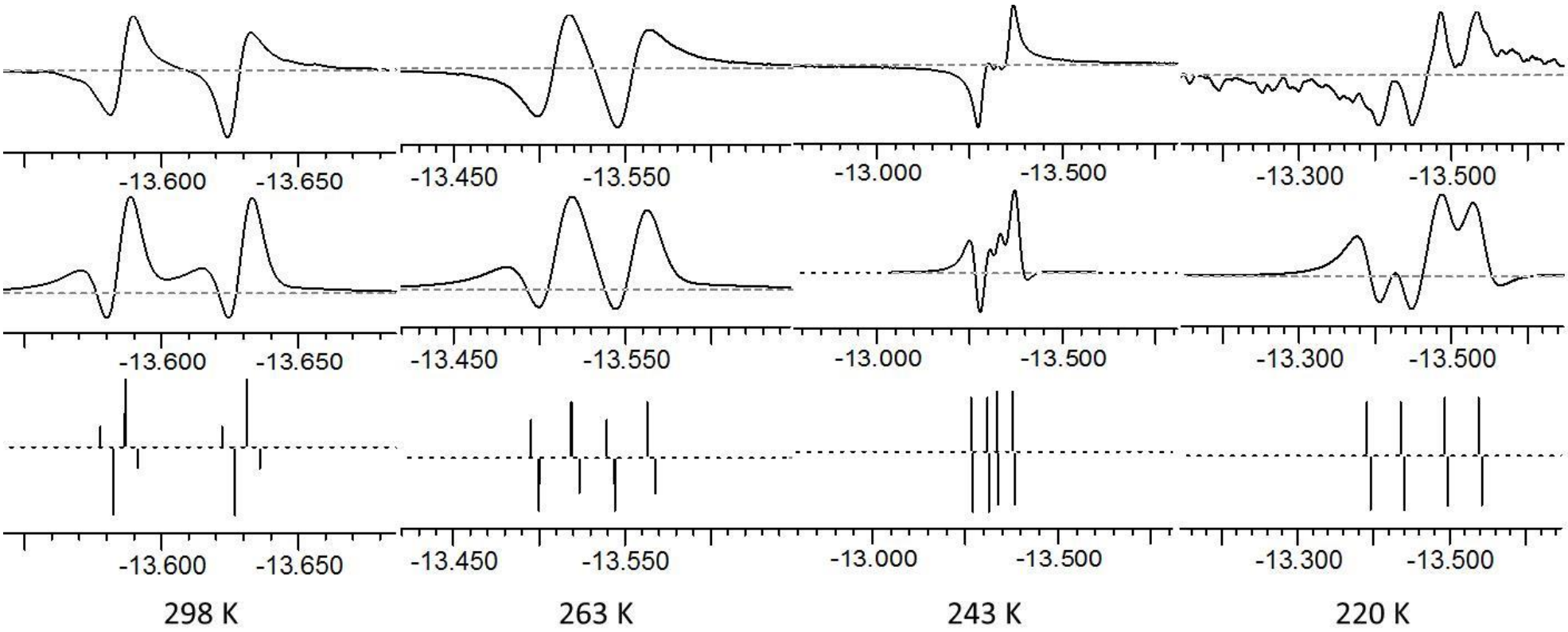

Figure 3.11: Comparison of the experimental hydride peaks (top) and fitted peaks (middle and bottom) at the temperatures labelled; middle includes line broadening to match to experimental and bottom spectra have no line broadening applied.

Having shown that **2.1** forms [(η^5-C_5H_5)Rh(H)$_2$(η^2-$CH_2CHSi(CH_3)_3$)] **3.1** when photolysed in the presence of *p*-H_2 the behaviour of this rhodium dihydride species was studied further. The PHIP-enhanced signal was only observed with multiple laser pulses. In addition to the increase in the amount of irradiation the sample is exposed to it also increases the time from the initial photolysis and the NMR experiment. If the addition of H_2 occurs slowly, it could be that it is this longer timeframe from the initial laser pulse, allowing the dihydride time to form, that is responsible for the enhanced signals being observed with multiple laser pulses. To investigate this, a series of experiments with one laser pulse and a pump-probe delay that relates to the duration of the irradiation were performed. The first delay used was 0.2 seconds, this reflects the time it took for two laser pulses to be fired, the delay was then incremented up to 6.2 seconds which is the extra time associated with 32 laser pulses. There were no hydride resonances detected in any of these spectra. This suggests that it is the additional irradiation, rather than time, that enables the dihydride to be detected.

The relationship between the observed enhancement and the number of laser pulses will be studied next. This was performed at 263 K and a series of NMR experiments were acquired where the number of laser pulses was increased from 1 to 64 with a 0.2 second delay between pulses. The sample was shaken in between each experiment to refresh the parahydrogen in solution. The resulting hydride resonance was processed in magnitude mode owing to the antiphase nature of the PHIP signals and the signal-to-noise ratio of the resonance was plotted against the number of laser pulses (Figure 3.12). This reveals an initial increase in enhancement with more laser pulses followed by a plateau between 32 and 64 laser pulses. In these experiments, we are in the asynchronous addition of parahydrogen regime and therefore only the $2I_zS_z$ term is coherently retained in the product. From the moment the H_2 has added to the metal centre, this spin encoded state begins to relax back to the Boltzmann distribution and the possible enhancement reduces accordingly. With the larger number of laser pulses there is a trade-off between the higher enhancements due to more product

forming and lower enhancements due to the relaxation of the parahydrogen-derived spin states.

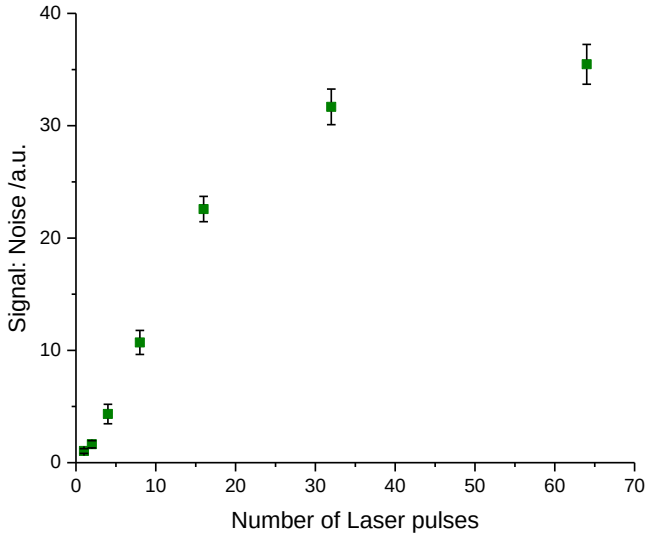

Figure 3.12: Plot showing the relationship between the number of laser pulses and signal-to-noise ratio of the enhanced rhodium dihydride resonance.

By varying the delay between the last laser pulse and the NMR scan, it could be possible to observe this growth of product and at longer delay times, the relaxation of the parahydrogen derived spin states. To investigate this, an optically dilute sample of **2.1** was prepared in d_8-toluene and 3.5 μL of trimethylvinylsilane was added. Using the ^{1}H NMR spectrum, it was determined that there was a sub-stoichiometric quantity of vinylsilane relative to **2.1**, therefore a larger degree of decomposition of the starting material may be observed. A second sample, therefore, was also prepared with 9 μL of trimethylvinylsilane which represented a 15 fold excess of ligand relative to **2.1** by ^{1}H NMR spectroscopy.

To investigate the variation of the observed hydride enhancement as a function of the pump-probe delay a series of experiments were acquired at 263 K using 32 laser pulses, now with a 0.1 s delay between laser pulses. This is the shortest repeat rate for the laser and in the testing; this resulted in larger enhancements than the 0.2 s delay, since there is a shorter time for relaxation to occur in between laser pulses. There are a number of variables to be considered during the course of this study. Firstly, the proportion of *p*-H_2 in solution will

reduce during the reaction, as any H_2 lost from the complex will no longer be enriched with the *p*-H_2 encoded spin state. Secondly, since the laser only irradiates a small region of the NMR sample the reactivity is localised to a narrow region of the sample[15] and therefore there will be a localise area of product in the active region of the NMR spectrum whilst the reactive precursor will be outside of this region. The amount of the **2.1** will also reduce as a function of the irradiation; this reduces the possible enhancement observable. To manage these variables the experiments will be run in pairs; the first experiment will have a set pump-probe delay of 0.5 ms to act as a control and the second experiment will have a variable delay. After the second experiment, the sample will be shaken. This will account for the change in the concentration of **2.1** during the irradiation period and any drops in enhancement due to lower quantities of *p*-H_2. Preliminary tests determined this to be less significant than the drop in the concentration of **2.1** as replenishing the sample which fresh *p*-H_2 resulted in enhancements comparable to the enhancements before the *p*-H_2 was refreshed rather than the enhancements obtained when the previous *p*-H_2 was added. Whilst shaking the sample will redistribute the product and starting material throughout the solution and will replenish the solution with parahydrogen from the headspace.

The first sample was studied with pump-probe delay from 0.025 s up to 7 s. These were processed in magnitude mode and the integral from the variable delay normalised against its control experiment. These were then plotted against the pump-probe delay (Figure 3.13). This shows that there is possibly an initial growth period during the first 0.05 s followed by an exponential decay in the enhancement. The second sample, the sample with an excess of trimethylvinylsilane, was studied using the same approach. To investigate whether the initial growth period is real smaller increments in the pump-probe delay will be used during this time. The normalised integrals are then plotted against the pump-probe delay in Figure 3.14, which shows the same initial rise during the shorter delay times followed by a decay in enhancement. It would suggest that during this time the dihydride complex is still forming. The

decay after this growth is due to the relaxation of the terms resulting from the $2I_zS_z$ component of the *p*-H_2 singlet state as described by Figure 3.15. The decay in enhancement of both samples was fitted to exponential decay functions. In the first sample the enhancement decayed with a rate constant of 0.53 ± 0.05 s^{-1}. This corresponds to a relaxation constant, T_1, of 1.89 ± 0.18 s and in the second sample a rate constant of 1.00 ± 0.09 s^{-1} was obtained giving a T_1 of 1.00 ± 0.09 s. The ^{1}H NMR spectra for the two samples were compared to rationalise this difference. Sample 1 had a lower concentration of **2.1**; this could cause small variation in T_1. More significantly, the C_6D_6 solvent used for sample 2 contained a greater amount of water compared to sample 1 and this can reduce T_1 values. Both values of T_1 are consistent with a T_1 of a metal hydrides species obtained using standard NMR methods.[53, 54]

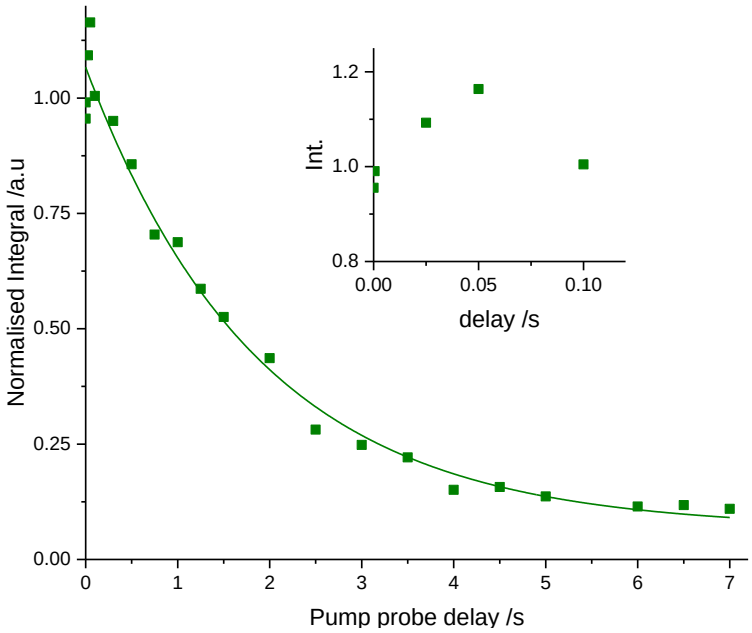

Figure 3.13: Plot showing the normalised hydride enhancement as a function of the pump-probe delay after 32 laser pulses 0.1 seconds apart. Insert shows an expansion for t = 0-0.14 to highlight the initial growth period. The decay of the enhancement was fitted to an exponential decay y = 0.07 ± 0.03 + 1.00 ± 0.03$e^{-(0.53 \pm 0.05\ s^{-1})t}$.

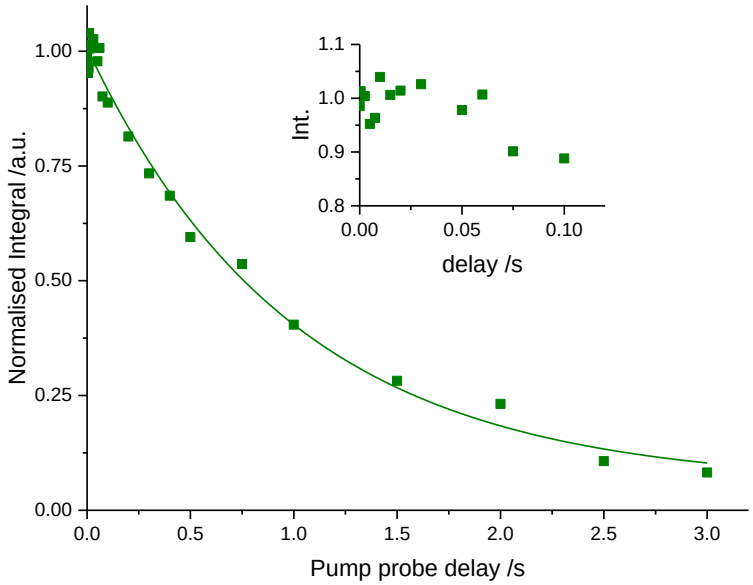

Figure 3.14: Plot showing the normalised hydride enhancement as a function of the pump-probe delay after 32 laser pulses 0.1 seconds apart. Insert shows an expansion for t = 0-0.14 to highlight the initial growth period. The decay of the enhancement was fitted to an exponential decay $y = 0.06 \pm 0.03 + 0.95 \pm 0.03e^{-(1.00 \pm 0.09\ s^{-1})t}$.

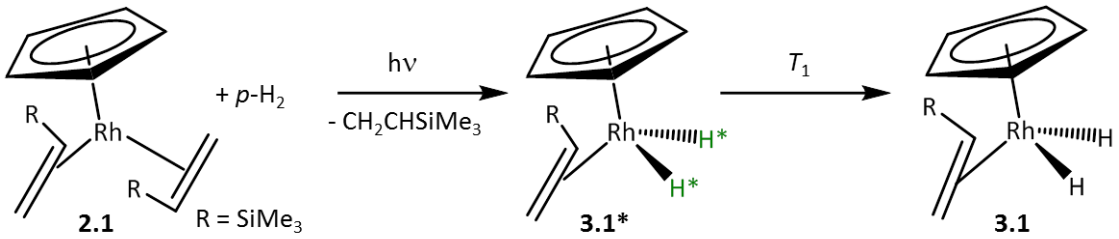

Figure 3.15: Reaction scheme showing the process described in Figure 3.13 and Figure 3.14.

The control experiments recorded during the study for both samples were also analysed. This time the integrals were normalised against the integral of the first measurement allowing the change in the enhancement with irradiation time to be observed. These were plotted against the experiment number (Figure 3.16 -Figure 3.17). In both samples there is a steep drop off the in the enhancement observed. These were fitted using a linear regression with the equation $y = c - mx$ where the gradient, m, for both samples were $(3.77 \pm 0.15)\ x10^{-2}$ and $(4.01 \pm 0.24)\ x10^{-2}$ respectively showing the drop in enhancement recorded was, within experimental error, the same in both samples. The 95% confidence limit on both of these regressions is highlighted in Figure 3.16 and Figure 3.17 by the shaded area and shows that the sample with the excess trimethylvinylsilane has greater scatter than the sample without the excess. From

this, we can conclude that the product is relatively stable over the time course of this study and thus does not lose H_2 thermally to give a fragment, which can react with the free trimethylvinylsilane in solution to reform the starting material, and hence why there is no real difference between the two samples. This also suggests that the product is less photoactive at 355 nm than the starting material and therefore the dihydride cannot efficiently be replaced with fresh parahydrogen.

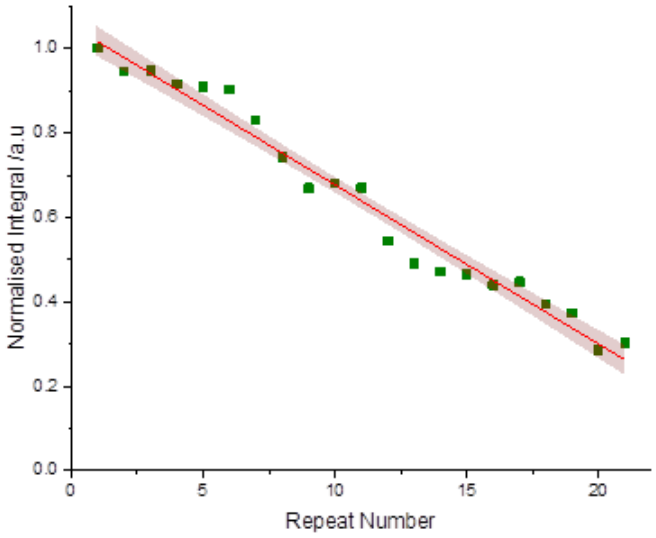

Figure 3.16: Plot showing the enhancements of the control experiments as a function of the repeat number normalised against the enhancement of the first experiment. Fitted $y = 1.05 \pm 0.02 – (3.77 \pm 0.15)\ x10^{-2}x$ grey region signifies the 95% confidence limit for the fitting.

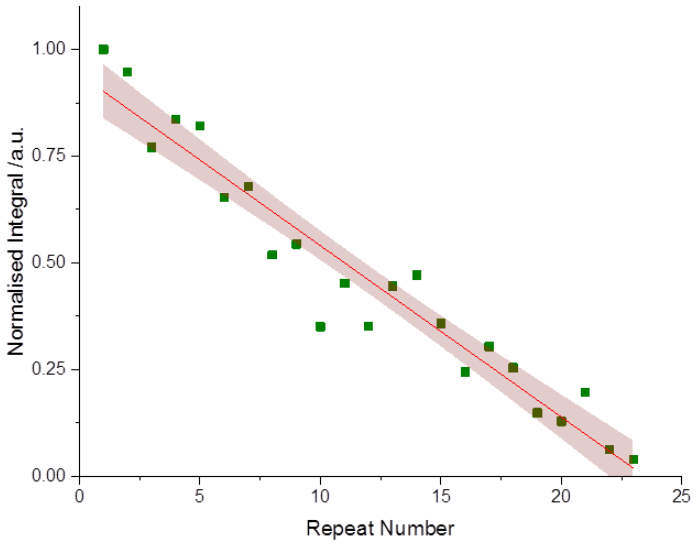

Figure 3.17: Plot showing the enhancements of the control experiments as a function of the repeat number normalised against the enhancement of the first experiment. Fitted $y = 0.94 \pm 0.03 – (4.01 \pm 0.24)\ x10^{-2}x$ grey region signifies the 95% confidence limit for the fitting.

In summary

- $CpRh(CH_2CHSiMe_3)(H)_2$ **3.1** is formed with PHIP-enhanced signals following the photochemical reaction of **2.1** with *p*-H_2 using multiple laser pulses.
- The two hydride ligands are chemically different and form two ABX hydride resonances which exhibit a temperature dependence in the chemical shift difference in the two hydride ligands.
- The observed PHIP-enhanced signals initially increase in intensity with an increasing number of laser pulses. After 32 laser pulses a plateau is reached when the relaxation of the parahydrogen-derived states balance out the higher levels of irradiation.
- The relaxation time for the enhanced hydride resonance is 1.89 s in one measurement and 1.00 s according to a second measurement, where the two samples differed in their concentration of free trimethylvinylsilane. The difference in the relaxation times was attributed to the presence of water in the second sample.
- Lower photoactivity of the product $CpRh(CH_2CHSiMe_3)(H)_2$ was observed, compared to the $CpRh(CH_2CHSiMe_3)_2$ starting material, at 355 nm.

3.3 Photochemistry of **2.4** with *p*-H_2 – to form **3.1**

In Chapter 2, it was demonstrated that DMSO may be lost photochemically from **2.4** and that this generated the same reactive intermediate as **2.1**. To investigate whether the loss DMSO from **2.4** provides more efficient generation of this intermediate, **2.4** was studied with *p*-H_2. A sample of **2.1** was prepared and 5 µL of DMSO added; the sample was irradiated *ex-situ* for 10 minutes which allowed the formation of **2.4**. The sample was then degassed and filled with 3 bar *p*-H_2. The sample was irradiated at 263 K with 32 laser pulses 0.1 seconds apart with a pump probe delay of 0.5 ms and a PHIP-enhanced hydride signal for **3.1** was observed. The enhancement was compared to samples of **2.1** and found to be were considerably smaller than when **2.1** was used as the precursor. For this reason, it was not pursued further.

3.4 Synthesis of $[(\eta^5\text{-}C_5H_5)Rh(P^*Ph^*)(C_2H_4)]$ **3.2**

The synthesis of $[(\eta^5\text{-}C_5H_5)Rh(P^*Ph)(C_2H_4)]$ **3.2**, where P*Ph refers to the chiral phosphine (2S, 5S) 2,5 dimethyl, 1 phenyl phospholane, is reported in the literature.[6] The chiral phosphine was synthesised by the procedure published by Suzuki *et al*[139] and Burk *et al*[140] which is outlined in Figure 3.18. The first step involves the mesylation of (2R, 5R)-2,5 hexanediol which gave A as a colourless oil in 72% yield. A was then reacted with phenyllithium to give the target phospholane in 80% yield. The phosphine was then added to $[Rh(C_2H_4)_2Cl]_2$ using a reaction time of 20 minutes, to limit the substitution of the ethylene ligands to one per rhodium centre. The target half sandwich complex was prepared by reacting the rhodium dimer with lithium cyclopentadienyl and resulted in a dark brown oil as the product. A ^{1}H NMR spectrum of this product (Figure 3.19) revealed a notable amount of the bis(ethylene) complex $CpRh(C_2H_4)_2$, in addition to other small impurities, which would suggest that the first part of this step did not reach completion. The key ^{1}H NMR features of $CpRh(C_2H_4)_2$ are a Cp resonance at δ 5.09 and two broad doublets at δ 2.90 and 1.12 (J_{HH} 11 Hz) for the coordinated ethene ligands. Sublimation was used to purify the material. Prior to the sublimation the ratio of **3.1**: $CpRh(C_2H_4)$ was 1: 0.85 but after the sublimation the ratio it was only 1: 0.75 indicating that only a relatively small amount of the bisethylene complex was removed. Nonetheless, this sample was used in subsequent studies.

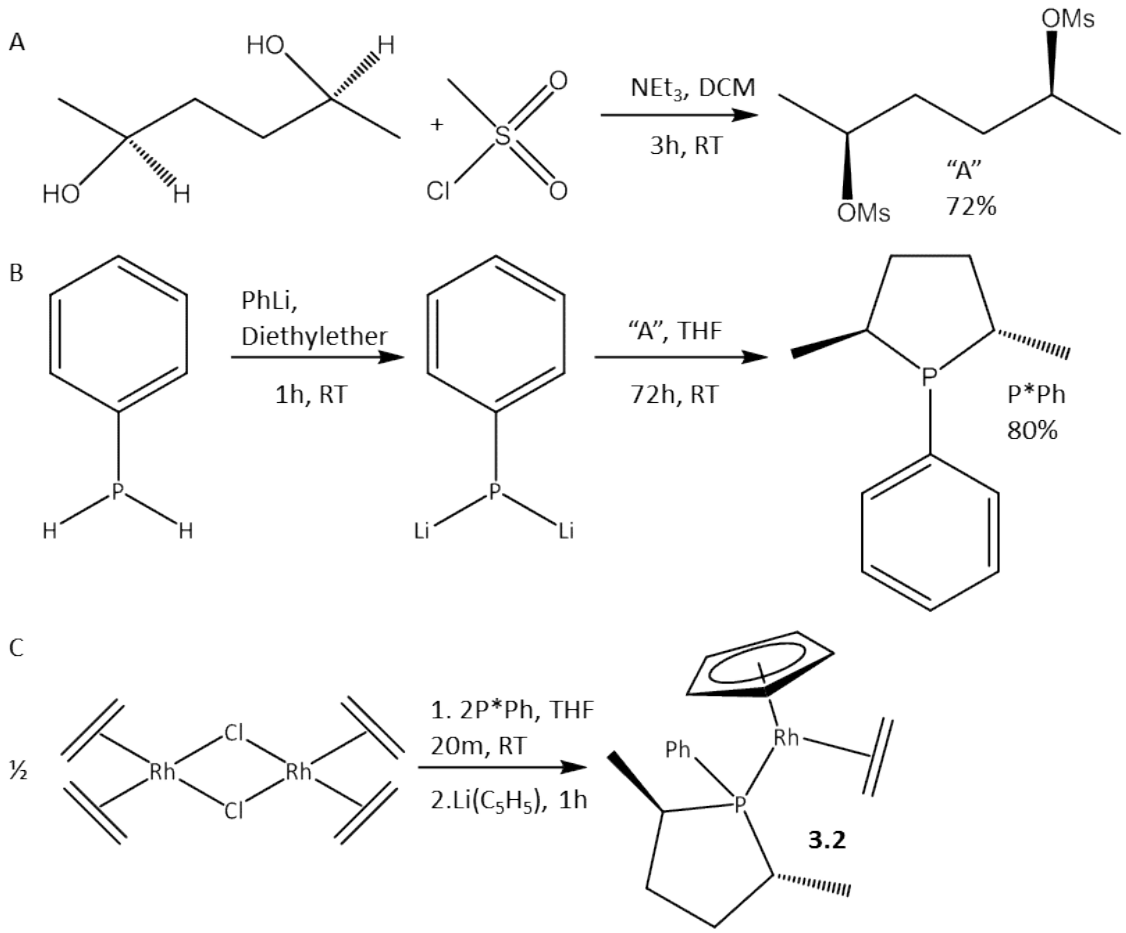

Figure 3.18: Synthetic route to form $[(\eta^5\text{-}C_5H_5)Rh(P^*Ph)(C_2H_4)]$ **3.1**.

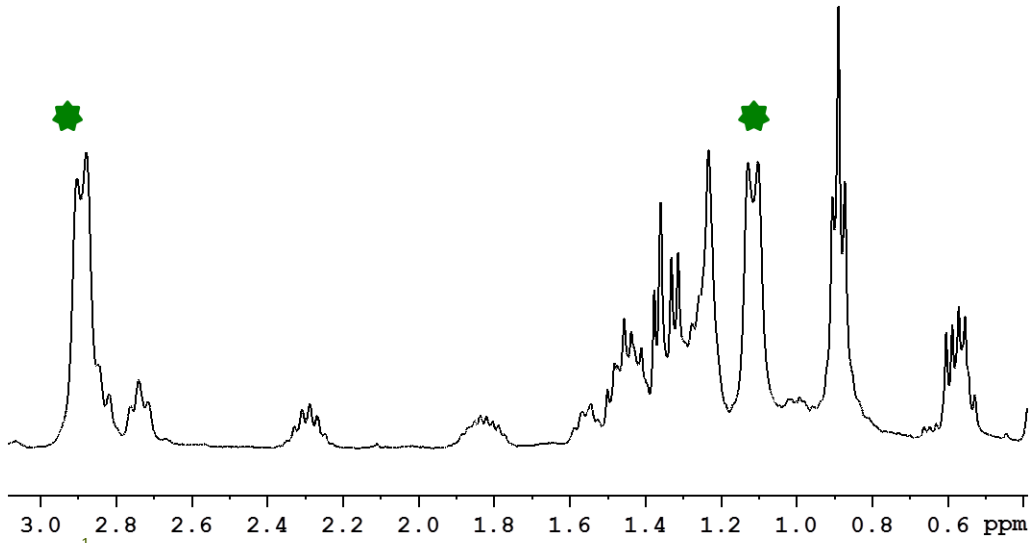

Figure 3.19: ^{1}H NMR spectrum of **3.2** in C_6D_6 at 298 K. Green stars denote resonances associated with $CpRh(C_2H_4)_2$.

3.5 NMR characterisation of **3.2**

A sample of the brown oil was prepared in C_6D_6 to allow for the characterisation of **3.2**. In the $^{31}P\{^1H\}$ spectrum there is a doublet at δ 75.0, J_{PRh} 203 Hz (Figure 3.20), this coupling is consistent with a Rh^I complex. A ^1H-^{31}P 2D HMQC was used to correlate this resonance with the proton resonances associated with the phosphine ligand. The ortho-proton was identified at δ 7.68 (t 8 Hz) which simplified to a doublet with phosphorus decoupling. This resonance showed a correlation in a $^1H\{^{31}P\}$-$^1H\{^{31}P\}$ 2D COSY NMR spectrum to a resonance at δ 7.08, a multiplet which was shown to corresponding to both the *meta* and *para* protons of the phenyl ring based on a later ^1H-^{13}C 2D HMQC measurement. The carbon-phosphorus couplings for each of these carbon environments were measured in a 1D $^{13}C\{^1H\}$ NMR spectrum to be 10.5, 8.7 and 2.5 Hz for the *ortho*, *meta* and *para* carbons respectively.

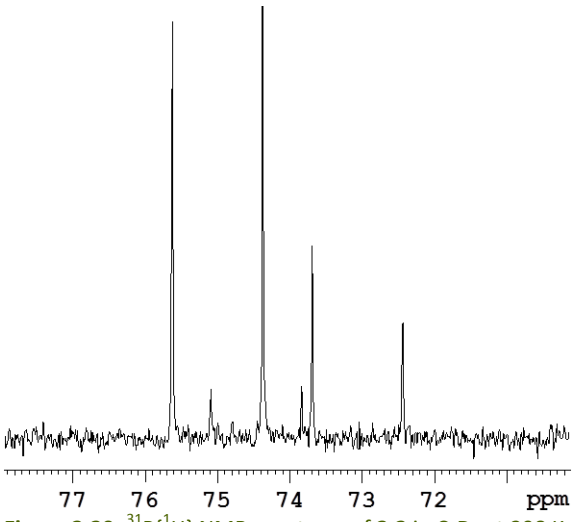

Figure 3.20: $^{31}P\{^1H\}$ NMR spectrum of **3.2** in C_6D_6 at 298 K.

The ^1H-^{31}P HMQC spectrum was also used to identify the methyl groups on the phospholane ligand as resonating at δ 0.57 (dd, J_{HP} 13.3, J_{HH} 6.6 Hz) and 1.34 (dd, J_{HP} 18.2, J_{HH} 7.2 Hz). A ^1H-^{13}C 2D HMQC was then used to correlate these proton resonances to the respective carbon resonance and a 1D $^{13}C\{^1H\}$ NMR spectrum used to determine the carbon-phosphorus coupling. The resonance at δ 0.57 showed a correlation to a carbon signal at δ 15.4 (s), and the signal at δ 1.34 to carbon resonance at δ 21.6 (d, 11.8 Hz). The methyl resonance at δ 0.57 was

assigned to position 8 and the methyl resonance at δ 1.34 to position 7 based on the literature values for these resonances.[6] The remaining resonances of the phospholane ring were identified using $^{1}H\{^{31}P\}$-$^{1}H\{^{31}P\}$ 2D COSY and NOESY NMR measurements, whilst the Cp ring was characterised as δ_H 5.09 (s), δ_C 85.9 (t, J_{CP} 3, J_{CRh} 3 Hz). These observations are summarised in Figure 3.21 and are in good agreement with the values in the literature.[6]

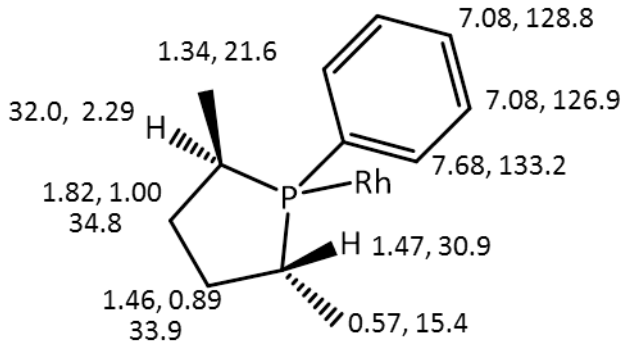

Figure 3.21: Summary of the ^{1}H and ^{13}C NMR chemical shifts for the coordinated phospholane ligand in **3.2**, Cp and ethene ligands omitted.

Finally, the coordinated ethylene ligand was identified as yielding two pairs of exchanging protons at δ 2.83 (t, 9.9, 10 Hz) and 1.30 (m) and δ 2.72 (t 9.7, 9.9 Hz) and 1.54 (m). The chirality of the phosphine accounts for there being four separate resonances. A ^{1}H-^{13}C HMQC measurements identified the two protons at δ 1.30 and 2.72 as being from one CH_2 group, with a carbon chemical shift of 24.1 (d, J_{CRh} 15 Hz) and the two protons at δ 1.54 and 2.83 as belonging to a second CH_2 group with a carbon chemical shift of 22.4 (d, J_{CRh} 15 Hz). The chemical shifts and multiplicities of these resonances are in agreement with the literature characterisation; however the assignments of the couplings are not. The ^{1}H resonances were characterised as having coupling to phosphorus, however, when $^{1}H\{^{31}P\}$ NMR spectra were acquired the multiplicities of these resonances were unchanged suggesting they do not containing phosphorus couplings. These couplings however are consistent with $^{3}J_{HH}$ couplings in an ethene ligand with four inequivalent protons. The $^{3}J_{HH}$ *trans* and *cis* couplings are of similar magnitude (~10 Hz) whilst the small $^{2}J_{HH}$ geminal coupling is contained within the broadness of the resonances. The carbon resonances for the coordinated alkene were also

reported to couple to phosphorus, this couplings are more likely to arise from the rhodium metal centre based on the rhodium-carbon couplings measured in Chapter 2. The full characterisation is detailed in Table 3.2.

3.6 Photochemistry of **3.2** with H_2 – to form **3.3**

3.6.1 Using broadband in-situ irradiation

It is known in the literature that the CpRh(P) intermediate may activate aromatic C–H such as those in benzene[2, 138, 141] therefore d_{12}-cyclohexane was chosen as to the solvent in the following photochemical reactions with **3.2**. To investigate whether **3.3** may form photochemically from **3.2** a sample was prepared in d_{12}-cyclohexane, which was degassed and 3 bar of H_2 was added. The sample was irradiated using the *in-situ* photolysis set up on the 400 MHz spectrometer (Experimental Section 8.3.3). The sample was irradiated for 10 minutes and hydride resonances consistent with the expected rhodium hydride started to appear at δ –14.1 (dd, J_{HRh} 36.6, J_{HP} 28.0 Hz) and –14.9 (dd, J_{HRh} 38.8, J_{HP} 28.2 Hz).[6] The sample was then degassed and refilled with *p*-H_2. In a series of proton NMR experiments, with a 45° pulse, the hydrides did not display the expected antiphase characteristics typical of PHIP signals.[14] The sample was then photolysed for further 55 minutes and during this time the two hydride resonances grew in intensity. In addition, a new resonance started to form in the $^{31}P\{^1H\}$ NMR spectrum (Figure 3.23), a doublet at δ 85.6 (J_{PRh} 160 Hz). The ^1H and ^{31}P resonances are consistent with the literature values for **3.3**.[6] In addition to this product there were many new peaks in the Cp region of the spectrum and a broad resonance in the hydride region of the spectrum at δ –13.9. A second new phosphorus signal at δ 80.8 (d, J_{PRh} 190 Hz) is also seen suggesting that **3.3** is not cleanly formed through the photochemical reaction of **3.2** and H_2.

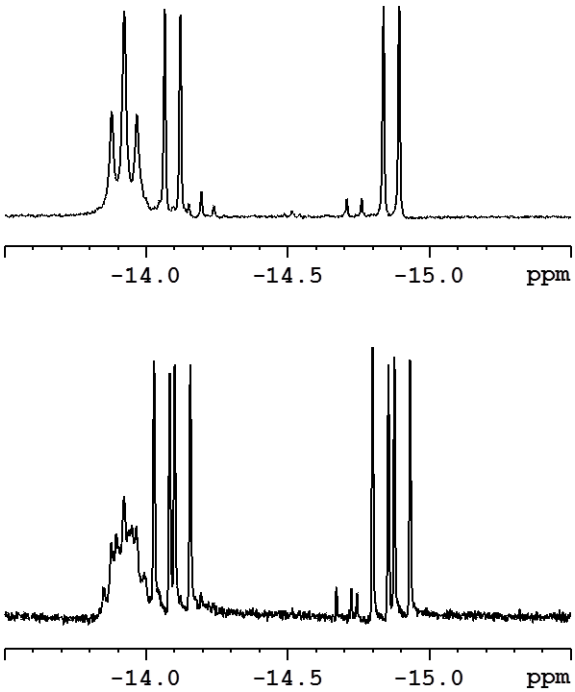

Figure 3.22: Hydride region of the ^{1}H (bottom) and $^{1}H\{^{31}P\}$ (top) NMR spectra at 298 K in d_{12}-cyclohexane following the irradiation of **3.2** in the presence of H_2.

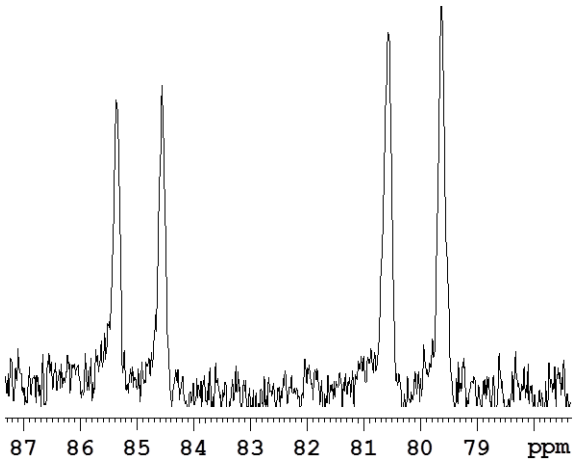

Figure 3.23: $^{31}P\{^{1}H\}$ NMR spectrum at 298 K in d_{12}-cyclohexane of **3.3** and **3.4** formed from the irradiation of **3.2** in the presence of H_2.

3.6.2 NMR characterisation of **3.3**

The defining features of the ^{1}H NMR spectrum of **3.3** are two hydride resonances at δ −14.1 and −14.9. In a ^{1}H-^{31}P 2D HMQC experiment these resonances showed correlations to the phosphorus resonance at δ 85.6 (d, J_{PRh} 160 Hz), which also shows correlations to proton resonances at δ 0.66, 1.24, 1.91 and 2.13 which are consistent with the methyl and methine groups adjacent to the phosphorus resonance. The two hydrides are both doublet of doublets

with couplings constants consistent with coupling to the rhodium metal centre and to the phosphorus of the phosphine ligand. No couplings consistent with proton-proton couplings were observed, nor were they reported in the literature characterisation of this complex.[6] The hydride resonances are reasonably sharp with linewidths of 3.5 Hz, measured at half height with no line broadening applied. This indicates that, if there is, coupling between these two protons it is small and could potentially be responsible for the lack of PHIP enhanced signals since coupling between the protons in *p*-H_2 must be retained in the product for PHIP signals to be observed.[14] Proton-proton coupling is usually related to the bond angle between the two protons,[142] this could be responsible for the lack of a measureable coupling between these two signals.

To investigate whether there is coupling between these protons a ^{1}H-^{1}H COSY was recorded. Using a standard COSY pulse sequence no cross peaks between the two hydrides were observed, consistent with the proton spectrum that there is not significant coupling between the hydrides. An alternative COSY pulse sequence was then chosen, one designed to detect longer-range couplings, which are typically small. If there is a small coupling between these two hydrides the use of this pulse sequence should reveal them. When a minimum delay, τ, of 150 ms was employed a cross peak was observed (Figure 3.24), which confirms the existence of a H–H coupling.

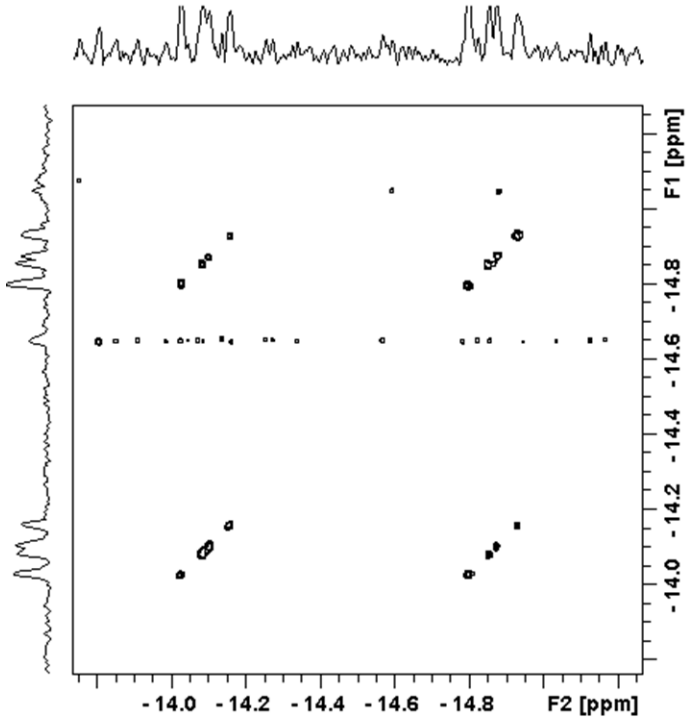

Figure 3.24: ^{1}H-^{1}H COSY NMR spectrum of the hydride region following the reaction of 3.2 with H_2 recorded at 298 K in d_{12}-cyclohexane.

To measure the coupling between the two hydride resonances a series of 1D COSY experiments were recorded with delay times which relate to scalar couplings from 1 Hz to 7 Hz using a 1/4J relationship. The experiment was set up to irradiate the proton resonance at δ −14.1. As the time delay decreased, the intensity of this resonance reduced and the second hydride resonance increased (Figure 3.25). The integral of the δ –14.9 proton, relative to the integral of the δ –14.0 proton, was plotted against the scalar coupling revealing the coupling to be approximately 2 Hz (Figure 3.26). This coupling is consistent with the value obtained for **3.1** and should be sufficient to allow for PHIP enhancements to be visible. To test this value, the ^{1}H NMR spectrum was simulated using g-NMR (Figure 3.27) first using standard NMR methods to determine if the 2.8 Hz coupling is consistent with the measured NMR spectrum (middle). The PHIP-enhanced spectrum was then simulated using the same coupling constants and antiphase resonances should be detected.

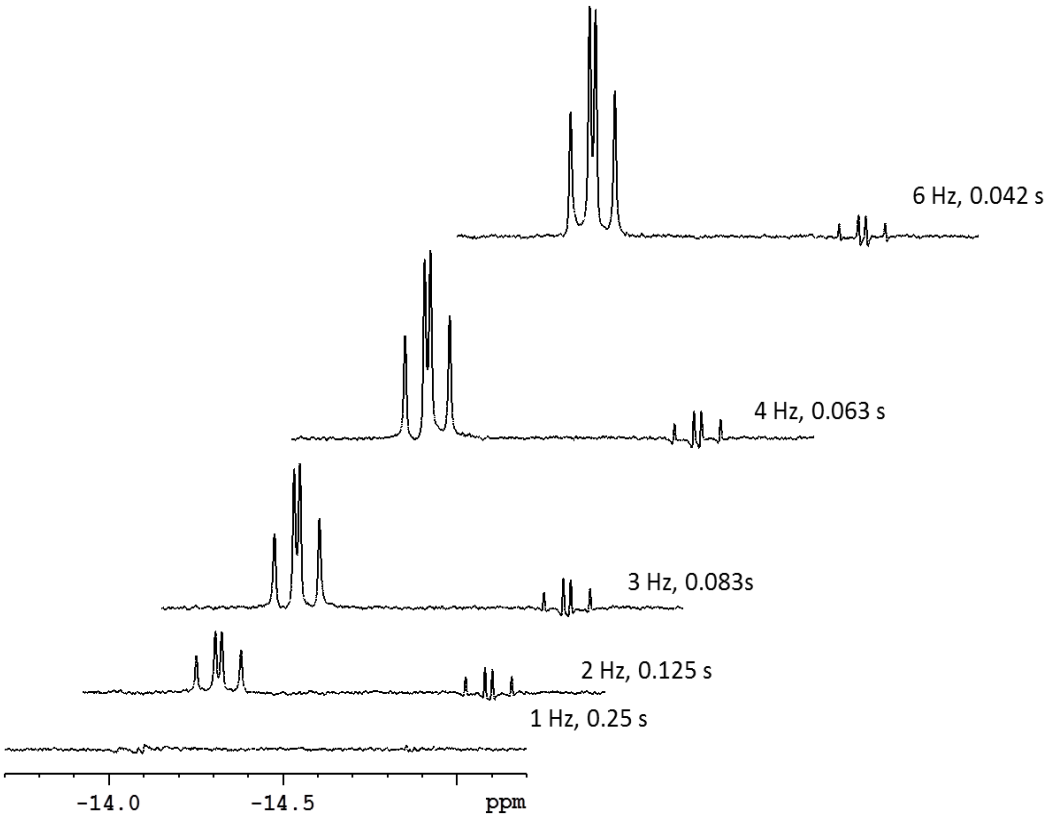

Figure 3.25: ^{1}H 1D COSY NMR spectra with incrementing delays.

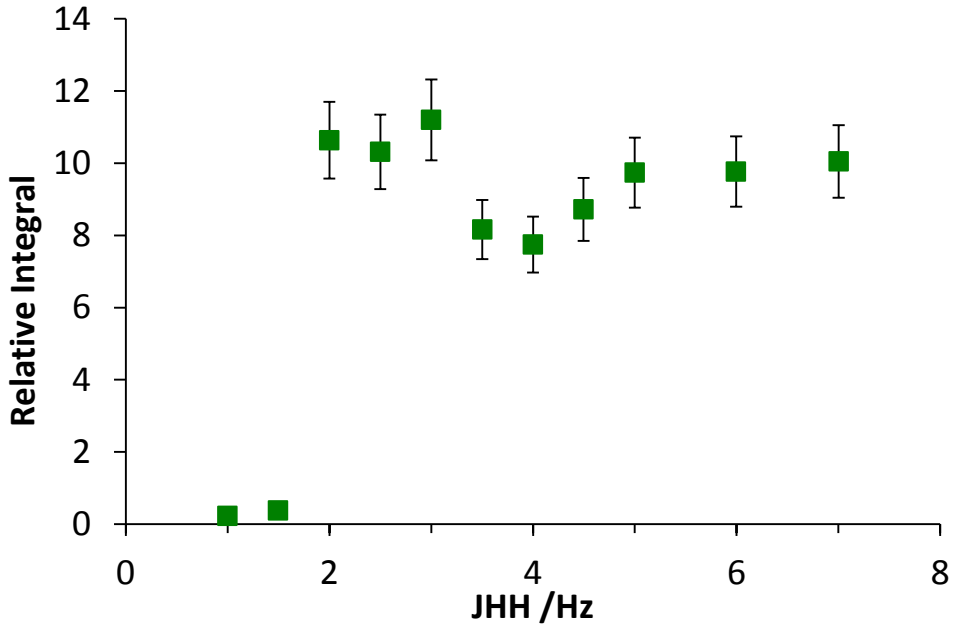

Figure 3.26: Hydride Integral against scalar coupling J_{HH}.

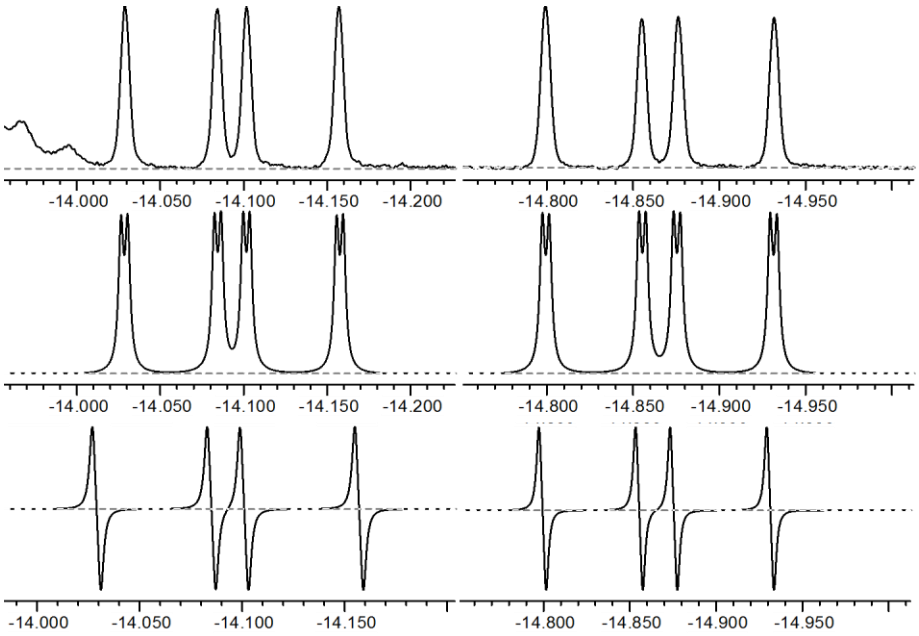

Figure 3.27: (top) ^{1}H NMR spectrum of **3.3** (middle) simulation of ^{1}H NMR spectrum (bottom) simulation of ^{1}H NMR spectrum with PHIP enhancements.

3.6.3 NMR characterisation of **3.4**

The broad resonance at δ –13.2 resolves to be a triplet with phosphorus decoupling, J_{HRh} 22 Hz. It also shows a correlation to the phosphorus resonance at δ 80.8 (d J_{PRh} 190 Hz). This complex is associated with a cyclopentadienyl resonance at δ_H 4.52, δ_C 85.1 but the characterisation of the coordinated phospholane ligand was not possible due to significant overlap with **3.2** and **3.3** in this region of the spectrum. The triplet multiplicity in the ^{1}H{^{31}P} NMR spectrum suggests that the hydrides couple to two rhodium centres and the observed coupling constant is consistent with bridging hydride ligands between two rhodium centres.[74] A proposed structure for this species is shown in Figure 3.28 although, with full characterisation not being possible, this is speculative.

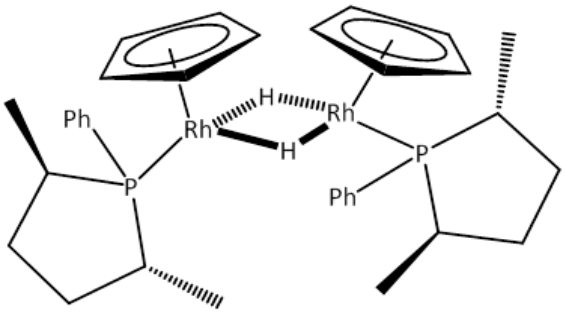

Figure 3.28: Proposed structure of **3.4**.

3.6.4 In-situ irradiation with a 355 nm light using a Nd:YAG laser

Since it was determined that there is a coupling between the two hydrides in **3.3** and that this should be sufficient to allow PHIP enhanced spectra to be acquired, this complex was next studied using the laser based *in-situ* photochemistry set up. An optically dilute sample of **3.2** in d_{12}-cyclohexane was prepared. The sample was then degassed and backfilled with 3 bar *p*-H_2 and studied using the laser-based *in-situ* photolysis setup (Experimental Section 8.3.2). The sample was then irradiated with single laser pulse and multiple laser pulse experiments to see if any PHIP enhanced resonances formed. No such resonances were observed. The number of laser pulses was then increased to account for 30 seconds irradiation and the proton and phosphorus spectra were analysed in order to observe the reaction using standard NMR methods. This was repeated a second time and no changes were evident. This complex was not studied further.

It has been reported on the basis of EXSY experiments that the two hydrides are in exchange with one another via a η^2-H_2 intermediate.[6] This could provide a route to relaxation quenching of any PHIP enhancements. A ^{1}H-^{1}H EXSY experiment was acquired which shows exchange cross peaks between the two hydride resonances. Each of the separate components only have one cross peak indicating that the couplings are retained in the exchange process confirming that it is an intramolecular exchange process. The T_1 values of the hydrides were measured to see if the dihydrogen intermediate significantly impacts on the relaxation of the hydride magnetisation. Using an inversion recovery approach the T_1 values for both hydrides were determined to be 564 ± 9 and 662 ± 10 ms, indicative of a dihydride species.[53, 54] This rules out the exchange pathway itself from causing spin relaxation. However, if the lifetime of the initial dihydrogen ligand during the oxidative addition process is comparable to the relaxation time of the former singlet state, the PHIP enhancements could still be quenched. The former

parahydrogen singlet state may also be quenched if the intermediate has a triplet ground state.

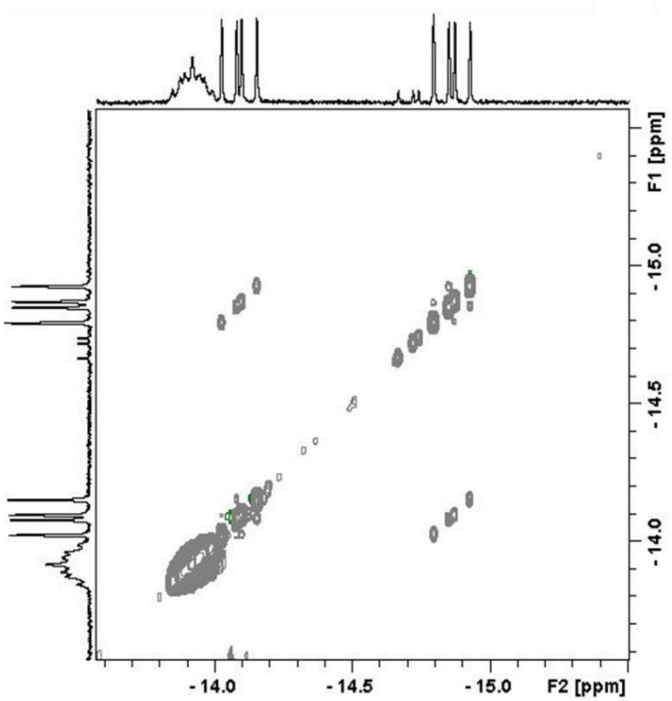

Figure 3.29: ^{1}H-^{1}H 2D EXSY NMR spectrum of **3.3** in d_{12}-cyclohexane at 298 K using a 0.2 second mixing time.

3.7 Conclusions

$[(\eta^5\text{-}C_5H_5)Rh(\eta^2\text{-}CH_2CHSi(CH_3)_3)_2]$ **2.1** has been studied with parahydrogen using *in-situ* photolysis with 355 nm light using a Nd:YAG laser coupled to a wide-bore 600 MHz spectrometer. With multiple laser pulses at 263 K, two PHIP enhanced hydride resonances were observed at δ –13.5 which correspond to the complex $[(\eta^2\text{-}C_5H_5)Rh(H)_2(\eta^2\text{-}CH_2CHSi(CH_3)_3)]$ **3.1** containing two chemically inequivalent hydrides. This species has previously been observed in York following continuous irradiation with a He-Cd cw laser at 203 K using a 400 MHz spectrometer.[74] The profiles of the hydride resonances were compared and discrepancies were observed. Repeating these experiments at variable temperatures revealed that the differences resulted from temperature effects.

It was found that with increasing number of laser pulses, the enhancements in **3.1** initially increased with the number of laser pulses before reaching a plateau. This can be explained by

a combination of there being more molecules of **2.1** forming **3.1** and therefore increasing the concentration and the resulting signal of **3.1**. The terms associated with *p*-H_2 relax in the same way as regular terms in NMR spectroscopy. This relaxation begins from the moment the *p*-H_2 adds to the metal complex and its symmetry is broken. When more laser pulses are used, there is a longer time period for the former parahydrogen terms to relax before they are interrogated by the NMR pulse. These two factors are in balance at the plateau where the formation of the new product approximately matches the relaxation.

The formation of **3.1** was next studied as a function of the pump-probe delay. Two samples were analysed, one with a sub-stoichiometric quantity of trimethylvinylsilane and a second with a 15 fold excess of trimethylvinylsilane. These revealed that with short pump-probe delays (<0.1 s) there is growth period this is followed by an exponential decay in the signal enhancement reflecting the relaxation of the former parahydrogen singlet state. The time constant for this relaxation (T_1) was 1.89 $\pm$ 0.18 s for the sample without an excess of trimethylvinylsilane and 1.00 $\pm$ 0.09 s with an excess of the ligand. This difference is thought to be due to the presence of water in the sample with an excess of trimethylvinylsilane. There is also a difference in the concentrations of **2.1** which could also contribute.

Control experiments were also performed with both samples, which revealed that whilst the presence of trimethylvinylsilane provides some stabilisation of the starting material there is still a significant drop in enhancement. This would also suggest that the product is less photoactive at 355 nm than the starting material.

[(η^5-C_5H_5)Rh(η^2-$CH_2CHSi(CH_3)_3$)(DMSO)] **2.4** was also studied with parahydrogen as the DMSO ligand was found to be photolabile in Chapter 2. A sample of **2.4** in d_8-toluene was investigated with *p*-H_2 using the same approach used with **2.1**. A PHIP-enhanced hydride resonance consistent with **3.1** was formed, however, the enhancement observed was notably less than

when **2.1** was used as the precursor. This would suggest that DMSO would not be an appropriate alternative precursor for the formation and study of **3.1**.

In the product **3.1**, the symmetry of the two hydrides is broken as a result of the trimethylsilane substituent on the bound alkene. This effect is small and the chemical shift difference is negligible (only 0.1 ppm at 220 K). [(η^5-C_5H_5)Rh(P*Ph)(C_2H_4) **3.2** was synthesised as it has been found to be a thermal precursor to [(η^5-C_5H_5)Rh(H)$_2$(P*Ph)] **3.3**.[6] The hydride resonances in this complex were reported to have ^{1}H chemical shifts of δ –13.71 and –14.47, a much more significant chemical shift difference than in **3.1**.

Firstly, to determine whether **3.3** can form photochemically from **3.2**, an NMR sample of **3.2** was prepared in d_{12}-cyclohexane. This was irradiated for 55 minutes under 3 bar of H_2 *in-situ* using broadband UV light and the expected hydride resonances were observed and a phosphorus resonance at δ 85.6 (d, J_{PRh} 160 Hz) consistent with the reported values for **3.3**. The proton-proton coupling was not observed in the hydride resonances, nor were they reported in the literature.[6] If the two hydrides do not couple to one another, it will inhibit the observation of PHIP enhancements. Using 1D and 2D COSY methods, it was determined that the two hydrides do exhibit a coupling to one another and that this coupling is approximately 2.0 Hz. This should be sufficient to allow PHIP enhanced spectra to be observed. This was confirmed by simulations in g-NMR. The complex was next studied using *in-situ* photolysis with 355 nm of light from a Nd: YAG laser and PHIP enhanced spectra were not observed. Possible explanations for this are the lifetime of the dihydrogen ligand during the oxidative addition process or the electronic state of the intermediate.

A second novel product was identified; this was associated with a broad resonance at δ –13.2 which resolved to be a triplet (J_{HRh} 22 Hz) following phosphorus decoupling. The NMR characteristics are consistent with a hydrogen bridged species [{(η^5-C_5H_5)Rh(P*Ph)(μ-H)}$_2$] **3.4** although full characterisation was not possible.

These studies have provided considerable insight into the requirements for *in-situ* photochemical reactions with parahydrogen which will be useful if further experimental designs. The study into the formation of **3.1** from **2.1** as a function of the pump-probe delay demonstrated that this *in-situ* NMR method can be used to detect the formation of thermally unstable products. The growth period at pump-probe delays <0.1 s would indicate that this technique could be used on reactions which occur on the subsecond or shorter timeframes. One of the motivations for using parahydrogen with this work was to investigate whether parahydrogen could be transfer to other ligands within the reaction products. The observation that the T_1 for the $2I_zS_z$ term of **3.1** is approximately one second provides a time limit for detection. The results in this chapter have also provided insights into the requirements in complex selection for *in-situ* NMR with parahydrogen detection. The study into the activity of **3.1** highlighted that the photoactivity of the product is important whilst the reaction between **3.2** and parahydrogen highlighted the lifetime of any dihydrogen transition state or intermediate can quench any parahydrogen enhancement.

3.8 NMR Data

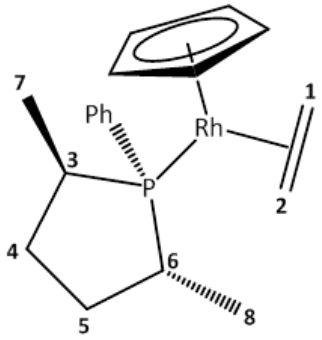

Figure 3.30: Structure of **3.2** with positions labelled.

Table 3.2: NMR Characterisation for [(η^5-C_5H_5)Rh(P*Ph)(C_2H_4)] **3.2**.

	δ/ppm (multiplicity, integration)	Coupling constant/Hz	Assignment	Group
^{1}H	7.68 (t, 2H)	J_{HP} 8, J_{HH} 8	*o*-H	P-(Ph)
	7.08 (m, 3H)		*m*-H & *p*-H	P-(Ph)
	5.08 (s, 5H)		$C_5\underline{H}_5$	Cp
	2.83 (t, 1H)	J_{HH} 10	$^1C\underline{H}_2$	C_2H_4
	2.72 (t, 1H)	J_{HH} 10	$^2C\underline{H}_2$	C_2H_4
	2.29 (m, 1H)		$^3C\underline{H}$	Phosphine
	1.82 (m, 1H)		$^4C\underline{H}_2$	Phosphine
	1.54 (m, 1H)		$^1C\underline{H}_2$	C_2H_4
	1.47 (m, 1H)		$^6C\underline{H}$	Phosphine
	1.46 (m, 1H)		$^5C\underline{H}_2$	Phosphine
	1.34 (dd, 3H)	J_{HP} 18.2, J_{HH} 7.2	$^7C\underline{H}_3$	Phosphine
	1.30 (m, 1H)		$^2C\underline{H}_2$	C_2H_4
	1.00 (m, 1H)		$^4C\underline{H}_2$	Phosphine
	0.89 (m, 1H)		$^5C\underline{H}_2$	Phosphine
	0.57 (dd, 3H)	J_{HP} 13.3, J_{HH} 6.6	$^8C\underline{H}_3{}^8$	Phosphine
^{13}C	133.2 (d)	J_{CP} 10.5	*o*-C	P-(Ph)
	128.8 (d)	J_{CP} 2.5	*p*-C	P-(Ph)
	126.9 (d)	J_{CP} 8.7	*m*-C	P-(Ph)
	85.9 (t)	J_{CP} 3, J_{CRh} 3	$\underline{C}_5H_5$	Cp
	34.8 (s)		$^4\underline{C}H_2$	Phosphine
	33.9 (s)		$^5\underline{C}H_2$	Phosphine
	32.0 (d)	J_{CP} 27	$^3\underline{C}H$	Phosphine
	30.9 (d)	J_{CP} 25	$^6\underline{C}H$	Phosphine
	24.1(d)	J_{CRh} 15	$^2\underline{C}H_2$	C_2H_4
	22.4 (d)	J_{CRh} 15	$^1\underline{C}H_2$	C_2H_4
	21.6 (d)	J_{CP} 12	$^7\underline{C}H_3$	Phosphine
	15.4 (s)		$^8\underline{C}H_3$	Phosphine
^{31}P	75.0 (d)	J_{PRh} 203	P	Phosphine

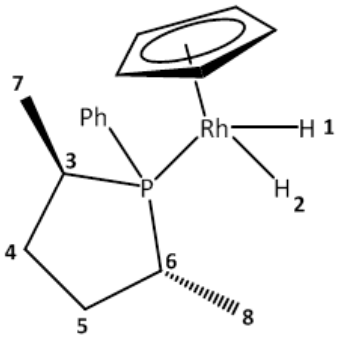

Figure 3.31: Structure of **3.3** with positions labelled.

Table 3.3:NMR Characterisation for [(η^5-C_5H_5)RhH_2(P*Ph)] **3.3**.

	δ/ppm (multiplicity, integration)	Coupling constant/Hz	Assignment	Group
^{1}H	–14.1 (dd, 1H)	J_{HRh} 28 J_{HP} 36	H_1	Rh–H
	–14.9 (dd, 1H)	J_{HRh} 28 J_{HP} 38	H_2	Rh–H
	2.13 (overlap)		CH/CH_3	Phosphine
	1.91 (overlap)		CH/CH_3	Phosphine
	1.24 (overlap)		CH/CH_3	Phosphine
	0.66 (overlap)		CH/CH_3	Phosphine
^{31}P	84.9 (d, 1P)	J_{PRh} 160	P	Phosphine

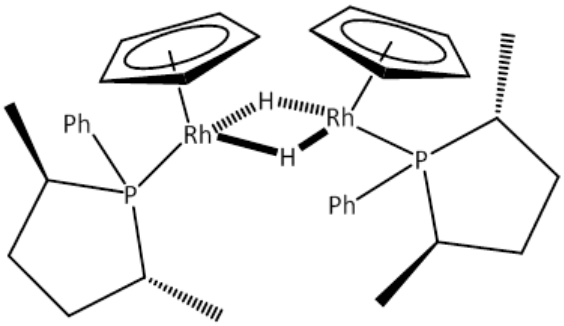

Figure 3.32: Structure of **3.4** with positions labelled.

Table 3.4: NMR Characterisation for [(η^5-C_5H_5)Rh(P*Ph)(μ-H)]$_2$ **3.4**.

	δ/ppm (multiplicity, integration)	Coupling constant/Hz	Assignment	Group
^{1}H	4.52 (s, 5H)		C_5H_5	Cp
	–13.9 (m, 2H)	J_{HRh} 22	Rh-H	Rh-H-Rh
^{13}C	85.0		C_5H_5	Cp
^{31}P	80.1 (d, 2P)	J_{PRh} 190	P	Phosphine

4 Photochemistry of $[(\eta^5\text{-}C_5H_5)Rh(alkene)_2]$ with phenyl methyl sulfoxide

4.1 Introduction

In Chapter 2 the reactivity of $[(\eta^5\text{-}C_5H_5)Rh(\eta^2\text{-}CH_2CHSi(CH_3)_3)_2]$ (**2.1**), $[(\eta^5\text{-}C_5H_5)Rh(\eta^2\text{-}C_8H_{14})_2]$ (**2.2**) and $[(\eta^5\text{-}C_5H_5)Rh(\eta^4\text{-}C_8H_{12})]$ (**2.3**) were investigated with DMSO. For **2.1** and **2.2** this resulted in the loss of one of the alkene ligands and the coordination of DMSO; **2.3** however, did not show any reactivity towards DMSO. The reactivity of the photoproduct formed from **2.1** and DMSO, $[(\eta^5\text{-}C_5H_5)Rh(\eta^2\text{-}CH_2CHSi(CH_3)_3)(DMSO)]$, **2.4** towards triethylsilane and trimethylvinylsilane was then studied and its DMSO ligand was found to be labile. This prompted the study of **2.4** with parahydrogen to investigate whether the loss of DMSO in **2.4** provided a more efficient route to the intermediate than the analogous process from **2.1**. The purpose of this study was to see whether the observations seen with DMSO are replicated with other sulfoxides. Of particular interest was whether phenyl methyl sulfoxide coordiates to the metal centre and if it did coordinate, would it be photolabile and how would this activity compare to that of DMSO and the respective alkene ligands. In this Chapter, the reactivity of **2.1** and **2.2** with phenyl methyl sulfoxide is described. This sulfoxide has two different substituents and, owing to the lone pair on the central sulfur atom, they are chiral (Figure 4.1).[143]

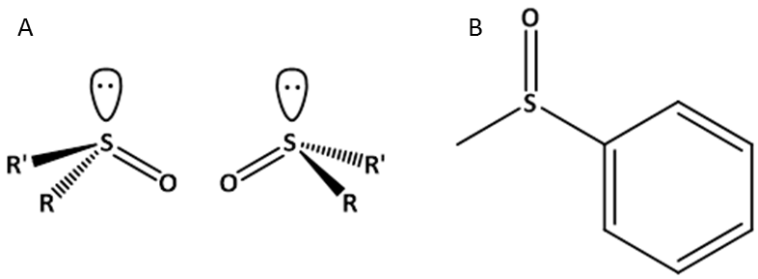

Figure 4.1: (A) Structures of the two enantiomers of sufoxides when R≠R' (B) Phenyl methyl sulfoxide.

Chirality is generally associated with organic molecules but it is also observed in organometallic systems. There are three types of chirality commonly associated with

organometallic complexes. These are centred,[144] planar[144-146] and helical chirality[147, 148], as outlined in Figure 4.2.[147, 149] The combination of two chiral centres in a molecule gives rise to diastereomers. Diastereomers are a form of structural isomers, but unlike enantiomers, they are not mirror images of one another and consequently they can have different chemical and physical properties. This means they are distinguishable by NMR spectroscopy.[149]

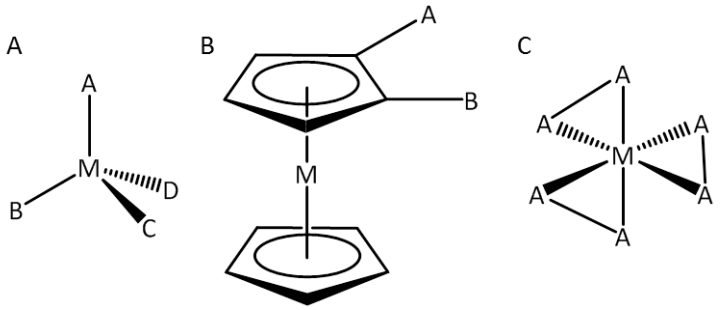

Figure 4.2: Three different types of chirality seen in organometallic systems (A) Centred chirality, (B) Planar chirality; A≠B and (C) Helical chirality.

One further reason for looking at these systems was to create a dihydride with magnetically distinct hydride ligands in a photoproduct containing an asymmetric sulfoxide (Figure 4.3). Unfortunately, this proved unsuccessful and these studies will not be described further. Nevertheless, reactivity of **2.1** and **2.2** was observed towards phenyl methyl sulfoxide and this will be now be described.

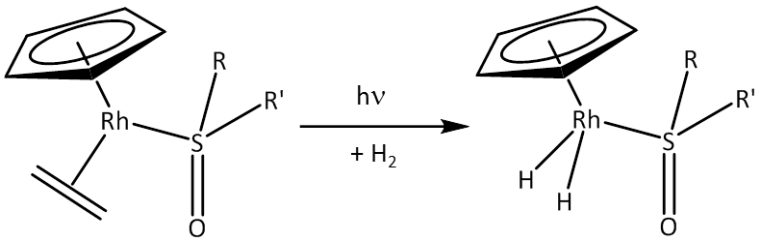

Figure 4.3: Hypothesised reaction between sulfoxide products and H_2.

4.2 Photochemistry of **2.2** with PhSOMe

First, the reaction of **2.2** and phenyl methyl sulfoxide is discussed. **2.2** contains a symmetrical alkene and therefore only one product is expected by NMR spectroscopy (Figure 4.4). The

impact of the asymmetric sulfoxide is likely to be observed, however, in the coordinated cyclooctene ligand with the two CH groups being inequivalent.

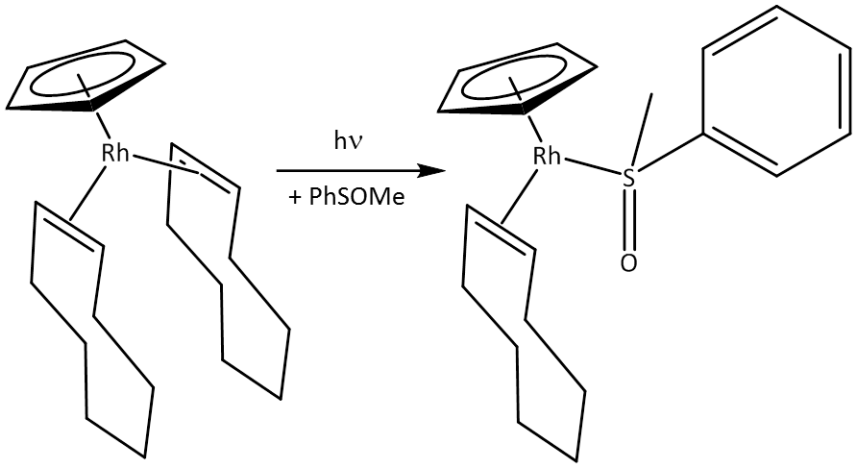

Figure 4.4: Proposed reaction between **2.2** and PhSOMe.

First to check that the sulfoxide would not absorb UV light preferentially over the rhodium complex the UV-vis spectra of **2.2** and PhSOMe were acquired in C_6H_6 (Figure 4.5). It was found that at wavelength of light not cut of by the glass **2.2** is a stronger absorber and therefore, a sample containing 3.3 mg of **2.2** and was prepared 9 mg of PhSOMe. This provided a 7.4 fold excess of the free ligand relative to the rhodium complex. This was then irradiated for 45 minutes *ex-situ* using a broadband UV lamp. The reaction was followed by ^{1}H NMR spectroscopy and a single product was formed (Figure 4.6), based on there being one new Cp resonance at δ 4.98. Characterisation by NMR spectroscopy revealed this product to be the expected monosubstitution product CpRh(COE)(PhSOMe) **4.1** (Figure 4.4) and no evidence of the bis sulfoxide complex, $CpRh(PhSOMe)_2$, was observed. A ^{1}H NMR spectrum of PhSOMe was also recorded to check for any impurities in the sulfoxide and none were detected.

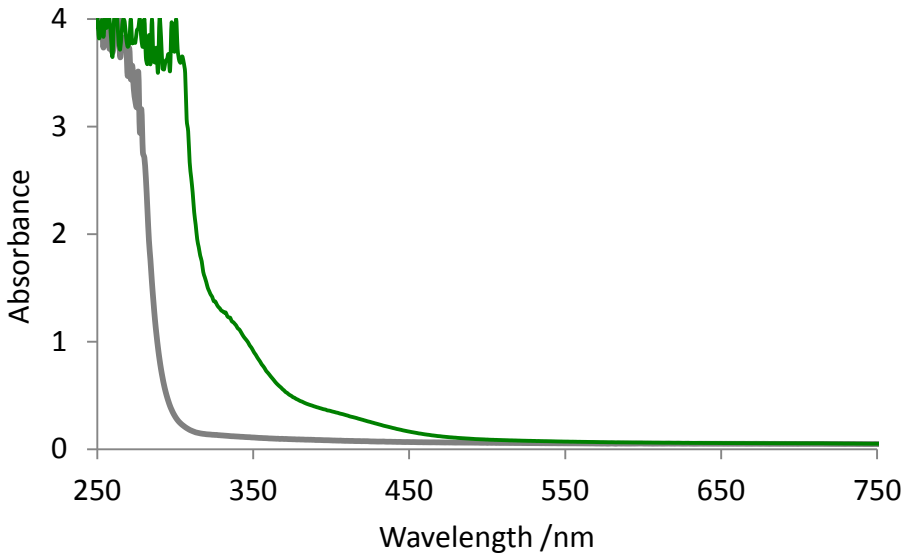

Figure 4.5: UV-Visible spectra of 3.4 mg of **2.2** and 37 mg PhSOMe, in 0.5 mL C_6H_5

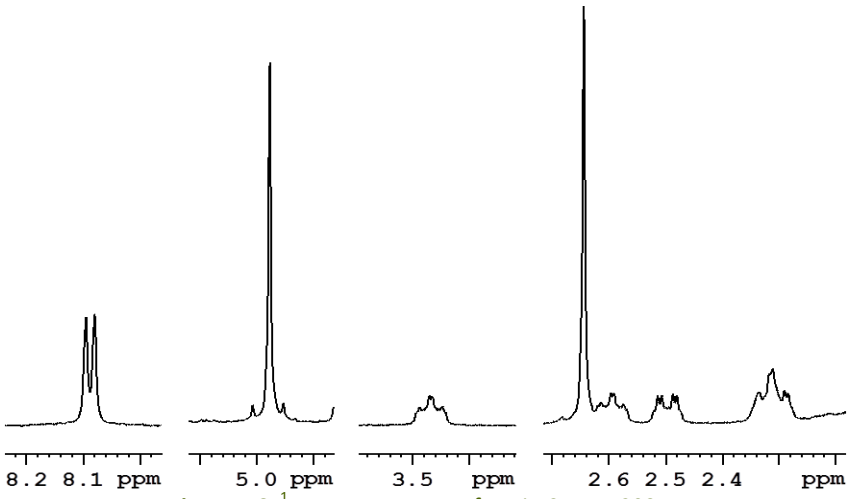

Figure 4.6: ^{1}H NMR spectrum of **4.1** in C_6D_6 at 298 K.

In addition to the Cp resonance, there is a singlet at δ 2.64 (Figure 4.6) corresponding to three protons suggesting that this corresponds to the methyl group of the sulfoxide. A 0.6 ppm chemical shift difference was seen between this resonance and free PhSOMe (δ_H 2.03, δ_C 43.5) which indicates that the ligand coordinates through sulfur rather than oxygen.[131] This is corroborated by the carbon data for these resonances, in a 2D ^{1}H-^{13}C HMQC measurement the bound methyl peak shows correlation to a carbon environment at δ 57.8, downfield from the free ligand which is also in keeping with a sulfur-binding mode.[57, 132] The methyl resonance at δ 2.64 shows an nOe to a proton at δ 8.08 and is consistent with the *ortho* position on the

phenyl ring of the bound sulfoxide. Both the methyl resonance and the *ortho* proton exhibit nOe correlations to the cyclopentadienyl ligand confirming the coordination of the sulfoxide in the rhodium product.

Other noteworthy resonances correspond to the coordinated alkene. There are two broad triplet resonances at δ 3.47 (H_{1a}) and 2.60 (H_{1b}); which show correlations to separate carbon environments at δ 61.3 (d J_{CRh} 15.7 Hz) and 60.4 (d J_{CRh} 15.5 Hz) in a ^{1}H-^{13}C HMQC spectrum. This would suggest that these signals correspond to a bound alkene protons of the cyclooctene ring. These two positions are now distinct from one another owing to the asymmetry on the sulfoxide (Figure 4.7). Both H_{1a} and H_{1b} contain two 10 Hz couplings, reflecting the coupling between themselves and to the corresponding equatorial protons of position 2 (H_{2a} and H_{2b}). Using COSY and NOESY correlations H_{2b} was identified a broad triplet of triplets at δ 2.31 with 11 Hz couplings reflecting coupling between itself and both H_{1b} and $H_{2b'}$. Smaller couplings are hidden in the broadness of this signal. Its partner proton, $H_{2b'}$ was identified, using correlations in a ^{1}H-^{13}C HMQC, as a signal at δ 1.67. In this case the multiplicity could not be determined due to overlap with other signals. The signals associated with H_{2a} and $H_{2a'}$ were identified as δ 2.50 and δ 1.62 using COSY and NOESY correlations. The resonance at δ 2.50 is a doublet of quartets (J_{HH} 13, 3.5 Hz), since there is only one large coupling matching a ^{2}J coupling between methylene protons, this proton can be assigned as $H_{2a'}$, leaving δ 1.62 as H_{2a}. Overlap with other resonances obscured the multiplicity of this resonance. These observations are summarised in Figure 4.7. nOe correlations between the COE resonances and the *ortho* proton of the sulfoxide's phenyl resonance were also observed. In combination, these features support the characterisation of this product as [(η^{5}-C_5H_5)Rh(η^{2}-C_8H_{14})((Ph*S*(O)Me)] **4.1**, see Figure 4.29 for the structure and Table 4.10 for the full details of its NMR characterisation.

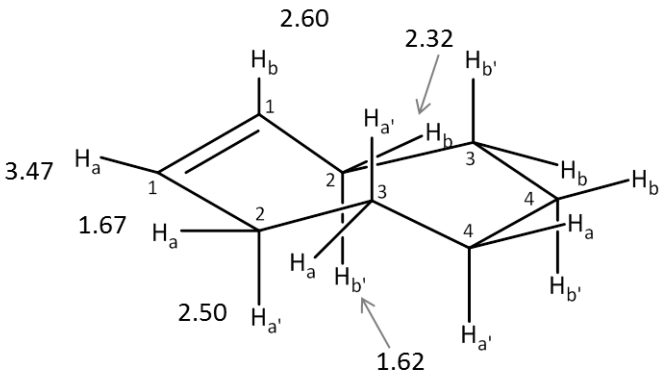

Figure 4.7: Assignments of the unique position on the coordinated COE ligand in **4.1** and its ^{1}H chemical shifts.

Having characterised the product, the series of ^{1}H NMR spectra recorded during the irradiation period were analysed using the procedure outlined in Experimental Section. The relative amounts of **2.2** and **4.1** were plotted against the irradiation time revealing the formation of a photostationary state comprising 60% **4.1** and 20% **2.2**; approximately 20% decomposition was observed also. The identity of the decomposition product was identified, there was a darkening of the reaction solution and some brown precipitate was observed which would indicate that a substance has formed which is not soluble in benzene. This process may be modelled using relaxation kinetics and the principles of this are described in the Appendix.

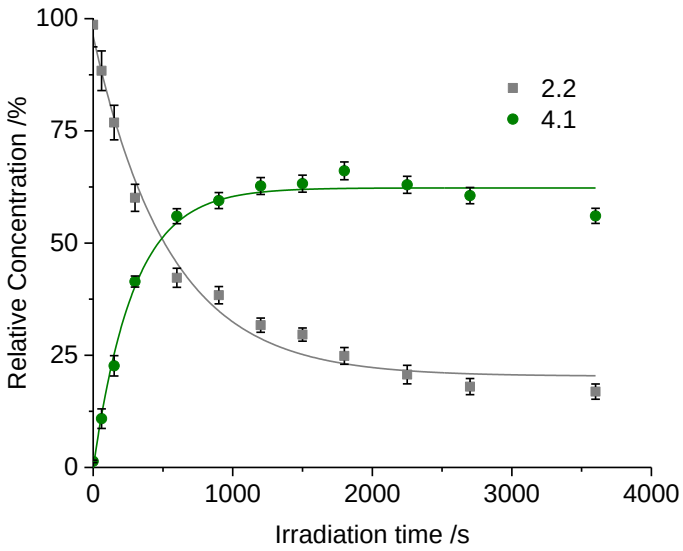

Figure 4.8: Time profile showing the changes in concentration of 2.2 and 4.1 following irradiation of **2.2** in the presence of PhSOMe, these were fitted to Equation (4.7), the results of which are given in

Table 2.11.

This reaction could follow the behaviour of a single step, bimolecular, process based on the kinetic model A described by Figure 4.9, in which case it would be associated with an equilibrium constant, K_{eq}, of 0.39 ± 0.06 using the equilibrium concentrations (Equation (4.1)). Or alternatively, the reaction could be zeroth order with respect to the concentration of the sulfoxide, as was seen with **2.1** and DMSO in Section 2.5, in which case the kinetic model B should be used instead and K_{eq} is now (5.78 ± 0.88) x10^{-2} using Equation (4.2).

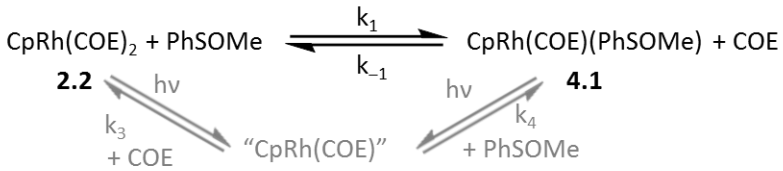

Figure 4.9: Kinetic Model A for the reaction between **2.2** and PhSOMe.

$$K_{eq} = \frac{k_1}{k_{-1}} = \frac{[4.1]_{eq}\,[COE]_{eq}}{[2.2]_{eq}[PhSOMe]_{eq}} = \frac{\varepsilon_{2.2}\Phi_{2.2}k_3}{\varepsilon_{4.1}\Phi_{4.1}k_2} \quad (4.1)$$

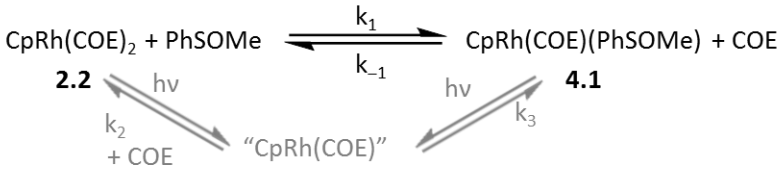

Figure 4.10: Kinetic Model A for the reaction between **2.2** and PhSOMe.

$$K_{eq} = \frac{k_1}{k_{-1}} = \frac{[4.1]_{eq}\,[COE]_{eq}}{[2.2]_{eq}} = \frac{\varepsilon_{2.2}\Phi_{2.2}k_3}{\varepsilon_{4.1}\Phi_{4.1}k_2} \quad (4.2)$$

The kinetics of this process may also be analysed using the integrated rate expression Equation (4.3), derived in the Appendix, where *a* is the equilibrium concentration, *b* is the difference in the initial and equilibrium concentrations and k_{obs} is the observed rate constant. The growth of **4.1** and decay of **2.2** were fitted to Equation (4.3), the results of which are given in

Table 2.11. The description of k_{obs} will depend on the kinetic model.

$$y = a + be^{-k_{obs}t} \quad (4.3)$$

where

a= $[A]_{eq}$

b= $[A]_0 - [A]_{eq}$

k_{obs}=

Table 4.1: Fitting results for the changes of **2.2** and **4.1** as a function of irradiation using Equation (4.7).

	a /%	b /%	k_{obs} /mol^{-1} dm^3 s^{-1}
[**2.2**]	22.0 ± 1.9	74.7 ± 2.7	(1.97 ± 0.27) x10^{-3}
[**4.1**]	63.5 ± 0.8	-63.4 ± 1.6	(3.31 ± 0.33) x10^{-3}

To ascertain if the reaction rate is influenced by the concentration of the sulfoxide a stock solution containing 9 mg of **2.2** and 1.5 mL of C_6D_6 was prepared and 9 mg of ferrocene was added as an internal standard. This was aliquoted into three NMR tubes and the following amounts of PhSOMe were added with the excess of ligand relative to **2.2** given in brackets: 9 mg (8.3), 18 mg (16.5) and 36 mg (33.0). These were irradiated in turn *in-situ* using the same broadband UV lamp as the first experiment. Significant unidentified decomposition was observed during the first experiment which could be due to thermal decomposition of the products caused by the heating of the lamp. The *in-situ* approach uses a liquid (ethanol) light guide to direct the light from the lamp to the sample inside the spectrometer and this distance reduces thermal heating. ^{1}H NMR spectra were recorded approximately every minute for 3 hours; this longer irradiation time reflects the lower power of the *in-situ* irradiation approach.

For each sample the ^{1}H NMR spectra were analysed using the approach outlined in the Experimental Section 8.4, and a photostationary state was established between **2.2** and **4.1** (Figure 4.11-Figure 4.13). At the photostationary state, there is approximately 25% **2.2** and 56% **4.1** and almost 20% decomposition in each of the samples. This would suggest that the concentration of the sulfoxide does not affect the distribution of the complexes. The rates of growth and decay of **2.2** and **4.1** were fitted to Equation (4.3) and the results of this are shown

in Table 4.2. The k_{obs} values were the same across the different samples indicating that this reaction is zero order with respect to the concentration of the sulfoxide and thus kinetic model B is appropriate and k_{obs} is defined by Equation (4.4). Interesting, the k_{obs} values from **2.2** and **4.1** are different. The k_{obs} for the two complexes should be the same as regardless of the kinetic model k_{obs} for the two complexes are defined by the same components. It is plausible that this difference is as a consequence of the observed decomposition and would suggest that the decomposition is predominantly associated with one of the complexes.

$$k_{obs} = k_1 + k_{-1}([COE]_{eq} + [4.1]_{eq}) \quad (4.4)$$

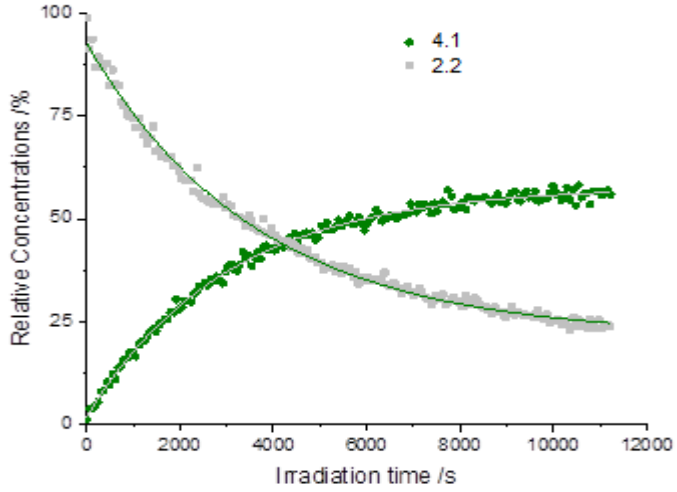

Figure 4.11: Time profile showing the changes in concentration of **2.2** and **4.1** following irradiation of **2.2** in the presence of PhSOMe, these were fitted to Equation (4.7), the results of which are given in Table **2.3** (entry 1).

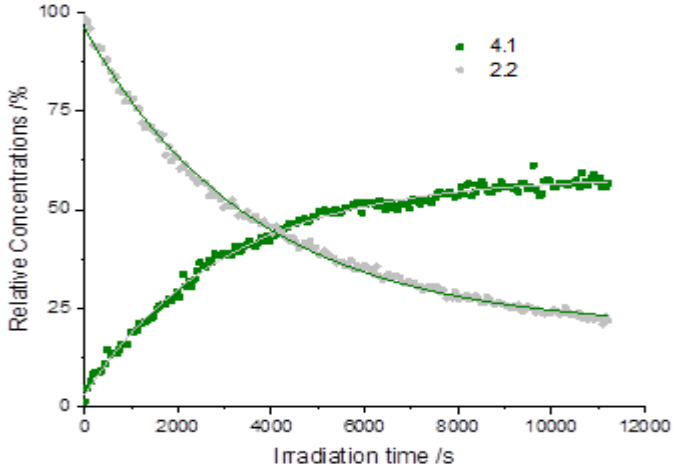

Figure 4.12: Time profile showing the changes in concentration of **2.2** and **4.1** following irradiation of **2.2** in the presence of PhSOMe, these were fitted to Equation (4.7), the results of which are given in Table **2.3** (entry 2).

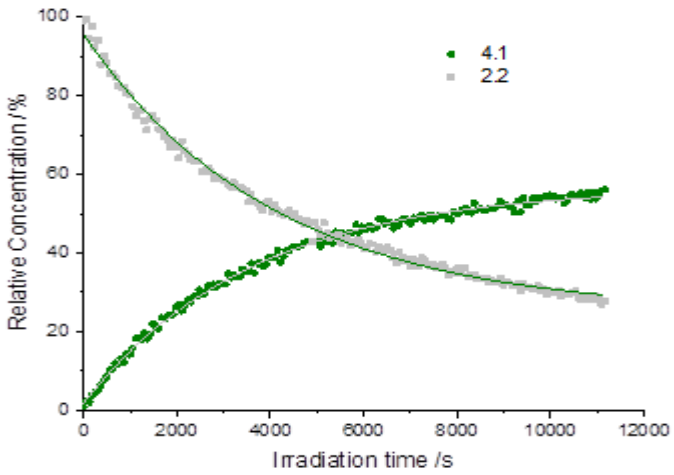

Figure 4.13: Time profile showing the changes in concentration of **2.2** and **4.1** following irradiation of **2.2** in the presence of PhSOMe, these were fitted to Equation (4.7), the results of which are given in Table **2.3** (entry 3).

Table 4.2: The results of the fitting of the changes in concentration of **2.2** and **4.1** to Equation (4.3).

Entry	Molar Excess PhSOMe		a /%	b /%	k_{obs} /mol^{-1} dm^3 s^{-1}
1	8.6	[**2.2**]	21.3 ± 0.4	71.6 ± 0.4	(2.75 ± 0.13) x10^{-4}
2		[**4.1**]	57.8 ± 0.2	-56.0 ± 0.3	(3.31 ± 0.15) x10^{-4}
3	16.5	[**2.2**]	19.7 ± 0.3	76.5 ± 0.3	(2.79 ± 0.04) x10^{-4}
4		[**4.1**]	58.4 ± 0.2	-55.5 ± 0.3	(3.31 ± 0.06) x10^{-4}
5	33	[**2.2**]	24.6 ± 0.4	71.0 ± 0.4	(2.43 ± 0.12) x10^{-4}
6		[**4.1**]	56.8 ± 0.2	-55.0 ± 0.3	(2.76 ± 0.12) x10^{-4}

An alternative method of determining the kinetics of this reaction involves a differential approach where chemical exchange, including decomposition, is used in conjunction with the Solver routine of Excel (Experimental 8.4.3). This was performed on the initial sample and allowed the values of k_1 and k_{-1} to be determined as (1.97 ± 0.27) x10^{-3} and (3.47 ± 0.32) x10^{-2} mol^{-1} dm^3 s^{-1} respectively. Substituting these values into Equation gives an observed rate constant of (2.82 ± 0.15) x10^{-3} mol^{-1} dm^3 s^{-1} and an equilibrium constant of (5.12 ± 0.71) x10^{-3} using Equation (4.1). The value for the observed rate constant is much closer to the value obtained using the product **2.2**, which would suggest that decomposition occurs via **4.1**. This was corroborated by the Solver routine fitting a rate for decomposition from **4.1** but not from **2.2** and is consistent with the other studies where this degree of decomposition was not

observed. The equilibrium constant is within error of the value calculated based on their concentrations, thereby validating the two approaches.

Having determined that the concentration of the sulfoxide does not influence the observed reactivity the equilibrium constant for each of the samples were calculated using Equation (4.2) and are given in Table 4.3. All the values of the equilibrium constant are approximately 2.5 x10^{-2} which suggests that the equilibrium **2.2** was favoured over **2.9**. The expressions for k_{obs} and K_{eq} can be combined in order measure k_1 and k_{-1} (Equations (4.5) and (4.6)) these are given in Table 4.4 and show that across the three samples k_1 and k_{-1} are the same and in each case k_1 is smaller than k_{-1}. These rate constants can also be defined in terms of the photochemical and thermodynamic properties (Equations (4.5) and (4.6)). The trend in rate constants can be rationalised by the quantum yield of **4.1** being higher than that of **2.2** meaning that PhSOMe is more readily lost than a COE or alternatively COE preferentially coordinates to the reactive intermediate over the sulfoxide.

Table 4.3: Equilibrium constants for each of the samples.

Entry	[**2.2**] /%	[**4.1**] /%	Molar Excess PhSOMe	K_{eq}
1	24.3 ± 0.9	56.1 ± 1.3	8.6	(2.69 ± 0.19) x10^{-2}
2	23.0 ± 1.0	56.9 ± 1.0	16.5	(2.98 ± 0.22) x10^{-2}
3	29.1 ± 1.0	54.5 ± 1.0	33	(2.06 ± 0.12) x10^{-2}

$$k_1 = \frac{k_{obs}K_{eq}}{K_{eq} + [4.1]_{eq} + [COE]_{eq}} = \frac{\Phi_{2.2} I_0 l \varepsilon_{2.2} k_3}{k_2[COE] + k_3} \qquad (4.5)$$

$$k_{-1} = \frac{k_{obs}}{K_{eq} + [4.1]_{eq} + [COE]_{eq}} = \frac{\Phi_{4.1} I_0 l \varepsilon_{4.1} k_2}{k_2[COE] + k_3} \qquad (4.6)$$

Table 4.4: Rate constants for each of the different samples.

Entry	Molar Excess PhSOMe		k_1 /mol^{-1} dm^3 s^{-1}	k_2 /mol^{-1} dm^3 s^{-1}
1	8.6	[**2.2**]	$(1.57 \pm 0.11) \times 10^{-4}$	$(5.81 \pm 0.57) \times 10^{-3}$
2		[**4.1**]	$(1.89 \pm 0.13) \times 10^{-4}$	$(7.00 \pm 0.66) \times 10^{-3}$
3	16.5	[**2.2**]	$(1.64 \pm 0.06) \times 10^{-4}$	$(5.52 \pm 0.35) \times 10^{-3}$
4		[**4.1**]	$(1.94 \pm 0.08) \times 10^{-4}$	$(6.55 \pm 0.44) \times 10^{-3}$
5	33	[**2.2**]	$(1.25 \pm 0.10) \times 10^{-4}$	$(6.07 \pm 0.54) \times 10^{-3}$
6		[**4.1**]	$(1.42 \pm 0.10) \times 10^{-4}$	$(6.90 \pm 0.58) \times 10^{-3}$

4.3 Photochemistry of **2.1** with PhSOMe

The reactivity of **2.1** towards PhSOMe was investigated. The combination of both an asymmetric alkene and sulfoxide is predicted to give two products by NMR spectroscopy with each product comprising two enantiomers (Figure 4.15). The Cahn-Ingold-Prelog priority rule was used to assign the stereochemistry of the coordinated sulfoxide.[150, 151] The stereochemistry of the rhodium centre was determined by arbitrarily assigning the priority order as CH_2, Cp, CHSi and S=O (Figure 4.14) and then using the Cahn-Ingold-Prelog rule to give the R and S isomer.[150, 151] A sample containing 4.3 mg of **2.1** and 11 mg of PhSOMe was prepared in C_6D_6. This provided a 6.7 fold excess of the sulfoxide substrate compared to the rhodium complex. The sample was then irradiated for 90 minutes in total.

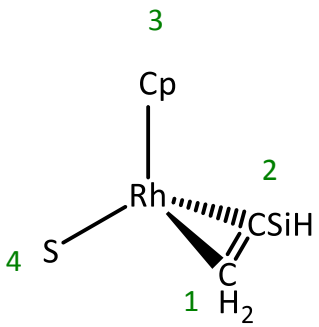

Figure 4.14: The arbitrarily assign priorities for the four groups coordinated to the rhodium centre.

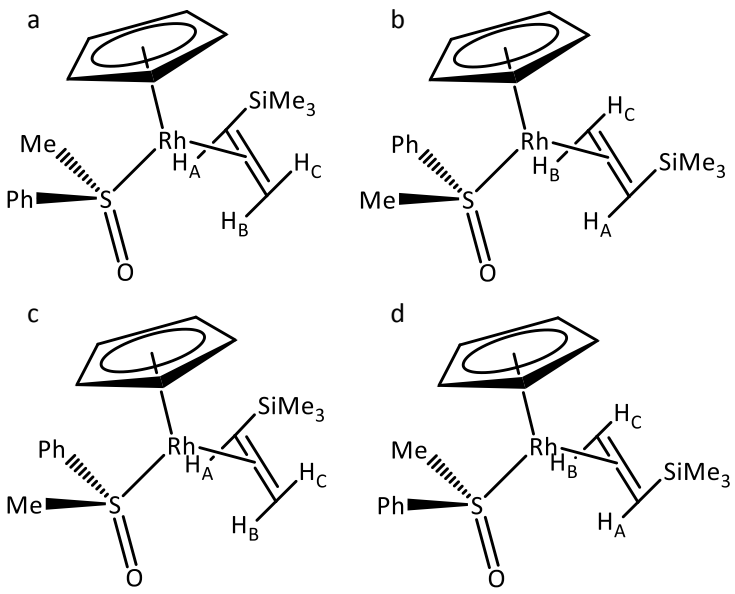

Figure 4.15: Possible isomers for the photoproduct **4.2**. a and b are the SR and RS isomers whilst c and d are the RR and SS isomers.

During the irradiation process, the growth of two new rhodium half sandwich species, with Cp resonances at δ 5.07 and 5.06 (Figure 4.16), were observed. It is expected that these are diastereomers of one another. The two products were characterised by NMR spectroscopy and the key features of this characterisation will now be detailed.

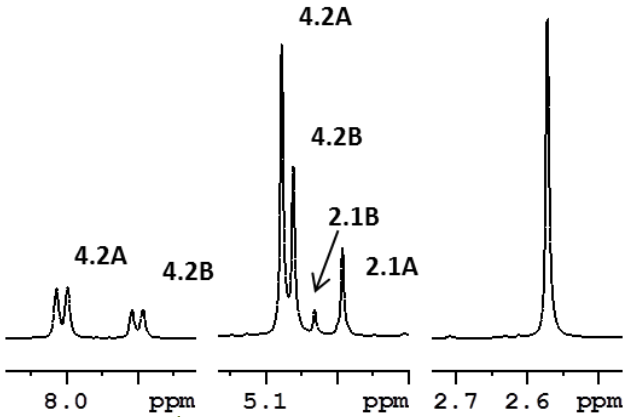

Figure 4.16: ^{1}H NMR spectrum of **4.2** in C_6D_6 at 298 K.

In addition to the two Cp peaks, there are two resonances in the ^{1}H spectrum at δ 8.01 and 7.98 due to the *ortho* protons on the phenyl ring in each of the two products (Figure 4.16). The proton at δ 8.01 shows an nOe to the Cp resonance at δ 5.07 and there is also an nOE between the resonances at δ 5.06 and 7.98 indicating that the new products do contain a coordinated

sulfoxide. Unexpectedly, there is only one signal consistent with the methyl group on the bound sulfoxide in the ^{1}H NMR spectrum; it does however, show a correlation to two different carbon environments in a 2D ^{1}H-^{13}C HMQC spectrum at δ 57.4 and 54.6 (Figure 4.17). This shows that coincidentally the proton resonances in the two isomers appear at the same chemical shift. Both of the *ortho* protons show an nOe to this methyl resonance confirming that the two peaks correlate to the different isomers. Based on the size of the carbon peaks, the peak at δ 57.4 can be assigned as part of the major isomer with the δ 5.07 Cp resonance and the δ 54.6 resonance to the minor isomer. As with **4.1**, there is a large chemical shift difference of 0.6 ppm in the proton spectrum between the free and bound ligand.[131] Whilst in the carbon NMR spectrum there is a downfield shift in the carbon resonances of the bound methyl resonances of the sulfoxide ligand.[57, 132] In combination, these values indicate coordination through the central sulfur atom.

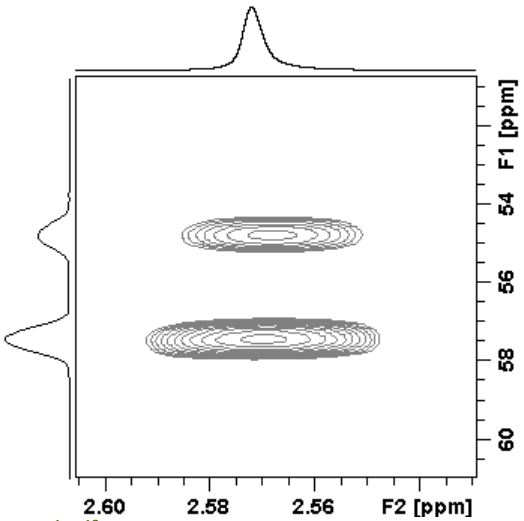

Figure 4.17: ^{1}H-^{13}C HMQC NMR spectrum of **4.2** in C_6D_6 at 298 K.

Having determined the products both contain a coordinated sulfoxide the next step was to assign these products to the possible diastereomers. Considering the only isomers observed in the starting complex have the trimethylsilyl substituent pointing up on the coordinated alkene, it is assumed this will also be true in the products and therefore there are four possible diastereomers (Figure 4.15). These may be grouped as two pairs of enantiomers. One pair has

the trimethylsilyl substituent on the same side as the phenyl group of the sulfoxide (Figure 4.15a-b) and the second pair has it on the same side as the methyl group (Figure 4.15c-d).

Using the nOe correlations between the Cp ring and the trimethylsilyl group, and the bound alkene resonances, the trimethylvinylsilane signals for each product were identified. Once these resonances had been assigned, the relative orientation of the trimethylvinylsilane and the sulfoxide could also be ascertained by nOe correlations. In the major product, **4.2A**, nOes between both H_C (δ 1.38) and the trimethylsilyl substituent (δ 0.01) and the *ortho* proton (δ 8.01) on the sulfoxide were detected (Figure 4.19). This was corroborated by an nOe between the methyl group on the sulfoxide (δ 2.55) and H_A (δ 2.98) on the vinylsilane (Figure 4.18 left) and therefore can be assigned to the RS/SR diastereomers (Figure 4.15). In the minor product, **4.2B**, an nOe was detected between the methyl on the sulfoxide (δ 2.55) and the trimethylsilyl (δ 0.18) and thus identifies this as the isomer where these two groups are on the same side (Figure 4.18 right) and therefore corresponds to the RR/SS isomers (Figure 4.15). An nOe between the *ortho* proton on the phenyl group (δ 7.98) and H_B on the vinylsilane supports this assignment (Figure 4.19). This characterisation is summarised in Table 4.11, for **4.2A** and Table 4.12 for **4.2B**.

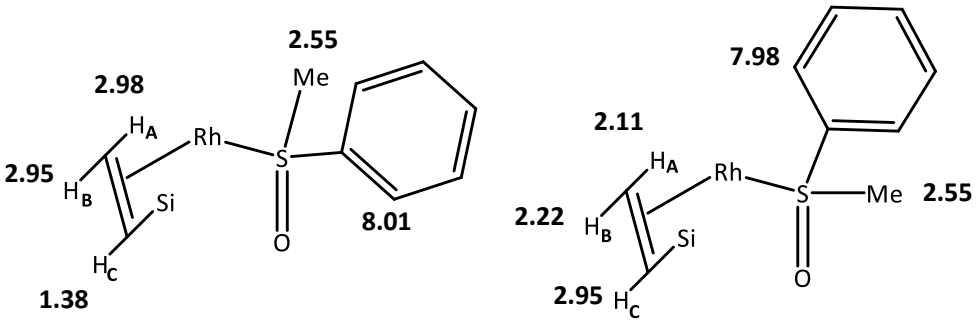

Figure 4.18: Summary of ^{1}H assignments for **4.2A** (left) and **4.2B** (right).

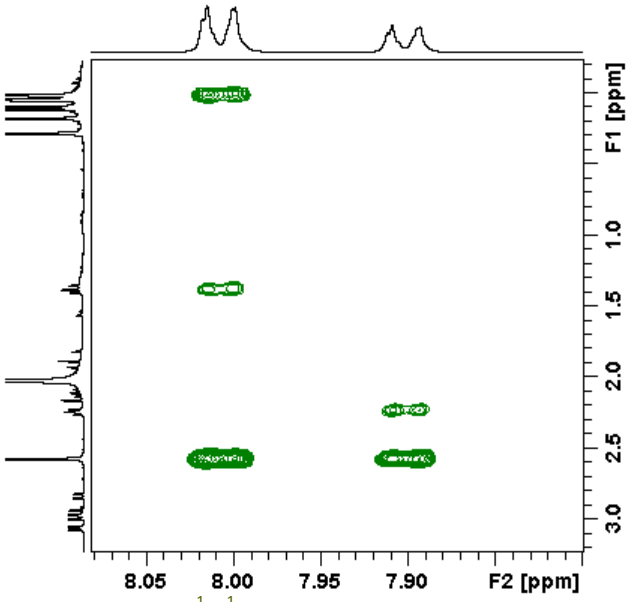

Figure 4.19: ^{1}H-^{1}H 2D NOESY of **4.2** in C_6D_6 at 298 K.

Having characterised the two products, the ^{1}H NMR spectra recorded during the irradiation process were next analysed using the method described in the Experimental 8.4. The concentrations of each of the species relative to the initial rhodium concentration determined. The concentrations of the two product isomers were combined allowing a comparison in the stability and activity between **2.1** and **4.2**. The changes in concentration with irradiation time were plotted (Figure 4.20) which shows the formation of a photostationary state containing approximately 75% of **4.2** and 15% of the starting material **2.1**, approximately 10% decomposition was observed.

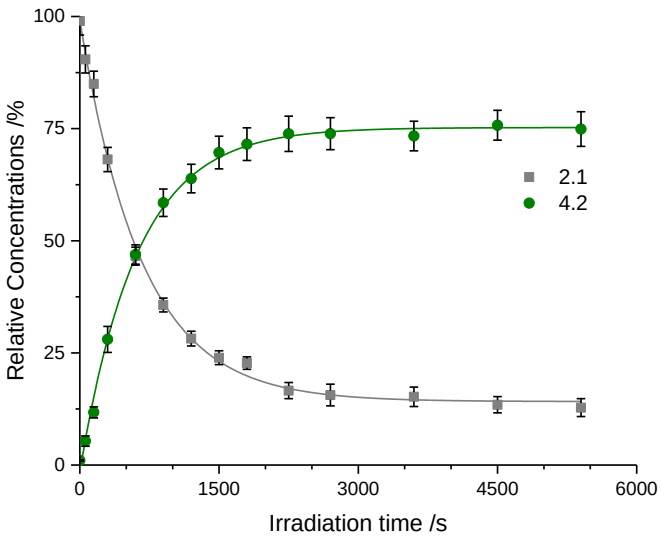

Figure 4.20: Time plot showing the change in concentrations of **2.1** and **4.2** as a function of irradiation time.

The kinetic model for this process is given by Figure 4.21, since the reaction between **2.1** and DMSO, and **2.2** and PhSOMe showed a zero order dependence on the sulfoxide, it is assumed that this is the case here also. The change in concentration of **2.1** and **4.2** were fitted to Equation (4.7) where *a* is the equilibrium concentration, *b* is the difference in initial and equilibrium concentrations and k is the observed rate constant for the formation of the photostationary state and defined by Equation (4.8). The equilibrium concentrations were used to give an equilibrium constant for this reaction of 0.107 ± 0.008 (Equation (4.9)). The equilibrium constant can also be defined in terms of the thermal and photochemical properties of the reaction (Appendix). A K_{eq} of 0.1 would suggest that either that the sulfoxide in **4.2** is more photolabile than the alkene in the **2.1** or that the reactive intermediate preferentially coordinates the alkene.

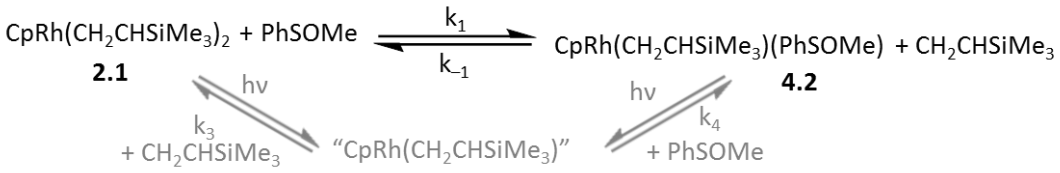

Figure 4.21: The simple kinetic model between **2.1** and **4.2**.

$$y = a + be^{-k_{obs}t} \qquad (4.7)$$

Where

a= $[A]_{eq}$

b= $[A]_0 - [A]_{eq}$

k_{obs}= $k_1 + k_{-1}([CH_2CHSiMe_3]_{eq} + [4.2]_{eq})$ (4.8)

$$K_{eq} = \frac{[4.2]_{eq}[CH_2CHSiMe_3]_{eq}}{[2.1]_{eq}} = \frac{\varepsilon_{2.1}\Phi_{2.1}k_3}{\varepsilon_{4.2}\Phi_{4.2}k_2} = \frac{k_1}{k_{-1}} \qquad (4.9)$$

Table 4.5: Fitting results for the changes of **2.1** and **4.2** as a function of irradiation using Equation (4.7) for each of the sample.

	a /%	b /%	k_{obs} /mol^{-1} dm^3 s^{-1}
[**2.1**]	14.2 ± 0.8	85.0 ± 1.2	(8.99 ± 0.35) x10^{-2}
[**4.2**]	75.2 ± 0.7	–76.7 ± 1.1	(9.76 ± 0.40) x10^{-3}

A more complicated kinetic model is required to observe the behaviour of the two diastereomers of **4.2** (Figure 4.22). This shows that **2.1**, **4.2A** and **4.2B** all may undergo photodissociation of a ligand to form the same reactive intermediate. The concentrations of **2.1**, **4.2A** and **4.2B** were plotted against irradiation time (Figure 4.23), the photostationary state now contains approximately 42% of the major isomer **4.2A**, 33% of the minor isomer **4.1B** and 15% of the starting material **2.1**. The rates of change for each of rhodium species were fitted using Equation (4.7) and are shown in Table 4.6. The k_{obs} for each of the species reflects the individual reactions described in Figure 4.24.

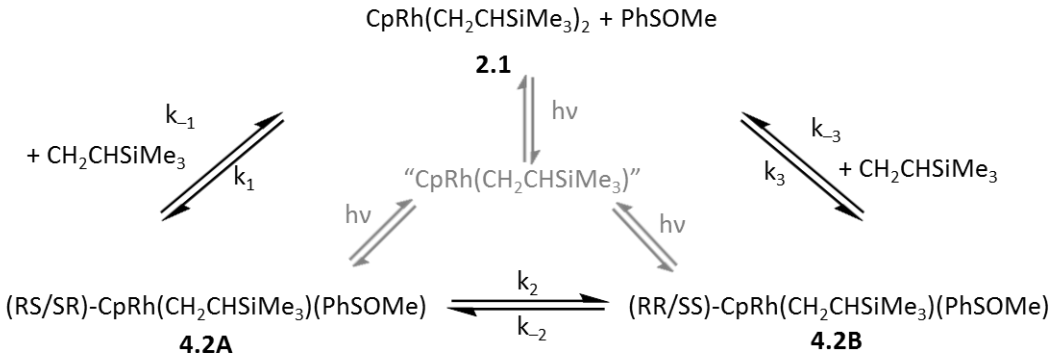

Figure 4.22: Full kinetic model for the reaction between **2.1** and PhSOMe.

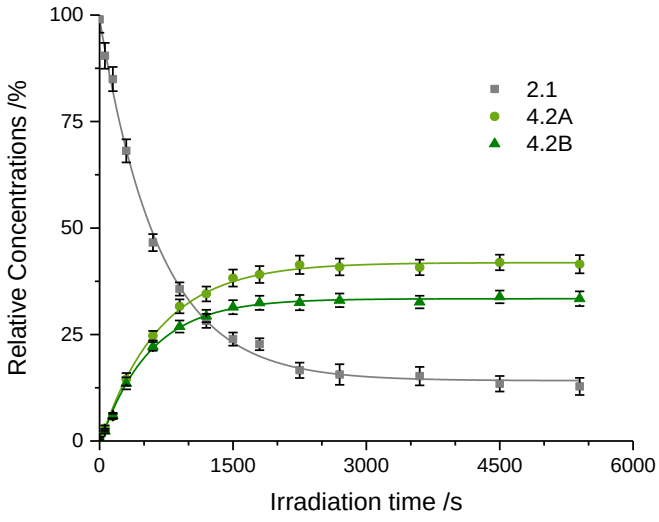

Figure 4.23: Time plot showing the change in concentrations of **2.1**, **4.2A** and **4.2B** as a function of irradiation time.

Table 4.6 Fitting results for the changes of **2.1** and **4.2A** and **4.2B** as a function of irradiation using Equation (4.7) for each of the sample, k_{obs} describes process A-C (labelled) in Figure 4.24.

	a /%	b /%	k_{obs} /mol dm^3 s^{-1}	k_{obs}	Reaction
[**2.1**]	14.2 ± 0.8	85.0 ± 1.2	(1.5 ± 0.06) x10^{-3}	$k_{obs}^{2.1}$	A
[**4.2A**]	41.9 ± 0.5	–42.6 ± 0.7	(1.5 ± 0.07) x10^{-3}	$k_{obs}^{4.2A}$	B
[**4.2B**]	33.4 ± 0.3	–34.3 ± 0.5	(1.8 ± 0.07) x10^{-3}	$k_{obs}^{4.2B}$	C

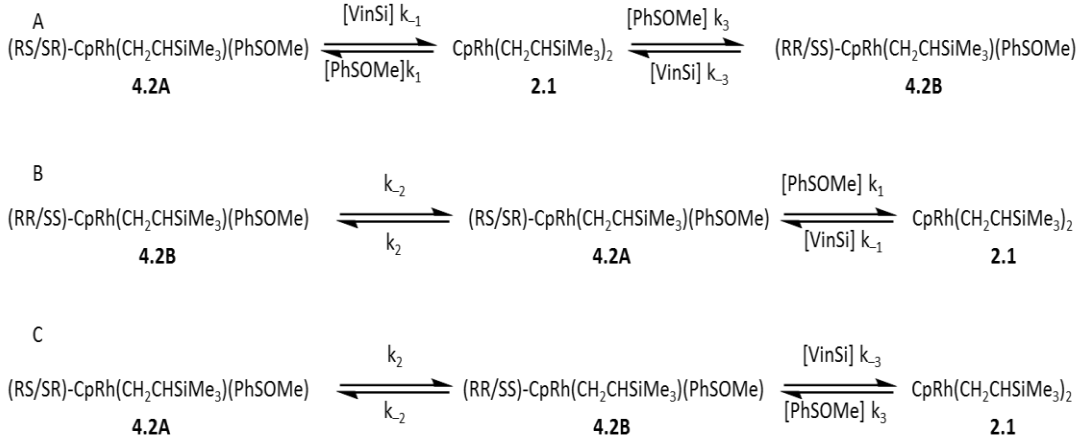

Figure 4.24: Each of the three pathways described separately for each k_{obs}.

The equilibrium constants for each of the equilibria were calculated using both the equilibrium concentrations and using the differential model (Experimental 8.4.3, Table 4.7). K_2 reflects the equilibrium between **4.2A** and **4.2B** and has a value of ~0.8 showing that there is a preference for isomer A, where the phenyl group of the sulfoxide is on the same side as the trimethylsilyl substituent on the coordinated alkene. This could be either due to the quantum yield of **4.2B** being larger than that of **4.2A** and thus the sulfoxide of **4.2B** is more labile providing a more efficient route to the intermediate. Alternatively, the difference could be attributed to there being a thermodynamic preference for the coordination of the sulfoxide with the trimethylsilyl substituent on the same side as the phenyl ligand.

Table 4.7: Equilibrium constant for each of the reversible steps in the kinetic model.

i	K_i*	K_i**
1	(5.94 ± 0.46) x10^{-2}	(5.33 ± 0.44) x10^{-2}
2	0.80 ± 0.02	0.78 ± 0.10
3	(4.74 ± 0.35) x10^{-2}	(4.11 ± 0.19) x10^{-2}

*based on concentrations, ** based on differential model

4.4 Photochemistry of **2.1** with DMSO and PhSOMe

To investigate whether there is a preference for different sulfoxides, a sample containing 7 mg of **2.1**, 7.5 µL of DMSO and 15 mg of PhSOMe in C_6D_6 was prepared, where both ligands were in 5.5 fold excess relative to **2.1**. The sample was then irradiated for 1 hour during which time the growth in signals associated with **2.4**, **4.2A** and **4.2B** were observed by ^{1}H NMR spectroscopy. These spectra were analysed according to the Experimental and the relative concentrations plotted against irradiation time. The concentrations of **4.2A** and **4.2B** were combined so that the isomerisation between them does not need to be considered. A photostationary state was achieved during this irradiation time and contains 51% **2.4**, 22% **4.2** and 21% **2.1**. The sample was then left for 18 days, at room temperature and protected from ambient light, and the relative concentrations were now 66% **2.4**, 13% **4.2** and 23% **2.1** demonstrating that the phenyl methyl sulfoxide is thermally labile and that there is a thermal preference for DMSO coordination over phenyl methyl sulfoxide.

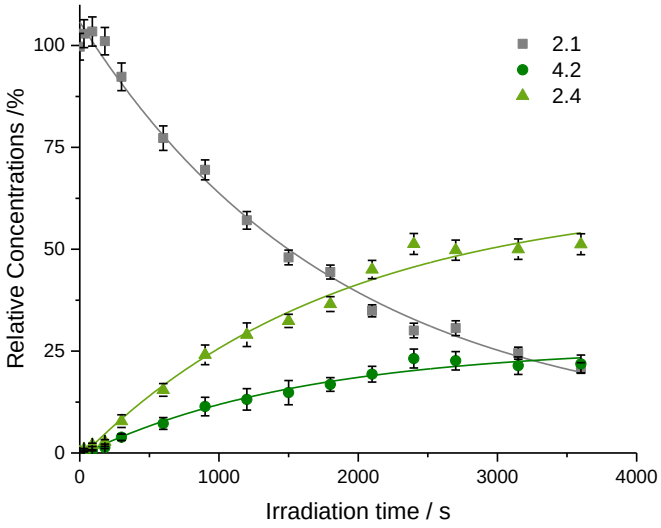

Figure 4.25: Time profile showing the reaction of 2.1 with DMSO and PhSOMe.

The kinetic model for this system is described in Figure 4.26 where each complex may undergo photodissociation of a ligand to form the same intermediate, CpRh($CH_2CHSiMe_3$). All three species are in equilibrium with one another and the equilibrium constant for each step can be calculated using the equilibrium concentrations (Equation (4.10), Figure 4.27). Note, when a

ligand was in large excess it was not included in these calculations based on previous observations where the rate was found to be independent of ligand concentation when the ligand was in excees. The results of this are summarised in Table 4.8, the equilibrium between **2.4** and **4.2** lies on the side of **2.4** indicating that the quantum yield of **4.2** is higher and therefore the loss of PhSOMe occurs more readily than DMSO. The other explanation is that DMSO more readily coordinates to the intermediate consistent with observation a growth in the proportion of **2.4** and loss of **4.2** when the sample was left at room temperature and protected from ambient light.

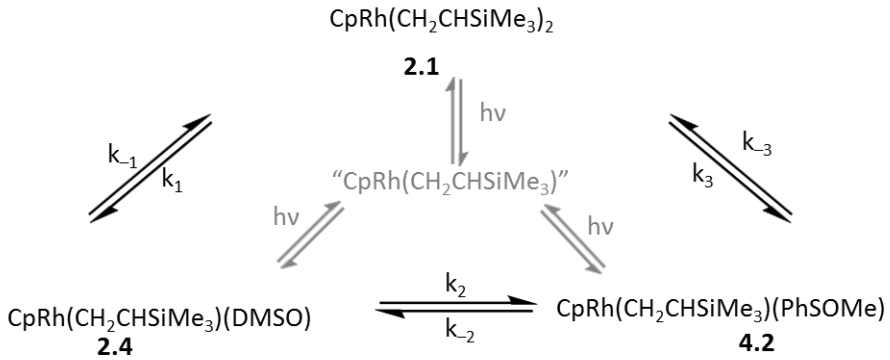

Figure 4.26: Kinetic model for the reaction between **2.1**, DMSO and PhSOMe

$$K_{eq} = \frac{[C]_{eq}[D]_{eq}}{[A]_{eq}[B]_{eq}} = \frac{\varepsilon_A \Phi_A k_{\mathrm{IC}}}{\varepsilon_C \Phi_C k_{\mathrm{IA}}} \qquad (4.10)$$

$$A + B \underset{k_{-1}}{\overset{k_1}{\rightleftharpoons}} C + D$$

Figure 4.27: Assignments for Equation (4.10)

Table 4.8: Equilibrium constant for each of the reversible steps in the kinetic model

I	K_i*	K_i**
1	$(5.9 \pm 1.3)\ x10^{-2}$	1.52 ± 0.11
2	0.44 ± 0.02	0.23 ± 0.03
3	$(2.56 \pm 0.60)\ x10^{-2}$	0.38 ± 0.04

*Excess of DMSO and PhSOMe

**Excess of DMSO, PhSOMe and $CH_2CHSiMe_3$

Table 4.9 Fitting results for the changes of 2.1, 2.4 and 4.2 as a function of irradiation using Equation (4.7) for each of the sample

	a /%	b /%	k_{obs} /mol dm^3 s^{-1}	k_{obs}	Reaction
[**2.1**]	5.6 ± 5.6	100.2 ± 5.2	(5.43 ± 0.80) x10^{-4}	$k_{obs}^{2.1}$	A
[**2.4**]	63.2 ± 4.7	– 64.6 ± 4.4	(5.42 ± 0.99) x10^{-4}	$k_{obs}^{2.4}$	B
[**4.2**]	26.1 ± 1.8	–26.7 ± 1.7	(6.33 ± 1.01) x10^{-4}	$k_{obs}^{4.2}$	C

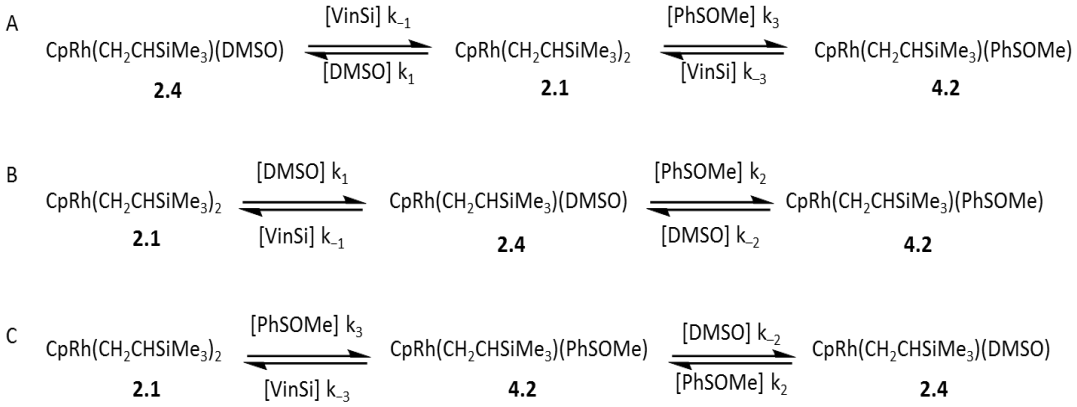

Figure 4.28: Each of the three pathways described separately for each $k_{obs.}$

The equilibrium constants K_1 and K_2 would be consistent with **2.1** being favoured in both equilibria. This would suggest that if an excess of trimethylvinylsilane was also added, a growth in the signals associated with **2.1** would result. To investigate this, 13 µL of trimethylvinylsilane was added providing 4.7 fold excess of ligand relative to the total rhodium content, in addition to a 5.0 and 5.3 fold excesses of DMSO and PhSOMe respectively. The sample was then irradiated for an hour generating 47% **2.4**, 11% **4.2** and 32% **2.1**. This provides evidence that both sulfoxides are photolabile. The equilibrium constants for each of the steps were measured again, now the equilibrium between **2.4** and **2.1** favours **2.4** consistent with the observation in Chapter 2. From this it can concluded that the order of reactivity across the different ligands is DMSO, trimethylvinylsilane and phenyl methyl sulfoxide. This could reflect the preference of the common intermediate to coordinate the respective ligands and link to the steric effects of the different ligands. The phenyl group on PhSOMe is larger than the methyl group of DMSO and the vinylsilane contains a bulky trimethylsilyl group. The electronic properties of the ligands may also influence the preference for the different ligands, the exact

nature of this interation would require further work. Alternatively, this could reflect the photolability of the different ligand with the phenyl methyl sulfoxide being the most labile and DMSO the least. This could also be influenced by the electronic properties of the different ligands.

4.5 Conclusions

It has been demonstrated that both **2.2** and **2.1** will undergo a photochemical reaction when irradiated in the presence of phenyl methyl sulfoxide. In the case of **2.2** a single product, **4.1**, forms containing a single coordinated sulfoxide ligand which is bound to the rhodium centre through the sulfur. Using a single step, bimolecular equilibrium, the equilibrium constant was calculated to be 0.32 ± 0.02. This process was repeated using three samples from a stock solution with incrementing amounts of phenyl methyl sulfoxide. In each sample the equilibrium comprised of 20% **2.2** and 60% **4.1** showing that the concentration of the sulfoxide did not influence the concentrations of **2.2** and **4.1**. The relaxation kinetics for these samples were also analysed and revealed that the equilibrium constant reduced with increasing sulfoxide concentration which was attributed to an increase in the quantum yield with increasing free ligand concentration.

The reactivity of **2.1** towards PhSOMe was studied next. Upon irradiation, as expected, two products formed, these were characterised as being diastereomers of one another. Both products were consistent with the trimethylsilyl substituent of the coordinated ligand pointing up towards the cyclopentadienyl ligand. In the major product, **4.2A**, the phenyl group of the sulfoxide was found to be on the same side of the complex as the trimethylsilyl group, whereas in the minor product, **4.2B**, the methyl group of the sulfoxide was on the same side as the trimethylsilyl group. The kinetics associated with this reaction were modelled using relaxation kinetics (Appendix). The equilibrium constant between the two isomers of **4.2** was 0.34 ± 0.03. Indicating a preference for **4.2A**, which either suggests that the sulfoxide in **4.2B** is more

photolabile owing to a higher quantum yield or the sulfoxide preferentially, coordinates in the orientation seen in **4.2A**. The contribution of both isomers were combined to analyse the equilibrium between **4.2** and **2.1** giving an equilibrium constant of 0.77 ± 0.06, demonstrating that **2.1** is favoured in the equilibrium

The equilibrium constants between both **2.1** and **2.2** with PhSOMe were smaller than similar values obtained using DMSO as the sulfoxide. To investigate their relative reactivity a sample of **2.1** was prepared and analysed containing an excess of DMSO and PhSOMe. Following irradiation, the major product was **2.4**, indicating that coordination of DMSO is favoured over PhSOMe. The sample was left for 18 days and the loss of **4.2** and growth of **2.4** was observed. An excess of trimethylvinylsilane was added, the sample was irradiated for a further hour and the conversion of **2.4** to **2.1** was observed. The equilibrium constants were measured and now the K_{eq} between **2.1** and **2.4** was 1.32 ± 0.10 matching the value obtained in Chapter 2.5 when equal quantities of DMSO and vinylsilane were used. The order of reactivity was found to be PhSOMe, vinylsilane and DMSO where DMSO was the least photolabile.

In this work I have demonstrated that PhSOMe will reaction with "CpRh(alkene)" fragments and that this ligand is photochemically and thermally labile. In the study with **2.1** with both DMSO and PhSOMe exhibited different activity demonstrating that changing the substitutents on the sulfoxide can influence behaviour providing a route for tuning reactivity. The product distribution following the reaction between **2.1** and PhSOMe showed that the asymmetric nature of the sulfoxide can be used as a marker for chirality through the observation of diastereomers, akin to chemical shift reagents.

4.6 Structures and NMR Data

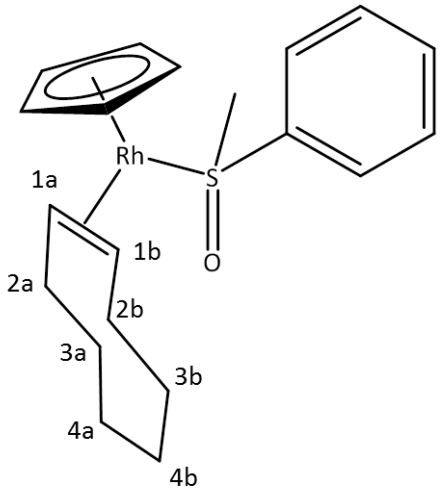

Figure 4.29: Proposed structure of [(η^5-C_5H_5)Rh(η^2-C_8H_{14})((Ph*S*(O)Me)] **4.1**

Table 4.10: NMR Characterisationfor [(η^5-C_5H_5)Rh(η^2-C_8H_{14})((Ph*S*(O)Me)] **4.1**

	δ/ppm (multiplicity, integration)	Coupling constant/Hz	Assignment	Group
^{1}H	8.08 (d, 2H)	J_{HH} 7.5	$\underline{H}_o$	PhSOMe
	7.12 (overlap)		H_m and H_p	PhSOMe
	4.98 (s, 5H)		$C_5\underline{H}_5$	Cp
	3.47 (tt, 1H)	J_{HH} 10.0, 2.6	CH^{1a}	COE
	2.64 (s, 3H)		$C\underline{H}_3$	PhSOMe
	2.60 (tt, 1H)	J_{HH} 10.0, 2.6	CH^{1b}	COE
	2.50 (dq, 1H)	J_{HH} 13.0, 3.5	$CH_2^{2a'}$	COE
	2.31 (br t, 2H)	J_{HH} 11.0	CH_2^{2b}	COE
	1.67 (overlap)		CH_2^{2a}	COE
	1.62 (overlap)		$CH_2^{2b'}$	COE
	1.7-1.1 (overlap)		CH_2^{3} and CH_2^{4}	COE
13C	129.0		$\underline{C}H_m$ and $\underline{C}H_p$	PhSOMe
	125.8		$\underline{C}H_o$	PhSOMe
	88.3		$\underline{C}_5H_5$	Cp
	61.3 (d)	J_{CRh} 15.7	$\underline{C}H^{1a}$	COE
	60.4 (d)	J_{CRh} 15.5	$\underline{C}H^{1b}$	COE
	57.8		$\underline{C}H_3$	PhSOMe
	33.2		$\underline{C}H_2^{2a}$	COE
	31.6		$\underline{C}H_2^{2b}$	COE
	26.5		$CH_2^{3 \text{ or } 4}$	COE
	26.0		$CH_2^{3 \text{ or } 4}$	COE

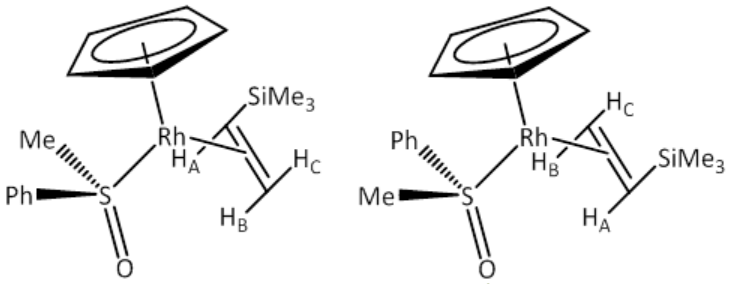

Figure 4.30: Proposed structures of RS/RS-[(η^5-C_5H_5)Rh(η^2-$CH_2CHSiMe_3$)((Ph*S*(O)Me)] **4.2A**

Table 4.11: NMR Characterisation for RS/RS-[(η^5-C_5H_5)Rh(η^2-$CH_2CHSiMe_3$)((Ph*S*(O)Me)] **4.2A**

	δ/ppm (multiplicity, integration)	Coupling constant/Hz	Assignment	Group
^{1}H	8.01 (d, 2H)	J_{HH} 8.4	H_o	PhSOMe
	7.09 (overlap)		H_m & H_p	PhSOMe
	5.07 (s)		C_5H_5	Cp
	2.98 (d, 1H)	J_{HH} 13	H_C	$CH_2CHSiMe_3$
	2.95 (overlap)		H_B	$CH_2CHSiMe_3$
	2.55 (s, 3H)		Me	PhSOMe
	1.38 (dd, 1H)	J_{HH} 11, 14	H_A	$CH_2CHSiMe_3$
	0.01 (s, 9H)		$Si(CH_3)_3$	$CH_2CHSiMe_3$
^{13}C	125.6		C_o	PhSOMe
	85.9		C_5H_5	Cp
	57.4		Me	PhSOMe
	43.3		CH	$CH_2CHSiMe_3$
	38.9		CH_2	$CH_2CHSiMe_3$
	0.25		$Si(CH_3)_3$	$CH_2CHSiMe_3$

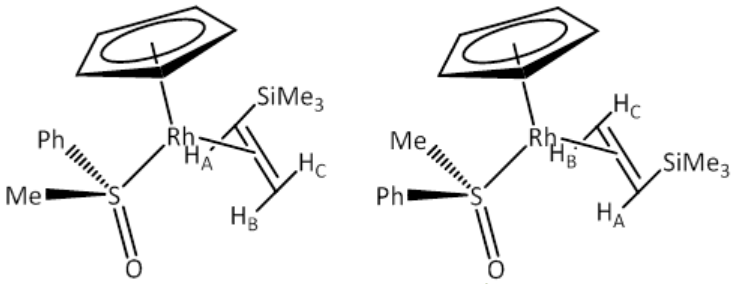

Figure 4.31: Proposed structure of RR/SS-[(η^5-C_5H_5)Rh(η^2-$CH_2CHSiMe_3$)((Ph*S*(O)Me)] **4.2B**

Table 4.12: NMR Characterisation of RR/SS-[(η^5-C_5H_5)Rh(η^2-$CH_2CHSiMe_3$)((Ph*S*(O)Me)] **4.2B**

	δ/ppm (multiplicity, integration)	Coupling constant/Hz	Assignment	Group
^{1}H	7.98 (d, 2H)	J_{HH} 8	H_o	PhSOMe
	7.05 (overlap)		H_m & H_p	PhSOMe
	5.06 (s, 5H)		C_5H_5	Cp
	2.95 (d, 1H)	J_{HH} 13.5	H_C	$CH_2CHSiMe_3$
	2.55 (s, 3H)		Me	PhSOMe
	2.22 (overlap)		H_B	$CH_2CHSiMe_3$
	2.11 (overlap)		H_A	$CH_2CHSiMe_3$
	0.18 (s, 9H)		$Si(CH_3)_3$	$CH_2CHSiMe_3$
^{13}C	125.0		C_o	PhSOMe
	86.2		C_5H_5	Cp
	54.6		Me	PhSOMe
	42.5		CH	$CH_2CHSiMe_3$
	37.0		CH_2	$CH_2CHSiMe_3$
	0.49		$Si(CH_3)_3$	$CH_2CHSiMe_3$

5 Synthesis, Characterisation and Photochemistry of $[Ru(H)_2(CO)(PPh_3)(Xantphos)]$ **5.1**

5.1 Introduction

This Chapter focusses on the photochemical reactivity of $[Ru(H)_2(CO)(PPh_3)(Xantphos)]$ **5.1**, where xantphos refers to 4,5-Bis(diphenylphosphino)-9,9-dimethylxanthene. In recent years the use of xantphos-derived ligands has become more widespread.[152, 153] This has included the use of the xantphos as an additive with $Ru(H)_2(CO)(PPh_3)_3$ reactions involving the alkylation of activated methylene compounds using benzyl alcohol.[154] This method allowed the relative activity of a range of different bidentate phosphines to be examined and allowed the benefit of xantphos as a ligand to be observed. When xantphos was used as the additive phosphine 100% conversion to product was observed within 3 hours with 0.5 mol% of the catalyst. The related phosphine 2,2'-bis(diphenylphosphino)diphenyl ether (DPE) only achieved 8% conversion under the same conditions.[154] The combination of $Ru(H)_2(CO)(PPh_3)_3$ and xantphos was subsequently used in the synthesis of 2,5-disubstituted furans,[76, 155] pyrroles[155, 156] and nitriles.[157]

The mechanism of the alkylation reaction was next studied in more detail. It had been proposed to proceed via a hydrogen-borrowing mechanism (Figure 5.1A). To investigate this mechanism the ruthenium xantphos complex $Ru(H)_2(CO)(PPh_3)(Xantphos)$ was synthesised and its reactivity towards benzyl alcohol and a ketonitrile (Figure 5.1B) was studied, where the ketonitrile is acting as the activated methylene source.[158] The reaction was found to proceed via the reductive elimination of H_2 and subsequent oxidative addition of the O–H bond of benzyl alcohol. Benzaldehyde is formed following a β-hydride elimination, and this goes on to react with the ketonitrile to the internal alkene which subsequently gets hydrogenated by the metal complex.

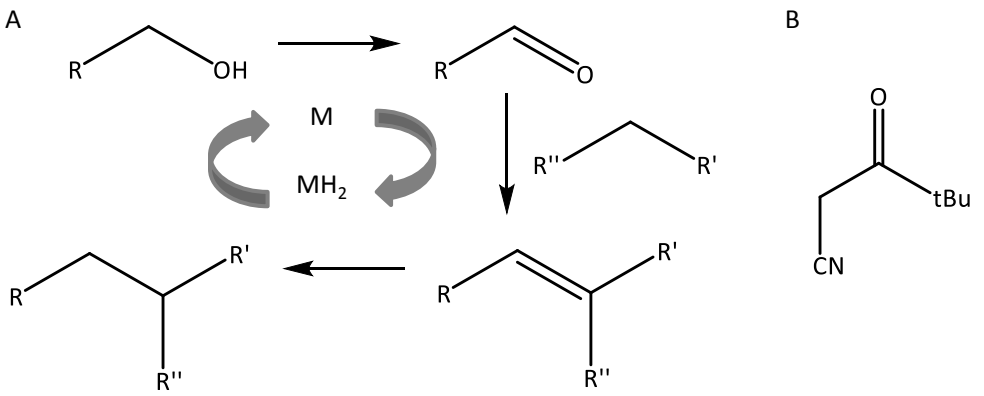

Figure 5.1: (A) Schematic representation of hydrogen borrowing route to C–C bond formation reactions between aromatic alcohols and activated methylene sources, an example of which is given by (B).

Xantphos is a wide bite angle phosphine having a natural bite angle of 108°, by contrast dppe has a natural bite angle of 86°.[152] The experiments described so far have concerned metal complexes with the xantphos ligand in a *cis* coordination mode; however, it is also capable of *trans*[159] [160] and κ^3-POP pincer coordination modes.[161-163] $Ru(H)_2(CO)(PPh_3)$(Xantphos) **5.1** has also been utilised in the hydrogenolysis of β-O-4 aryl linker in lignin where the compound in Figure 5.2 has been used as a model reagent.[164] Dehydrogenation of the alcohol gives the corresponding ketone which after hydrogenolysis yields acetophenone and guaiacol. They studied the mechanism of this catalytic process in more detail and observed the loss of H_2 from **5.1** after heating in toluene. This process also resulted in the loss of the PPh_3 ligand and they proposed that a square planar intermediate "Ru(CO)(xantphos)" was formed (Figure 5.3), the xantphos now acts as a tridentate (POP) ligand. They proposed that the dimer coordinates to this species and dehydrogenation of the alcohol function results.

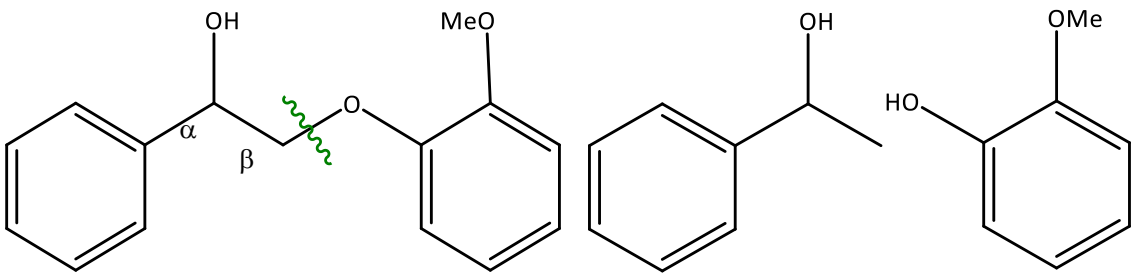

Figure 5.2: (left) Structure of the model lignin reagent, cleavage of the highlighted bond results forming acetophenone (middle) and guaiacol (right).[164]

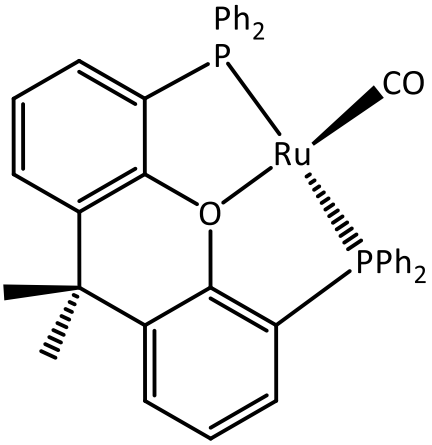

Figure 5.3: Proposed intermediate formed following the heating of $Ru(H)_2(CO)(PPh_3)$(Xantphos) in toluene.[164]

Ruthenium dihydride complexes have been long studied photochemically. This chemistry has recently been extensively reviewed by Perutz and Procacci.[55] Light may promote the reductive elimination of H_2 and as well as the loss of other ligands within the system.[90, 96, 97, 99] As far as our literature searches have revealed, the photochemical activity of **5.1** has not been studied. The photochemistry of similar complexes has been investigated (Introduction Section 1.5) and therefore it was anticipated that **5.1** would also be photoactive. To investigate this, **5.1** was irradiated *ex-situ* in the presence of different substrates which are known to coordinate to similar ruthenium systems.[90, 91, 96, 98] Once the photochemical activity of **5.1** was established it was then studied *in-situ* with *p*-H_2. Recent work in York has found that *in-situ* photolysis can be used to add *p*-H_2 to a suitbable photochemical precursor in a spin coherent fashion allowing the ZQ_x component of the parahydrogen singlet state (Introduction Section 1.2.5).[15] The reported study used $Ru(H)_2(CO)(PPh_3)_3$ as the precursor and the parahydrogen singlet state was observed to evolve as a function of the chemical shift difference between the two hydride ligands. This complex bares many similarities to **5.1** therefore it was hoped that this behaviour would also be observed in **5.1** also.

When deciding which substrates to study the photochemical activity of **5.1** a number of factors were considered. Ethene was chosen as a substrate as the liberated H_2 is likely to hydrogenate ethene and therefore H_2 will no longer be in solution to bind to the metal centre to reform the

starting material and therefore products are likely to be observed even if the starting material is favoured over the product. Whereas the pyridine derived and DMSO substrates were studies as these ligands are known to coordinate to transition metals and through the characterisation of the resulting products it can provide evidence as to which ligands are photolabile in the starting complex. One of the aims of this research was to study the addition of *p*-H_2 to **5.1** and therefore triethylsilane was included as a substrate of interest since this also contains a bond which adds to a metal centre via an oxidative addition process and help to ascertain whether **5.1** would be a suitable candidate for a study with *p*-H_2. Its advantage of triethylsilane over *p*-H_2 is that the expect product is different to the starting complexes and therefore can be used to confirm expected activity as the absence of PHIP-enhanced signals could be caused by several factors only one of which is the hydride ligands not being lost photochemically to get an intermediate which can add *p*-H_2.

5.2 Synthesis and NMR characterisation of **5.1**

5.2.1 Synthesis of $[Ru(H)_2(CO)(PPh_3)(Xantphos)]$ **5.1**

The synthetic route used to prepare $[Ru(H)_2(CO)(PPh_3)(Xantphos)]$ **5.1** is described in Figure 5.4. The precursor, $Ru(H)_2(CO)(PPh_3)_3$, was synthesised from $RuCl_3.3H_2O$ using the small scale method of Grushin with a 91.1% yield.[165] A substitution reaction was then performed to exchange two of the PPh_3 ligands in $Ru(H)_2(CO)(PPh_3)_3$ to give the target complex **5.1** in a yield of 33.7% based on ruthenium.[158]

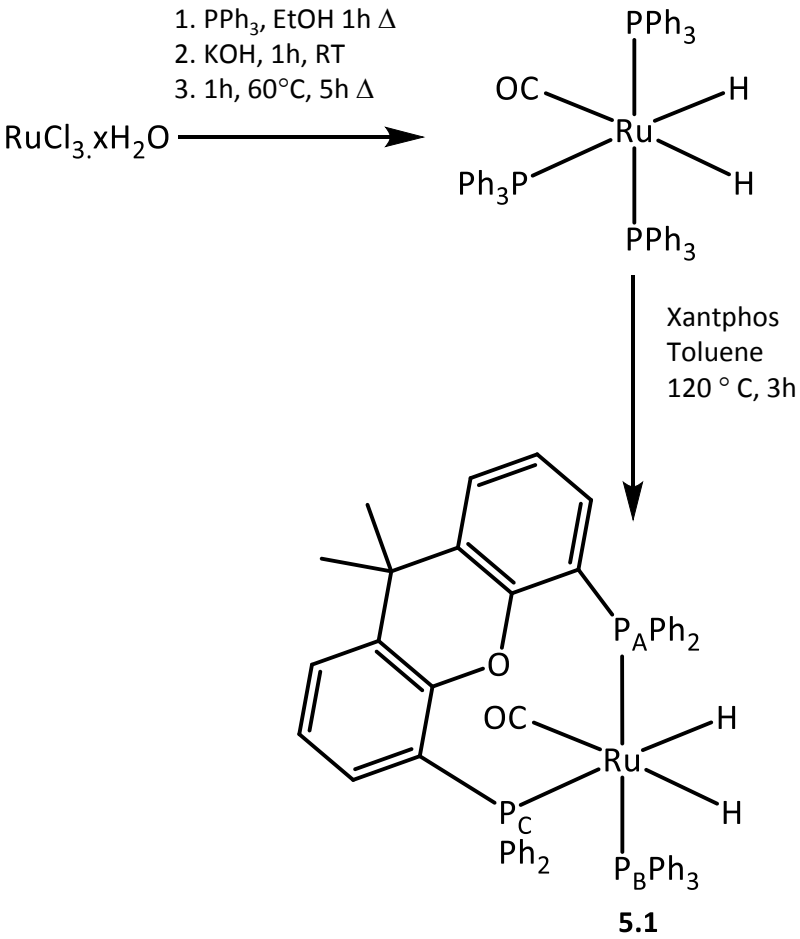

5.1

Figure 5.4: Reaction scheme for the synthesis of $[Ru(H)_2(CO)(PPh_3)(Xantphos)(CO)]$ **5.1**.

5.2.2 NMR characterisation

An NMR sample of the product was prepared in C_6D_6 to allow for characterisation. In the ^1H NMR spectrum, two diagnostic signals were seen in the hydride region at δ –6.72 and –8.67. The $^{31}P\{^1H\}$ NMR spectrum, however, consisted only of two clear resonances, a doublet at δ 58.3 (J_{PP} 240 Hz) and a broad singlet at δ 30.4 and a third broad resonance at δ 45. The two clear resonances integrate as 1: 1; this would suggest they both correspond to one phosphorus each and that there is some form of fluxionality within the system obscuring the third resonance. Similar observations have previously been made on this complex, and other similar xantphos complexes.[101, 158, 166, 167] Collectively, these studies have identified movement within the middle ether-containing ring of the xantphos ligands (Figure 5.6).

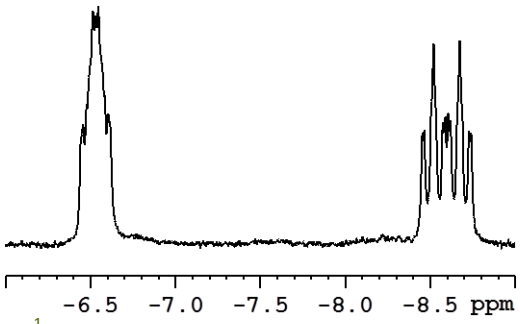

Figure 5.5: ^{1}H NMR spectrum (hydride region) of **5.1** in C_6D_6 at 298 K.

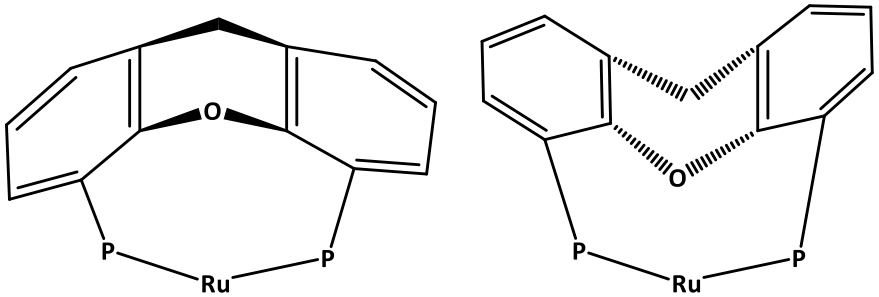

Figure 5.6: Conformational changes associated with ruthenium xantphos complexes according to the literature.[167]

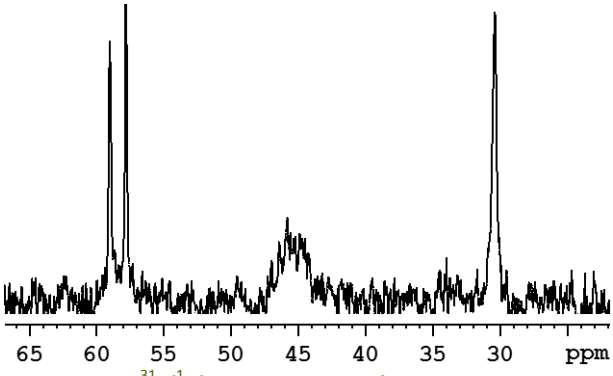

Figure 5.7: $^{31}P\{^{1}H\}$ NMR spectrum of **5.1** in C_6D_6 at 298 K.

A $^{31}P\{^{1}H\}$ NMR spectrum was subsequently recorded at 203 K in d_8-toluene and three sharp resonances dominate (Figure 5.8) with the broad resonance now resolving as a doublet of 240 Hz at δ 47.6. The large phosphorus-phosphorus coupling would indicate that this corresponds to one of the two phosphorus resonances *trans* to second phosphorus atom. The two phosphorus resonances that at first glance appear at δ 47.6 and 58.7 form an AB quartet as identified by the "roofing" effect seen in the appearance of the doublets. This phenomenon is observed when in a strong coupling regime (Figure 5.9).[32] In the weak coupling regime the coupling between resonances is considerably smaller than their chemical shift difference and a

pair of doublets is seen (Figure 5.9). In **5.1**, the chemical shift difference is 2245 Hz which is only 9 times larger than the coupling of 240 Hz. In weakly coupled spectra, the two lines in each doublet are separated by the scalar, J, coupling and centred around the chemical shift. In strongly coupled spectra the doublets are still separated by the scalar coupling, however, the chemical shift is no longer in the middle of the doublets and therefore it cannot be measured directly (Figure 5.9). The chemical shifts are determined using Equations (5.1) and (5.2) where Σ is –(2 + 3) or –(1 + 4), D is (3 – 1) or (4 – 2) and J is (2 – 1) or (4 – 3) where 1-4 refer the frequency of each of the lines.[32] This analysis gives chemical shifts for P_A and P_B of δ 58.7 and 47.6 showing that the strong coupling effect is minor.

$$\nu_1 = \frac{1}{2}(\Sigma + \sqrt{D^2 - J^2}) \quad (5.1)$$

$$\nu_2 = \frac{1}{2}(\Sigma - \sqrt{D^2 - J^2}) \quad (5.2)$$

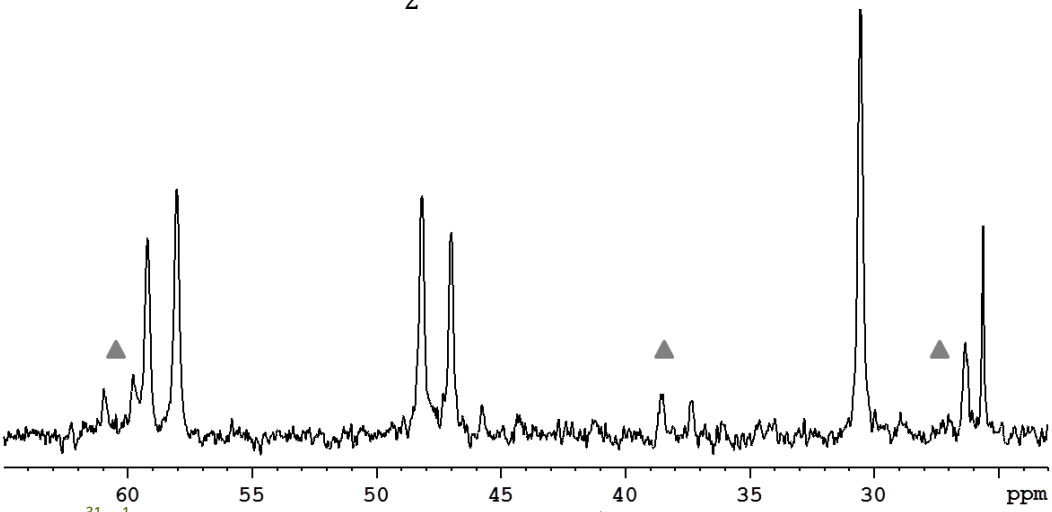

Figure 5.8: $^{31}P\{^1H\}$ NMR spectrum of **5.1** in d_8-toluene at 203 K ▲ denotes signals associated with minor product.

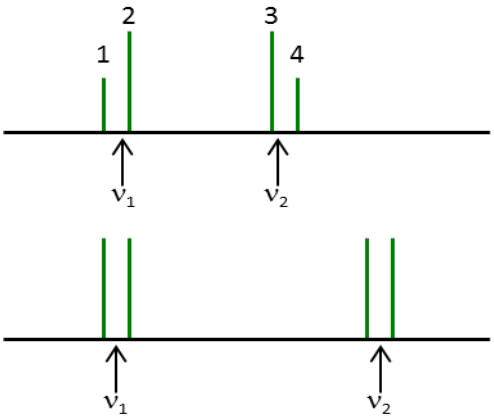

Figure 5.9: Schematic representation of (top) strong coupling and (bottom) weak coupling.

The $^{31}P\{^{1}H\}$ NMR spectrum also contains similarly distorted signals for a second product (highlighted by ▲ in Figure 5.8). $^{1}H\{^{31}P\}$ and ^{1}H NMR spectra recorded at 203 K also showed two sets of hydride resonances (Figure 5.10). The multiplicities in both sets of resonances have a similar appearance suggesting that they result from similar structural motifs and would be consistent with a conformational difference in the xantphos ligand (Figure 5.6).[8, 17-19]

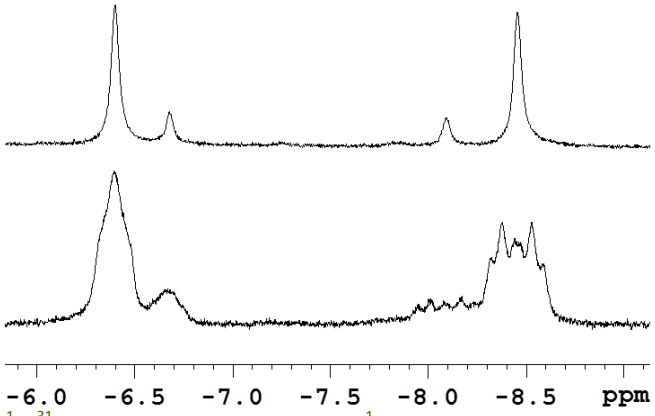

Figure 5.10: (top) $^{1}H\{^{31}P\}$ NMR spectrum and (bottom) ^{1}H NMR spectrum of **5.1** in d_8-toluene at 203 K.

The NMR characterisation of this complex in literature is limited. The phosphorus resonances were not assigned and the details of the xantphos were not previously reported. Two dimensional NMR spectra were acquired in order to provide full NMR characterisation of the complex. In the ^{1}H NMR spectrum there are two singlet resonances at δ 1.38 and 1.46 which correspond to the two methyl groups on the xantphos backbone. The aromatic region is highly complex because of the number of inequivalent aromatic ring ^{1}H resonances all of which couple to phosphorus. The proton resonances associated with the triphenylphosphine ligand are easily separated from the other resonances owing to all the phenyl groups being equivalent and yielded ^{1}H NMR signals at δ 7.69 and 6.92 since all three phenyl groups are equivalent. In a ^{1}H-^{13}C HMQC spectrum the resonance at δ 6.92 correlates to two carbon environments, in a 1: 2 ratio, which is consistent overlapping the *meta*- and *para*- proton signals. A correlation between the proton signal at δ 7.69 and the phosphorus resonance at δ 58.3 in a ^{1}H-^{31}P 2D HMQC spectrum acquired with a coupling of 10 Hz identified this proton as being due an *ortho*-proton.

Similarly, the *ortho*-protons for the pendent phenyl ligands on P_C were identified yielding signals at δ 7.34 and 7.25. In the $^{1}H\{^{31}P\}$-$^{1}H\{^{31}P\}$ 2D EXSY experiment (Figure 5.12) these resonances were found to be linked by exchange cross peaks (δ 7.34 and 7.75, 7.25 and 7.84). There are four further exchanging pairs of protons, demonstrating that interconversion of P_A and P_C is possible. These were assigned to the specific positions using a $^{1}H\{^{31}P\}$-$^{1}H\{^{31}P\}$ 2D COSY NMR experiment as summarised in Figure 5.11. The phenyl groups pointing out of the plane were identified through nOe correlations between these resonances and the methyl group on the xantphos backbone at δ 1.38.

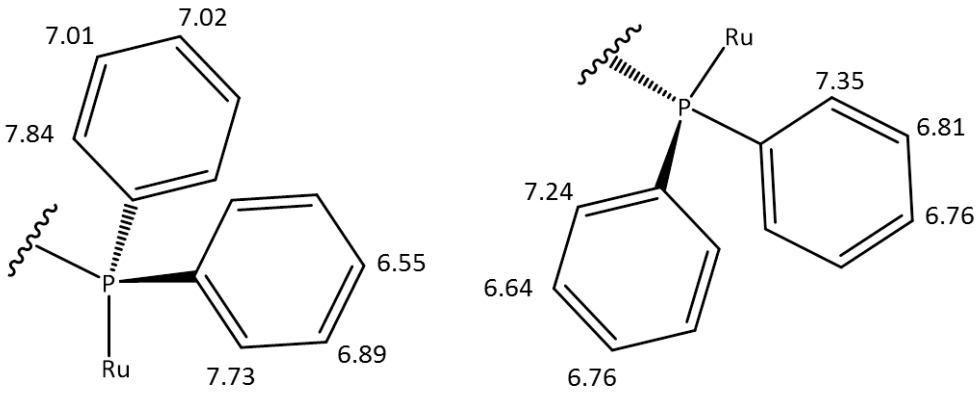

Figure 5.11: ^{1}H NMR chemical shift assignments of the phenyl ligands on the xantphos ligand, left P_A, right P_C.

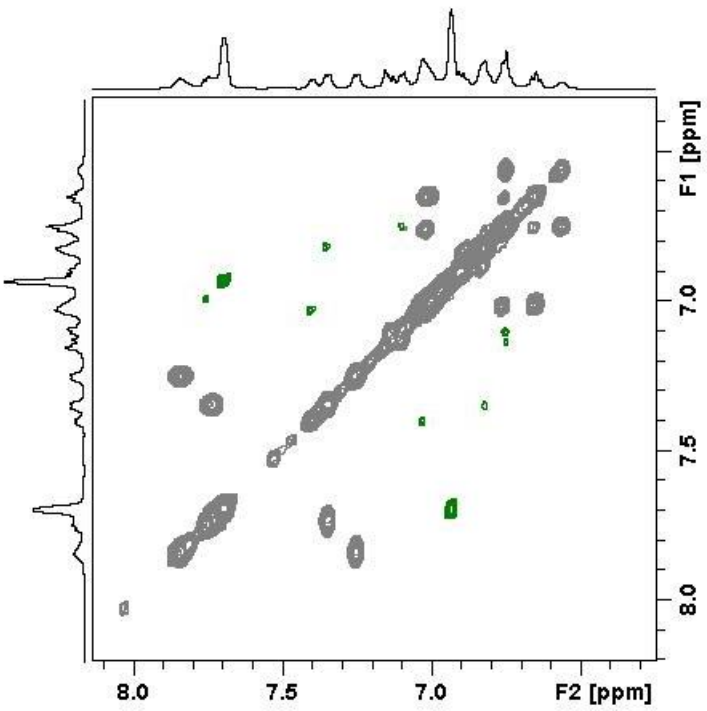

Figure 5.12: $^{1}H\{^{31}P\}$-$^{1}H\{^{31}P\}$ 2D EXSY of **6.1** in C_6D_6 at 298 K.

There are two reported mechanisms through which ligand exchange has been observed in octahedral complexes, the first being via a η^2-H_2 followed by ligand rotation in the dihydrogen transition state (Figure 5.13)[85, 168] and the second by a trigonal twist approach (Figure 5.14).[169] In this complex there is exchange observed between the hydride ligand and between the two coordinated phosphine atoms to the xantphos ligand. The exchange in the hydride resonances shows cross peaks to separate components of other hydride resonances indicating that the spins involved in the coupling retain their coupling during the exchange process.[169] The exchange of the aromatic protons is only observed between specific aromatic rings; specifically, the A1 ring exhibits exchange with C1 but not A2 or C2 and vice versa for A2 (for labels see Figure 5.11). Both of these observations are consistent with an intramolecular exchange process. The lack of exchange between the CO and PPh_3 ligands, however, is inconsistent with the dihydrogen rotation followed by the rotation of the remaining ligand and therefore the exchange process can be attributed to a trigonal twist mechanism.

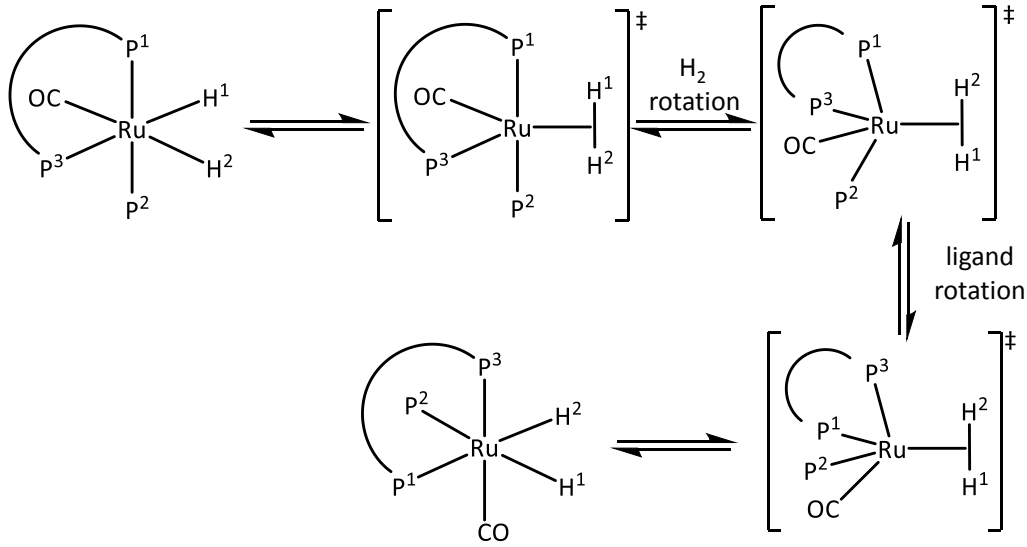

Figure 5.13: Mechanism 1 for exchange in octahedral complexes – the η^2-H_2 method, adapted from Schott *et. al.* for $[Ru(H)_2(CO)_2(dppe)]$.[83]

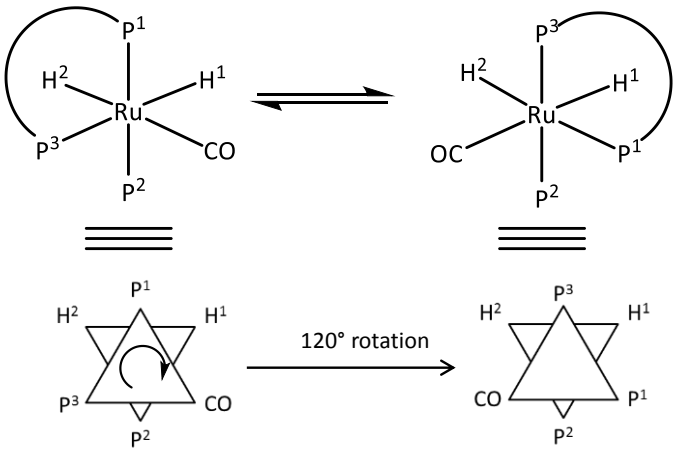

Figure 5.14: Trigonal twist mechanism.[170]

The kinetics of this process can be extracted from the EXSY spectrum, due to overlap this was only possible for the *ortho* protons. The relevant rows from the 2D were extracted as 1D spectra and the peaks associated with the diagonal and exchange cross peak were integrated. Using Equation (5.3), these allowed the exchange rate, k_{ex}, to be calculated as 1.8 s^{-1} for the exchange between A1 and C1 and as 1.6 s^{-1} for the exchange between A2 and C2. This was repeated with the hydride resonances giving an rate of exchange of 2.4 s^{-1}. The hydride exchange rate in $Ru(H)_2(CO)_2(dppe)$ was reported to be 1.20 s^{-1} at 306 K whilst the exchange of the phenyl rings was measured as 1.28 s^{-1} also at 306 K. These rates are the same order of magnitude as the values measured for **5.1** although the exchange rates in **5.1** are slightly faster. It is difficult to say whether this difference is within the error of the measurements or not. The hydride exchange rates were measured in similar compounds where dppe was replaced with PMe_2Ph or PMe_3 the exchange rates at 350 K were just 0.77 and 0.96 respectively, notably lower than the values measure here. This would suggest that there is a lower barrier to exchange in **5.1** compared to similar systems, possible explanations for this are a low barrier to rotation as part of the trigonal twist mechanism or a greater degree of bonding interactions between the two hydride ligands facilitating the exchange between the two hydride environments.

$$\ln\left(\frac{\frac{a_A}{a_{AB}}+1}{\frac{a_A}{a_{AB}}-1}\right)=k_{ex}t_m \tag{5.3}$$

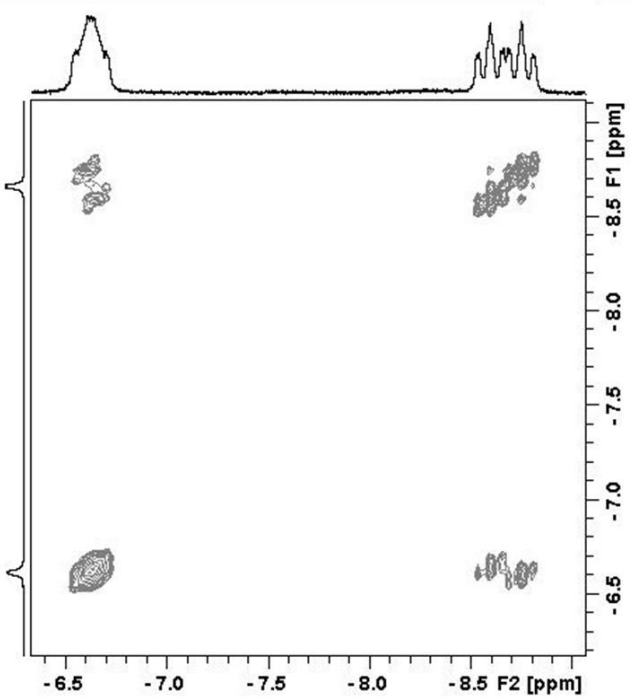

Figure 5.15: ^{1}H-^{1}H 2D EXSY NMR spectrum of **5.1** in C_6D_6 at 298 K.

5.3 Photochemistry of **5.1** with ethene to form **5.2**

The photochemistry of **5.1** was first studied with ethene. Ruthenium-phosphine dihydride complexes, similar to **5.1**, have been shown to lose H_2 photochemically and coordinate ethene.[90, 92, 94, 96, 98] Any liberated H_2 is likely to hydrogenate one equivalent of ethene based on ruthenium and limit the back reaction to reform **5.1**. An NMR sample of **5.1** and ethene was prepared in C_6D_6, the UV-Vis spectrum of **5.1** is shown in Figure 5.16. ^{1}H NMR spectra were acquired over the course of 3 hours to determine whether **5.1** and ethene react thermally. During this time, no changes were evident in the ^{1}H NMR spectrum. The sample was then irradiated, *in-situ*, using broadband UV light for 2 hours. After this time, there was an 80% reduction in the intensity of the NMR resonances associated with **5.1** and the growth of new signals consistent with a metal alkene complex present at δ 2.81 and 1.65 (Figure 5.17). Additionally, singlets at δ 4.47 and 0.80 were detected consistent with dihydrogen and ethane

respectively suggesting that the reductive elimination of H_2 has occurred during the reaction and that some ethene has become hydrogenated. The product was then characterised by NMR spectroscopy.

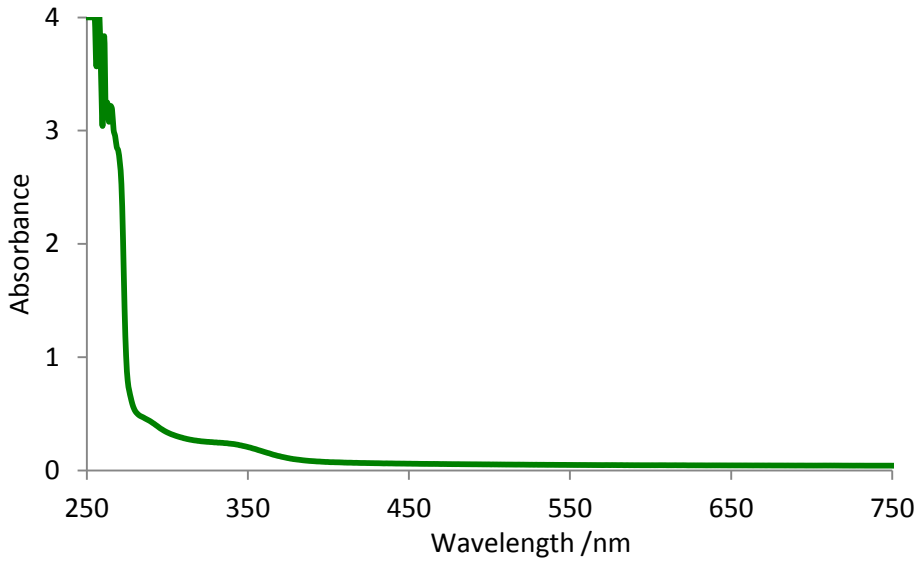

Figure 5.16: UV-Vis spectrum of **5.1** in C_6D_6

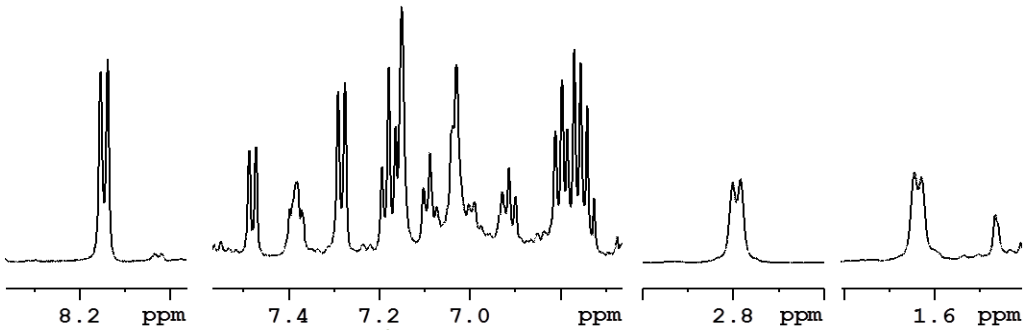

Figure 5.17: $^{1}H\{^{31}P\}$ NMR spectrum of **5.2** in C_6D_6 at 298 K.

In the $^{31}P\{^{1}H\}$ NMR spectrum there is a peak δ –5.4 consistent with free triphenylphosphine and a single phosphorus environment associated with the product, a singlet at δ 51.3. This would suggest that PPh_3 has been lost from the ruthenium complex during the reaction and xantphos is symmetrical in the product (Figure 5.18). In a ^{1}H-^{31}P 2D HMQC NMR experiment, acquired with a coupling constant of 10 Hz, correlations between this phosphine resonance and three aromatic resonances at δ 8.15, 7.48 and 7.29 were observed. These are consistent with *ortho*-protons, relative to the phosphorus atom, on each of the three phenyl groups.

Integrating these resonances relative to the bound ethene signals revealed that these *ortho*-protons correspond to 4: 2: 4 protons. This would suggest that the resonance at δ 7.48 corresponds to the *ortho*-proton on the phenyl group on the backbone of the xantphos ligand and the other two protons the *ortho*-protons on the pendent phenyl groups. Using a $^{1}H\{^{31}P\}$-$^{1}H\{^{31}P\}$ 2D COSY NMR experiment the *meta*- and *para*-resonances for each of the phenyl groups were assigned, these are summarised in Figure 5.19.

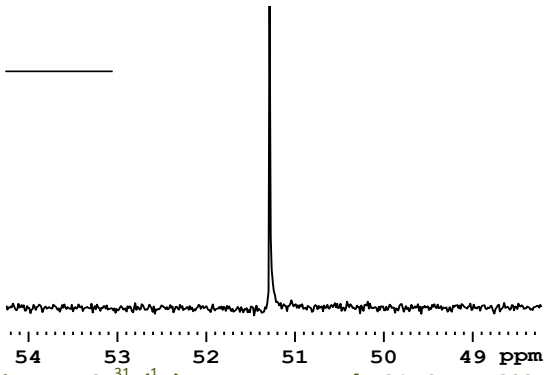

Figure 5.18: $^{31}P\{^{1}H\}$ NMR spectrum of **5.2** in C_6D_6 at 298 K.

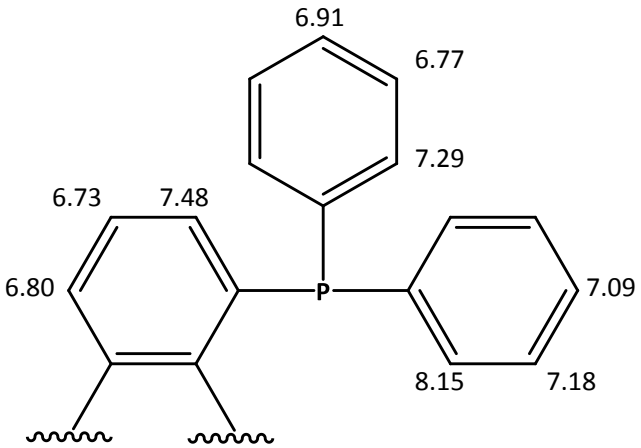

Figure 5.19: Assignments of the aromatic protons in **5.2**.

In a $^{1}H\{^{31}P\}$-$^{1}H\{^{31}P\}$ 2D EXSY NMR experiment exchange cross peaks were observed between the two ethene ^{1}H resonances indicating that interconversion between these sites is possible. Rotation about the metal alkene bond could account for this given that only one ^{31}P signal is seen. Both of the ethene resonances show an nOe correlation to a proton at δ 8.15 which has already been assigned as an *ortho*- proton on one of the pendent aromatic rings. This would identify this aromatic ring as pointing towards the bound alkene (Figure 5.20).

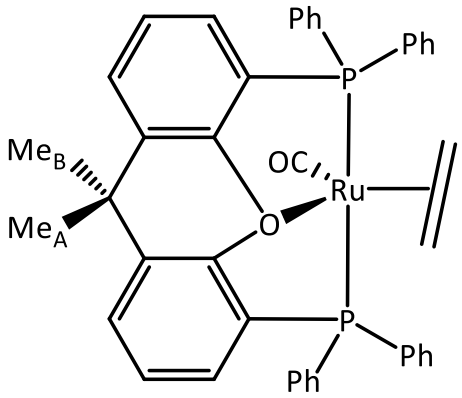

Figure 5.20: Proposed structure of the product **5.2**.

The resonances associated with the two methyl groups on the backbone of the xantphos ligand in **5.2** are found at δ 1.24 and 1.03. There is an nOe between both of these methyl groups and the proton at δ 6.80 supporting its assignment as the *para*-proton of the aromatic ring. There is also an nOe between the proton resonance at δ 6.73 and the methyl at δ 1.24, the suggests that this resonance corresponds to Me_A which points towards the xantphos ligand and that the other methyl resonance is the methyl ligand which points away from the xantphos ligand, Me_B.

By combining these observations it can be concluded the product is consistent with the structure depicted in Figure 5.20. In the equatorial plane, there is an ethene and a CO ligand. Whilst the xantphos ligand is coordinated as a POP ligand with the two phosphorus atoms being *trans* to one another. It is proposed that the oxygen is also coordinated based on the formation of a hydride resonance at δ –16.58, indicative of a hydride *trans* to oxygen, when this complex is reacted with *p*-H_2 (See Section 5.8.2). In the literature there are many examples of Xantphos coordinating as a POP ligand rather than as a bidentate ligand. A crystal structure database search was performed to compare the number of transition metal complexes with bi- and tri-dentate xantphos lignads (Figure 5.21) revealing 95 crystal structures containing a tridentate xantphos-derived ligand and 177 structures containing a bidentate xantphos-derived ligands. When this was repeated for ruthenium complexes there were 25 tridentate xantphos ligands compared with 11 bidentate ligands demonstrating the propensity for

xantphos ligands to have different coordination modes across similar structures. The change in coordination mode has also been proposed as part of mechanistics cycles.[164] Full details of this characterisation and the full structure can be seen in Table 5.3 and Figure 5.63.

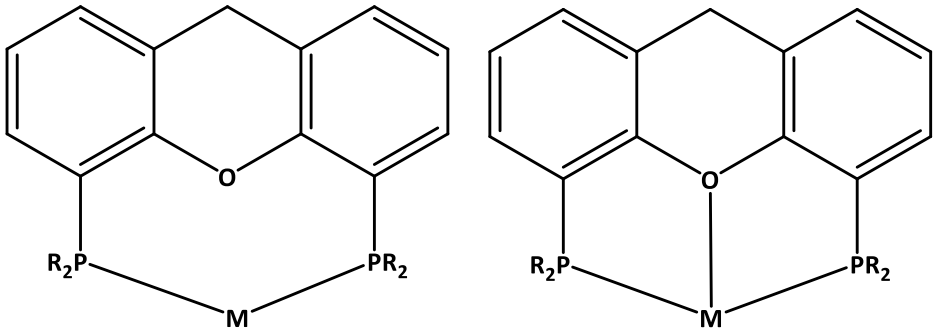

Figure 5.21: Substructures used in crystal structure database search

5.4 Photochemistry of **5.1** with pyridines

Having determined that **5.1** is photoactive, its reactivity towards 4-methyl pyridine, 4-tert-butylpyridine and ^{15}N-pyridine was studied. First, a sample of **5.1** was prepared in C_6D_6 and 5 µL of 4-methyl pyridine added. The sample was irradiated for 3.5 hours. After this time a product was detected that was associated with hydride resonances at δ –7.51 (H_A) and –5.97 (H_B) (Figure 5.22 top). These signals were shown to couple to one another in a ^{1}H-^{1}H COSY experiment which indicates that a dihydride species has formed (**5.3**). Both of these resonances have a doublet of doublets of doublets multiplicity indicating that one of the phosphorus environments has been lost. This is supported by a signal at δ –5.4 in the ^{31}P{^{1}H} NMR spectrum for free PPh_3. H_A exhibits a large coupling to phosphorus indicating a *trans* relationship between the two nuclei. In the corresponding ^{1}H-^{31}P 2D HMQC spectrum there are correlations between these hydrides resonances and phosphorus resonances at δ 34.7 and 24.3. The phosphorus signal at δ 24.3 was assigned as arising from a group *trans* to H_A since its correlation was observed when an 80 Hz coupling was used. 2-dimensional NMR spectra were then acquired to locate the coordinated 4-methyl pyridine resonances that were expected in this product but none were seen.

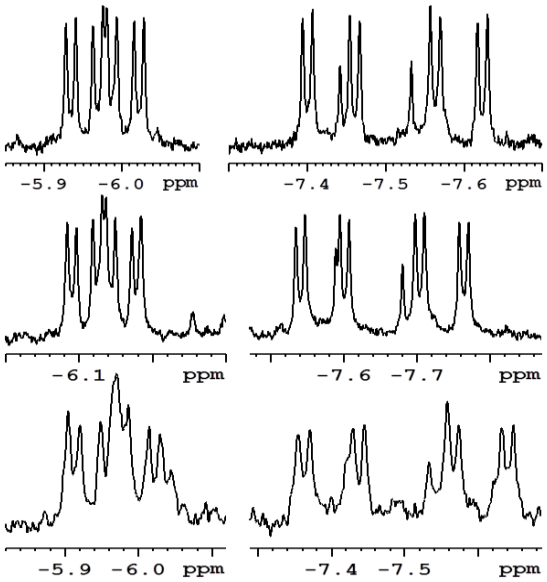

Figure 5.22: ^{1}H NMR spectrum of **5.1** following irradiation in the presence of 4-methyl pyridine (top) 4-tert-butylpyridine (middle) and ^{15}N-pyridine (bottom).

Since the characterisation of the product was inconclusive further studies were performed with different pyridines. 4-tert-butylpyridine was chosen to see if the change in substitutent would improve the binding of the pyridine to the metal centre allowing the product to form in high concentrations. It was also hoped that the larger substituent might allow nOe correlations to be observed. ^{15}N-pyridine was chosen for the ^{15}N label as this would potentially allow ^{15}N couplings to be observed in the hydride resonances if they were significantly large enough, e.g. a trans coupling. It would also offer the possibility of making ^{1}H-^{15}N HMQC measurements to aid the characterisation of the product following a reaction with **5.1**. When samples using 4-tert-butylpyridine or ^{15}N-pyridine were used in place of 4-methyl pyridine irradiation resulted in the same product **5.3** formed in each case. Figure 5.22 shows the hydride region for each of these samples and provides evidence for a common product. The sample containing 4-tert-butylpyridine was prepared in d_8-toluene rather than C_6D_6, which accounts for the small chemical shift difference. The NMR observations associated with this product are summarised in Figure 5.23.

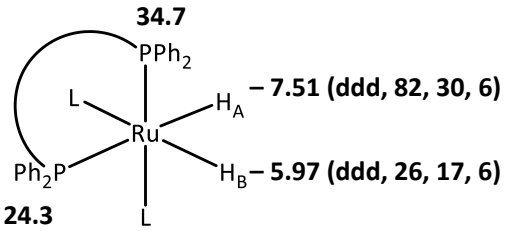

Figure 5.23: Summary of NMR characteristics of product **5.3**, formed following the reaction between **5.1** and the different pyridines; L is undefined at this stage, see Section 5.5.

5.5 Photochemistry of **5.1** with $PhCH_2OH$ or CO

In 2009, Ledger *et al*.,[158] observed that $Ru(H)_2(CO)_2$(xantphos) formed via the decarbonylation of benzyl alcohol and this was associated with hydride resonances at δ –6.13 and −7.65 and phosphorus resonances at δ 24.6 and 35.1 which are consistent with those of species, **5.3**. To investigate whether the product **5.3** corresponds to this dicarbonyl containing complex a sample of **5.1** and CO was prepared in C_6D_6. It was left overnight protected from ambient light to observe any thermal reactivity. No changes were observed in the ^{1}H NMR spectra. It was then irradiated for 4.5 hours and two new hydride resonances at δ –5.96 (ddd, 26.0, 17.5, 6.5) and –7.47 (ddd, 81.6, 30.5, 6.5) were observed. The characteristics of these signals matches those for H_A and H_B in **5.3**. In corresponding ^{1}H-^{31}P HMQC spectra, these resonances show correlations to phosphorus resonances at δ 24 and 35. From this it can be concluded that in the reaction between **5.1** and pyridines the photochemical loss of CO and PPh_3 results and that the liberated CO can coordinate in place of the PPh_3 in the axial position generating the product $Ru(H)_2(CO)_2$(Xantphos) **5.3**. In the ^{31}P{^{1}H} NMR spectrum there was also a singlet peak at δ 28 consistent with the tricarbonyl complex $[Ru(CO)_3$(Xantphos)] **5.4** which results from the photosubstitution of H_2 with CO. These products were then characterised by NMR spectroscopy. For **5.3** the aromatic resonances could not be assigned as both phosphine resonances showed correlations to the protons with the same chemical shifts. The assignments which could be made are summarised in Table 5.4. The full structure of **5.4** is given in Figure 5.65 and its characterisation summarised in Table 5.5.

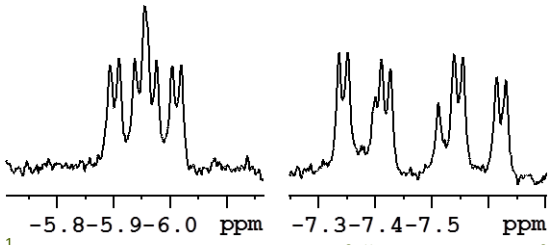

Figure 5.24: ^{1}H NMR spectrum in C_6D_6 at 298 K following reaction of **5.1** with CO.

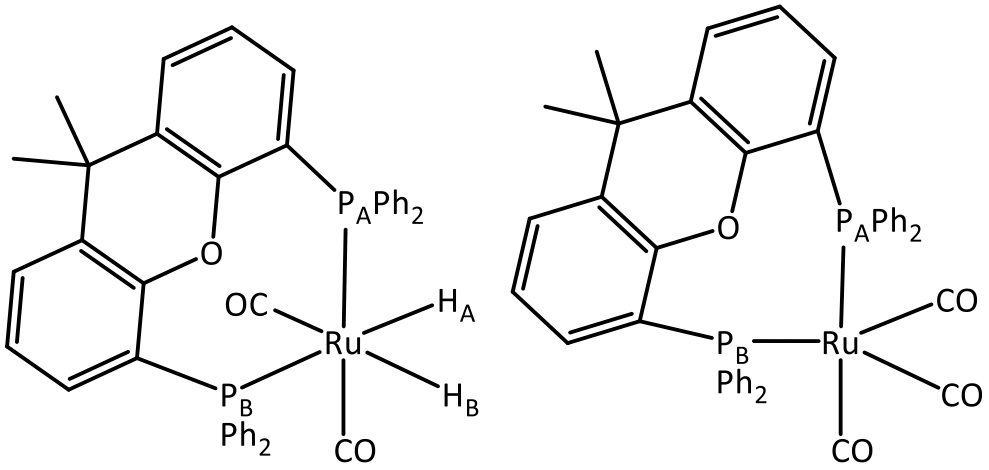

Figure 5.25: Structures of products (left) $Ru(H)_2(CO)_2$(Xantphos) **5.3** and (right) $Ru(CO)_3$(Xantphos) **5.4**.

Ledger *et. al.,*[158] first formed **5.3** by heating **5.1** to 120 °C in toluene for 2 hours with an excess of benzyl alcohol which acts as the source of CO. To investigate whether this process occurs photochemically a sample of **5.1** was prepared in C_6D_6 and 5 µL of benzyl alcohol was added. The sample was left for 2 hours 45 minute to observe any thermal reactivity and then irradiated for 3 hours. During this time as predicted, the resonances associated with **5.3** grew in intensity. A minor product, **5.5**, associated with a hydride resonance at δ –6.22 (dd 63, 28 Hz) and phosphorus resonances at δ 36.2 and 56.5 was also seen. Alongside these signals, a signal at grew δ 9.6 in keeping with the aldehyde proposed to form during this reaction.[158] It is likely that the minor product arises from the O–H activation of benzyl alcohol but no further characterisation was attempted. In conclusion, CO redistribution can account for the observed product in these reactions.

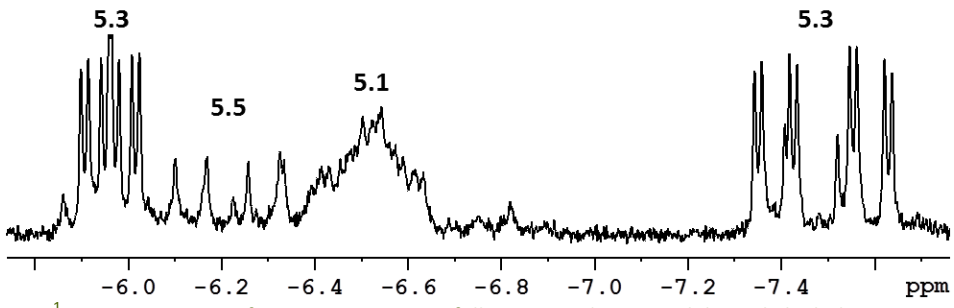

Figure 5.26: ^{1}H NMR spectrum of **5.1** in C_6D_6 at 298 K following irradiation with benzyl alcohol giving **5.3** and **5.5**.

5.6 Photochemistry of **5.1** with DMSO

Next, the photochemistry of **5.1** was studied with DMSO. An NMR sample containing **5.1** and 2 µL of DMSO in C_6D_6 was prepared. No thermal reaction was evident initially and the sample was then irradiated for 3.5 hours in *in-situ* using broadband UV light according to the Experimental 8.3.3. After this time six new hydride resonances appeared (Figure 5.27) and could be grouped into three dihydride complexes by a ^{1}H{^{31}P}-^{1}H{^{31}P} COSY experiment. Approximately 50% of **5.1** was retained. The proton resonances at δ −5.95 and −7.49 are consistent with **5.3**, leaving two products to be characterised. Product 1, **5.6**, is associated with signals at δ –8.10 and –10.33 and product 2, **5.7**, is associated with signals at δ –9.90 and –11.22

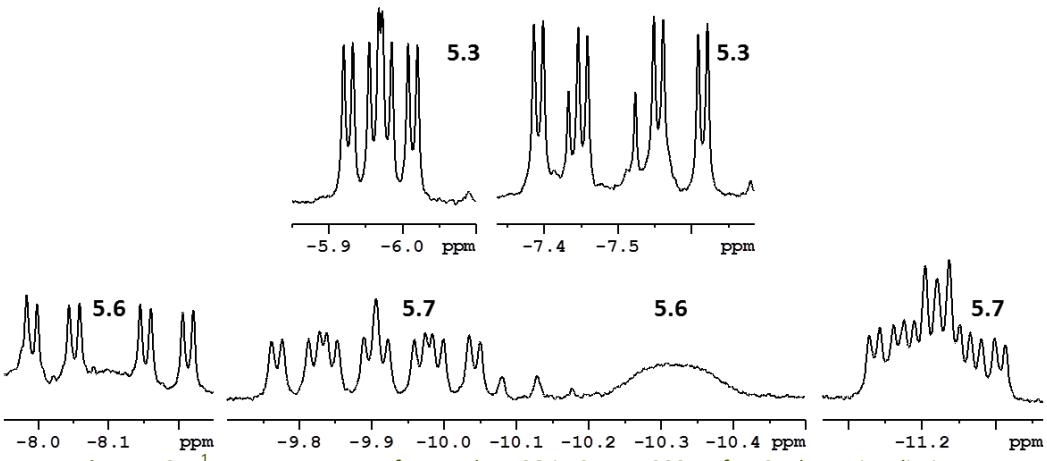

Figure 5.27: ^{1}H NMR spectrum of **5.1** and DMSO in C_6D_6 at 298 K after 3.5 hours irradiation.

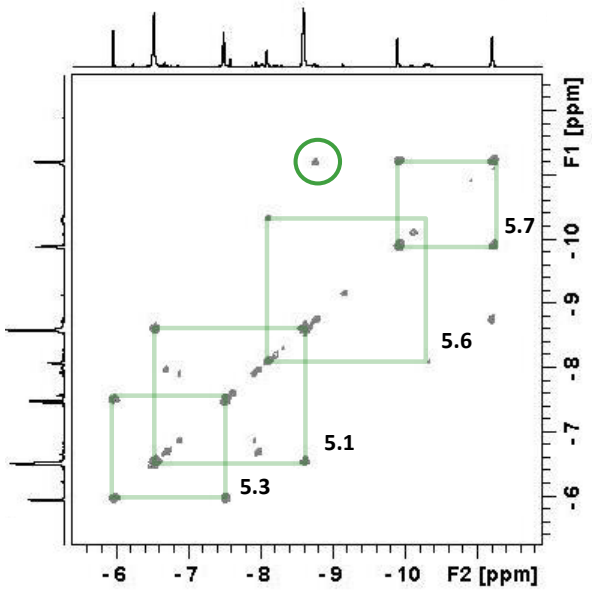

Figure 5.28: $^{1}H\{^{31}P\}$-$^{1}H\{^{31}P\}$ 2D COSY NMR spectrum (hydride region only) following the reaction between **5.1** and DMSO in C_6D_6 at 298 K.

The hydride resonance at δ –10.33 is broad and has no distinguishing features. A $^{1}H\{^{31}P\}$ NMR spectrum was acquired and this resonance remained broad suggesting that fluxionality, rather than overlapping scalar coupling, is responsible for the broadness. The second hydride resonance of this species is observed at δ –8.10 and has doublet of doublet of doublets multiplicity with 81, 31 and 8 Hz couplings respectively. It simplifies into doublet (8 Hz) following phosphorus decoupling. This is consistent with a dihydride species showing coupling to one phosphorus atom *trans* to the hydride and a second *cis* to the hydride. Limited information could be obtained on this product using the room temperature measurements and, therefore, second sample was prepared in d_8-toluene to allow for low temperature NMR experiments to be acquired. Upon cooling to 253 K, the broad resonance resolved to be a doublet of doublets of doublets with 31.5, 15.5 and 8 Hz couplings and allowed the two phosphorus environments were identified as δ 27.1 (d, 30 Hz P_B) and 36.4 (d, 30 Hz P_A) using ^{1}H-^{31}P 2D HMQC measurements. In addition to the expected correlations between these phosphorus signals and their connected aromatic protons, correlations to the methyl resonances of bound DMSO were also observed. These are associated with proton resonances at δ 1.72 and 2.52 and carbon signals at δ 55.2 and 50.3 respectively. These carbon chemical

shifts indicate that the DMSO ligand is coordinated through its sulfur.[132] The source of the fluxionality in this complex was not identified, exchange was not observed between the two hydride resonances which suggest that hydride exchange is not responsible. In **5.1**, the xantphos ligand was associated with two conformers which could interchange at room temperature; it is feasible that this is responsible for the exchange in this product also.

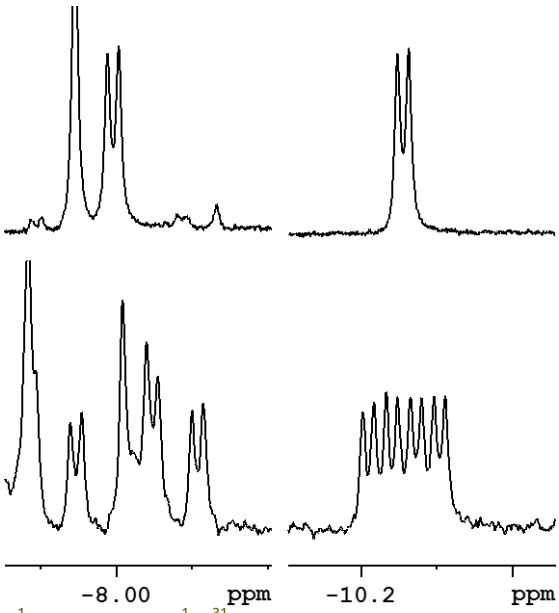

Figure 5.29: ^{1}H (bottom) and $^{1}H\{^{31}P\}$ NMR spectra of **5.6** at 253 K in d_8-toluene.

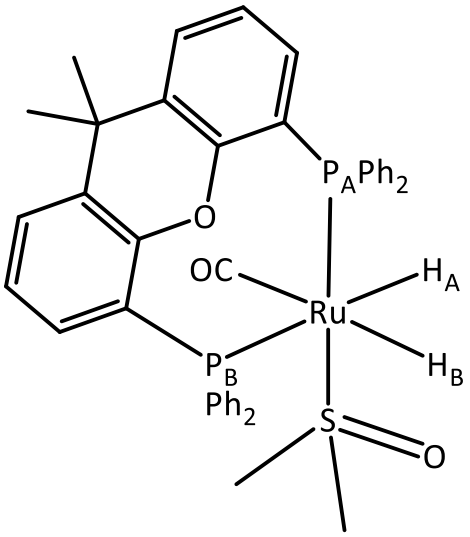

Figure 5.30: Proposed Structure for **5.6**.

The characterisation of **5.7** will now be detailed. The defining features of its NMR spectrum are two hydride resonances, note the cross peak in the circled in Figure 5.28 is a minor product

which contains a hydride overlapping with the δ –11.22 hydride resonance. The first is observed at δ –9.90 and has a dddd multiplicity (71, 38, 26, 7.5 Hz) which is consistent with a complex with three distinct phosphorus environments; two of which are *cis* relative to this hydride and a third that is *trans*. The second hydride resonance (δ –11.22) also shows coupling to three phosphorus environments (37, 30.5, 17 Hz), in addition to the proton-proton coupling, each of the phosphorus couplings are suggestive of a *cis* arrangement. It can be concluded that in this product, the PPh_3 has been retained and therefore **5.7** must relate to the photosubstitution of the CO ligand. This is confirmed by the two hydride signals showing correlations to three phosphorus environments in a ^{1}H-^{31}P 2D HMQC measurement at δ 31.3 (dd 17, 18 Hz), 43.8 (dd 245, 18 Hz) and 54.7 (dd 245 17 Hz) (Figure 5.31). The δ 54.7 phosphorus resonance shows correlations to protons signals at δ 7.85, 6.95 and 7.69 and these were assigned as the *ortho*-, *meta*- and *para*-protons of the PPh_3 ligand. Due to significant overlap in the ^{1}H NMR spectrum only some of the aromatic protons of the xantphos ligand were identified. The resonances that could be assigned are summarised in Figure 5.32.

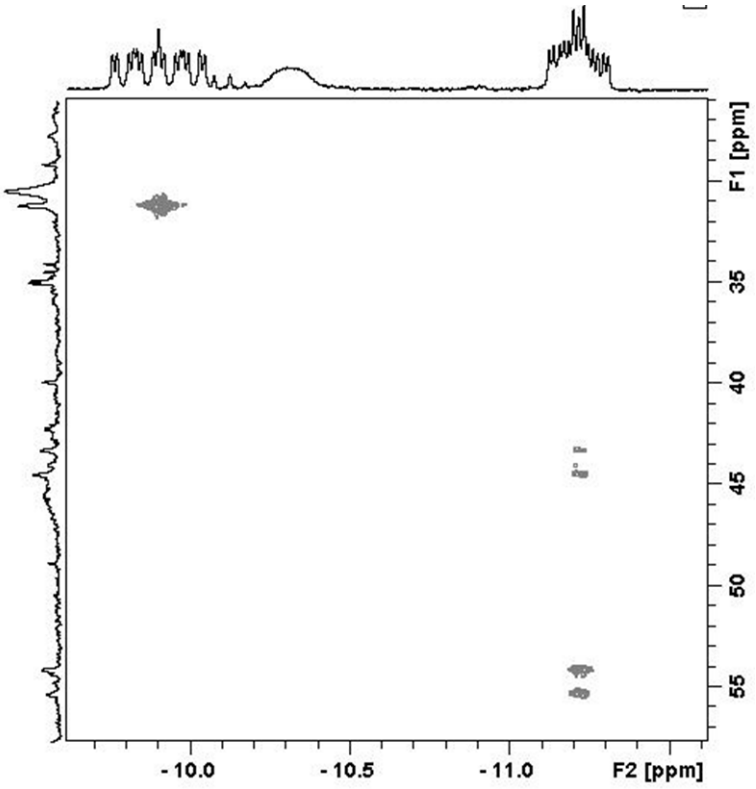

Figure 5.31: ^{1}H-^{31}P HMQC of **5.7** at 298 K in C_6D_6.

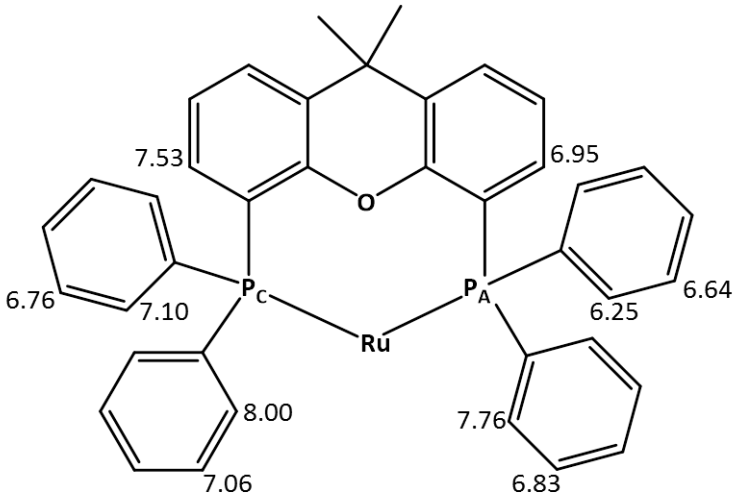

Figure 5.32: Summary of ^{1}H assignments for the xantphos ligand in **5.7**.

There were also correlations between the xantphos phosphorus resonances and the methyl resonances associated with a coordinated DMSO ligand. The phosphorus resonance at δ 43.7 shows a correlation to a proton resonance at δ 1.20 (δ_C 50.1) and whereas the resonance at δ 31.1 shows a correlation to δ 2.13 (δ_C 54.6). A COSY correlation between these two proton resonances corroborates that both resonances are from the same ligand. This observation confirms the assumption that CO has been lost from **5.1** and DMSO has coordinated in the vacant site. The carbon chemical shift of both methyl groups are downfield relative to free DMSO indicating coordination is via the sulfur atom.[132] From this information, the structure of **5.7** is proposed to be consistent with Figure 5.33. Full details of this characterisation and the full structure can be seen in Figure 5.68 and Table 5.8. The observation of **5.7** therefore provides support in the assignment of **5.3** in the other studies since it demonstrate that the CO ligand is also photolabile, in addition to the PPh_3 and H_2 ligands.

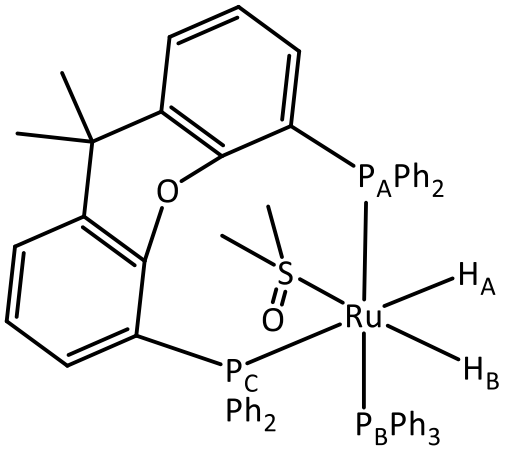

Figure 5.33: Proposed structure for **5.7**.

5.7 Photochemistry of **5.1** with Et_3SiH

The photochemistry of **5.1** was next studied in the presence of triethylsilane. An NMR sample of **5.1** was prepared in C_6D_6 and 10 µL of triethylsilane was added. The sample was irradiated *ex-situ* for 10 minutes during which time several new hydride containing products formed (Figure 5.34). This is reflected in the observation of a resonance at δ –3.09, corresponding to **5.8**, a triplet (J_{HP} 24 Hz) which simplifies to a singlet following phosphorus decoupling. The second product, **5.9**, is associated with a peak at δ –8.06 which is a doublet of doublets (J_{HP} 56, 17 Hz). This also simplifies to a singlet with phosphorus decoupling. The multiplicity shown in both of these resonances is consistent with monohydride species which couple to two phosphorus nuclei. Free triphenylphosphine was detected in the $^{31}P\{^1H\}$ NMR spectrum following irradiation supporting the observation that PPh_3 has been lost from the products. Finally, there are broad resonances at δ –9.05 and –7.59 indicating a product exhibiting fluxionality. This could be due to the η^2 coordination of either dihydrogen or triethylsilane. It is unclear from these measurements whether these resonances are associated with a third product or part of the other two products.

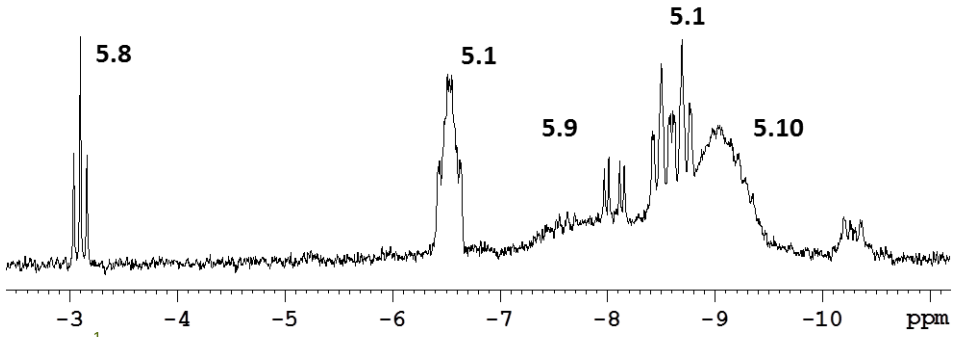

Figure 5.34: ^{1}H NMR spectrum in C_6D_6 at 298 K following 10 minutes irradiation of **5.1** in the presence of triethylsilane.

Low-temperature measurements were performed in d_8-toluene which allowed the broad resonances to be attributed to a third product. NMR characterisation allowed the three products to be assigned the structures shown in Figure 5.35. The minor product (only 3% of the reaction mixture), **5.9** contains a ligand, L which is likely to be a CO ligand, liberated from **5.1** during the formation of **5.8**. However, due to its weak intensity the characterisation of this product was limited and will not be discussed further. The key features of the characterisation of the two major products, **5.9** and **5.10**, will now be detailed.

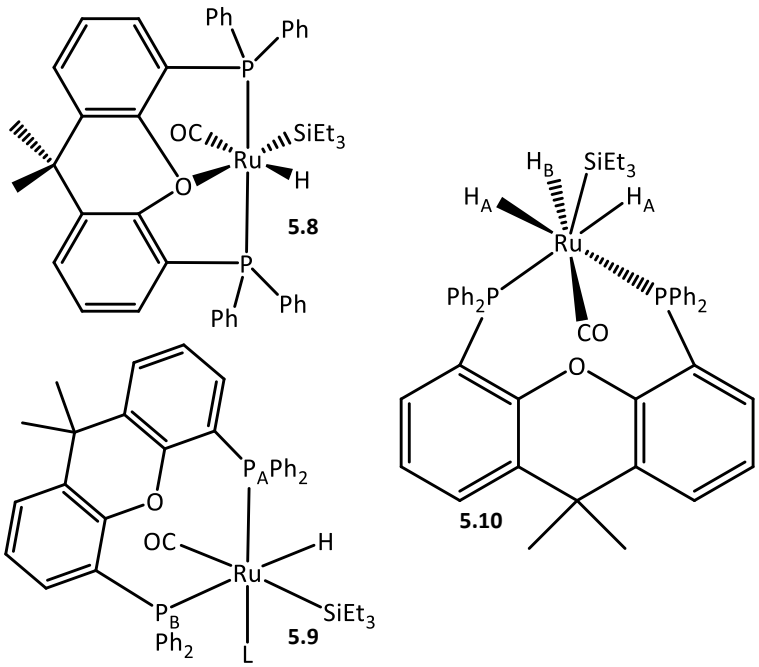

Figure 5.35: Proposed structures for the products **5.8**, **5.9** and **5.10** formed through the reaction of 5.1 with triethylsilane, L in 5.9 is undefined.

5.7.1 Characterisation of $[Ru(H)_3(Si(CH_2CH_3)_3)(Xantphos)]$ **5.10**

Upon cooling to 230 K the broad resonance now, resolve as two multiplets in the ^1H NMR spectrum at δ –7.30 and –9.12. The peak at δ –7.30 (tt 16.5, 6 Hz) only contains proton-phosphorus couplings indicative of a *cis* orientation, whereas the peak at δ –9.12 is a pseudo doublet (35 Hz) with second order couplings indicating some form of magnetic inequivalence. These resonances became a triplet (δ –7.30 J_{HH} 6 Hz, H_A) and doublet (δ –9.12 J_{HH} 6Hz, H_B) in a $^1H\{^{31}P\}$ NMR spectrum and they integrate as 1: 2 (Figure 5.36). The observed resonances are therefore suggestive of a trihydride species with two of the hydrides equivalent. The peak at δ –9.12 was modelled in g-NMR in order to gather more information on its couplings. The pseudo doublet corresponds to the sum of the of the *trans* and *cis* proton-phosphorus couplings, ($J_{HP_{Btrans}}$+ $J_{HP_{Bcis}}$).[15, 171] Aside from the doublet feature, there are few distinguishing features in this proton resonance. The presented couplings were determined based on their optimal fit to the experimental peak; values of $J_{HP_{Btrans}}$and $J_{HP_{Bcis}}$ of 62 and −24 Hz were obtained with J_{HH} 6 Hz and J_{PP} 20 Hz using the manual iteration mode.

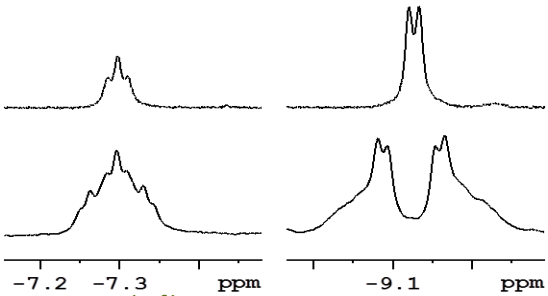

Figure 5.36: ^1H (bottom) and $^1H\{^{31}P\}$ (top) NMR spectrum at 230 K in d_8-toluene of **5.10**.

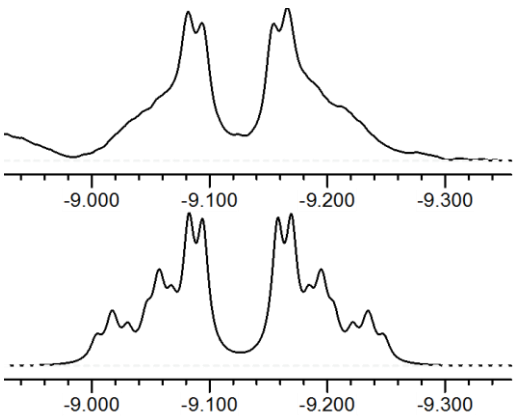

Figure 5.37: (top) experimental spectrum (bottom) simulated spectrum using g-NMR.

The low temperature NMR experiments also revealed a fourth set of resonances at δ –8.90 and –8.47 which were again characteristics of a H_3P_2 unit. In an $^1H\{^{31}P\}$:$^1H\{^{31}P\}$ EXSY experiment, performed at 205 K on a 700 MHz spectrometer, the two hydride signals of **5.10** were found to be in exchange with these resonances. Their profiles in the ^1H and $^1H\{^{31}P\}$ NMR spectra match those of **5.10** suggesting that the two interchanging species have the same structural motif. It is therefore proposed that these are two conformers of one another which differ only on the orientation of the xantphos backbone, as was also seen with **5.1** (Figure 5.6). Exchange was also observed between the hydrides in both conformers and would explain the broadness and temperature dependence of the hydride resonances. This exchange can be readily explained by a mechanism similar to a σ-CAM route only without the dissociation of the ligand.[41] The exchange between the hydrides of the same conformer was found to more facile that the conformational change by comparing the size of the exchange peaks in the $^1H\{^{31}P\}$-$^1H\{^{31}P\}$ EXSY experiment. This indicates that the hydride exchange has a lower barrier than the flip of the xantphos ligand.

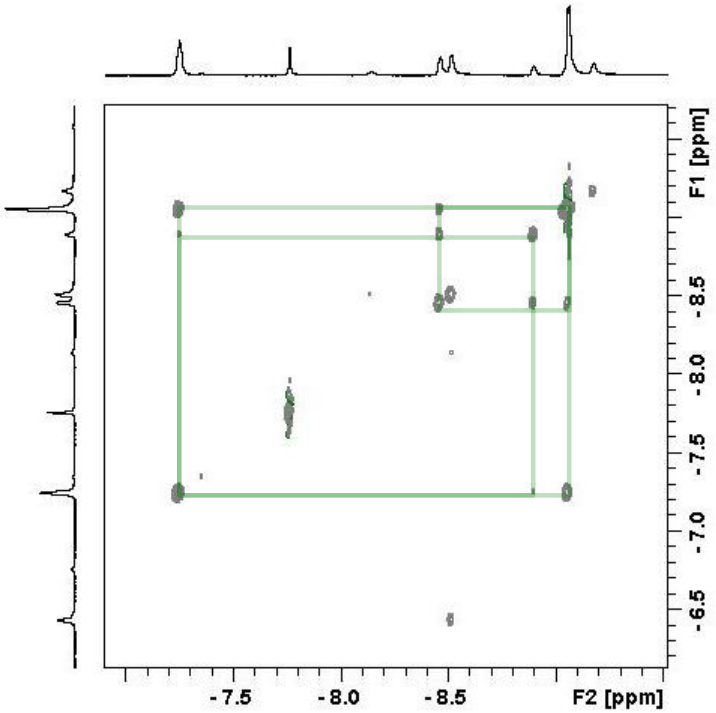

Figure 5.38: $^1H\{^{31}P\}$:$^1H\{^{31}P\}$ 2D EXSY experiment at 205 K (700 MHz) of **5.10** in d_8-toluene.

In order to confirm that these are classical hydride resonances there values respective T_1 values were measured using an inversion recovery method, at 200 K on a 500 MHz NMR spectrometer. Since the T_1 of an η^2-(H–H) bond is much smaller that the analogous oxidative addition ligands these measurements can allow $M(H)_2$ and M-η^2-(H_2) systems to be distinguished from one another.[54] T_1 values of 0.62 $\pm$ 0.04 and 0.68 $\pm$ 0.02 s were obtained for H_a and H_b respectively. Similar values were also obtained for the starting material, **5.1**, (H_A 0.53 $\pm$ 0.03 s, H_B 0.72 $\pm$ 0.02 s) and are consistent with the oxidative addition of dihydrogen and therefore it can be concluded that **5.10** does not contain a dihydrogen ligand.[54] It does not however, rule out a η^2-(H–Si) ligand.

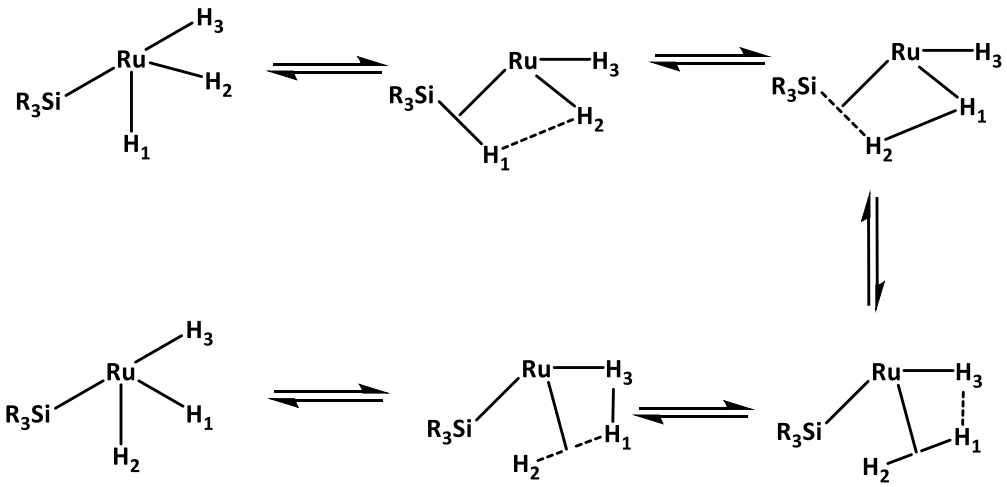

Figure 5.39: Proposed mechanism for hydride exchange.

The magnitude of the proton-silicon coupling constant can distinguish between an η^2-(H–Si) ligand and the oxidative addition of the Si–H bond. An $^1H^{29}Si$ 2D HMQC (Figure 5.40) was acquired which showed the presence of four $SiEt_3$ containing species, in addition to free Et_3SiH, however, it did not show any correlations between these silicon signals and the hydride resonances. This likely to be due to the phosphorus couplings making any potential cross peaks too broad to be observed, it was not possible to decouple phosphorus during these measurements. In the ^1H and $^1H\{^{31}P\}$ NMR spectra there are no disernable silicon satellites to allow the coupling to be measured. Both resonances are approximatley 40 Hz broad at their

baseline, in the $^{1}H\{^{31}P\}$ NMR spectrum which could obscure couplings smaller than this and would suggest that J_{HSi} is of the order of 20 Hz, or smaller and therefore consistent with the oxidative addition of Et_3SiH.

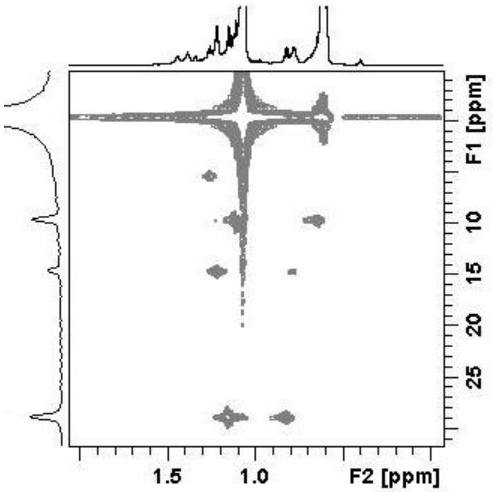

Figure 5.40: ^{1}H-^{29}Si HMQC of **5.1** following irradiation in the presence of Et_3SiH at 203 K in d_8-toluene.

A $^{1}H\{^{31}P\}$-$^{1}H\{^{31}P\}$ NOESY experiment was acquired to assign the Et_3Si resonances corresponding to each of the products. Unforunately the nOe cross peaks lacked adequate resolution to assign the hydride ligands to specfic ethyl resonances. This experiment does, however, confirm that each of the products contain an $SiEt_3$ group.

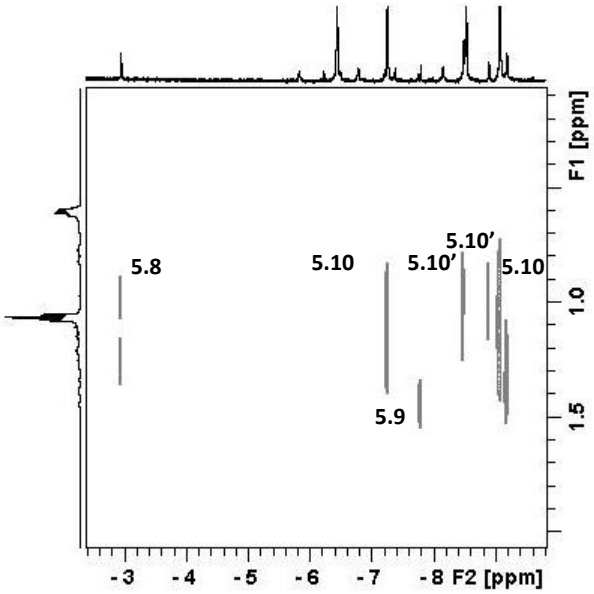

Figure 5.41: $^{1}H\{^{31}P\}$-$^{1}H\{^{31}P\}$ NOESY at 205 K (700 MHz) of **5.10** in d_8-toluene.

Finally, the NMR characteristics of the xantphos ligand were analysed. In keeping with the proposed structure of **5.10**, the two hydrides at δ –7.30 and –9.12 only show correlations to one phosphorus environment resonating at δ 32.5. This in turn shows correlations to aromatic protons at δ 6.62, 6.67 and 6.72 which would be consistent with the *ortho*- protons, signal overlap restricted any further assignments from being made.

The NMR observations are summarised below:

- There are metal hydride environments in **5.10** one at δ –7.30 and –9.12.
- There is a second isomer is evident with hydride signals at δ –8.90 and –8.47.
- The two isomers are present in a 4: 1 ratio and exchange between all four hydride resonances is observed.
- In each isomer, there is one hydride which corresponds to one proton and couples to two equivalent phosphorus environments which are *cis* relative to this ligand.
- The second hydride environment corresponds to two protons which are chemically equivalent but magnetically inequivalent and also couple to two phosphorus environments; one with a *cis* position, relative to the hydride ligand and a second *trans* to the ligand.
- The T_1 measurements for hydride ligands rule out a dihydrogen ligand and no discernible silicon satellites suggest there is no η^2-(H–Si) ligand either.
- There is only one phosphorus environment at δ 32.5 associated with the major isomer of **5.10**.

Possible structures that obey these observations are given below (Figure 5.42). Complexes A and B involve the loss of CO, in A there is a vacant site in place of the CO and in B the oxygen of the xantphos ligand has coordinated in this site. Both of these possibilities would result in a hydride chemical shift at a lower frequency that seen in this complex. Complex C is a 7 co-ordinate complex and the CO ligand has been retained. There are analogous osmium based

complex known in the literature such as $Os(H)_3(SiMe_3)(CO)(PPh_3)_2$,[172] this contains one hydride *trans* to CO, δ −8.82 (J_{HP} 19.4 $J_{H_AH_B}$ 3.4 Hz) and two chemical equivalent, magnetically inequivalent hydride resonances at δ −9.20. The couplings for this resonance were calculated from a simulated spectrum to be J_{HP} −29.9, J_{HP} 39.49, $J_{H_BH_B}$ 6.2 and J_{PP} −20 Hz. Whilst these couplings are not an exact match for the values simulated in **5.10** they are not dissimilar either and could be explained through the differences in the phosphine ligand. The chemical shifts of the hydride resonances in both complexes are consistent with one another and therefore the structure of **5.10** is thought to resemble that of structure C (Figure 5.42).

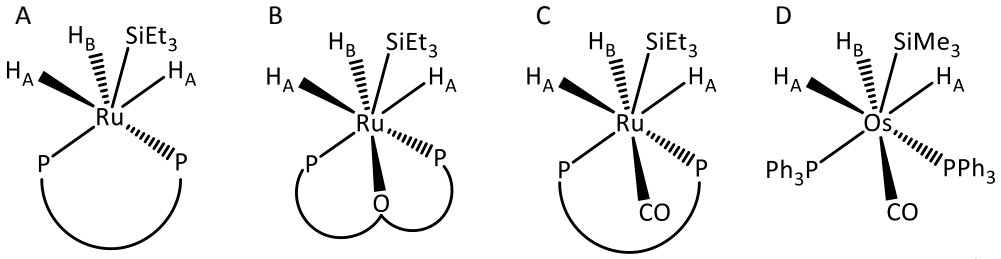

Figure 5.42: (A)-(C) Possible structures for the complex **5.10**, (D) An analogous osmium complex.[172]

5.7.2 Characterisation of [Ru(H)(CO)(Si(CH$_2$CH$_3$)$_3$)(Xantphos)] **5.8**

The defining feature of product **5.8** is a proton resonance at δ −3.09, corresponding to a monohydride, which is coupled to two phosphorus nuclei (J_{HP} 23 Hz). In a ^{1}H-^{31}P-HMQC this proton shows a correlation to just one phosphorus environment at δ 57.9 indicating that the xantphos ligand is symmetric in the product. There are two possible options which would be consistent with the observations (Figure 5.43). Structure A, is an analogue of **5.3**, the characteristics of the corresponding hydride resonance in **5.3** is a proton chemical shift of −5.96 with coupling to the two phosphorus environments are 25 and 17 Hz. This is not in keeping with the observations here. In the Section 5.8, the formation of a dihydride **5.11** containing a κ^3-(POP)-Xantphos ligand will be demonstrated. This has a similar structural motif to structure B and the corresponding hydride ligand in **5.11** is observed at δ –3.60 with a triplet coupling to phosphorus of 25 Hz, fitting the observation here in **5.8**. It is on this basis that **5.8**

has been assigned as containing a κ^3-(POP)-Xantphos ligand. The proton environments of this xantphos ligand were located using 2D NMR measurements and are summarised in Figure 5.44**Error! Reference source not found.**. For the full structure and NMR characteristics of **5.8** please refer to Figure 5.69 and Table 5.9.

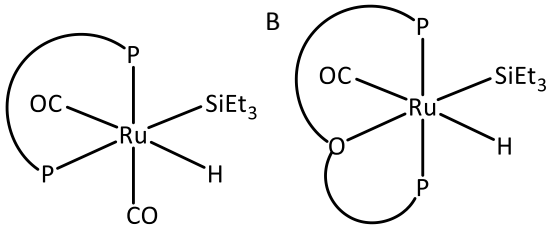

Figure 5.43: Possible structures consistent with the characteristics of **5.8**

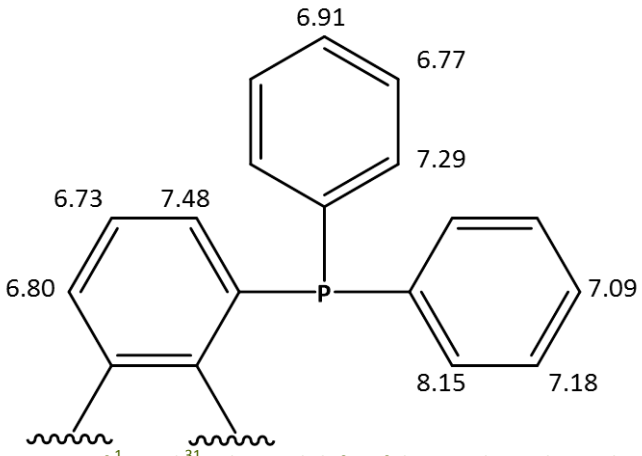

Figure 5.44: Summary of ^{1}H and ^{31}P chemical shifts of the coordinated xantphos ligand in **5.8**.

5.8 Parahydrogen studies

The studies so far have demonstrated that **5.1** is photoactive with the loss of CO, PPh_3 and H_2 being observed. The reactivity of **5.1** was next studied with parahydrogen with the different ligands already investigated. Initial studies used the *in-situ* setup with a broadband UV lamp as the light source (Experimental Section 8.3.3) to determine whether PHIP enhancements can be observed in the photoproducts. This approach uses continuous irradiation, this means that the elimination and addition of H_2 from each molecule does not occur at the same time. Since the addition of parahydrogen to the metal centre does not occur in a time-precise manner the decoherence of the ZQ_x component results. Therefore, the ^{1}H NMR spectra will be recorded

using 45° pulses to interrogate the $2I_zS_z$ component of the singlet state. Once these studies proved successful, these reactions were then be performed using the laser-based *in-situ* set up which allows for time resolved measurements to be performed (Experimental Section 8.3.2).

5.8.1 Photochemistry of **5.1** with ^{15}N-pyridine and *p*-H_2

When **5.1** was irradiated in the presence of 4-methyl-, 4-tert-butyl- or ^{15}N-pyridine a common product formed and characterised a [Ru(H)$_2$(CO)$_2$(Xantphos)] **5.3**. By combining the irradiation of **5.1** and ^{15}N-pyridine with parahydrogen, it was hoped that the potential signal enhancements will allow pyridine-containing products to be observed. An NMR sample of **5.1** and ^{15}N-pyridine in C_6D_6 was degassed and backfilled with parahydrogen. The sample was irradiated during the acquisition of ^{1}H and ^{1}H{^{31}P} NMR spectra and PHIP enhanced NMR signals were observed for **5.1** (Figure 5.45 ▲). It can therefore be concluded that the reductive elimination of H_2 has occurred from **5.1** resulting in a reactive intermediate with a singlet electronic state and thus highlights that **5.1** has, at least, some of the required characteristics for the study into the evolution of the former parahydrogen singlet state.

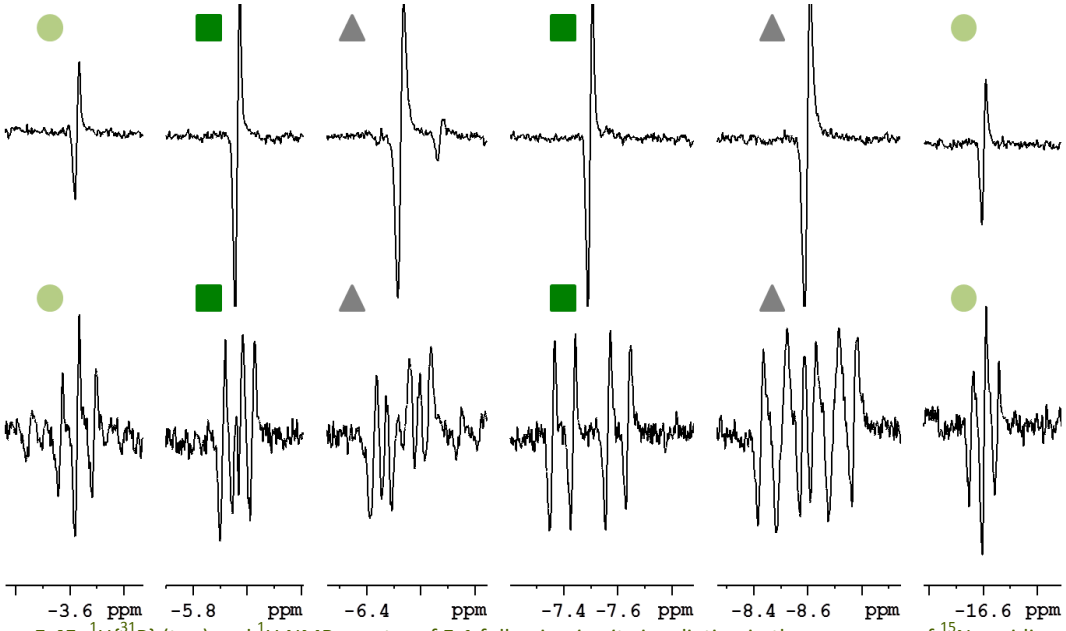

Figure 5.45: ^{1}H{^{31}P} (top) and ^{1}H NMR spectra of **5.1** following *in-situ* irradiation in the prescence of ^{15}N-pyridine and *p*-H_2. Key: ▲ **5.1**, ■ **5.3** ● new product **5.11**.

Four further PHIP enhanced hydride resonances were detected. Two of these are consistent with **5.3** (Figure 5.45 ■), the product previously observed to form through the photochemical reaction of **5.1** in the presence of ^{15}N-pyridine. The third product **5.11** (Figure 5.45 ●) yields resonances at δ –16.58 (td J_{HP} 19.5, J_{HH} 6 Hz, H_A) and δ –3.60 (td J_{HP} 25, J_{HH} 6 Hz, H_B), are consistent with a dihydride species with two phosphorus nuclei in a *cis* orientation relative to the hydride that may be equivalent. H_A is at a chemical shift consistent with a hydride *trans* to an electron donating group. There are two possible sources this group, the coordination of a pyridine group in place of the CO ligand or, alternatively, the coordination of the central oxygen in the xantphos ligand, as observed in **5.2**. ^{15}N-pyridine was chosen over 4-methyl pyridine or 4-tert-butyl pyridine as the source of pyridine owing to the labelled nitrogen which will allow any *trans*-hydride-nitrogen couplings to be observed. In the third product only coupling due to the phosphorus and hydride ligands was observed, suggesting that the product does not contain a coordinated pyridine ligand *trans* to H_A. A ^{1}H-^{31}P HMQC was recorded with parahydrogen enhancements and both hydride ligands were found to couple to single phosphorus environment at δ 58.7 and thus shows that the xantphos ligand is symmetrical in the product most likely in a *trans* coordination mode which would also be consistent with a κ^3-POP xantphos ligand. This product was not detected without the use of parahydrogen enhancements thereby limiting its characterisation.

5.8.2 Reactivity of **5.2** with *p*-H_2

To investigate whether **5.11**, the product observed in 5.8.1, contains a κ^3-POP ligand or a coordinated pyridine, the reaction of **5.2** was studied with parahydrogen. A sample of **5.2** was degassed and backfilled with 3 bar *p*-H_2. Immediately after the addition of *p*-H_2 two PHIP enhanced hydride ligands were detected (Figure 5.46 bottom) at –16.58 (td J_{HP} 19.5, J_{HH} 5.7 Hz) and δ –3.60 (td J_{HP} 25, J_{HH} 6 Hz, H_A) due to the same species as was observed with pyridine. After 3 minutes only ~50% of **5.2** remained and after 30 minutes **5.11** was no longer visible in

the equilibrium ^{1}H NMR spectrum and the reformation of **5.1** via the coordination of PPh_3 followed. It can be concluded that this product contains a κ^3-POP xantphos ligand (Figure 5.47) rather than pyridine. These signals were now also observable using standard NMR methods (Figure 5.46 top); there are other unassigned signals overlapping with the δ –3.6 proton resonance.

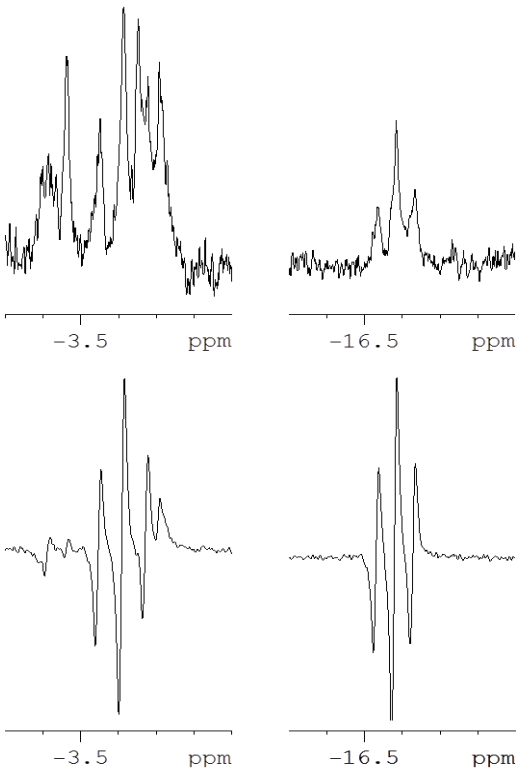

Figure 5.46: ^{1}H NMR spectrum after addition of *p*-H_2 to **5.2** forming **5.11** (bottom) hyperpolarised (top) standard NMR spectra.

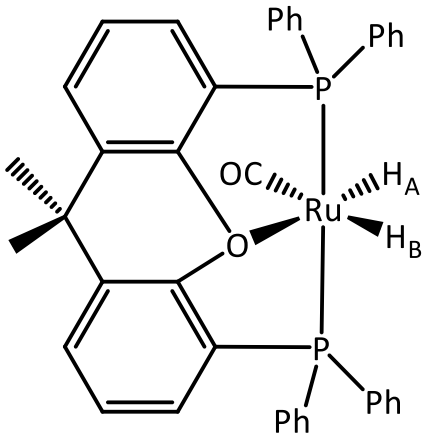

Figure 5.47: Proposed structure of **5.11**.

5.8.3 Photochemistry of **5.1** with PPh_3

In a number of reactions discussed in this chapter, the photochemical loss of PPh_3 has been observed. The reaction between **5.1** and PPh_3 will now be followed with *p*-H_2 to see if this limits the formation of side products such as **5.3** or **5.11**.

A sample of **5.1** and PPh_3 was prepared in C_6D_6 to investigate whether this affects the reactivity of **5.1**. The sample prepared and pressurised with 3 bar *p*-H_2. It was then irradiated *in-situ* and $^1H\{^{31}P\}$ NMR spectra recorded during this time and PHIP-enhanced hydride resonances for **5.1** and **5.3** were observed. The formation of **5.3** suggests that CO can compete with PPh_3 for coordination in the axial position. Unlike the reaction between **5.1** and pyridine signals associated with **5.11** were not detected which would suggest that the excess of PPh_3 reduces the κ^3 coordination mode of the xantphos ligand.

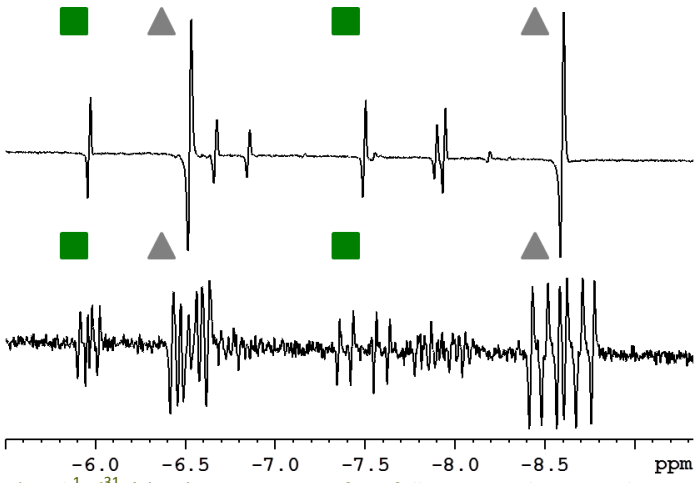

Figure 5.48: ^1H (bottom) and $^1H\{^{31}P\}$ (top) NMR spectra of **5.1** following irradiation in the presence of PPh_3 and *p*-H_2 in C_6D_6 at 298 K. Key: ▲ **5.1**, ■ **5.3** ● **5.11**.

5.8.4 Photochemistry of **5.1** with DMSO and *p*-H_2

An NMR sample containing **5.1** and 3 µL of DMSO was prepared in C_6D_6. It was then degassed and pressurised with 3 bar of *p*-H_2. The sample was irradiated and $^1H\{^{31}P\}$ NMR spectra were acquired during this time. These revealed hyperpolarised hydride signals for **5.1** (▲), **5.3** (■) and **5.11** (●). Interestingly, the proton resonances associated with **5.6** and **5.7** were not PHIP

enhanced. This would suggest that their hydride ligands are not photolabile or alternatively that the loss of DMSO is more prevalent.

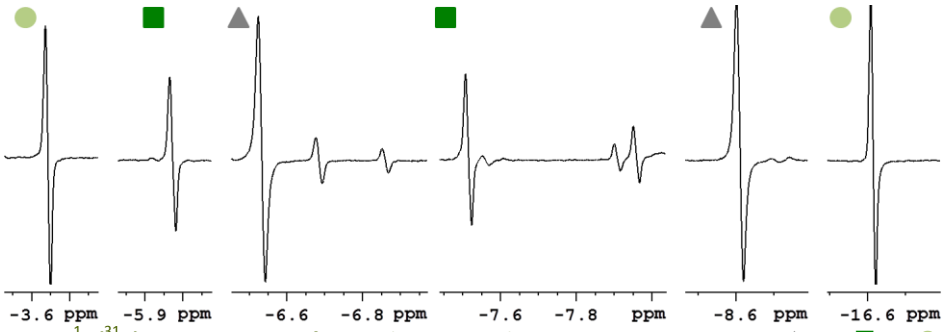

Figure 5.49: $^{1}H\{^{31}P\}$ NMR spectrum of **5.1** with DMSO and *p*-H_2, at 298 K in C_6D_6. Key: ▲ **5.1**, ■ **5.3** ● **5.11**.

These studies have demonstrated that **5.1** will undergo photoinduced H_2 reductive elimination and that when this occurs in the presence of *p*-H_2, PHIP enhanced hydrides may be observed both in the starting material. Additionally, they confirmed that CO and PPh_3 are photolabile.

5.9 Time-Resolved parahydrogen Studies

Having demonstrated that PHIP enhanced hydride signals are observed when **5.1** is irradiated under 3-bar *p*-H_2 further studies were performed using the laser based *in-situ* photolysis set up (Experimental Section 8.3.2). This involved preparing an optically dilute sample of **5.1** in d_8-toluene under 3 bar of *p*-H_2. At 600 MHz the chemical shift difference between the two hydrides of **5.1** is approximately 1230 Hz. Hence, if the zero quantum coherence of the parahydrogen singlet state is retained in the product the signal intensity of the former parahydrogen protons should oscillate at 1230 Hz. Consequently, a single laser pulse and a 90° RF pulse with a pump probe delay of 0.2 ms, should lead to a signal maximum in the response. Unfortunately, no PHIP enhanced signals were observed. The pump-probe delay was therefore varied to see if this would elicit a signal, and the experiment was repeated with a 45° pulse. Still no PHIP enhanced spectra were obtained. The difference between these experiments and the earlier studies, which did elicit PHIP enhanced signals for **5.1**, is that this is using 355 nm of

light versus broadband UV light. Furthermore, the earlier results were observed using continuous irradiation and in this experiment single laser pulses were used instead.

The experiment was therefore repeated with free PPh_3 present to minimise the impact of phosphine loss and PHIP was still not seen after 0.2 ms delay. However, when longer d1 delays were used (0.1 – 0.5 seconds) and signal averaging used (Figure 5.50) a weak response was observed (Figure 5.51). This suggests that the addition of H_2 occurs on a slower timescale than would permit the coherent retention of the zero quantum coherence.

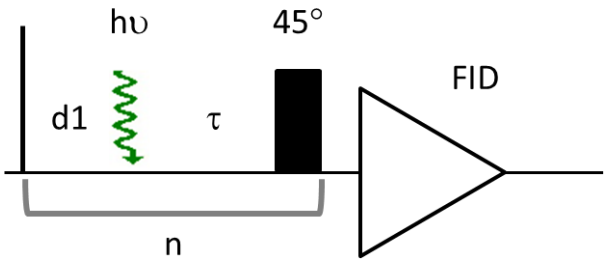

Figure 5.50: Pulse sequence for *in-situ* photolysis with signal averaging.

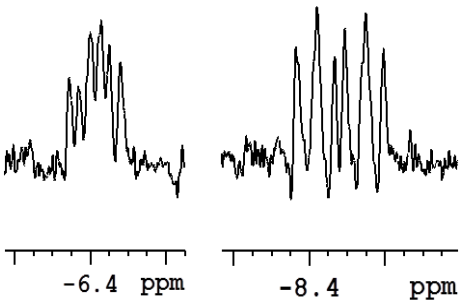

Figure 5.51: ^{1}H PHIP enhanced NMR spectrum of **5.1**, PPh_3 and *p*-H_2 in C_6D_6 at 298 K following irradiation using 8 scans and a pump-probe delay of 0.5 seconds.

To improve the signal intensity phosphorus decoupling experiments were performed. To aid the optimisation of the decoupling protocol, experiments with multiple laser pulses and a single RF pulse were acquired to give more of the PHIP-enhanced product. Using 8 laser pulses 0.1 seconds apart and a 3 ms pump probe delay and with the phosphorus decoupling centred at 40 ppm, two antiphase doublets were observed although one is broad (Figure 5.52 bottom). The same experiment was repeated with an OPSY ^{1}H NMR experiment and now only one

antiphase peak is now observed at δ –6.4, the broad second hydride resonance is no longer observable (Figure 5.52 top).

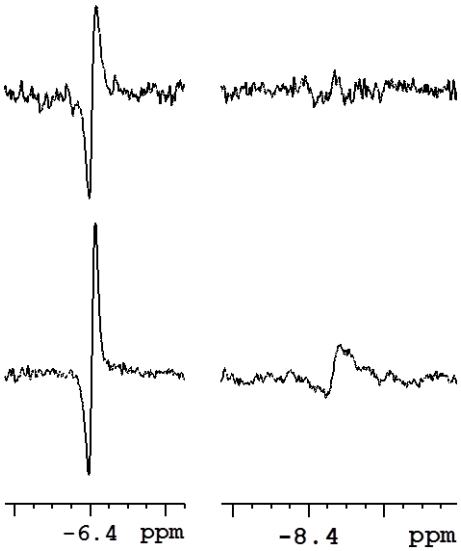

Figure 5.52: $^{1}H\{^{31}P\}$ PHIP NMR spectra for **5.1**, PPh_3 and *p*-H_2 in C_6D_6 at 298 K acquired using 8 laser pulses, 0.1 seconds apart with a pump-probe delay of 3 ms. (top) with an OPSY pulse sequence and (bottom) with a zg pulse sequence.

Despite only being able to observe one of the hydride ligands with the OPSY experiment the benefits from filtering out the thermal contributions are significant. This experiment was therefore used to monitor the growth of the signal with increasing pump-probe delays. A series of experiments were acquired using 4 NMR scans, 1 laser pulse per scan, a 30 second delay between NMR scans to allow for complete relaxation and an incremented pump-probe delay from 0.1 to 1.2 seconds. The hydride resonance was integrated and plotted against the pump-probe delay (Figure 5.53), revealing that there is an initial growth period followed by a decay. This result reflects the slow addition of *p*-H_2 to the metal centre and the subsequent relaxation of this state and demonstrates that the addition of H_2 in **5.1** occurs on a slower timescale than the evolution of the zero quantum coherence. This provides an explanation as to why no PHIP enhanced spectra were obtained with the shorter pump-probe delays which relates to the evolution of the former parahydrogen singlet state under the difference in chemical shifts of the dihydride ligands.

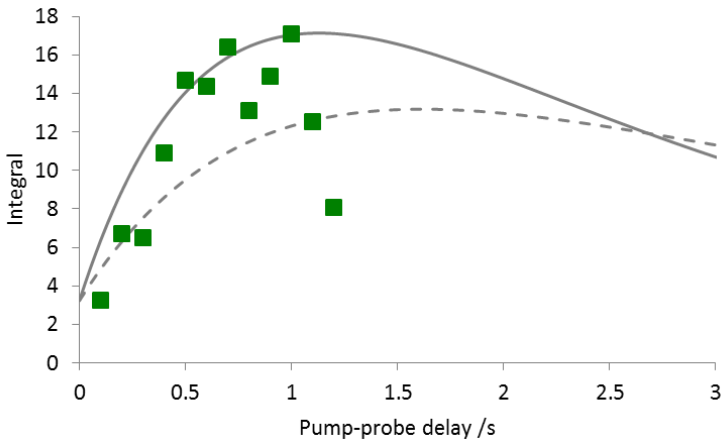

Figure 5.53: Hydride integral of **5.1** plotted against pump-probe delay using an OPSY pulse sequence, with 4 NMR scans, 1 laser pulse per NMR scan and a 30 second interscan delay, grey lines denote manual fitting, solid line = entry 1 and dashed line entry 2.

Further studies were performed on **5.1** using either, 4-tert-butylpyridine or 4-methyl pyridine, in place of free PPh_3 which allowed both hydride ligands to be observed with PHIP enhancements (Figure 5.54). In both cases, the reactivity was observed using 8 NMR scans, a single laser pulse per NMR scan and a 10 second interscan delay. For the sample containing 4-tert-butylpyridine the experiments were collected in series starting with a pump-probe delay of 0.1 s and finishing with a 5 s delay. For the sample containing 4-methylpyridine, the experiments were acquired randomly in order to reduce any systematic errors to reduce the error in the measurements. In both samples, the ^{1}H NMR spectra were integrated and these integrals plotted against the pump-probe delay (Figure 5.55–Figure 5.56). These too show a growth in signal of **5.1** followed by decay in signal due to the relaxation. The scatter in the results with randomised data collection is less than when they were acquired sequentially; however, there is still considerable variation. This is likely to be due to the errors in the measurement of the integrals owing to poor signal-to-noise due to poor PHIP enhancements.

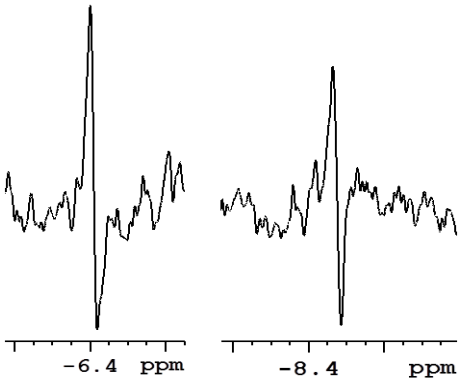

Figure 5.54: $^{1}H\{^{31}P\}$ PHIP enhanced NMR spectrum of **5.1** following 8 scans with 1 laser pulse per scan with a 0.8 s pump probe delay.

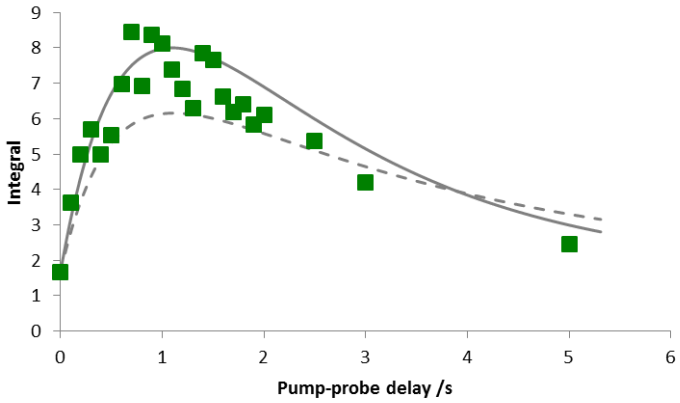

Figure 5.55: Integral of **5.1** against pump-probe delay, from sample containing 4-tert-butylpyridine, grey lines denote manual fitting, solid line = entry 3 and dashed line entry 4.

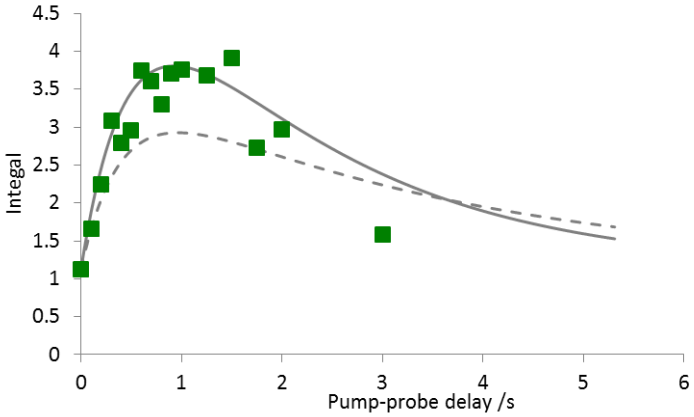

Figure 5.56: Integral of **5.1** against pump-probe delay, from sample containing 4-methylpyridine, grey lines denote manual fitting, solid line = entry 5 and dashed line entry 6.

This process can described as a two-step process where the addition of H_2 is followed by the relaxation of the parahydrogen spin state which can modelled by Equation (5.4) where A is the amplitude, k_1 the observed rate of addition, k_2 the relaxation time of the $2I_zS_z$ term and c is a constant.[87] Due to the poorly defined curves and the errors in the measurements, it was not

possible to fit the data precisely to Equation (5.4),[87] values of k_1 and k_2 however were manually estimated to give the upper and lower bounds of the data. The resulting curves displayed alongside the experimental data (grey lines) and the associated parameters are summarised in Table 5.1. These give an estimate of the observed rate constant, k_1, of between 0.3 and 0.5 s^{-1}.

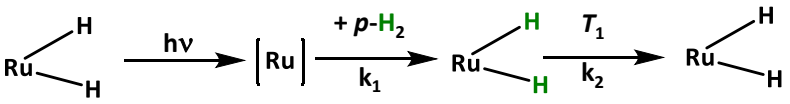

Figure 5.57: Reaction scheme for the reaction between a dihydride species and *p*-H_2 with slow addition of H_2.

$$S = A \times \frac{k_1}{k_2 - k_1} \times \left(e^{-k_1 t} - e^{-k_2 t}\right) + c \tag{5.4}$$

Table 5.1: Parameters obtained by manual fitting of observations to Equation (5.4) to give the upper and lower bounds of the observed rate constant, k_1.

Entry	A	k_1/s^{-1}	k_2/s^{-1}	c
1	57	0.6	1.25	3.24
2	50	0.35	1	3.24
3	33	0.5	1.5	1.65
4	42	0.3	2	1.65
5	17	0.5	2.1	1.13
6	20	0.3	2.5	1.13

In conclusion, **5.1** undergoes reductive elimination of H_2 upon irradiation at 355 nm. When performed under 3 bar of *p*-H_2 **5.1** is reformed with spin encoded hydride ligands. This addition was found to occur on a slower timescale than the evolution of the zero quantum coherence and therefore the signal was dephased. As a consequence, the evolution of the parahydrogen singlet state as a function of the difference in chemical shift could not be observed. The addition of H_2 to **5.1** was found to occur with a rate on the order of 0.5 s^{-1}.

Complex **5.1** was also studied using multiple laser pulses, yielding PHIP enhanced resonances for [$Ru(H)_2(CO)_2$(Xantphos)] **5.2** and [$Ru(H)_2(CO)(\kappa^3$-POP-Xantphos)] **5.11** as well as **5.1** (Figure 5.58). After a period of irradiation, the signals associated with **5.11** were visible with a single NMR scan, a single laser pulse and short pump-probe delay suggesting that the addition of H_2 in this complex would occur on a suitable time frame for coherent retention of the

parahydrogen singlet state. At 600 MHz, the chemical shift difference between the two hydride ligands of **5.11** is 7780 Hz. Preliminary studies showed PHIP enhanced signals with a 150 µs delay and no signal at 300 µs in keeping with an oscillation frequency of ~7000 Hz (Figure 5.59). Unfortunately, **5.11** did not prove to be thermally stable and it did not form in sufficient concentration for its oscillatory behaviour to be studied reflecting the preference for PPh_3 coordination to reform **5.1**. In the literature there are stable ruthenium complexes with xantphos derived POP ligands, that may prove more successful precursors for $[Ru(H)_2(\kappa^3$-POP-Xant)] species.

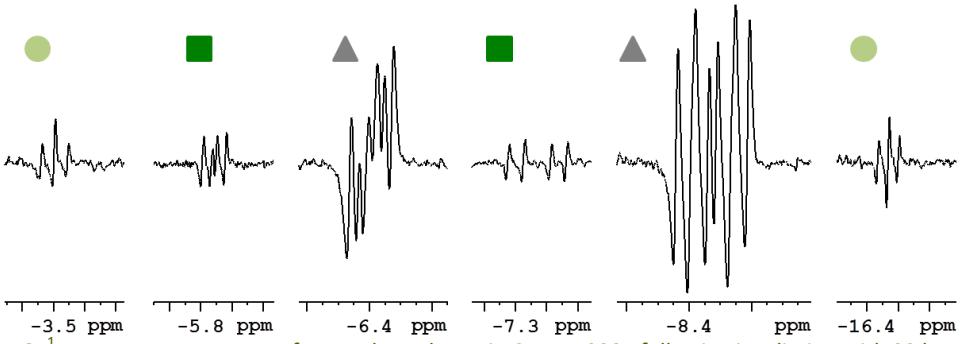

Figure 5.58: ^{1}H PHIP NMR spectrum of **5.1**, PPh_3 and *p*-H_2 in C_6D_6 at 298K following irradiation with 32 laser pulses at 355 nm Key: ▲ **5.1**, ■ **5.3** ● **5.11**.

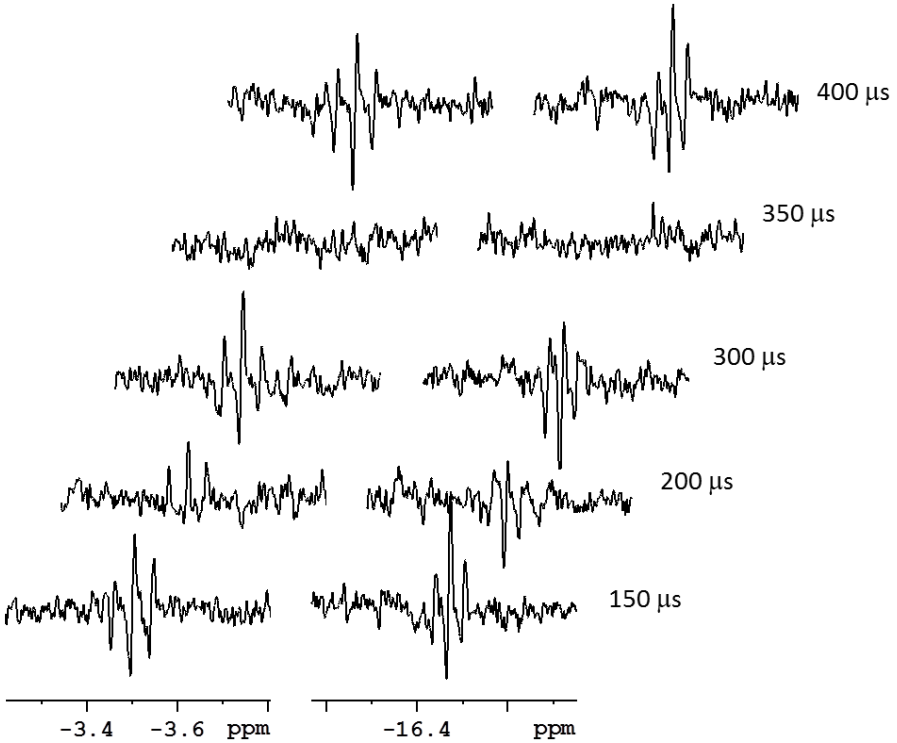

Figure 5.59: ^{1}H NMR spectra of **5.11** in C_6D_6 at 298 K, with 1 laser pulse, 1 NMR pulse with an incrementing delay (labelled) between them.

5.10 Conclusions

The ruthenium dihydride complex $[Ru(H)_2(CO)(PPh_3)(Xantphos)]$ **5.1** was synthesised and characterised by NMR spectroscopy. Low temperature measurements revealed fluxionality within the coordinated xantphos backbone which was rationalised by the flipping of the central ether containing ring on the xantphos ligand. This observation was consistent with the literature for related systems. Exchange between the two coordination sites of the xantphos ligand, as well as between the two hydride ligands, was also observed. The exchange process was attributed to a trigonal twist mechanism.[169]

The photochemical activity of **5.1** was studied initially with ethene where irradiation resulted in a single product **5.2** which contained only one phosphorus resonance. It was proposed that this product contained a κ^3-POP xantphos ligand in addition to the coordinated ethene. Its formation demonstrated that both the hydride ligands and the triphenylphosphine ligand may be lost photochemically.

The loss of both CO and PPh_3 was also observed when **5.1** was irradiated in the presence of pyridine derived ligands through formation of the bis-carbonyl product **5.3**. The identity of **5.3** was confirmed via the reaction between **5.1** and CO where the tricarbonyl product **5.4** was also detected. It was proposed that its formation came about through the loss CO from a second molecule of **5.1**. Subsequent reactions between **5.1** and DMSO corroborated this assumption by the substitution of CO with DMSO in **5.7**. Another DMSO containing product was observed, **5.6**, where the substitution of PPh_3 was observed. This product yielded one broad hydride resonance at δ –10.33 which resolved to be a doublet of doublets of doublets (J_{HP} 31.5 and 15.5 Hz, J_{HH} 7.5 Hz) upon cooling to 253 K which allowed this product to be characterised.

Following on from this study, **5.1** was studied in the presence of triethylsilane. Initial studies showed the formation of two monohydride species, both of which showed coupling to two

phosphorus environments, and a broad fluxional species. Low temperature characterisation was performed revealing the broad resonance as a trihydride species contained two equivalent hydrides which contain second ordered coupling to phosphorus and a third hydride which only contained *cis* couplings to phosphorus. All of the hydrides species were determined to correspond to the oxidative addition of the H_2 using T_1 measurements. It was not possible to measure the hydride-silyl coupling (J_{HSi}) to determine the whether silane has added oxidatively to the metal centre. There are no discernible silicon satellites on the hydride resonances which would suggest that they are contain within the broadness of the peak making it unlikely that the silane ligand is coordinated as an η^2-(Si–H) ligand. Therefore it is likely that the complex is a novel Ru^{IV} species. A second set of signals were also observed with low temperature experiments, since there is only one possible arrangements of the ligands which fits the NMR characteristics this was postulated to be due to a similar fluxional process as was observed in **5.1**. The photochemical reactivity of **5.1** with each of the ligands is summarised in Figure 5.60.

Following this, **5.1** was studied with the ^{15}N-pyridine, triphenylphosphine or DMSO using parahydrogen and *in-situ* photolysis with broadband irradiation. PHIP enhanced hydrides were observed for **5.1** and **5.3** demonstrating that these species will undergo the reductive elimination of H_2 following irradiation with an intermediate which has a singlet electronic state. A new product was also observed and this was proposed to be due to [$Ru(H)_2(CO)(\kappa^3$-POP-Xantphos)] **5.11** based on its observation in the reaction between **5.2** and *p*-H_2. Other species were detected with weaker signals but only limited information was obtained on them. One possible explanation is the isomerisation of the ruthenium systems. The experiments with **5.1** and DMSO only revealed PHIP signals for common products and not the DMSO containing products, **5.6** and **5.7** and was attributed to either the lack of H_2 exchange in these products or the preferable loss of DMSO. The observations made during the parahydrogen reactions are summarised in Figure 5.61.

The observation in these studies that the xantphos ligand can switch between being a bidentate and κ^3-POP pincer type ligand supports observations in the literature that reaction mechanisms proceed via κ^3-POP xantphos intermediates.[102] The loss of the PPh_3 ligand in addition to the hydride ligands are consistent with observations seen during thermal reactions of **5.1** and similar products.[56, 102, 173] The thermal reactions proceed at high temperatures, typically between 343–423 K;[101, 166] it would be interesting to investigate whether these reported reactions can proceed photochemically and therefore at lower temperatures. Furthermore, if these studies were performed using parahydrogen the detection of reaction intermediates would be an intereting prospect. Additionally, n the reaction between X and Y, the formation of **5.1** was identified as the deactivation product it would be interesting to see if photochemistry could be used to turn **5.1** back into a reactive species.

Finally, time-resolved experiments were performed. The intention was to study the evolution of the former parahydrogen singlet state as a function of the chemical shift difference between the two hydride ligands of **5.1**. The addition of H_2 to **5.1** was found to occur on a slower time scale than would facilitate such studies with an observed rate constant estimated to between 0.3 and 0.5 s^{-1}. This demonstrates that this approach may be used on reactions which take place on a subsecond timeframe. The use of *in-situ* photolysis with parahydrogen provides a clearly defined starting point creating terms which can later be interrogated by a suitable RF pulse allowing the monitioring of a reaction that takes prior to the NMR experiment. The synchronicity of the laser and NMR spectrometer allows the advantages of signal averaging to be used whilst retaining the time resolution between the laser pump and NMR probe step.

When multiple laser pulse experiments were performed enhanced hydrides corresponding to **5.3** and **5.11** were also observed. The hydride resonances associated with **5.11** were observed with single laser and NMR pulses with short pump-probe delays (in the order of microseconds)

and preliminary results were consistent with an oscillation on a timescale of 7000 Hz in keeping with the chemical shift difference between the two hydride resonances in **5.11**. This complex, however, proved to be thermally unstable which limited these studies. In 2014[15] it was first reported that the combination of *in-situ* photochemistry and parahydrogen allows for the synchronised addition of *p*-H_2 to the ruthenium centre permitting the ZQ_x component of the parahydrogen singlet state to be retained and thus its evolution as a function of the chemical shift difference to be observed. These preliminary results would suggest that this observation is possible in other ruthenium systems also. So far, this observation has only been observed in systems where the addition of H_2 to the metal centre has occurred on a much faster timescale than the evolution of the ZQ_x component of the singlet state. It is predicted that that if we were to observed the growth of a dihydride species as well as the oscillation it is more likely that this will be observed when there is a large chemical shift difference between the two hydrides and thus the oscillation occurs at a faster rate. The 7000 Hz frequency in **5.11** would fit this bill and therefore other κ^3-POP xantphos containing complexes be interesting targets for future work.

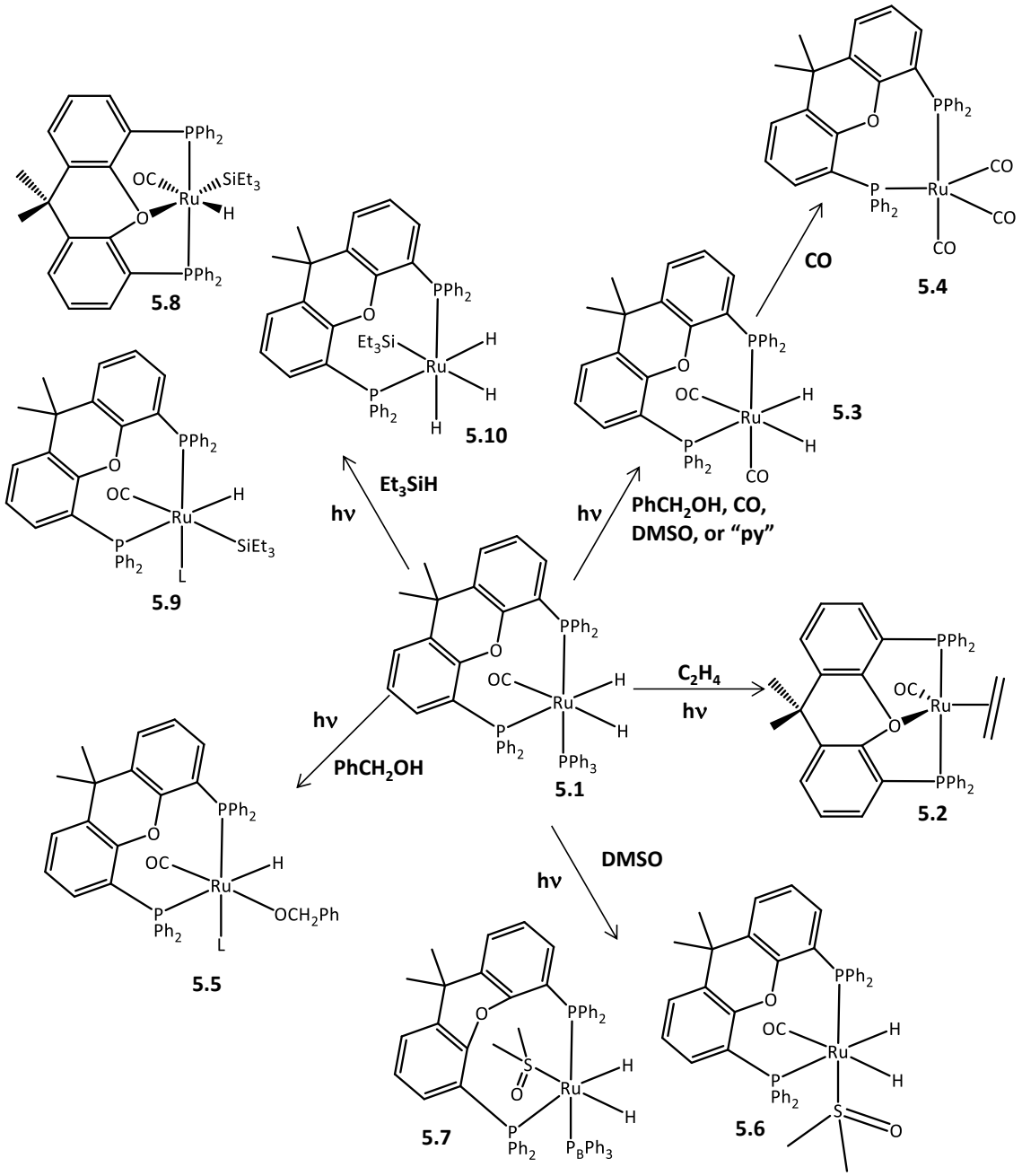

Figure 5.60: Summary of the photochemical reactivity of $Ru(H)_2(CO)(PPh_3)$(Xantphos) **5.1** with C_2H_4, DMSO, $PhCH_2OH$, Et_3SiH, CO and "py" where py refers to ^{15}N-pyridine, 4-methylpyridine and 4-tert-butylpyridine.

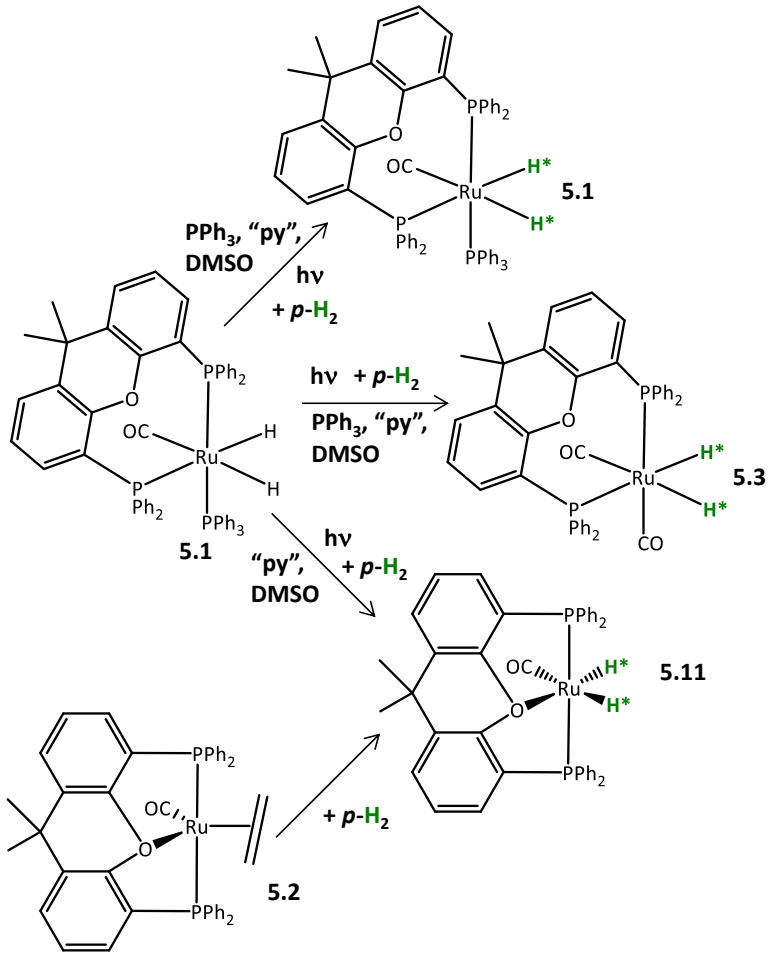

Figure 5.61: Summary of the reactions of **5.1** and **5.2** with parahydrogen in the presence of PPh_3, DMSO and "py" where py refers to ^{15}N-pyridine, 4-methylpyridine and 4-tert-butylpyridine.

5.11 Structures and NMR data

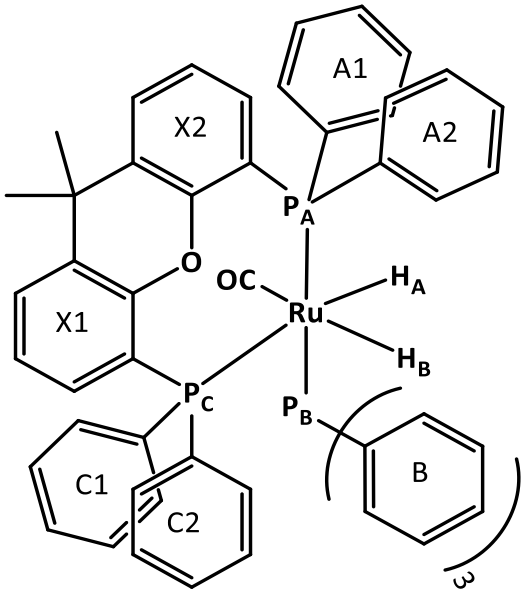

Figure 5.62: Fully labelled structure of $[Ru(H)_2(CO)(PPh_3)(Xantphos)(PPh_3)]$ **5.1**.

Table 5.2: NMR Characterisation for $[Ru(H)_2(CO)(P\text{-}Ph_3)(Xantphos)(PPh_3)]$ **5.1**.

	δ/ppm (multiplicity)	Coupling constant/Hz	Assignment	Group
^{1}H	7.84 (br)		*o*-H^{A1}	Xantphos
	7.73 (overlap)		*o*-H^{A2}	Xantphos
	7.69 (br)		*o*-H^{B}	PPh_3
	7.35 (t)	J_{HP}, H_{HH} 8.2	*o*-H^{C2}	Xantphos
	7.24 (t)	J_{HP}, J_{HH} 8.2	*o*-H^{C1}	Xantphos
	7.02 (overlap)		*p*-H^{A1}	Xantphos
	7.01 (overlap)		*m*-H^{A1}	Xantphos
	6.92 (overlap)		*m* & *p*-H^{B}	PPh_3
	6.89 (overlap)		*m*-H^{A2}	Xantphos
	6.81 (br)		*m*-H^{C2}	Xantphos
	6.76 (br d)	J_{HH} 6.8	*p*-H^{C1}	Xantphos
	6.64 (t)	J_{HH} 7.2	*m*-H^{C1}	Xantphos
	1.46 (s, 3H)		Me^{A}	Xantphos
	1.38 (s, 3H)		Me^{B}	Xantphos
	–8.67* (dddd)	J_{HP} 77.1, 33.4, 26.6, J_{HH} 7	H_A	Ru–H
	–6.62* (dddd)	J_{HP} 36.6, 29.6, 16.1, J_{HH} 7	H_B	Ru–H
^{13}C	134.6		*o*-C^{A1}	Xantphos
	133.9		*o*-C^{A2}	Xantphos
	133.6		*o*-C^{C1}	Xantphos
	133.4		*o*-C^{C2}	Xantphos
	132.1		*o*-C^{B}	PPh_3
	128.0		*p*-C^{B}	PPh_3
	127.2		*m*-C^{B}	PPh_3
^{31}P	58.3 (d, 1P)	J_{PP} 240	P_B	PPh_3
	47.6 (d, 1P)	J_{PP} 240	P_A	Xantphos
	30.4 (s, 1P)		P_C	Xantphos

*Couplings measured using g-NMR

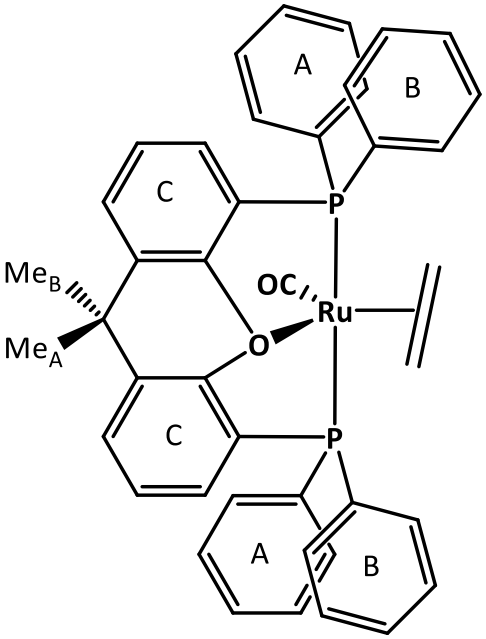

Figure 5.63: Structure of [Ru(C_2H_4)(CO)(Xantphos)] **5.2**.

Table 5.3: NMR Characterisation for [Ru(C_2H_4)(CO)(Xantphos)] **5.2**.

	δ/ppm (multiplicity, integration)	Coupling constant/Hz	Assignment	Group
^{1}H	8.15 (m, 4H)	J_{HH} 7.6	*o*-H^B	Xantphos
	7.48 (m, 2H)	J_{HH} 7.6	*o*-H^C	Xantphos
	7.29 (m, 4H)	J_{HH} 7.6	*o*-H^A	Xantphos
	7.18 (m, 4H)	J_{HH} 7.6	*m*-H^B	Xantphos
	7.09 (m, 2H)	J_{HH} 7.6	*p*-H^C	Xantphos
	6.91 (m, 2H)	J_{HH} 7.3	*p*-H^A	Xantphos
	6.80 (overlap)		*p*-H^C	Xantphos
	6.77 (overlap)	J_{HH} 8	*m*-H^A	Xantphos
	6.73 (overlap)	J_{HH} 8	*m*-H^C	Xantphos
	2.79 (d, 2H)		CH_2	C_2H_4
	1.63 (d, 2H)		CH_2	C_2H_4
	1.24 (s, 3H)		Me$_A$	Xantphos
	1.03 (s, 3H)		Me$_B$	Xantphos
^{13}C	133.5		*o*-C^B	Xantphos
	131.7		*o*-C^C	Xantphos
	131.6		*o*-C^A	Xantphos
	128.9		*p*-C^B	Xantphos
	128.1		*m*-C^B	Xantphos
	127.6		*p*-C^A	Xantphos
	125.7		*m*-C^C	Xantphos
	124.9		*m*-C^C	Xantphos
	124.8		*p*-C^C	Xantphos
	31.0		$CH_3{}^B$	Xantphos
	30.7		CH_2	C_2H_4
	21.8		$CH_3{}^A$	Xantphos
^{31}P	51.3 (s, 2P)		P	Xantphos

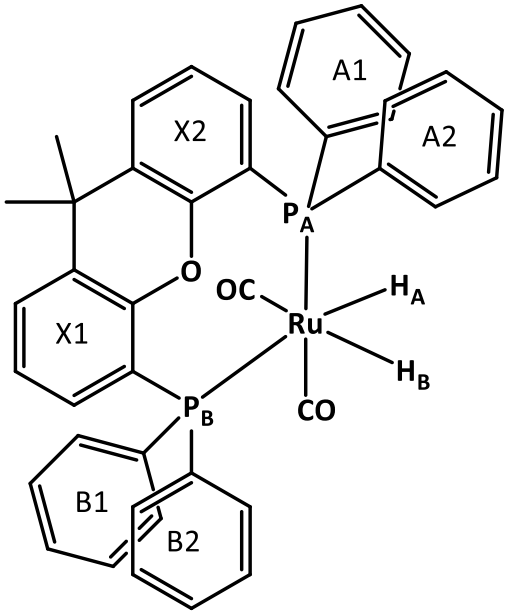

Figure 5.64: Structure of $[Ru(H)_2(CO)_2(Xantphos)]$ **5.3**.

Table 5.4: NMR Characterisation for $[Ru(H)_2(CO)_2(Xantphos)]$ **5.3**.

	δ/ppm (multiplicity)	Coupling constant/Hz	Assignment	Group
^{1}H	7.57 (overlap)		*o*-H^{A1}	Xantphos
	7.49 (overlap)		*o*-H^{B2}	Xantphos
	6.76 (overlap)		*m*-H^{A1}	Xantphos
	6.67 (overlap)		*m*-H^{A2}, *o*-H^{B1}	Xantphos
	6.47 (overlap)		*o*-H^{A2}	Xantphos
	–7.51 (ddd)	J_{HP} 81.6, 30.5, J_{HH} 6.5	H_A	Ru–H
	–5.97 (ddd)	J_{HP} 26.0, 17.5, J_{HH} 6.5	H_B	Ru–H
^{31}P	34.9 (d)	J_{PP} 23.6	P_A	Xantphos
	24.3 (d)	J_{PP} 23.6	P_B	Xantphos

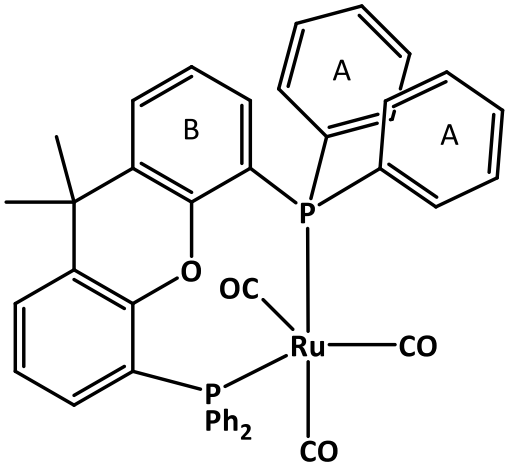

Figure 5.65: Structure of [Ru(CO)$_3$(Xantphos)] **5.4**.

Table 5.5: NMR Characterisation for [Ru(CO)$_3$(Xantphos)] **5.4**.

	δ/ppm (multiplicity)	Coupling constant/Hz	Assignment	Group
^{1}H	7.62 (br)		*o*-H$_A$	Xantphos
	7.08 (d)	J_{HH} 7.8	*p*-H$_B$	Xantphos
	6.93 (overlap)		*m*-H$_A$	Xantphos
	6.74 (t)	J_{HH} 7.5	*m*-H$_B$	Xantphos
	6.64 (t)	J_{HH} J_{HP} 7.8	*o*-H$_B$	Xantphos
^{31}P	27.8 (s)		P	Xantphos

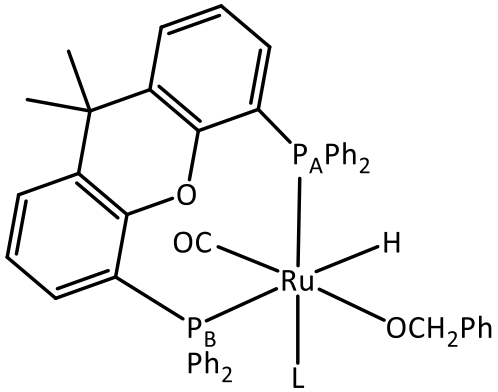

Figure 5.66: Structure of [Ru(H)(OCH$_2$Ph)(CO)(L)(Xantphos)] **5.5**.

Table 5.6: NMR Characterisation for [Ru(H)(OCH$_2$Ph)(CO)(L)(Xantphos)] **5.5**.

	δ/ppm (multiplicity)	Coupling constant/Hz	Assignment	Group
^{1}H	–6.22 (dd)	J_{HP} 62.8, 27.7	Ru–H	Ru–H

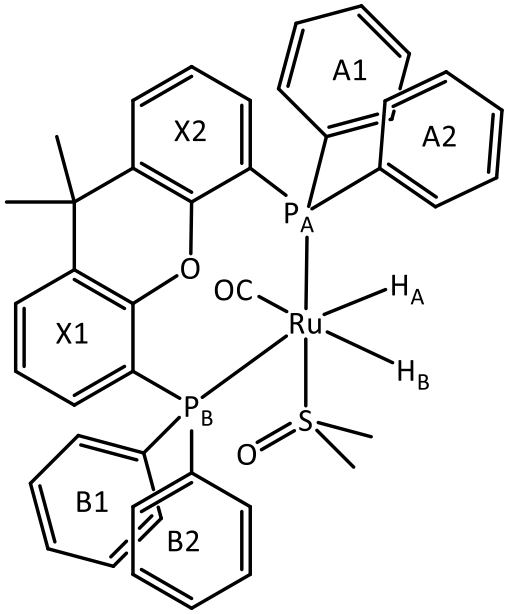

Figure 5.67: Structure of [Ru(H)$_2$(CO)(DMSO)(Xantphos)] **5.6**.

Table 5.7: NMR Characterisation for [Ru(H)$_2$(CO)(DMSO)(Xantphos)] **5.6**.

	δ/ppm (multiplicity)	Coupling constant/Hz	Assignment	Group
^{1}H	6.71 (overlap)		*o*-H P^{A}	Xantphos
	6.39 (overlap)		*o*-H P^{B}	Xantphos
	1.72 (s)		Me$_A$	Ru–DMSO
	2.52 (s)		Me$_B$	Ru–DMSO
	–8.10 (ddd)	J_{HP} 80.9, 30.1, J_{HH} 7.6	H$_A$	Ru–H
	–10.33 (ddd)	J_{HP} 31.5, 15.5, J_{HH} 7.6	H$_B$	Ru–H
^{13}C	50.3		Me$_B$	Ru–DMSO
	55.2		Me$_A$	Ru–DMSO
^{31}P	27.1 (d)	J_{PP} 30	P$_A$	Xantphos
	36.4 (d)	J_{PP} 30	P$_B$	Xantphos

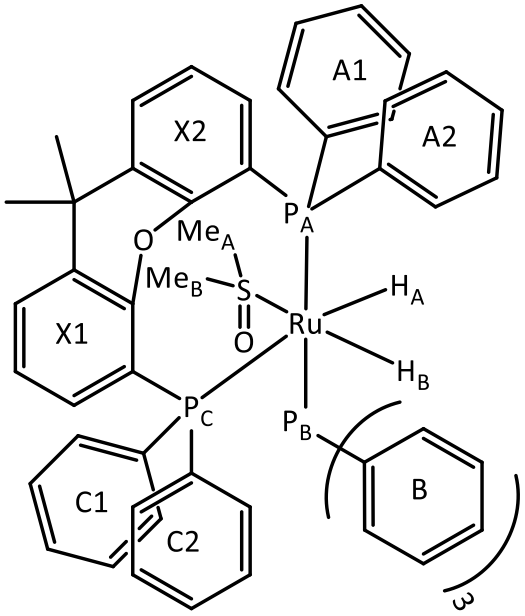

Figure 5.68: Structure of $[Ru(H)_2(DMSO)(PPh_3)(Xantphos)]$ **5.7**.

Table 5.8: NMR Characterisation for $[Ru(H)_2(DMSO)(PPh_3)(Xantphos)]$ **5.7**.

	δ/ppm (multiplicity, integration)	Coupling constant/Hz	Assignment	Group
^{1}H	8.00 (overlap)		*o*-H^{C1}	P_C-Xantphos
	7.85 (t, 6H)	J_{HH} 8 J_{HP} 9	*o*-H^{B}	P_BPh_3
	7.76 (overlap)		*o*-H^{A2}	P_A-Xantphos
	7.69 (m, 3H)		*p*-H^{B}	P_BPh_3
	7.53 (overlap)		*o*-H^{X1}	P_C-Xantphos
	7.10 (overlap)		*o*-H^{C2}	P_C-Xantphos
	7.06 (overlap)		*m*-H^{C1}	P_C-Xantphos
	6.95 (overlap)		*m*-H^{B}	P_BPh_3
	6.95 (overlap)		*o*-H^{X2}	P_A-Xantphos
	6.83 (overlap)		*m*-H^{A2}	P_A-Xantphos
	6.76 (overlap)		*m*-H^{C2}	P_C-Xantphos
	6.64 (t, 2H)	J_{HH} 7	*m*-H^{A1}	P_A-Xantphos
	6.25 (t, 2H)	J_{HP} 7 J_{HH} 7	*o*-H^{A1}	P_A-Xantphos
	2.13 (s, 3H)		Me_B	Ru–DMSO
	1.20 (s, 3H)		Me_A	Ru–DMSO
	–9.90 (dddd, 1H)	J_{HP} 71, 38, 26 J_{HH} 7.5	H_A	Ru–H
	–11.22 (dddd, 1H)	J_{HP} 37, 31, 17 J_{HH} 7.5	H_B	Ru–H
^{13}C	50.1		Me_A	Ru–DMSO
	54.6		Me_B	Ru–DMSO
	134.4		*o*-C^{B}	P_BPh_3
	133.9		*p*-C^{B}	P_BPh_3
	127.3		*m*-C^{A1}	P_A-Xantphos
^{31}P	31.3 (dd, 1P)	J_{PP} 17, 18	P_C	Xantphos
	43.8 (dd, 1P)	J_{PP} 245, 18	P_A	Xantphos
	54.7 (dd, 1P)	J_{PP} 245, 17	P_B	PPh_3

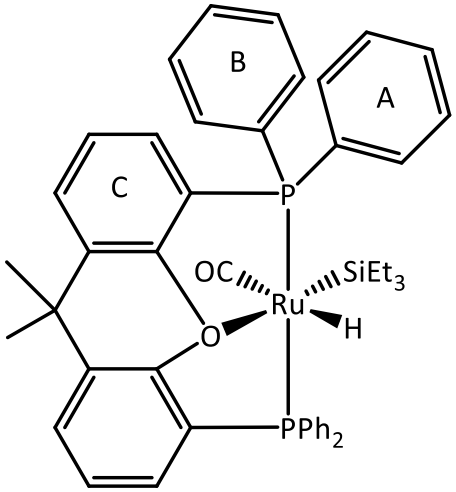

Figure 5.69: Proposed structure of [Ru(H)($SiEt_3$)(CO)(Xantphos)] **5.8**.

Table 5.9: NMR Characterisation for Ru(H)($SiEt_3$)(CO)(Xantphos)] **5.8**.

	δ/ppm (multiplicity)	Coupling constant/Hz	Assignment	Group
^{1}H	8.51 (m)	J_{HH} 7.5	*o*-H^{B}	Xantphos
	7.95 (m)		*o*-H^{A}	Xantphos
	7.31 (t)	J_{HH} J_{HP} 7.0	*o*-H^{C}	Xantphos
	7.20 (overlap)		*m*-H^{B}	Xantphos
	7.14 (overlap)		*m*-H^{A}	Xantphos
	7.07 (overlap)		*p*-H^{B}	Xantphos
	7.01 (overlap)		*p*-H^{A}	Xantphos
	–3.09 (t)	J_{HP} 23.8	H	Ru–H
^{13}C	134.3		*o*-C^{B}	Xantphos
	132.8		*o*-C^{A}	Xantphos
	132.2		*o*-C^{C}	Xantphos
^{31}P	57.9 (s)		P	Xantphos

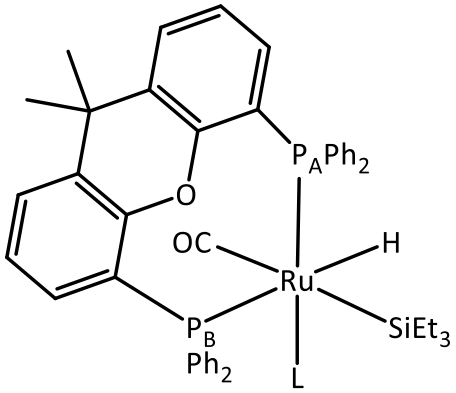

Figure 5.70: Structure of [Ru(H)(SiEt$_3$)(CO)(L)(Xantphos)] **5.9**.

Table 5.10: NMR Characterisation for [Ru(H)(SiEt$_3$)(CO)(L)(Xantphos)] **5.9.**

	δ/ppm (multiplicity)	Coupling constant/Hz	Assignment	Group
^{1}**H**	–8.06 (dd)	J_{HP} 56.4, 16	H	Ru–H
^{31}**P**	26.7 (br)		P_A	Xantphos
	27.6 (br)		P_B	Xantphos

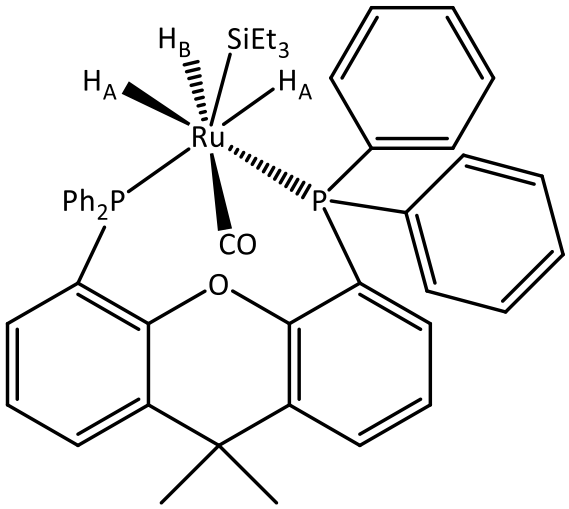

Figure 5.71: Structure of [Ru(H)$_3$(SiEt$_3$)(Xantphos)] **5.10**.

Table 5.11: NMR Characterisation for [Ru(H)$_3$(SiEt$_3$)(Xantphos)] **5.10**.

	δ/ppm (multiplicity, integration)	Coupling constant/Hz	Assignment	Group
^{1}**H**	6.72		*o-H*	Xantphos
	6.67		*o*-H	Xantphos
	6.62		*o*-H	Xantphos
	–7.30 (t)	J_{HH} 6	H_B	Ru–H
	–9.12 (d)	J_{HH} 6	H_A	Ru–H
^{31}**P**	32.5		P	Xantphos

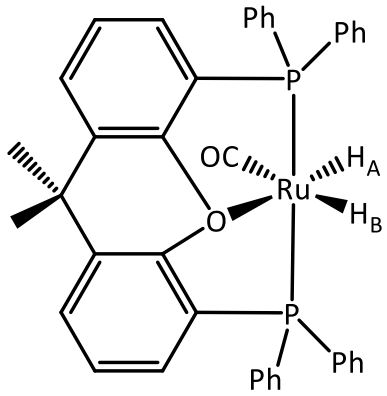

Figure 5.72: Structure of $[Ru(H)_2(CO)(Xantphos)]$ **5.11**.

Table 5.12: NMR Characterisation for $[Ru(H)_2(CO)(Xantphos)]$ **5.11**.

	δ/ppm (multiplicity)	Coupling constant/Hz	Assignment	Group
^{1}**H**	–3.60 (td)	J_{HP} 25.0, J_{HH} 6	H_B	Ru–H
	–16.58 (td)	J_{HP} 19.5, J_{HH} 6	H_A	Ru–H

6 Synthesis, Characterisation and Photochemistry of *cis*-[Ru(H)$_2$(dppp)$_2$] **6.1** with parahydrogen

6.1 Introduction

One of the goals of this research was to study hydrogenation reactions using parahydrogen. Parahydrogen is a hyperpolarisation source and can create NMR signals much larger than would be seen with standard NMR methods. In Section 1.2.4.2 the theory of NMR is described in terms of product operators using thermal equilibrium magnetisation. By using parahydrogen the starting states in an NMR experiment are different and this means that the starting states are different to those associated with thermal equilibrium magnetisation. The resulting observations within an NMR experiment will also be different, therefore it is important to understand the behaviour of parahydrogen during an NMR experiment in order to interpret the observations when it is used in hydrogenation reactions There are two scenarios for parahydrogen addition to a metal complex and these were described. The first occurs when parahydrogen reacts slowly with a metal complex which results in the decoherence of the ZQ_x term and therefore only the $2I_zS_z$ term remains.[28] After excitation with an RF_x pulse, this $2I_zS_z$ term gives rise to the terms I_yS_z and I_zS_y, which are responsible for the antiphase PHIP NMR signals that are commonly seen.[25, 27] Owing to the sin2θ relationship associated with the creation of these terms, they have a maximum intensity when a 45° pulse is used. If a 90° pulse were used instead, no PHIP enhanced NMR signals would be observed.

A second scenario is seen when the addition of parahydrogen to a metal complex occurs in a time precise manner and, as such, the decoherence of the ZQ_x term is not observed. The use of *in-situ* photochemistry has provided a route for rigorous time control in the addition of parahydrogen to a metal centre and thus provides a route to this second scenario.[15] This was recently exemplified for the first time using Ru(H)$_2$(CO)(PPh$_3$)$_3$ and *cis*-[Ru(H)$_2$(dppe)$_2$][15] although it had been predicted in the original paper theorising that *p*-H$_2$ could be used a

hyperpolarisation source.[24] Both of these complexes lose H_2 during the 10 ns laser pulse and the reactive intermediates re-add H_2 on a microsecond timescale. When this is performed under a headspace of *p*-H_2, the resultant hydride ligands retain the spin encoded *p*-H_2 spin state. Once the symmetry of the former parahydrogen singlet state has been broken in the product, the zero quantum term of the singlet state evolves. There are two mechanisms through which this can occur. The first is via the introduction of chemical inequivalence (Figure 6.1A) and evolution of the zero quantum terms occurs as a function of the difference in chemical shift between the two former parahydrogen protons. This process has been demonstrated using $RuH_2(CO)(PPh_3)_3$.[15] Initially, the terms which result from the ZQ_x and $2I_zS_z$ starting states are in balance and thus RF excitation leads to no visible signal. Subsequently, the evolution of ZQ_x changes this situation so that detectable signal results. ZQ_x actually evolves into ZQ_y by a $\cos(\Omega_I-\Omega_S)\tau$ relationship and the resulting NMR signal's amplitude will therefore oscillate at a frequency of $1-\cos(\Omega_I-\Omega_S)\tau$, where τ is the time between the addition of parahydrogen and the application of the RF pulse. The new ZQ_y term also generates observable magnetisation following excitation. These associated terms are $2I_zS_x$ and $2I_xS_z$ when the pulse is applied along x and are maximised with a 90_x° RF pulse. Their amplitude oscillates at a frequency of $\sin(\Omega_I-\Omega_S)\tau$. By incrementing the delay between the laser pump and NMR probe steps followed by a suitable NMR experiment, PHIP-enhanced hydride resonances with oscillating signal intensity will result. Using a 90° pulse, the oscillatory behaviour of the ZQ_y component of the singlet state in $Ru(H)_2(CO)(PPh_3)_3$ was found to fit a sine curve with an oscillation frequency of 1101 ± 3 Hz matching the chemical shift difference of the two hydride ligands.[15] A summary of this is detailed below.

- The observable terms that result from $2I_zS_z$ and ZQ_x cancel one another out at time zero meaning no signal results; however, following addition to a metal complex ZQ_x evolves into ZQ_y at a frequency of $(\Omega_I-\Omega_S)\tau$.

- Amplitudes of NMR signals resulting from $2I_zS_z$ and ZQ_x are expected to oscillate at a frequency of $1–\cos(\Omega_I–\Omega_S)\tau$ and, in ^{1}H NMR-pulse-acquire NMR experiments, signal is observed with sin2θ relationship between signal intensity and the RF pulse angle meaning signals are maximised with a 45° RF pulse
- Amplitudes of NMR signals resulting from ZQ_y term are expected to oscillate with a $\sin(\Omega_I–\Omega_S)\tau$ frequency. In a ^{1}H NMR-pulse-acquire NMR experiment there is a sin θ relationship between signal intensity and RF pulse angle such that 90° RF pulses maximise signal intensity.

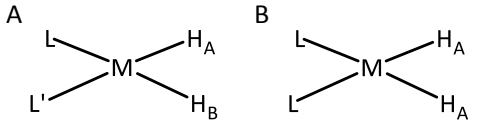

Figure 6.1: Schematic representation of a complex with (A) two chemically inequivalent hydrides and (B) two chemically equivalent but magnetically inequivalent hydrides.

A related situation is achieved when the two hydride ligands are in magnetically distinct but chemically equivalent environments (Figure 6.1B) Complexes of the type *cis*-$[Ru(H)_2(PP)_2]$, where PP refers to a bidentate phosphine, have been demonstrated to undergo fast photochemical loss and subsequent recoordination of H_2[90, 92] and therefore are candidates for this type of study. The behaviour of *cis*-$[Ru(H)_2(dppe)_2]$ **6.2** was first reported and this work we extended this study to the dppp analogue *cis*-$[Ru(H)_2(dppp)_2]$ **6.1** (Figure 6.2) where dppp refers to the bidentate phosphine 1,3-(diphenylphosphino)propane to investigate whether this phenomenon could be extended to other complexes and to allow add to the understanding of the theory behind this phenomenon. In these complexes the two hydride ligands are chemically equivalent and therefore there is no chemical shift difference for them to evolve under. However, they may evolve under scalar coupling. Multiple quantum coherences cannot evolve under the coupling between the two spins, however, they may evolve as a function of other couplings within the spin system. Using *cis*-$[Ru(H)_2(dppe)_2]$ it was demonstrated that the PHIP-enhanced hydride ligands evolved as a function of the difference in the scalar coupling

between the hydride ligands and the phosphorus ligands in the same plane as the hydride ligands. They were found to oscillate at a rate of 83 ± 5 Hz with a sine function, using a 90° pulse.[15] This relates to $J_{PH_{trans}} - J_{PH_{cis}}$ and was consistent with the product operator analysis for these reactions; this analysis will be discussed in due course. This work sets out to determine if this phenomenon is observable with a different chelating phosphine, dppp rather than dppe. If this is the case, the NMR experiment will be changed in order to examine how this changes the NMR read out of this evolution.

6.2 Synthesis and NMR characterisation of *cis*-[Ru(H)$_2$(dppp)$_2$] **6.1**

The synthetic approach used to prepare *cis*-[Ru(H)$_2$(dppp)$_2$] **6.1** is outlined in Figure 6.2. The ruthenium cyclooctadiene precursor was synthesised from $RuCl_3.xH_2O$ with an isolated yield of 4.3 g, or 80.2 %, based on ruthenium.[174] The target dihydride complex was then synthesised from this precursor using a literature procedure.[175] This gave an isolated yield of 0.62 g of *cis*-[Ru(H)$_2$(dppp)$_2$] **6.1**, which gives a percent yield of 52.9 % based on ruthenium.

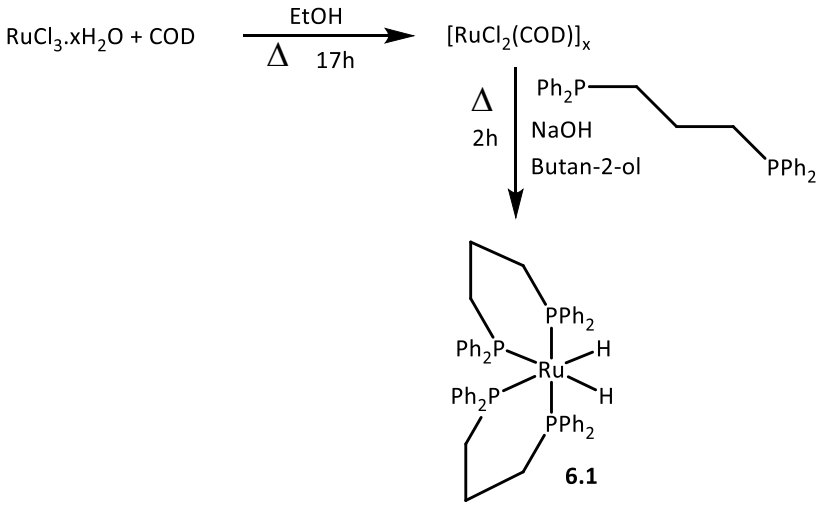

Figure 6.2: Synthetic route used for the synthesis of *cis*-[Ru(H)$_2$(dppp)$_2$] **6.1**.

An NMR sample of **6.1** was then prepared in C_6D_6 to allow characterisation. The resulting $^{31}P\{^1H\}$ NMR spectrum (Figure 6.4) shows two triplets (J_{PP} 27 Hz) at δ 28.3 and 33.0, consistent with the literature values for this complex.[175] 2D ^1H-^{31}P HMQC correlations were used to

assigned to the two phosphorus environments in **6.1** (Figure 6.3A) as the *trans* phosphorus-hydride coupling is much larger than the *cis* phosphorus-hydride coupling. When a 67 Hz coupling was used a correlation between the hydride resonance, at δ –7.53, and the phosphorus signal at δ 28.3 was seen, and thus this can then be assigned as P_B (Figure 6.3A).

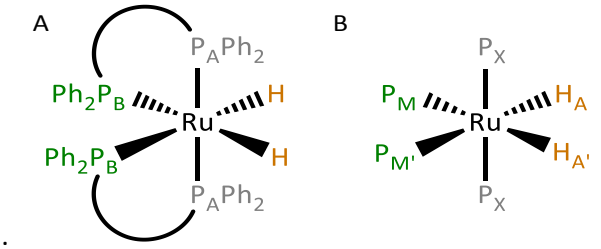

Figure 6.3: (A) Labelling the different phosphorus environments in **6.1** (propyl backbone simplified by curve). (B) Labelling of the different spins within **6.1**.

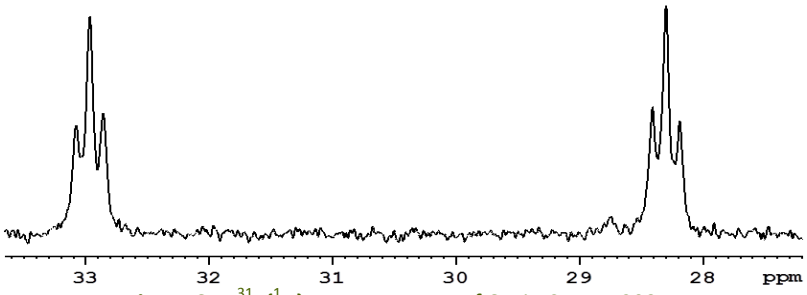

Figure 6.4: $^{31}P\{^{1}H\}$ NMR spectrum of **6.1** in C_6D_6 at 298 K.

The main resonance of note in the proton spectrum is the hydride resonance at δ –7.53 (Figure 6.5 top). This is a complicated highly second order signal owing to the magnetic inequivalence of the two hydride ligands due to their coupling to the phosphine ligands. The hydride forms an AA'MM'X_2 spin system with the phosphorus ligands, using the assignments in Figure 6.3B. Analysis of the hydride's NMR signal is therefore highly challenging and is detailed separately in Section 6.2.1.

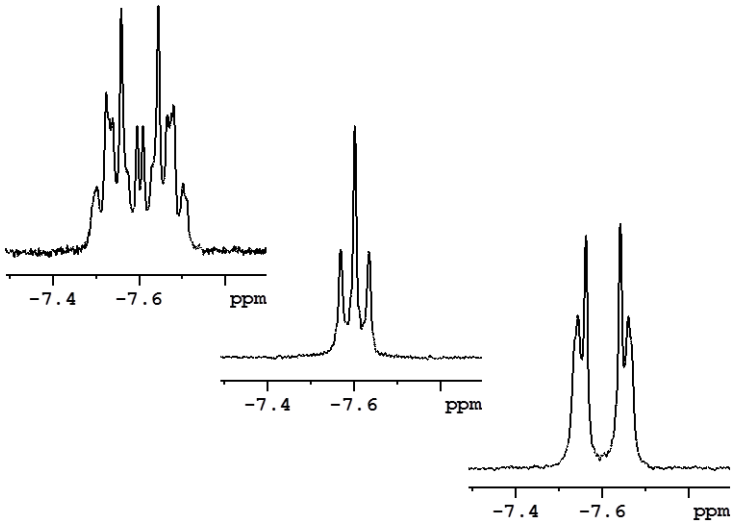

Figure 6.5: Hydride resonance for *cis*-$[Ru(H)_2(dppp)_2]$ **6.1** recorded in C_6D_6 at 298 K; (top) fully coupled hydride resonance, (middle) selective decoupling of the equatorial phosphines (P_B) and (bottom) selective decoupling of the axial phosphines (P_A).

The proton spectrum of the dppp ligand is further complicated by each of the four phenyl rings being inequivalent, the protons on the propyl bridge being diastereotopic (Figure 6.6) and finally, by the presence of phosphorus coupling. The dppp ligands therefore were characterised using $^1H\{^{31}P\}$ spectra in conjunction with 2D NMR methods and the results of this analysis can be found in Table 3.2. The coupling between the aromatic protons and the phosphines could not be measured due to overlap with the proton-proton coupling and not all of the resonances were full assigned due to overlap in both the proton and carbon spectrum.

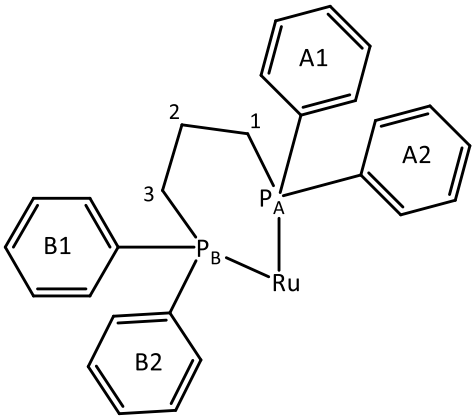

Figure 6.6: Fragment of **6.1** showing the full dppp ligand.

6.2.1 Analysis of the hydride AA'MM'X_2 spin-system

In order to ascertain some of these couplings a series of selective decoupling experiments were performed to remove the effect of P_A and P_B in turn. The decoupling of P_B results in a triplet with a coupling of 20.0 Hz, reflecting the coupling between P_A and the hydrides, (Figure 6.5 middle) whilst a second order multiplet results from the decoupling of P_A (Figure 6.5 bottom). Using the fully coupled spectrum the coupling constants for the AA'MM'X_2 spin systems were simulated using the manual iteration function within g-NMR.

The coupling constant between P_A and the hydride ligand of 20.0 Hz obtained from the selective decoupling experiments was used as the starting point in the simulation. During the iteration process, it became apparent that the coupling constant was larger than 20.0 Hz and a value of 21.6 Hz was obtained indicating that the decoupling experiments were not fully selective. The reduced coupling is obtained is as a consequence of the P_A resonance being partially irradiated in addition to P_B, is this due to the proximity of the two phosphorus resonances. The results from the simulation are shown in Figure 6.7 and in Table 6.1. The couplings between the phosphine ligands were also included in the fit. These were $J_{P_AP_{A'}}$ 200 Hz, $J_{P_AP_B}$ 27 Hz and $J_{P_BP_{B'}}$ 7 Hz. A pseudo doublet is observed in this hydride, and it is known that this corresponds to the sum of the *trans* and *cis* couplings ($J_{HP_{Btrans}}+J_{HP_{Bcis}}$).[15, 171] This was measured as being 51.5 Hz which is in good agreement with the value calculated from the coupling constants determined in g-NMR. Being able to determine the couplings within the hydride resonance is important, as this will play a role in how the *p*-H_2 singlet state evolves after its addition to the metal centre. It is important to note that *cis*- J_{HP_B} is set as negative in the simulation; this is not a unique solution. If the sign for each of the couplings were reversed, the same result would be obtained.

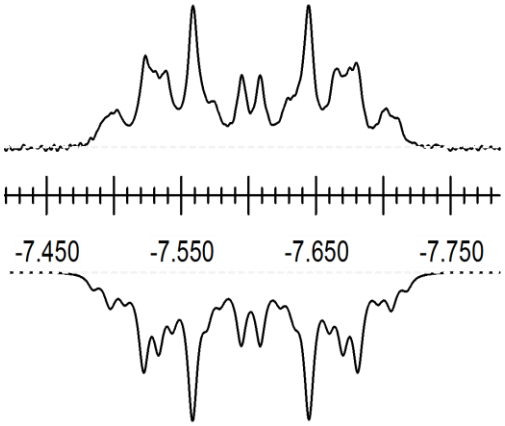

Figure 6.7: Experimental (top) and simulated (bottom) hydride signal of **6.1** in C_6D_6 at 298 K at 600 MHz.

Table 6.1: Couplings obtained using g-NMR.

	Coupled Nuclei		**Coupling/Hz**
J_{HH}	$H_AH_{A'}$		6.4
$J_{HP_{Btrans}}$	$H_AP_{M'}$	$H_{A'}P_M$	67.0
$J_{HP_{Bcis}}$	H_AP_M	$H_{A'}P_{M'}$	–15.2
$J_{HP_{Acis}}$	H_AP_x	$H_{A'}P_X$	21.6

Using a long-range ^1H-^1H COSY experiment, correlations between the hydrides and both the propyl linker protons in the dppp ligand and the *ortho* protons on the phenyl ligands were detected. This demonstrates that the coupling between the hydride ligands and the dppp ligand expands beyond the central phosphorus and adds an extra level of complexity in the assignment of all the components of the hydride resonance. These couplings were not included in the fitting of the hydride resonance.

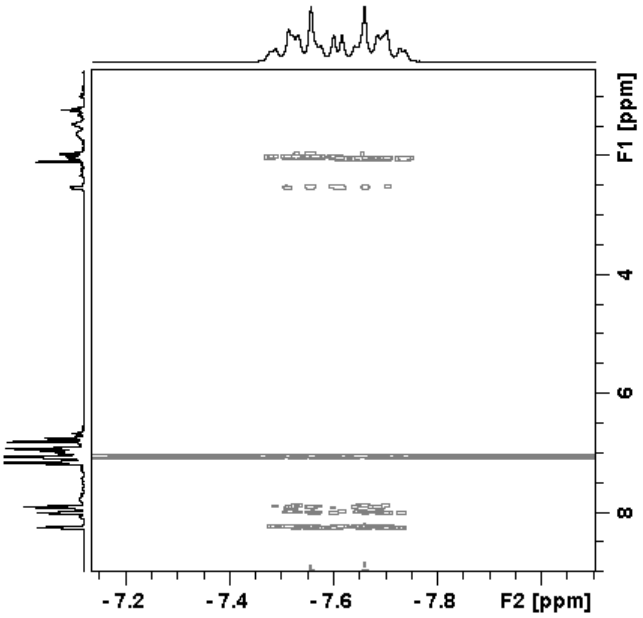

Figure 6.8: Long range ^{1}H-^{1}H COSY experiment of **6.1** in C_6D_6 at 298 K.

6.3 Predicted behaviour of the former parahydrogen singlet state

The effect of this magnetic inequivalence on the evolution of the former parahydrogen singlet state will now be discussed. The four nuclei involved in the effect can be labelled as detailed in Figure 6.9. The two hydrides are *I* and *S* and the two phosphines *R* and *T*. The coupling between *I* and *R* is different to the coupling between *I* and *T*; likewise, it is different to the coupling between *S* and *T*. The coupling between the hydrides and the axial phosphines (labelled P_A in Figure 6.3A) are the same for both hydrides. This change in labelling reflects standard NMR practice and nothing more.

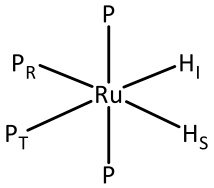

Figure 6.9: Structure showing the equatorial spins labelled as *I* and *S* for the hydrides and *R* and *T* for the phosphines, backbone and phenyl groups of the phosphine ligands have been omitted.

Since the two hydrides in **6.1** have the same chemical shift there is no chemical shift difference for the ZQ_x spin state to evolve under. While the zero quantum coherences do not evolve

under the coupling between the two spins (*I* and *S*), they do evolve as a function of the couplings within the spin system. Owing to the equal coupling between the hydrides and the axial phosphines, this evolution is limited only to those including *R* and *T* spins. The theoretical evolution of the ZQ_x as a function of J_{IT} and J_{ST} was analysed and is outlined below.[13, 32, 176] These transformations follow the scheme outlined in Figure 1.13, which shows how the starting zero quantum terms evolve into terms that also contained the phosphorus spins *R* and *T*. The terms which result from this evolution can be grouped first according to those that make up ZQ_x and ZQ_y (see section XX for the definitions of the zero quantum coherences) and then according to the trigonometric identities described in Section 1.2.4 by Equations (1.12) and (1.13). The final result is given in Equation (6.1). This procedure can be repeated for the coupling between the hydrides and the phosphine, R and the resulting analysis demonstrates that the *ZQ* terms should evolve as function of the difference in scalar coupling between the *trans* phosphorus hydride coupling and the *cis* phosphorus hydride coupling or $J_{PH_{trans}}$–$J_{PH_{cis}}$. Note the $2I_zS_z$ term does not evolve under scalar coupling and thus remains unchanged during the delay in question.[13, 32, 176]

$$
\begin{aligned}
2I_xS_x + 2I_yS_y \xrightarrow{\frac{\pi}{2}J_{IT}\tau I_z} \quad & 2I_xS_x \cos\frac{\pi}{2}J_{IT}\tau + 4I_yS_xT_z \sin\frac{\pi}{2}J_{IT}\tau + 2I_yS_y \cos\frac{\pi}{2}J_{IT}\tau \\
& -4I_xS_yT_z \sin\frac{\pi}{2}J_{IT}\tau
\end{aligned}
$$

$$
\begin{aligned}
\xrightarrow{\frac{\pi}{2}J_{ST}\tau S_z} \quad & 2I_xS_x \cos\frac{\pi}{2}J_{IT}\tau \cos\frac{\pi}{2}J_{ST}\tau + 4I_xS_yT_z \cos\frac{\pi}{2}J_{IT}\tau \sin\frac{\pi}{2}J_{ST}\tau \\
& +4I_yS_xT_z \sin\frac{\pi}{2}J_{IT}\tau \cos\frac{\pi}{2}J_{ST}\tau + 2I_yS_y \sin\frac{\pi}{2}J_{IT}\tau \sin\frac{\pi}{2}J_{ST}\tau \\
& +2I_yS_y \cos\frac{\pi}{2}J_{IT}\tau \cos\frac{\pi}{2}J_{ST}\tau - 4I_yS_xT_z \cos\frac{\pi}{2}J_{IT}\tau \sin\frac{\pi}{2}J_{ST}\tau \\
& -4I_yS_xT_z \sin\frac{\pi}{2}J_{IT}\tau \cos\frac{\pi}{2}J_{ST}\tau + 2I_xS_x \sin\frac{\pi}{2}J_{IT}\tau \sin\frac{\pi}{2}J_{ST}\tau
\end{aligned}
$$

$$
= \quad ZQ_x \cos\frac{\pi}{2}(J_{IT} - J_{ST})\tau + ZQ_yT_z \sin\frac{\pi}{2}(J_{IT} - J_{ST})\tau \qquad (6.1)
$$

6.4 Testing the prediction

6.4.1 Reaction between *cis*-[Ru(H)$_2$(dppp)$_2$] **6.1** and *p*-H$_2$

The UV-Vis spectrum of **6.1** was recorded in C_6D_6 (Figure 6.10) and an optically dilute sample of *cis*-[Ru(H)$_2$(dppp)$_2$] **6.1** was prepared in C_6D_6 in a Young's tap NMR tube. This was done to investigate whether **6.1** undergoes the expected behaviour following synchronised addition of parahydrogen through the application of a 355 nm pulse of light from a Nd:YAG laser as described in the Experimental Section 8.3.2. When a 3 ms delay was introduced between the laser pulse and the 90° RF pulse a PHIP enhanced signal was observed at δ –7.60 consistent with the formation of **6.1** (Figure 6.11). A 3 ms delay was chosen as this should allow time for evolution of the ZQ_x component into ZQ_y which can be observed with a 90° pulse whilst being a short delay relative to relaxation of the *ZQ* coherences and therefore this effect should be minimised.

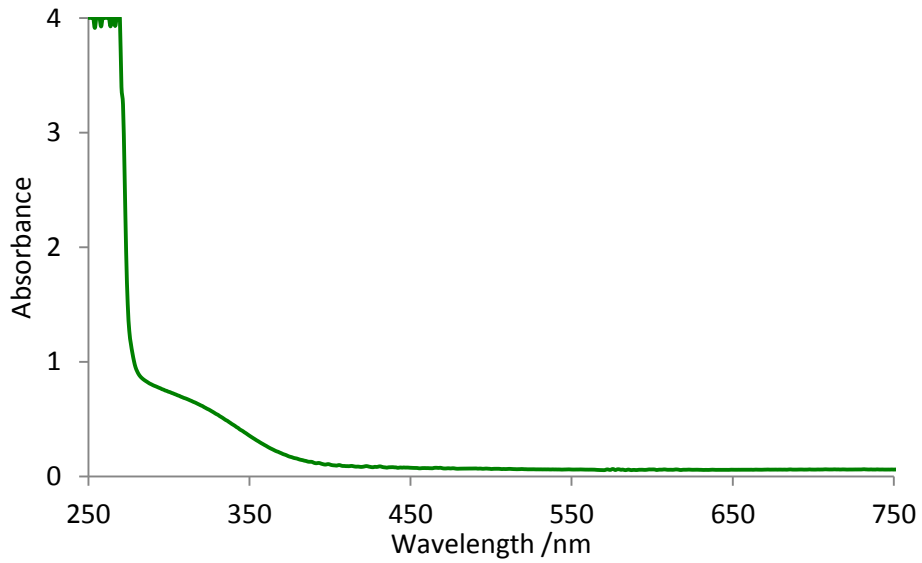

Figure 6.10: UV-Vis spectrum of **6.1** in C_6D_6

Figure 6.11: PHIP enhanced hydride resonance of **6.1** recorded in C_6D_6 at 298 K with a 3 ms delay between the laser pulse and a single 90° NMR pulse.

Interestingly the profile of the hydride resonance is considerably less complex than the hydride profile obtained without the use of parahydrogen (Figure 6.5). Now, rather than the complicated second order splitting pattern, the hydride has the form of an antiphase doublet of triplets of doublets. The largest doublet coupling is 81.0 Hz and relates to $J_{PH_{trans}}$–$J_{PH_{cis}}$, referring to the equatorial phosphine ligands. The triplet (21.7 Hz) reflects the coupling between the hydrides and the axial phosphines and finally the doublet is the coupling between the two hydrides (7 Hz). These values are consistent with those obtained using g-NMR. One of the advantages of using parahydrogen is that it allows the sign of J_{HH} coupling to be determined. If the antiphase doublet corresponding to J_{HH} is down-up, it signals that the coupling is negative, or as in the case here the doublet is up-down which denotes a positive coupling. This information could not be gleaned from the Boltzmann distribution hydride resonance. Furthermore, by combining the observed coupling for $J_{PH_{trans}}$ and $J_{PH_{cis}}$ from the hyperpolarised signal and the thermal signal the separate couplings can be solved using simultaneous equations. This gives values of $J_{PH_{trans}}$ and $J_{PH_{cis}}$ of 66.3 and −14.8 Hz respectively, consistent with the simulated values.

6.4.2 Validating the protocol

It has been determined that **6.1** will lose H_2 photochemically and forms a product which displays PHIP enhancements. Since we observed signal with a 90° pulse, the reaction must retain, at least some, coherent behaviour in the xy plane. Before probing this further, it is important to quantify the reproducibility of the result. In this reaction, parahydrogen is the limiting reagent; for the PHIP induced signal to yield the same signal strength the parahydrogen in solution needs to be replenished. It is therefore necessary to see how many experiments can be performed before the sample needed to be shaken to replenish the parahydrogen. A series of pump-probe experiments with a delay of 3 ms were performed with a delay of 30 seconds between each measurement to allow for the complete relaxation of the product. Each of these spectra were integrated and measured as a percentage of the initial signal intensity and were then plotted against repeat number (Figure 6.12). This shows that there is a steady drop in the observed signal with each repeat experiment. In order to monitor the evolution of these terms a large number of experiments will be required. A balance needs to be struck between running as many experiments as possible for each shake whilst still obtaining enhancements comparable to the first experiment of each shake. After five measurements, the recorded signal intensity is approximately 90% of the first experiment. It was decided that this was the limit on an acceptable drop in signal intensity; therefore, the series with incrementing laser-pump, NMR-probe delay will be run in groups of 5 experiments before the sample is shaken. Subsequent studies showed that shaking the sample results in signals with comparable enhancements between different shakes.

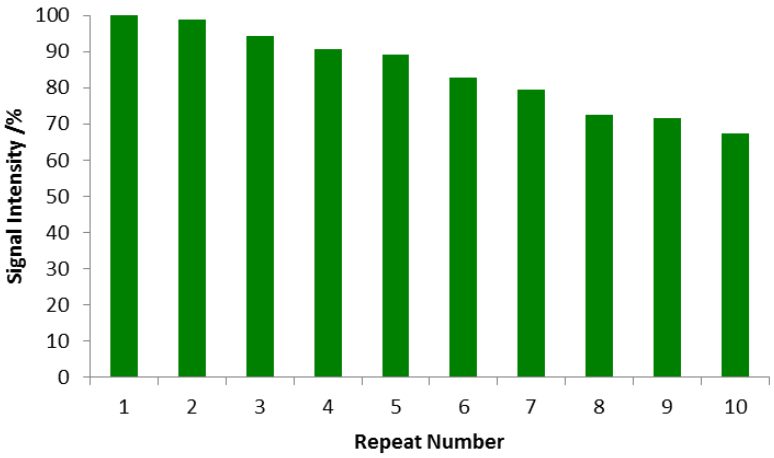

Figure 6.12: Signal intensity of **6.1** with each repeat measurement without shaking the sample.

6.4.3 Probing the evolution of ZQ_y

A series of experiments were then performed where the pump probe delay was sequentially increased from 0 s to 0.120 s in 0.001 s increments. Every five experiments the sample was shaken. These experiments were processed using the command *fmc*, this removes the phase encoding to allow for easy integration. The integrals of the hyperpolarised hydride resonances were plotted against the pump-probe delay (Figure 6.13). An oscillation is clearly visible with a frequency of 162 Hz. This is approximately double $J_{PH_{trans}}$–$J_{PH_{cis}}$. The alternative approach to integrating antiphase peaks is to integrate each of the components separately and subtract the negative (grey) components from the positive (green) components (Figure 6.15). When this approach was used, the resulting oscillation frequency was now 81 Hz (Figure 6.14).

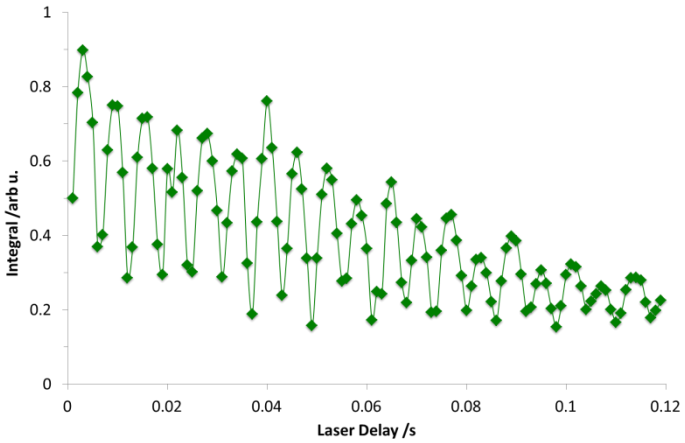

Figure 6.13: Hydride signal integral of **6.1** versus laser pump-NMR probe delay. Integral measured using magnitude calculated spectra.

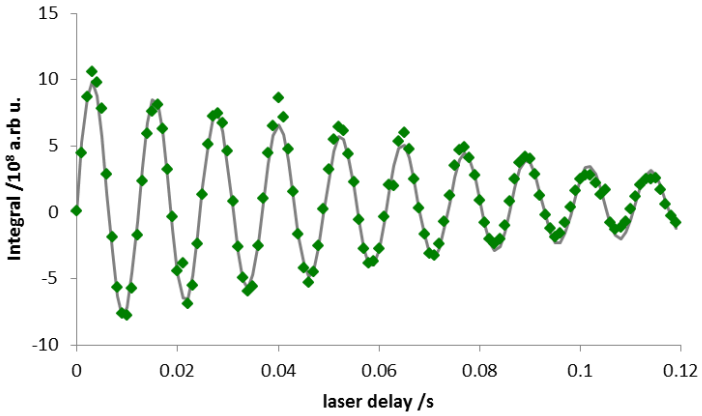

Figure 6.14: Hydride signal integral of **6.1** versus laser pump-NMR probe delay. Integral measured by integrating each of the components of the hydride individually and summing according to Figure 6.15. Grey line represents fitting in Matlab to Equation (6.2) performed by Meghan Halse.

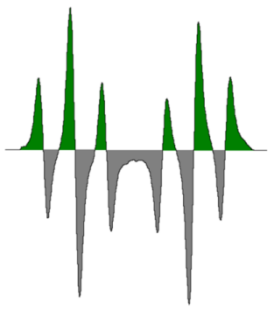

Figure 6.15: Schematic to demonstrate how the antiphase hydride signal was processed the up (green) components were added to the down (grey) components.

It has been demonstrated that the former parahydrogen singlet state evolves as a function of the difference in the scalar coupling between $J_{PH_{trans}}$–$J_{PH_{cis}}$, where P refers to the equatorial phosphine, P_B, from ZQ_x to ZQ_y. As detailed earlier, there is a cosine relationship in the contribution from ZQ_x and a sine relationship with ZQ_y. Furthermore, it was shown that the $2I_zS_z$ and ZQ_x terms evolve into observable magnetisation as a consequence of an RF pulse, θ, by sin2θ whereas ZQ_y evolves as a function of sinθ. The use of a 90° pulse, therefore, only interrogates the ZQ_y coherence and that the signal intensity can be fitted to the sine curve described by Equation (6.2). A refers to the amplitude of the signal, δυ the oscillation frequency, τ the delay time and the exponential term is to account for the relaxation of the terms and this is given by $T_{2,ZQ}$ and c is a constant relating to the offset of the signals amplitude. This was fitted in Matlab, in conjunction with Meghan Halse who developed the code, (see grey line Figure 6.14) and the values below were obtained. The important

parameters in this are the oscillation frequency, $\delta\upsilon$, which was measured as 81.1 $\pm$ 0.1 Hz, and the relaxation constant for the *ZQ* coherences, $T_{2,ZQ}$ which was measured as 84 $\pm$ 8 ms.

$$S = A\sin(2\pi\delta\upsilon\,\tau)e^{-\frac{\tau}{T_{2,ZQ}}} + c \qquad (6.2)$$

A = (9.5 $\pm$ 0.5) x10^8
$\delta\upsilon$ = 81.1 $\pm$ 0.1 Hz
$T_{2,ZQ}$ = 84 $\pm$ 8 ms
c = (0.7 $\pm$ 0.1) x10^8

6.4.4 Converting the 1D profile into a 2D map

The series of 1D data sets will now be converted in a 2D map where the second dimension reveals the ZQ_y evolution. A simplistic view of 2D NMR method involves four sequential steps; preparation, evolution, mixing and detection.[13, 32, 176] The initial preparation step converts the equilibrium magnetisation into transverse magnetisation by the application of an RF pulse. An evolution period follows the pulse and during this time the spins precess freely. Further encoding through additional pulses and evolution prior to data storage follows allowing spins which interact to be identified. The duration of the evolution period is incremented in a series of individual experiments to form the 2D map (Figure 6.16). This resembles the process performed here (Figure 6.16B) where the laser pulse acts as the preparation step. By combining these data sets into the 2D set and Fourier Transforming them in the second dimension, cross peaks should result reflecting the frequency of the evolution. The details of this process are outlined in full in the Experimental Section 8.4.4 and the result of this can be seen in Figure 6.17, which shows cross peaks at $\pm$ 81 Hz. Since there is almost no peak at 0 the difference between the two cross peaks is 162 Hz, it was this frequency which was measured when the amplitude was calculated in magnitude mode.

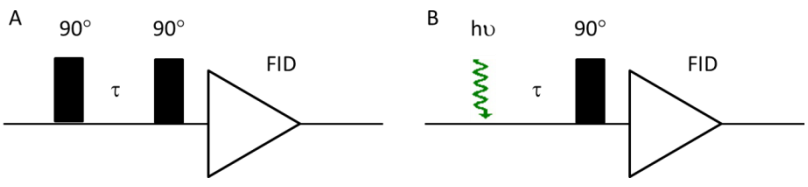

Figure 6.16: Schematic representations of (A) a simple 2D NMR pulse sequence and (B) the laser initiated pulse sequence.

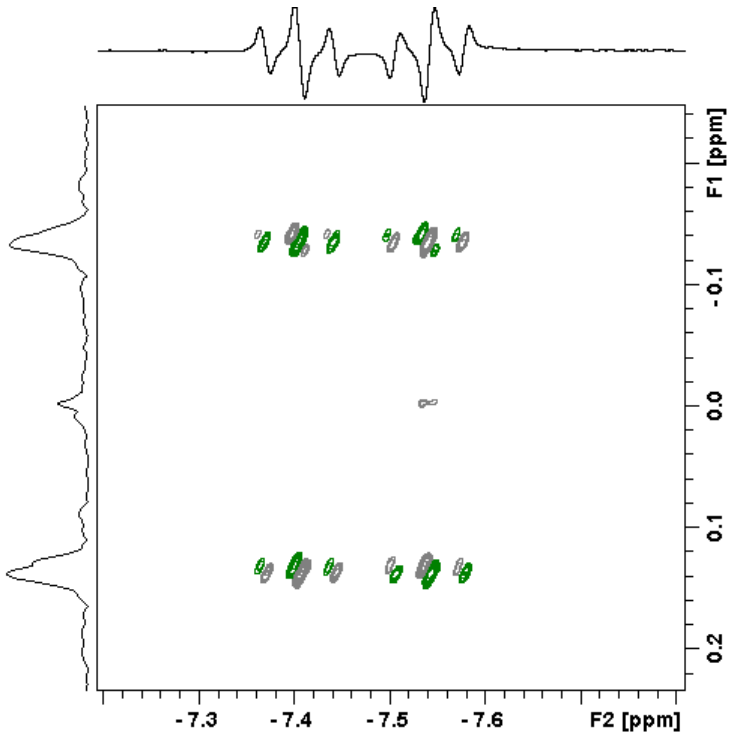

Figure 6.17: Two-dimensional pump-probe NMR spectra of **6.1** where F1 (vertical) dimension relates to the evolution of scalar coupling during the laser delay, τ.

6.5 Removing the thermal background

Whilst the evolutions with the previous experiments were observed using the hyperpolarised spin state of parahydrogen, weaker thermal magnetisation is also observed. A pulse sequence has been developed in York[177] that removes this thermal magnetisation, retaining only those terms, which result from the former singlet state. This approach is referred to as Only Parahydrogen Spectroscopy (OPSY) and is achieved by applying a double or zero quantum coherence filters, d-OPSY and z-OPSY respectively prior to data collection.[178] A schematic of this pulse sequence, with the laser initiation step included, is shown in Figure 6.18. In this work, only the d-OPSY protocol was used and thus the z-OPSY will not be discussed further.

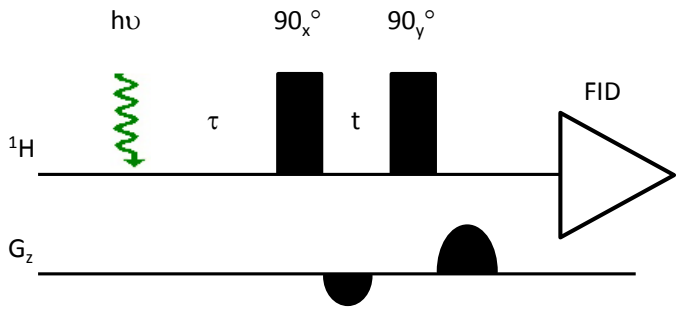

Figure 6.18: Schematic representation of the OPSY pulse sequence with laser initiation.

6.5.1 Analytical analysis of observable magnetisation using OPSY NMR methods

The theory of OPSY has been reported previously[178] but this focussed on the asynchronous addition of H_2 to the metal complex resulting in the decoherence of the ZQ_x term. The theoretical description of OPSY will now be described in the situation where the ZQ_x term is coherently retained.[13, 32, 176, 178] Following the laser initiation step and during the first delay, τ, the ZQ_x term evolves into ZQ_y as a function of the difference in scalar coupling between the *trans* and *cis* phosphorus-hydride couplings (ΔJ) in the same manner as already discussed therefore the analysis will start with this solution. The next step in the pulse sequence is a 90° pulse applied along x and the results of this are shown below in Equations (6.3)-(6.5). There is a delay period following this pulse. To see the evolution of the magnetisation during this delay the $2I_xS_x$ and $2I_yS_y$ terms need to be described in terms of zero and double quantum coherences. The equations for DQ_x and ZQ_x in Section 1.2.4 can be combined to give expressions which describe $2I_xS_x$ and $2I_yS_y$ according to Equations (6.6) and (6.7). These expressions can then be substituted for $2I_xS_x$ and $2I_yS_y$ in Equations (6.3)-(6.4) to give Equation (6.8). Since the gradients in this pulse sequence selectively retains the double quantum coherences, the analysis from here will only focus on the *DQ* coherences. These evolve during the delay according to the sum of the couplings ΣJ or $J_{PH_{trans}}+J_{PH_{cis}}$ to give Equation (6.9), following the 90_y° pulse the DQ_y coherence is converted into observable magnetisation

(highlighted in **green**). The observed evolution of magnetisation is therefore predicted to occur as a function of 1–cos (πΔJτ) during the laser pump-NMR probe delay.

$$2I_zS_z \xrightarrow{90^\circ I_x} \xrightarrow{90^\circ S_x} 2I_yS_y \tag{6.3}$$

$$(2I_xS_x + 2I_yS_y)\cos(\pi\Delta J\tau) \xrightarrow{90^\circ I_x} \xrightarrow{90^\circ S_x} (2I_xS_x + 2I_zS_z)\cos(\pi\Delta J\tau) \tag{6.4}$$

$$(2I_xS_y + 2I_yS_x)\sin(\pi\Delta J\tau) \xrightarrow{90^\circ I_x} \xrightarrow{90^\circ S_x} (2I_xS_z + 2I_zS_x)\sin(\pi\Delta J\tau) \tag{6.5}$$

$$2I_xS_x = DQ_x + ZQ_x \tag{6.6}$$

$$2I_yS_y = DQ_x - ZQ_x \tag{6.7}$$

$$2I_yS_y + 2I_xS_x\cos(\pi\Delta J\tau) = (DQ_x - ZQ_x) + (DQ_x + ZQ_x)\cos(\pi\Delta J\tau)$$

$$= ZQ_x(1 + \cos(\pi\Delta J\tau)) - DQ_x(1 - \cos(\pi\Delta J\tau)) \tag{6.8}$$

$$-DQ_x(1 - \cos(\pi\Delta J\tau)) \xrightarrow{\frac{\pi}{2}J_{IT}\tau I_z} \xrightarrow{\frac{\pi}{2}J_{IT}\tau S_z}$$

$$-DQ_x(1 - \cos(\pi\Delta J\tau))\cos(\pi\Sigma J\tau) - DQ_y(1 - \cos(\pi\Delta J\tau))\sin(\pi\Sigma J\tau) \tag{6.9}$$

$$= -(2I_xS_x - 2I_yS_y)(1 - \cos(\pi\Delta J\tau))\cos(\pi\Sigma J\tau) - (2I_xS_y + 2I_yS_x)(1 - \cos(\pi\Delta J\tau))\sin(\pi\Sigma J\tau)$$

$$\xrightarrow{90^\circ I_y} \xrightarrow{90^\circ S_y} \begin{matrix} -(2I_zS_z - 2I_yS_y)(1 - \cos(\pi\Delta J\tau))\cos(\pi\Sigma J\tau) \\ -(2I_zS_y + 2I_yS_z)(1 - \cos(\pi\Delta J\tau))\sin(\pi\Sigma J\tau) \end{matrix} \tag{6.10}$$

6.5.2 Testing the hypothesised evolution

In order to investigate the behaviour in an OPSY experiment an optically dilute sample of *cis*-$[Ru(H)_2(dppp)_2]$ **6.1** was prepared in C_6D_6 and pressurised with 3 bar of *p*-H_2. An OPSY based experiment was first recorded with a pump-probe delay of 6 ms and the resulting ^1H NMR

spectrum is shown in Figure 6.19. The only signal in the spectrum is the PHIP enhanced dihydride resonance confirming that removal of the thermal background is possible.

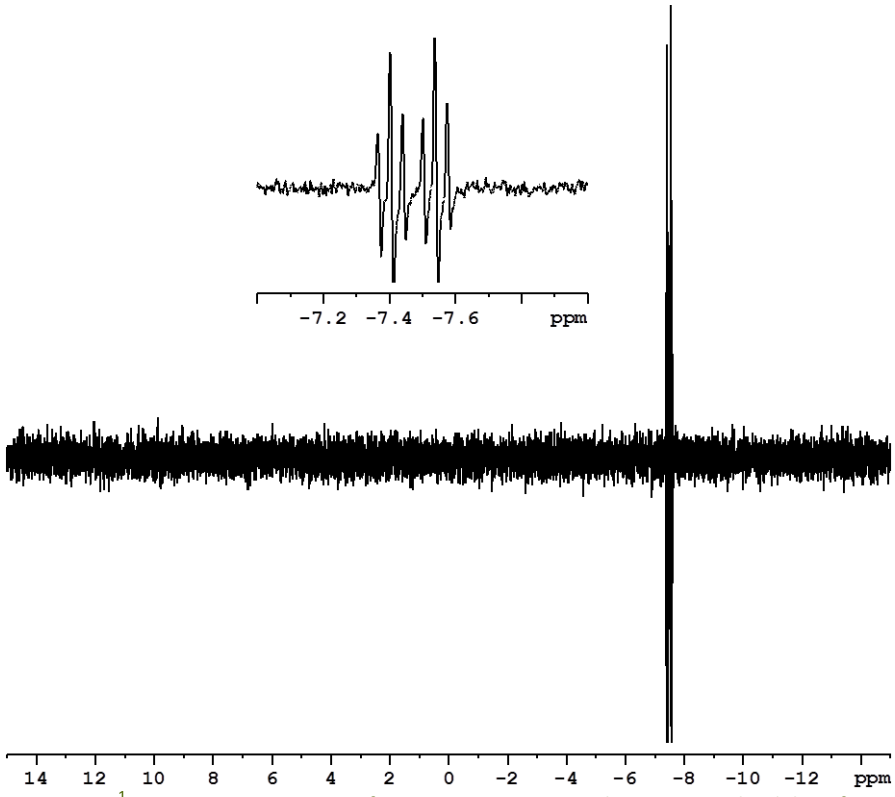

Figure 6.19: ^{1}H OPSY NMR spectrum of **6.1** in C_6D_6 at 298 K with a pump-probe delay of 6 ms.

A series of experiments were then recorded where the laser pump-probe delay was incremented from 0.0005 s to 0.1360 s in 0.0005 s steps. This time, ten experiments were possible between shaking the sample. This reflects subtle differences between samples such as concentration of **6.1** as well as the pressure and percentage of *p*-H_2.The first two experiments in each batch of 10 were repeats of the last two experiments from the previous batch to check that the results were reproducible. The series of experiments were performed over several days and the headspace of *p*-H_2 was periodically replaced with fresh *p*-H_2 because of the number of experiments that were acquired. Between each experiment, there was 30 second delay to ensure complete relaxation prior to the next measurement. System checks were also required after each shake and therefore the time associated with each measurement is not adequately represented by time of the NMR experiment alone. Periodically, fresh

parahydrogen was also required and the time constraints associated with this limited the number of parahydrogen refills which could be performed on one day. This introduces variability in the measurements, which relate to the exact alignment of the laser, the shimming of the sample and the signal enhancement from the parahydrogen. The effect of these factors was considered using control experiments acquired at the start of each session with a set pump-probe delay. The measurements were then normalised against these control experiments and it is these values which were plotted against the pump-probe delay (Figure 6.20).

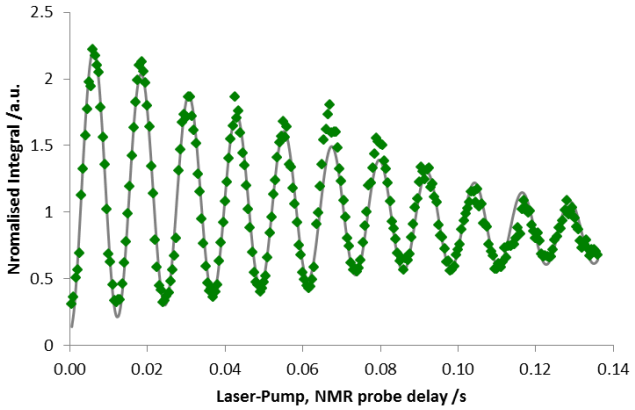

Figure 6.20: Hydride signal integral of **6.1** versus laser pump-NMR probe delay using an OPSY pulse sequence. Grey line represents fitting in Matlab to Equation (6.11) performed by Meghan Halse.

Figure 6.20 shows that the observed signal oscillates as the pump-probe delay is increased. This oscillation fits to a decaying 1–cosine curve, Equation (6.11), as predicted by the analytical analysis of the OPSY pulse sequence in Section 6.5.1 and shown in Figure 6.20 as the grey line. The two components of the cosine curve have different relaxation terms; $T_{1,2I_zS_z}$ that relates to the $2I_zS_z$ component and T_2 that relates to the zero quantum coherence. The value of $T_{1,2I_zS_z}$ is longer than that of $T_{2,ZQ}$ 325 $\pm$ 43 ms compared to 83 $\pm$ 6 ms since the $2I_zS_z$ term does not evolve during the delay period like the ZQ_x term does. This evolution provides a route to relaxation and hence why the $2I_zS_z$ component has a longer relaxation time than the ZQ_x. The frequency of the oscillations was measured as 81.5 $\pm$ 0.1 Hz consistent with the difference in *trans* and *cis* phosphorus-hydride couplings as predicted by the theory.

$$S = A(e^{-\frac{t}{T_{1,2IzSz}}} - \cos(2\pi\delta\upsilon)e^{-\frac{t}{T_{2,ZQ}}}) + c \qquad (6.11)$$

A = 1.11 ± 0.04
$\delta\upsilon$ = 81.5 ± 0.1 Hz
$T_{1,2IzSz}$ = 325 ± 43 ms
$T_{2,ZQ}$ = 83 ± 6 ms
c = 0.10 ± 0.05

As with the previous study, the series of 1D data sets can be converted into a 2D map showing the evolution of the $2I_zS_z$ and ZQ_x components in the second dimension and is shown in Figure 6.21. Unlike the 2D map from the 90° ^{1}H experiment, in addition to the cross peaks at $\pm$ 81 Hz there is a peak at zero which reflects the fact that the $2I_zS_z$ term does not evolve during the experiments.

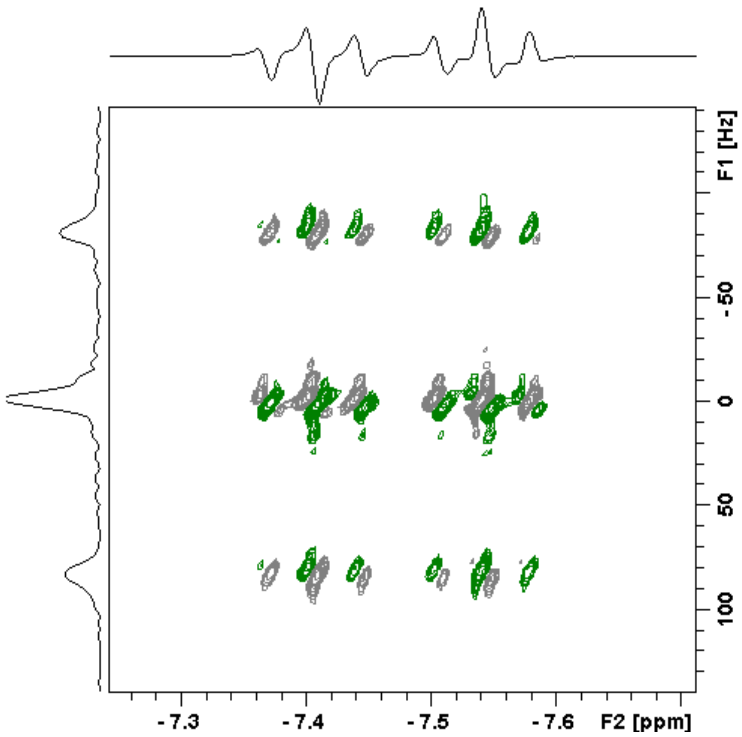

Figure 6.21: 2D NMR spectrum of **6.1**, which shows the observed evolution of **6.1** during the OPSY experiment in the F1 dimension.

6.6 45° pulse

The experiments so far have interrogated either the ZQ_x or ZQ_y terms separately. A simple 45° pulse allows the simultaneous observation of signals derived from both components at the

same time. To understand how the detected response can be analysed to tease out these separate evolutions, the concept of phase needs to be introduced.

The Fourier transformation of a free induction decay (FID) in NMR creates the spectrum. The resulting spectrum has a real and imaginary component with the real being absorptive (Figure 6.22A) and associated with the trace we analyse, whilst the imaginary part is dispersive (Figure 6.22B) in character and often overlooked. However, in most NMR spectra (Figure 6.22C), the idea of phase is known through the introduction of a phase correction which acts to separate out these two components. Mathematically, the signal is described by the expression in Equation (6.12) prior to the FID and Equation (6.13) afterwards, where $\Delta\omega$ refers to the frequency offset of the resonance whilst A and D refer to absorptive and dispersive functions respectively.[176]

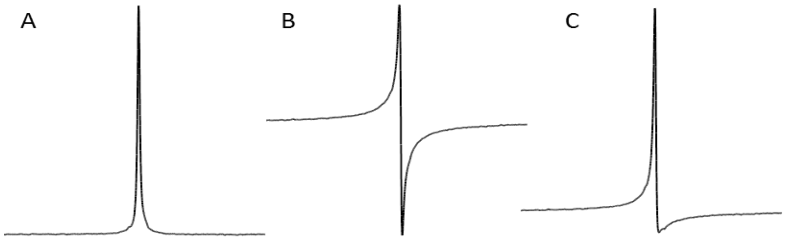

Figure 6.22: Schematic representation of a (A) Real signal, (B) Imaginary signal and (C) a signal with components of both.

$$S(t) = cos(\Omega t) + i\ sin(\Omega t) \tag{6.12}$$

$$S(\omega) = A(\Delta\omega) - i\ D(\Delta\omega) \tag{6.13}$$

The real and the absorptive components are 90° out of phase relative to one another. If we consider the I_x term, it is 90° out of phase with respect to the I_y term. Therefore the real spectrum would reflect I_x terms and the imaginary the I_y, or vice versa. When we now examine the effect of a 45° pulse on our PHIP enhanced hydride, we expect the pulse to create $2I_yS_z$ and $2I_zS_y$ terms from $2I_zS_z$ and ZQ_x and $2I_xS_z$ and $2I_zS_x$ from ZQ_y[13, 32, 176, 178]

In order to illustrate this a sample of **6.1** was prepared in C_6D_6, degassed and backfilled with 3 bar of *p*-H_2 and an experiment with a 45° pulse after a 0.0045 s pump-probe delay was acquired. The resulting hydride resonance was phased to give the real (A) and imaginary (B) components of the hydride of **6.1** as shown in Figure 6.23. The different behaviour in these components is seen through the change in appearance across the multiplet. In the real component both halves of the large doublet have the same orientation whereas in the imaginary part the two halves have the opposite orientation to one another.

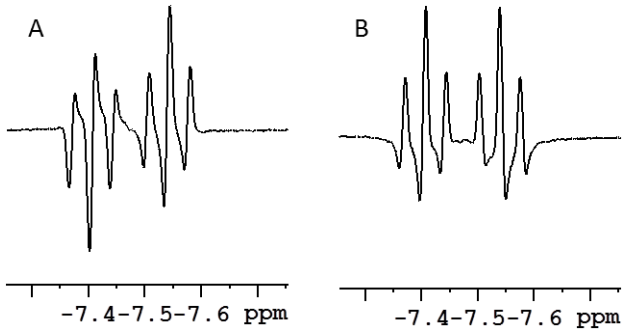

Figure 6.23: PHIP enhanced hydride spectrum for **6.1** in C_6D_6 at 298 K using a 45° pulse and a 4.5 ms pump probe delay; (A) shows the real component of the spectrum and (B) the imaginary.

A series of experiments with pump probe delays spanning from 0.0005 s to 0.1765 s, these were acquired over three days and appropriate controls were performed to allow for comparison and normalisation. These experiments were performed in groups of ten using the same approach as described in Section 6.5.2. To tease out the information from both the real and imaginary components of the spectrum each experiment was processed twice. First the real component (ZQ_x) was analysed. Each component of the multiplet was integrated separately and summed according to the schematic in Figure 6.24A. The phase was changed by 90° and the process repeated for the imaginary (ZQ_y) component of the spectrum (Figure 6.24B). The result of this analysis then plotted against the pump-probe delay and the expected behaviour observed (Figure 6.25 and Figure 6.26).

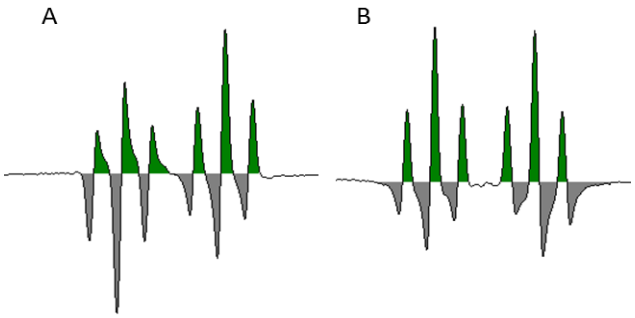

Figure 6.24: Schematic of the hydride resonance to show how the individual components get combined in the (A) real component and (B) the imaginary component of the spectrum. The **green** peaks are subtracted from **grey**.

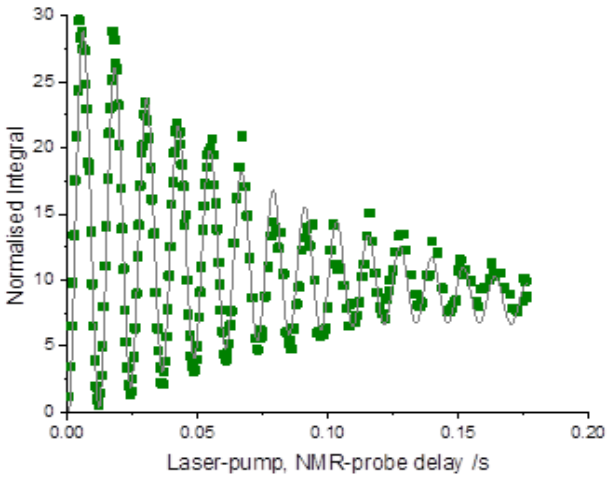

Figure 6.25: Time evolution of the **6.1** hydride resonance as a function of the pump-probe delay. Integrated according to Figure 6.24A to give the evolution of $2I_zS_z$ and ZQ_x. Grey line shows fitting in Origin to Equation (6.14).

$$S = A\left(e^{-\frac{t}{T_{1,2IzSz}}} - \cos(2\pi\delta\upsilon)e^{-\frac{t}{T_{2,ZQ}}}\right) + c \qquad (6.14)$$

A = 15.9 ±0.4
δυ = 82.2 ± 0.1 Hz
$T_{1,2IzSz}$ = 351 ± 25 ms
$T_{2,ZQ}$ = 75 ± 3 ms
c = –1.4 ± 0.4

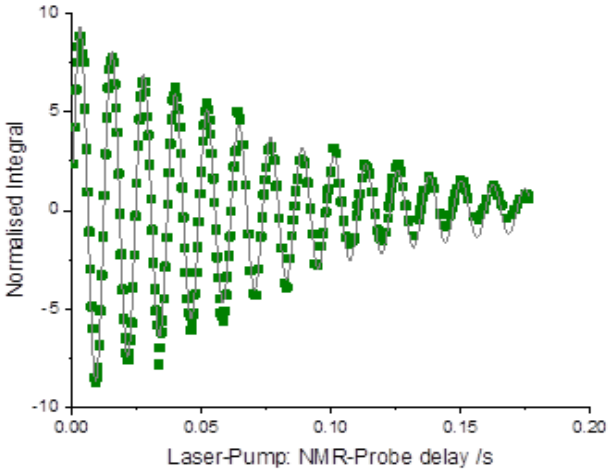

Figure 6.26: Time evolution of the **6.1** hydride resonance as a function of the pump-probe delay. Integrated according to Figure 6.24B to give the evolution of ZQ_y Grey line shows fitting in Origin to Equation (6.15).

$$S = A\sin(2\pi\delta\upsilon\,\tau)e^{-\frac{\tau}{T_{2,ZQ}}} + c \qquad (6.15)$$

A = 9.7 ± 0.1
δυ = 81.5 ± 0.1 Hz
$T_{2,ZQ}$ = 80 ± 2 ms
c = 0.0038±0.0252

The oscillations in Figure 6.25 and Figure 6.26 were fitted to decaying cosine and sine curves respectively in Origin using Equations (6.14) and (6.15). The associated parameters extracted from the fitting are listed below the equations. The oscillation frequency matches the difference in the *trans* and *cis* phosphine-hydride coupling. The exponential decay component relates to relaxation. The relaxation of the zero quantum coherence was determined to be 75 ± 3 ms in the real component and 80 ± 2 ms in the imaginary and therefore is consistent with the values determined in the 90° pulse and OPSY studies. Likewise, a relaxation time of 351 ± 25 ms was obtained for the $2I_zS_z$ term in agreement with the earlier value. I have therefore illustrated three separate methods to observe the evolution of the former parahydrogen singlet state using PHIP enhanced ^{1}H NMR spectra of **6.1**. These studies have yielded the same physical parameters and hence it can be concluded that we can be confident that the method of analysis is correct.

6.7 $^{31}P\{^{1}H\}$ NMR hyperpolarisation as a function of time

6.7.1 *cis*-$[Ru(H)_2(dppp)_2]$ **6.1**

All of the experiments so far have focussed on the detection of a hydride resonance. In **6.1** the axial phosphines are chemically and magnetically equivalent but the equatorial phosphines, like the hydride ligands, are in chemically equivalent but magnetically inequivalent environments. The transfer of the parahydrogen polarisation from the hydride ligands to the equatorial ^{31}P nuclei should therefore be possible.[15] These signals are predicted to oscillate according to the difference in scalar coupling also.

The phosphorus nuclei couple to the pendent phenyl groups and the propyl backbone of the dppp ligand in addition to the coupling to the hydride ligands. The evolution under this coupling would complicate the evolution however, it can be removed through the selective decoupling the aromatic and alkyl regions of the proton spectrum whilst retaining the coupling due to the hydride resonances. This was achieved by using the *waltz64* decoupler sequence centred at δ 5 in the ^{1}H spectrum and appears to have simplified the spectrum. The axial phosphine resonance now resembles a quintet-type multiplet due to coupling to both equatorial phosphines (J_{PP} 27 Hz) and both hydride ligands (J_{PH} 21.7 Hz). The equatorial phosphine resonance now displays second order characteristics similar to that of the hydride resonance (Figure 6.27). Having begun to optimise the decoupling using the thermal spectrum the settings were then used to record a hyperpolarised $^{31}P\{^{1}H\}_{sel}$ experiment. In the ^{1}H NMR spectrum the coupling network is more clearly defined in the hyperpolarised signal compared to the thermal as different states get populated. It is anticipated that couplings in the hyperpolarised ^{31}P spectrum would also be more clearly defined and this would aid in optimising the selective decoupling of the hydride resonances. Unfortunately, the resulting spectrum shows very poor enhancements even with a pump-probe delay consistent with an oscillation maximum limiting its use in the optimisation of the decoupling. Furthermore, this

would also inhibit the observation of the evolution of the former parahydrogen singlet state due to poor signal-to-noise.

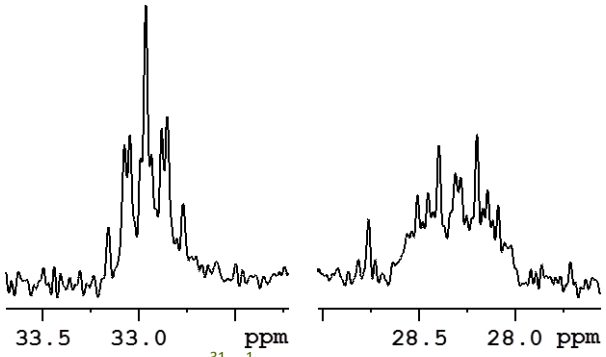

Figure 6.27: $^{31}P\{^{1}H\}_{sel}$ of **6.1** in C_6D_6 at 298 K.

6.7.2 *cis*-[Ru(H)$_2$(dppe)$_2$] **6.2**

A similar complex, *cis*-[Ru(H)$_2$(dppe)$_2$], **6.2**, where dppe refers to bis(diphenylphosphino)ethane, is used in the alignment of the laser and has previously been studied by the methods described in this Chapter.[15] The hydride in this complex resonates at δ –8.6; it was also hoped that this 1 ppm shift in the hydride resonance would improve the selectivity of the decoupling. The optimum decoupling parameters for this complex were achieved using the waltz64 decoupling sequence centred at δ 4 (Figure 6.28 top). A PHIP enhanced spectrum was also obtained with these parameters (Figure 6.28 bottom). The profile is now similar to the PHIP enhanced hydride. The laser pump-probe delay was then incremented to follow the oscillation of the zero quantum coherences. These were combined into a 2D spectrum (Figure 6.29) which shows two cross peaks at $\pm$ 83.9 Hz consistent with the difference in the scalar coupling in this complex.[15]

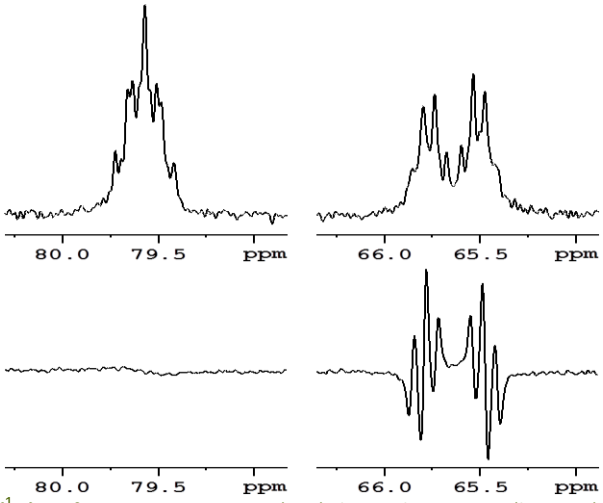

Figure 6.28: $^{31}P\{^{1}H\}_{sel}$ of **6.2** in C_6D_6 at 298 K (top) thermal spectrum (bottom) hyperpolarised.

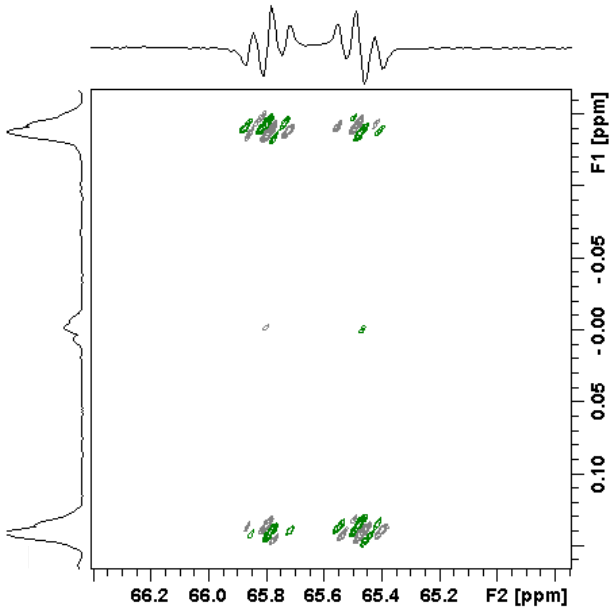

Figure 6.29: 2D map showing the evolution of the parahydrogen singlet state in the equatorial phosphine signal.

6.8 Conclusion

In this Chapter *cis*-[Ru(H)$_2$(dppp)$_2$] **6.1** was synthesised using the literature procedure.[174, 175] The two hydride ligands are chemically equivalent but magnetically inequivalent. Consequently, when **6.1** is formed with parahydrogen as the source of the hydride ligands, the symmetry of the former parahydrogen singlet state is broken and this can unlock the potential signal enhancements.

The use of *in-situ* photochemistry with NMR detection has allowed parahydrogen to add to suitable organometallic precursors in a time precise and synchronous fashion allowing for the retention and subsequent evolution of the zero quantum coherence of the parahydrogen singlet state. Suitable systems have a photolabile ligand which is lost during the laser pulse, react with dihydrogen on a time scale faster than the decoherence of the zero quantum component of the former parahydrogen singlet state and, in the dihydride product, contain the former parahydrogen protons in chemical and/or magnetically distinct environments. It was proposed that **6.1** would be a suitable complex based on its similarities to *cis*-$[Ru(H)_2(dppe)_2]$ which has already been successfully studied using this approach. Using a modified NMR pulse sequence to allow for the pulsing of the laser and a 90° ^{1}H NMR pulse it was demonstrated that **6.1** is suitable for these studies since the 90° pulse interrogates solely the ZQ_y component of the singlet state. This is only possible if decoherence has not occurred.

Having ascertained that **6.1** was suitable it was next studied with three different ^{1}H NMR experiments using a 90° pulse, an OPSY pulse sequence and finally a 45° pulse. How the former singlet state is expect to evolve under the respective pulse sequences was analysed and revealed that each of the terms was expected to evolve based on the difference in the scalar coupling between the equatorial phosphines *trans* and *cis* to the hydride ligands, $J_{PH_{trans}} - J_{PH_{cis}}$. The 90° pulse was expected to reveal the evolution of the ZQ_y component based on a sine function. Whilst the OPSY pulse sequence should interrogate a combination of the longitudinal two spin order term, $2I_zS_z$ and ZQ_x based on a 1–cosine function. The 45° pulse NMR experiment however was expected to give all of these terms in one experiment with the $2I_zS_z$ and ZQ_x component in the real spectrum and ZQ_y in the imaginary spectrum.

Each experiment was analysed in turn, revealing oscillating signals which matched the theoretical predictions. These were then fitted to appropriate decaying sine and 1–cosine curves. The results of this are summarised in Table 6.3. An oscillation frequency of

approximately 81 Hz was observed in each case and the relaxation of each of the components were measured as 80.5 ± 6 ms for the zero quantum coherence terms and 338 ± 37 ms for the $2I_zS_z$ components. The $2I_zS_z$ has a longer relaxation time as it does not evolve under scalar coupling.

Table 6.2: Summary of oscillatory behaviour of **6.1** with different pulse sequences.

Entry	Expt	Term(s)	Frequency, δυ /Hz	T_{2ZQ} /ms	T_{1IzSz} /ms
1	90°	ZQ_y	81.1 ± 0.1	84 ± 8	
2	OPSY	$2I_zS_z$, ZQ_x	81.5 ± 0.1	83 ± 6	325 ± 43
3	45°	$2I_zS_z$, ZQ_x	82.2 ± 0.1	75 ± 3	351 ± 25
4	45°	ZQ_y	81.5 ± 0.1	80 ± 2	

The hydride resonance in **6.1** is highly second ordered which means its couplings could not be readily measured from its ^{1}H NMR spectrum. The coupling constants were simulated in g-NMR and were summarised in Table 6.1 and the difference in scalar couplings was predicted to be 82.2 Hz. The hyperpolarised hydride resonance is considerably simpler than the corresponding thermal spectrum and now resembles a doublet of triplets of doublets. The largest doublet corresponds to $J_{PH_{trans}} - J_{Ph_{cis}}$ (81.0 Hz), whilst the triplet is as a result of the coupling to the axial phosphine ligands and the smaller doublet is the hydride-hydride coupling. Although many of the couplings could not be measured from the thermal spectrum, it does contain a doublet splitting due to $J_{PH_{trans}} + J_{PH_{cis}}$ which was measured as 51.5 Hz. By combining these two terms the specific values for the *trans* and *cis* components were measured to be 66.3 and −14.8 Hz respectively.

The transfer of polarisation onto the ^{31}P nuclei of the dppp ligands in the equatorial position was investigated next using selective decoupling experiments so that only the coupling between the phosphines and hydrides were retained. This was first performed on the thermal spectrum, but unfortunately the enhancements observed in the hyperpolarised ^{31}P spectrum were poor, which meant that this complex was unsuitable for this study as there was inadequate signal detected. An analogous complex *cis*-[Ru(dppe)$_2$H$_2$] **6.2** was used instead. As

well as offering larger enhancements than **6.1**, the chemical shift of the hydride ligands is at δ –8.60 which gives a greater chemical shift difference between the hydrides and the alkyl protons of the dppe ligand which can aid the selective decoupling experiments. The evolution of the former parahydrogen singlet state was observed at 83.9 Hz consistent with $J_{PH_{trans}} - J_{PH_{cis}}$ for this complex.

In conclusion, in this work I have validated the theory behind the evolution of the ZQ_x component of *p*-H_2 in a second chemically equivalent but magnetically inequivalent system. These studies were extended to include using OPSY measurements to observe the evolution with the thermal components of the spectrum removed and also to observe the transfer of polarisation on to the equatorial ^{31}P atoms where the singlet state also evolves according to $J_{PH_{trans}} - J_{PH_{cis}}$. One of the goals of this research has been to use parahydrogen to study rates of reactions, whilst the addition of parahydrogen to **6.1** and **6.2** occur on a faster timescale than can be studied using this method, an understanding of how the former singlet state evolves following synchronised addition to a metal complex will be crucial in moving towards time-resolved measurements.

6.9 NMR data

Table 6.3: NMR Characterisation of *cis*-$[Ru(H)_2(dppp)_2]$ **6.1**.

	δ/ppm (multiplicity)	Coupling constant/Hz	Assignment	Group
^{1}**H**	8.26 (m)	J_{HH} 7, 4	H_o	P_A-$(C_6H_5)_{A1}$
	7.16 (dd)	J_{HH} 8, 7	H_m	P_A-$(C_6H_5)_{A1}$
	7.06 (overlap)		H_p	P_A-$(C_6H_5)_{A1}$
	8.01 (m)	J_{HH} 7, 4	H_o	P_A-$(C_6H_5)_{A2}$
	6.81 (t)	J_{HH} 7	H_m	P_A-$(C_6H_5)_{A2}$
	6.76 (d)	J_{HH} 7	H_p	P_A-$(C_6H_5)_{A2}$
	7.91 (t)	J_{HH} 8, 8	H_o	P_B-$(C_6H_5)_{B1}$
	6.93 (t)	J_{HH} 7, 7	H_m	P_B-$(C_6H_5)_{B1}$
	6.97 (d)	J_{HH} 7	H_p	P_B-$(C_6H_5)_{B1}$
	7.15 (overlap)	J_{HH} 13.5, 6.5	H_o	P_B-$(C_6H_5)_{B2}$
	7.20 (overlap)*	J_{HH} 3	H_m	P_B-$(C_6H_5)_{B2}$
	7.20 (overlap)*		H_p	P_B-$(C_6H_5)_{B2}$
	2.54 (dt)	J_{HH} 12	$^{1}CH_2$	P_A-$(CH_2)_3$-P_B
	1.22 (brt)	J_{HH} 12.0, 6	$^{1}CH_2$	P_A-$(CH_2)_3$-P_B
	1.64 (m)	J_{HH} 12.0	$^{2}CH_2$	P_A-$(CH_2)_3$-P_B
	1.47 (q)		$^{2}CH_2$	P_A-$(CH_2)_3$-P_B
	2.05 (dd)		$^{3}CH_2$	P_A-$(CH_2)_3$-P_B
	1.98 (t)		$^{3}CH_2$	P_A-$(CH_2)_3$-P_B
	–7.60 (m)		Ru–H	Ru-$(H)_2$
^{13}**C**	132.8		C_o	P_A-$(C_6H_5)_{A1}$
	128.5		C_m	P_A-$(C_6H_5)_{A1}$
	128 (overlap)		C_p	P_A-$(C_6H_5)_{A1}$
	133.9		C_o	P_A-$(C_6H_5)_{A2}$
	128.0		C_m	P_A-$(C_6H_5)_{A2}$
	129.0		C_p	P_A-$(C_6H_5)_{A2}$
	136.3		C_o	P_B-$(C_6H_5)_{B1}$
	127.8		C_m	P_B-$(C_6H_5)_{B1}$
	127.1		C_p	P_B-$(C_6H_5)_{B1}$
	132.6		C_o	P_B-$(C_6H_5)_{B2}$
	128 (overlap)*		C_m	P_B-$(C_6H_5)_{B2}$
	128 (overlap)*		C_p	P_B-$(C_6H_5)_{B2}$
	25.6		$^{1}CH_2$	P_A-$(CH_2)_3$-P_B
	20.5		$^{2}CH_2$	P_A-$(CH_2)_3$-P_B
	33.0		$^{3}CH_2$	P_A-$(CH_2)_3$-P_B
^{31}**P**	33.0 (t)	J_{PP} 27.0	P_A	dppp
	28.3 (t)	J_{PP} 27.0	P_B	dppp

Note: the coupling of the aromatic protons was obtained from $^{1}H\{^{31}P\}$ spectra due and hence J_{PH} couplings were not measured; *Due to overlap in both ^{1}H and ^{13}C dimensions these resonances could not be assigned fully

7 Conclusions and Future Work

7.1 Half sandwich rhodium complexes

The photochemistry of a series half sandwich rhodium alkene complexes was studied in this thesis. Four complexes were synthesised for this purposed. The reactivity of **2.1**, **2.2** and **2.3** towards triethylsilane and trimethylvinylsilane was studied. These studies revealed a difference in activity between the two η^2-(alkene) containing complexes and the η^4-(COD) variant **2.3**. The reactivity of **2.3** was limited to the loss of both alkene groups of the COD ligand forming **2.1A** and **B** when reacted with trimethylvinylsilane and **2.6** when reacted with triethylsilane. The stepwise loss of the COE ligands was observed with **2.2** and hence in these reactions the monosubstitution products could be characterised. The reaction of **2.1** and **2.2** with DMSO only led to monosubstitution products, with the DMSO ligand coordinated through sulfur. No reactivity was observed between **2.3** and DMSO. This supports the assumption that $CpRh(DMSO)_2$ does not form. The reactivity of **2.1** and **2.2** was consistent with the reported chemistry of similar systems. This is particularly interesting for **2.2** owing to its similarities to the analogous ethene complex whilst the the synthetic preparation of the bis-COE dimer is simpler than the bis-ethene dimer and in the half sandwich complex the alkene ligands are not susceptible to being lost when vacuum is applied.

Further reactions were performed between **2.1** and **2.2** and phenyl methyl sulfoxide. This asymmetric sulfoxide gave rise to two products with **2.1** as the starting complex which were characterised as diastereomers owing to the chirality of the metal centre and the sulfoxide. Only a single product was formed with **2.2** as the precursor, owing to the symmetry of the alkene. Competition studies performed between **2.1** and DMSO, PhSOMe and trimethylvinylsilane revealed that the product containing DMSO is most favoured and PhSOMe products are the least favoured demonstrating that the choice of sulfoxide can influence the product distribution which could allow for reactivity to be tuned.

In these studies **2.1** and **2.4** were determined to be suitable precursors for the time-resolved studies with parahydrogen. These complexes provide two different routes, DMSO or vinylsilane loss, to the same reactive intermediate that is known to form the dihydride **3.1**.[74] Both complexes were found to capable of forming **3.1** with PHIP enhanced hydride signals being detected following *in-situ* irradiation with 355 nm light. The enhancements from **2.4**, however, were poorer than those from **2.1**. Further studies, therefore, were only performed using **2.1** as the precursor. Variable temperature measurements revealed a temperature dependence in the hydride chemical shifts. This was attributed to a process wherein the two hydride environments exchange sites. The signals associated with **3.1** could only observed with multiple laser pulses which limited the time-resolution of these measurements. Nevertheless, studies where the time from the last laser pulse and the NMR experiment was incremented were undertaken. From these studies, it can be concluded that the dihydride complex forms on timescales of the order of 50 ms. The $2I_zS_z$ spin state of the parahydrogen derived protons was found to have a lifetime of 1-2 seconds. This shows that the technique can be used to measure the rates of reactions on a much quicker timescale than standard NMR methods.

A third rhodium half sandwich complex, **3.2**, was studied with H_2, this complex is known to lose its coordinated alkene under irradiation and has previously been demonstrated to form a dihydride complex when heated with $NaBH_4$ in toluene/ethanol.[6] The intention in this work was to determine if the dihydride could form photochemically through the reaction of **3.2** with H_2, and if this process could be studied with parahydrogen. Reactions of **3.2** and H_2 did indeed result in the formation of the expected dihydride (**3.3**) and a second product proposed to have a dinuclear-hydride-bridged structure. The dihydride, **3.3**, did not give rise to PHIP enhanced hydrides; possible explanations for this included the absence of proton-proton couplings in the ^{1}H NMR spectrum and the exchange of the hydride resonances via a dihydrogen complex. Investigations into these possible explanations ruled out both them as the hydride-hydride coupling was demonstrating using COSY measurements and estimated to be ~2 Hz. Simulations

using g-NMR suggested that with this coupling PHIP enhanced signals should still be visible. The hydride resonances were found to have T_1's of ~0.6 s in keeping with a dihydride species and therefore should not quench the enhancements. The lifetime of the initial dihydrogen complex as part of the oxidation product was postulated as reason for the lack of PHIP.

7.2 Ruthenium dihydride complexes

The photoactivity of ruthenium dihydride complexes is well known and it is proposed that these might provide an alternative group of complexes suitable for time-resolved NMR measurements with parahydrogen. Literature searches revealed that only the thermal activity of $Ru(H)_2(CO)(PPh_3)$(Xantphos) **5.1** had been studied previously. Similar ruthenium dihydride complexes have been found to be photochemically active. To determine whether this was also the case for **5.1**, it was irradiated in the presence of ethene, CO, benzyl alcohol, DMSO and triethylsilane. This revealed that the hydride, PPh_3 and CO ligands were all photolabile and some products were formed by the loss of more than one of these ligands. A change in coordination mode of the xantphos ligand from κ^2-PP to κ^3-POP motif was also observed in **5.2**, **5.8** and **5.11**. These results demonstrate the extensive and varied photochemical properties of **5.1** which are dependent on the choice of free ligand, this **5.1** has suitable reactivity and thereby making it a promising candidate for time-resolved measurements using parahydrogen.

It has recently been demonstrated that *in-situ* photolysis provides a route for the coherent retention of the zero quantum component of the parahydrogen singlet state in the dihydride product. This zero quantum component then evolves according to the chemical shift difference of the parahydrogen protons and/or the differences in their scalar coupling which could be observed using appropriate NMR experiments. Two ruthenium dihydride complexes were studied; **5.1** and *cis*-$[Ru(H)_2(dppp)_2]$ **6.1**. **5.1** contains two chemically and magnetically

inequivalent hydride ligands and **6.1** contains two chemically equivalent but magnetically inequivalent hydride ligands. It was expected that the 355 nm laser pulse would result in the reductive elimination of H_2 and that a molecule of *p*-H_2 would add in its place. It was expected that by incrementing the time between this addition and the NMR experiment a signal oscillating at the difference in chemical shift or scalar coupling would result.

The addition of *p*-H_2 to **5.1** was found to occur on a timescale that evolution of the zero quantum coherence and therefore the dephasing of this term is seen. It was possible, however, to see the growth in the enhanced signals associated with **5.1** in a time-resolved manner. Whilst these measurements were hampered by poor signal-to-noise, despite the use of parahydrogen, it was possible to conclude that the addition of H_2 occurs on a timescale of the order of 0.5 s^{-1}. **6.1** however, was found to be suitable and a PHIP enhanced signal oscillating at a frequency of 81 Hz was observed, consistent with the difference in the *trans* and *cis* couplings between the hydrides and the equatorial phosphines. By changing the specifics of the NMR experiment the different components of the singlet state could be probed either individually or in combination. The $2I_zS_z$ term was found to relax with a T_1 of ~300 ms and the *ZQ* terms with a T_1 of 80 ms.

In conclusion, a wealth of varying photochemical activity has been observed with rhodium half sandwich and ruthenium dihydride complexes. The reactivity of **5.1** proved highly varied making it a promising candidate for further photochemical studies. A number of complexes with photolabile alkenes, DMSO and hydride ligands have been demonstrated to be suitable precursors for reactions with parahydrogen. The addition of parahydrogen to appropriate reaction intermediates has been demonstrated to occur, on varying timescales, from very short, in the case of **6.1**, to longer timescales on the order of 50 ms in **3.1** and 0.5 s in **5.1**. In the very short case, this allowed the coherent retention of the zero quantum coherence originating from the parahydrogen singlet state.

7.3 Future work

- The primary goal in this research was to develop a time-resolved NMR method that could be used to follow the evolution of a chemical reaction on a faster timescale than is currently possible. This would benefit from the wealth of structural information that NMR can give in comparison to other analytical methods. This goal still stands and the future work focuses on routes towards this goal.
- One of the requirements of this time-resolved approach is the presence of a photolabile ligand. In this research, the photolability of DMSO was highlighted and it would be interesting to investigate the scope of this photoactivity across a range of different complexes and sulfoxide ligands in the future.
- Following from the observation that COE is photolabile in **2.2** it would be interesting to investigate how its reactivity compares to ethene in complexes of the type CpRh(L)(alkene), where L is a phosphine. Previous studies have suggested that CpRhL can activate C–H bonds where the iridium analogue forms a vinyl hydride from the ethene ligand. It would be interesting to study the relative stability and quantum yields between ethene and COE complexes and also extend these studies to compare the activity of rhodium and iridium.
- The study into the reactivity of half sandwich rhodium complexes revealed limited activity with parahydrogen. One fo the explanations for this was the difference in the photoactivity between the Rh^{I} starting material and the Rh^{III} product. It would be interesting to investigate whether using a dihydride as the starting material gives a more promising result as this would allow the sample conditions to be optimised for the species to be followed making it more likely that the rate of its formation can be monitored.
- The observation that *in-situ* NMR methods can be used to observe the evolution of the parahydrogen singlet state is fascinating and extending these studies further is a future aim. **5.1** looked to be a promising candidate for these studies as hyperpolarised signals

were observed with a single laser pulse and single NMR scans. The downside to this complex was that **5.11** was not particularly stable. There are many ruthenium complexes contained POP-Xantphos ligands that would be interesting to study using this approach. Furthermore, the advantage of the xantphos ligand is its chelating behaviour, other similar multichelating lignads would also be of interest, for example Si-O-P-Xantphos derived ligand.[179]

- The complexes which undergo the above behaviour so far have been predominantly ruthenium dihydride systems. It would be interesting to extend these studies to metals beyond ruthenium. Requirements for these complexes are: they are photoactive at 355 nm, contain a photolabile ligand with limited thermal activity, have a singlet electronic structure and form a dihydride complex, rather than a dihydrogen complex, following the reaction with parahydrogen.
- The photochemistry of **5.1** was found to be extensively varied. It would be interesting to see if this diverse behaviour is observed with other ruthenium xantphos complexes and to look at a wider variety of substrates with these complexes.
- It would also be interesting to investigate whether some of the thermal reactions performed using **5.1** could be replicated with light rather than the high temperatures currently required and whether the use of parahydrogen could provide further insights into the reaction mechanisms.
- It has been reported that in some systems the formation of $Ru(H)_2$(Xantphos) complexes inhibits reactivity.[166, 180] It would be interesting to see whether the use of light to induce the reductive elimination of the hydride ligands would limit this deactivation pathway and/or whether using photochemistry the dihydride complex could become active. One example of this is seen in the amination of alcohols.

8 Experimental

8.1 General experimental

8.1.1 Solvent and reagents

All operations were performed under a N_2 atmosphere using standard Schlenk and vacuum lines and glove boxes under an inert atmosphere.

Deuterated solvents (C_6D_6, d_8-toluene and d_{12}-cyclohexane) were dried by stirring over sodium and distilled under high vacuum into small ampoules stored under N_2 in a glove box.

Analytical/reagent grade solvents (butan-2-ol, dichloromethane (DCM), diethyl ether, ethanol, isopropanol, and methanol) were obtained from Fisher Scientific and used without further purification. Acetone, diethyl ether, ethanol, heptane, hexane, pentane, tetrahydrafuran (THF) and toluene were either acquired from an Innovative Technologies anhydrous solvent engineering system or distilled using an appropriate dying method and stored under nitrogen in flame-dried ampoules.

Ethene, carbon monoxide, hydrogen, nitrogen and liquid nitrogen were supplied from BOC gases.

Hydrated ruthenium and rhodium trichloride, $RuCl_3.3H_2O$ and $RhCl_3.3H_2O$ were purchased from precious metals online. Trimethylvinylsilane and lithium cyclopentadienyl and phenyl phosphine were bought from Alfa Aesar. Cyclooctene (COE), 1,5 *cis*-*cis*-cyclooctadiene (COD), phenyllithium in diethyl ether, triphenylphosphine, dimethylsulfoxide (DMSO), 4-methyl pyridine, triethylsilane, ^{15}N-pyridine, 4-tert-butylpyridine, 4,5-Bis(diphenylphosphino)-9,9-dimethylxanthene (xantphos) and ferrocene were all purchased from Sigma Aldrich. (2R,5R)-2,5 hexanediol was bought from TCI, 1,3-Bis(diphenylphosphino)propane (dppp) was bought from Acros organics, phenyl methyl sulfoxide (PhSOMe) was bought from Fluka, and methyl

benzene sulfinate (PhSO(OMe)) was purchased from Fluorochem. All chemicals were used without further purification. Phenyl phosphine and lithium cyclopentadienyl were all stored in a glove box and trimethylvinylsilane phenyl methyl sulfoxide were stored in the fridge.

8.1.2 NMR spectroscopy

NMR data was collected using a three Bruker, Avance III 400 (^{1}H 400.13 MHz, ^{13}C 100.62 MHz and ^{31}P 162 MHz), a Bruker, Avance III HD 500 (^{1}H 500.13 /lMHz, ^{13}C 125.77 MHz, ^{31}P 202.46 MHz and ^{29}Si 99.36 MHz), a Bruker, Avance II 600 (^{1}H 600.12 MHz, ^{13}C 150.91 MHz and ^{31}P 242.93 MHz) and a Bruker Avance II 700 MHz (^{1}H 700.13 MHz, ^{13}C 176.05 MHz ^{31}P 283.43 MHz and ^{29}Si 139.10 MHz).

NMR data was acquired using Topspin versions 1.3, 2.1, 2.3, 3.2.6 and 3.5.5 depending on the instrument and any upgrades which were available during the course of this research. NMR data was processed using Topspin 2.1 initially, then Topspin 3.1 and 3.5.5 following upgrades. The Topspin plot editor was used to prepare spectra for presentation.

^{1}H and ^{13}C NMR spectra were reference relative to residual solvent resonances[135] benzene δ_H 7.15 and δ_C 128.4, toluene δ_H 2.09 and δ_C 20.4, cyclohexane δ_H 1.38 and δ_C 128.4, chloroform δ_H 7.26 and δ_C 77.2 and DMSO δ_H 2.50 and δ_C 39.5.

8.1.3 UV-Visible spectrometry

UV-Visible spectra were recorded in a 1 mm cuvette between 250 and 1100 nm using a Thermo Scientific Evolution Array UV-Visible Spectrophotometer and VisionCollect software.

8.2 Synthesis

8.2.1 Synthesis of $[\{Rh(C_2H_4)_2(\mu\text{-}Cl)\}_2]$[114]

$RhCl_3.xH_2O$ (1.96 g, 9.37 mmol) was added to a large Schlenk tube and dissolved in 3 mL water and 50 mL ethanol giving a dark red solution. A large round bottom flask was attached to the

top of the Schlenk tube and the solution was degassed using a freeze/thaw approach with liquid nitrogen and warm water. The Schlenk tube was backfilled with ethylene and left stirring at room temperature for 2-3 days. After this time a yellow precipitate formed. The reaction solution was transferred into a clean Schlenk and the solid was dried under vacuum and then isolated. The reaction solution was then returned to the large Schlenk tube with the round bottom flask acting as a cap, it was degassed and then placed under an ethylene atmosphere and left stirring for a further 20 hours. After this time, further precipitate formed which was isolated in the same manner as the first batch of product. The product was stored in a Schlenk tube under an atmosphere of ethylene. Total yield 1.014 g, 56%.

8.2.2 Synthesis of $[\{Rh(\eta^2\text{-}CH_2CHSi(CH_3)_3)_2(\mu\text{-}Cl)\}_2]$[115] and $[(\eta^5\text{-}C_5H_5)Rh(\eta^2\text{-}CH_2CHSi(CH_3)_3)_2]$[5] **2.1**

$[\{Rh(C_2H_4)_2(\mu\text{-}Cl)\}_2]$ (0.330 g, 0.85 mmol) and trimethylvinylsilane were added to a Schlenk tube under an inert atmosphere and were then dissolved in 12 mL dry diethyl ether. The solution was stirred vigorously at room temperature for 20 hours. After this time lithium cyclopentadienyl (0.123 g, 2.01 mmol) was added to the reaction mixture, without any purification or isolation of the vinylsilane dimer. The solution was stirred for a further hour, after this time the solvent was removed under vacuum and the product extracted into 3 x 10 mL dry pentane to give a yellow oil. This was recrystallised using a minimum amount of dry acetone and dried under vacuum at 195 K using a dry ice and acetone bath. Yield 0.195 g, 31% Characterisation summarised in Table 2.14 and Table 2.15.

8.2.3 Synthesis of $[\{Rh(\eta^2\text{–}C_8H_{14})_2(\mu\text{-}Cl)\}_2]$[117]

$RhCl_3.xH_2O$ (0.544 g, 2.60 mmol) was added to a large microwave vessel and dissolved in 11 mL 3:1 degassed isopropanol/water mixture under an inert atmosphere giving a dark red solution. To this solution cyclooctene (1.5 mL, 11.52 mmol) was added. The microwave tube cap was

crimped closed and was then heated in the microwave at 70 °C for a total of 25 minutes. After this time precipitate had begun to form, the solution was left for 2 days at room temperature during which time more precipitate formed. The reaction solution was then transferred into a Schlenk tube to allow for purification. The solvent was removed by cannula filtration and the remaining solid was washed with dry ethanol (3 x 10 mL) and then dried under vacuum. Yield 545 mg, 58%.

8.2.4 Synthesis of $[(\eta^5\text{-}C_5H_5)Rh(\eta^2\text{–}C_8H_{14})_2]$[5] **2.2**

$[\{Rh(C_8H_{14})_2(\mu\text{-}Cl)\}_2]$ (0.440 g, 0.61 mmol) and cyclopentadienyl lithium (0.11 g, 1.53 mmol) were added to a Schlenk tube in the glove box and were then dissolved in 20 mL dry tetrahydrafuran. The solution was stirred at room temperature for 1 hour under an inert atmosphere. After this time the solvent was removed under vacuum and the product extracted into dry pentane (3 x 20 mL) to give a yellow oil. This was recrystallised using a minimum amount of dry acetone and dried under vacuum at 195 K using a dry ice and acetone bath. Yield 0.325 g, 69% Characterisation detailed in Section 2.3.2 and summarised in Table 2.16.

8.2.5 Synthesis of $[\{Rh(\eta^4\text{–}C_8H_{12})(\mu\text{-}Cl)\}_2]$ [23]

$RhCl_3.xH_2O$ (0.100 g, 0.48 mmol) was added to a microwave tube and dissolved in 1 mL 5: 1 degassed ethanol/water mixture under an inert atmosphere to give a dark red solution and 0.15 mL cyclooctadiene (1.22 mmol) was added. The cap for the microwave tube was crimped closed and the tube was placed in the microwave where it was heated for a total of 15 minutes at 88 °C, after which time precipitated formed. The product was washed with hexane (3 x 5 mL) and then 5 mL of methanol and then left to dry. Yield 60 mg, 50%.

8.2.6 Synthesis of $[(\eta^5\text{-}C_5H_5)Rh(\eta^4\text{–}C_8H_{14})_2]$ **2.3**

$[\{Rh(C_8H_{12})(\mu\text{-}Cl)\}_2]$ (0.104 g, 0.21 mmol) and cyclopentadienyl lithium (0.035 g, 0.49 mmol) were prepared in 10 mL dry THF and left stirring for 1 hour in a Schlenk tube ,under an inert atmosphere, at room temperature. The solvent was then removed under vacuum and the product extracted into dry hexane (3 x 10 mL) and then left to dry giving a pale yellow solid. Yield 70 mg, 60% Characterisation detailed in Section 2.3.3 and summarised in Table 2.17.

8.2.7 Synthesis of (2R-5R)-2,5 hexanediol bismesylate[139]

(2R, 5R)-2,5 Hexanediol (508.5 mg, 4.3 mmol) was dissolved in dichloromethane (DCM, 12.5 mL) in a Schlenk tube to this 2 mL triethylamine (14.3 mmol) was added. The Schlenk tube was then placed in an ice bath and mesyl chloride (0.8 mL, 10.3 mmol) was added resulting in a colour change from clear to yellow. The Schlenk tube was then returned to room temperature and left stirring for 4 hours. After this time, a further 10 mL of DCM was added and the reaction mixture was transferred to a separating funnel. 10 mL of a 1M HCl solution was then added to neutralise the reaction. The mixture was allowed to settle and the organic layer was collected. The organic layer was then washed with 10 mL of brine, the mixture was allowed to settle and the organic layer was once again collected, it was then dried using magnesium sulfate. The solution was then filtered into a Schlenk tube and the solvent removed under vacuum giving a colourless oil. (Yield 850 mg, 72%) ^{1}H NMR (500.13 MHz, $CDCl_3$) δ 4.80-4.90 (2H, m CH^2), 3.00 (6H, s, $CH_3{}^4$), 1.70-1.80 (4H, m, $CH_2{}^3$), 1.42 (6H, d 6Hz, $CH_3{}^1$). ^{13}C NMR (125.76 MHz, $CDCl_3$) δ 79.0 (C^2), 38.6 (C^4), 31.0 (C^3), 21.1 (C^1).

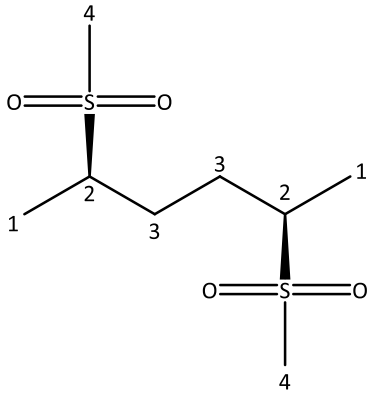

Figure 8.1: Structure of (2R-5R)-2,5 hexanediol bismesylate.

8.2.8 Synthesis of (2S, 5S) 2,5 dimethyl, 1-phenyl phospholane[140]

Phenyl phosphine (550mg, 5.0 mmol) was dissolved in 15 mL dry diethyl ether in a Schlenk tube in a glove box. It was then placed under argon on a Schlenk line and placed in a dry ice/acetone bath. Phenyl lithium in diethyl ether (6.6 mL, 7.2 mmol) was placed in a second Schlenk tube under Ar and was added dropwise by cannula into the phenyl phosphine solution, this resulted in a colour change from clear to orange and then to yellow. After the addition, the reaction mixture was removed from the ice bath and returned to room temperature and the solution stirred under an inert atmosphere for 1 hour. After this time the Schlenk tube was placed in a dry ice/acetone bath and (2S-5S)-2,5 hexanediol bismesylate (850 mg, 3 mmol), dissolved in 5 mL dry THF in a separate Schlenk tube, was added dropwise into the reaction flask. It was then returned to room temperature and left stirring over the weekend, 65 hours. The solvent was then removed under vacuum and the product extracted using dry heptane (3 x 15 mL) in a yield of 520 mg or 80% based on hexanediol bismesylate. ^{1}H NMR (500.13 MHz, C_6D_6) δ 7.45 (dd 8, 2 Hz, *ortho*H), 7.20 (t 8 Hz, *meta*H), 7.11 (d 6Hz, *para*H), 2.52 (m, ^{6}CH). 2.08 (m, ^{3}CH), 2.06 (m, $^{5}CH_2$), 1.73 (m, $^{4}CH_2$), 1.37 (m, $^{5}CH_2$), 1.27 (dd, J_{PH} 18.7, J_{HH} 7.2 Hz, $^{7}CH_3$), 1.13(m, $^{4}CH_2$), 0.78 (dd, J_{PH} 10.6, J_{HH} 7.1 Hz, $^{8}CH_3$). ^{13}C NMR (125.76 MHz, C_6D_6) δ 128.5 (*meta*), 128.0 (*para*), 127.0 (*ortho*), 36.8 ($^{4,5}CH_2$), 35.2 (^{3}CH), 34.9 (^{6}CH), 20.9 ($^{7}CH_3$), 15.2 ($^{8}CH_3$). ^{31}P NMR (202.46 MHz, C_6D_6) δ9.8. LIFDI MS: 192.11.

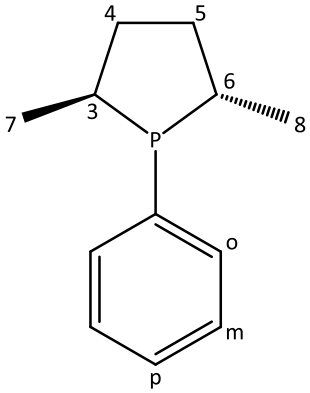

Figure 8.2: Structure of (2S, 5S) 2,5 dimethyl, 1 phenyl phospholane.

8.2.9 Synthesis of $[(\eta^5\text{-}C_5H_5)Rh(P^*Ph)(C_2H_4)]$ **3.2**[6]

$[Rh(C_2H_4)_2(\mu\text{-}Cl)]_2$ (128 mg, 0.33 mmol) and (2S, 5S) 2,5 dimethyl, 1 phenyl phospholane (127 mg, 0.66 mmol) were separately dissolved in 5 mL dry THF each in Schlenk tubes. The phospholane was added dropwise to the rhodium solution and it was left stirring at room temperature for 20 minutes. Lithium cyclopentadienyl (47 mg, 0.66 mmol) was then added and the reaction was left stirring for a further hour. After this time, the solvent was removed under vacuum and the product was extracted into dry hexane (3 x 10 mL). The ^{1}H NMR spectrum showed there to be 42% of $[(\eta^5\text{-}C_5H_5)Rh(C_2H_4)_2]$. To try to purify the product, a sublimation was performed using a cold finger. A yellow precipitate formed on the finger this was washed off into a vial with hexane. The remaining solid was checked by NMR and contained 37% of $[(\eta^5\text{-}C_5H_5)Rh(C_2H_4)_2]$. Characterisation detailed in Section 3.5 and summarised in Table 3.2.

8.2.10 Synthesis of $[Ru(H)_2(CO)(PPh_3)_3]$[165]

$RuCl_3.3H_2O$ (0.232 g, 0.89 mmol) was dissolved in 65 mL ethanol in a 100 mL 3 necked round bottom flask fitted with a reflux condenser and purged with N_2. The solution was heated under reflux under N_2 for 10 minutes and triphenylphosphine (PPh_3, 1.01 g, 3.85 mmol) was added and the solution stirred under reflux for a further hour during which time a dark brown precipitate formed. The solution was cooled to room temperature and KOH added (0.22 g, 3.92 mmol) and the solution stirred vigorously for 1 hour and a green solution resulted. The

solution was heated to 60 °C for 1 hour and refluxed for a further 5 hours, during this time the solution turned from green to yellow and a pale yellow precipitate formed. The solution was then cooled to room temperature to allow for purification and the solution was filtered and the resulting solid washed with 20 mL of ethanol, 20 ml of deionised water and a further 20 mL of ethanol. A pale yellow solid resulted in a yield of 742 mg or 91% based on ruthenium. NMR characterisation: ^{1}H NMR (500.13 MHz, C_6D_6) δ 7.83 (P_B-*o*-H), 7.47 (P_A-*o*-H), 7.31 (P_B-*m*-H), 7.00 (P_A-*m*-H), 6.90 (P_A-*p*-H), 6.84 (P_B-*p*-H), –6.47 (1H, tdd, J_{HP_A} 30.4, J_{HP_B} 15.2, J_{HH} 6.6 Hz, H_B), –8.31 (1H, dtd, J_{HP_B} 74.6, J_{HP_A} 28.7, J_{HH} 6.6 Hz, H_A). ^{31}P NMR (162.00 MHz, C_6D_6) δ 57.4 (2P, d, J_{PP} 17 Hz, P_A), 45.3 (1P, t, J_{PP} 17 Hz, P_B).

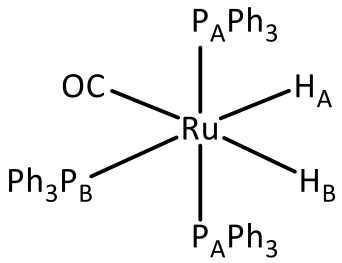

Figure 8.3: Structure of $Ru(H)_2(CO)(PPh_3)_3$.

8.2.11 Synthesis of $[Ru(H)_2(CO)(PPh_3)(Xantphos)]$[158] **5.1**

$[Ru(H)_2(CO)(PPh_3)_3]$ (0.70g, 0.76 mmol) was dissolved in dry and degassed toluene in a 3 necked 100 mL round bottom flask in a glove box and suba sealed under nitrogen and 4,5-bis(diphenylphosphino)-9,9-dimethylxanthene (xantphos, 0.55 g, 0.92 mmol). A reflux condenser was attached to round bottomed flask and the system purged with nitrogen. The solution was heated to 120 °C for 3 hours. The solution was then transferred into a Schlenk tube by cannulation and the solvent was removed under vacuum, a brown oily residue resulted. This was washed with ethanol (3 x 20 mL), pentane (30 mL) and a further 2 x 20 mL of ethanol to give an off-white solid. The solid was extracted into toluene (20 mL) and recrystallised from hexane (10 mL) to give the product in a 250 mg isolated yield, which gave a

34% yield based on ruthenium. The characterisation of this complex is described in Section 5.2.2 and summarised in Table 5.1.

8.2.12 Synthesis of $[Ru(COD)Cl]_2$ [174]

$RuCl_3.xH_2O$ (4.01 g, 19 mmol), 1,5-cyclooctadiene (5 mL, 40 mmol) and ethanol (40 mL) were added to a 250 mL round bottom flask fitted with a reflux condenser. The solution was heated to 80 °C and left under reflux with stirring for 17 hours. During this time a brown precipitate formed. The solution was left to return to room temperature and the solution filtered. The product was washed with diethyl ether and left to dry. Yield 4.33 g, 80%.

8.2.13 Synthesis of [*cis*-$Ru(H)_2(dppp)_2$] **6.1**[175]

$[RuCl_2(COD)]_x$ (0.355 g, 1.25 mmol), $Ph_2P(CH_2)_3PPh_3$ (dppp, 1.03 g, 2.5 mmol) and NaOH (1.05 g, 26.3 mmol) were dissolved in butan-2-ol (80 mL) in a Schlenk flask, the solution was degassed and placed under an argon atmosphere. The solution was then stirred and heated to 80 °C for 2 hours resulting in a yellow solution. After this time the solution was returned to room temperature and degassed water (100 mL) was added, the solution was stirred for 1 hour. After this time, stirring was stopped and the solution separated into two layers. The aqueous layer removed by cannula filtration. The remained solution was dried under vacuum to give a yellow solid. This was extracted into dry toluene (3 x 20 mL) and recrystallised from dry hexane (10 mL). Yield 0.62 g, 53% Characterisation detailed in Section 6.2 and summarised in Table 6.3.

8.2.14 Parahydrogen preparation

Parahydrogen was prepared by passing H_2 with thermal equilibrium spin distribution over a Fe_2O_3/charcoal catalyst as temperatures in the region of 30 K. This facilitated the conversion from ortho- to para- hydrogen, at these temperatures H_2 gas which is approximately 97 % *p*-H_2 may be isolated,[181] the exact composition will vary from one day to the next. In the absence of

a paramagnetic species and once this gas has returned to room temperature it will retain this proportion of *p*-H_2.

8.3 Photolysis Methods

8.3.1 External UV photolysis set up

For the *ex-situ* photochemical studies an Oriel 200 W Hg-Xe arc lamp was used providing a source of broadband UV light. A 5 cm water filter was used to minimise any heating of the sample and thus limit any thermal reactivity. The sample was kept in the NMR spinner and placed in a clamp (Figure 8.4) this was to ensure that the sample was always the same distance from the lamp and that the solution experienced the same amount of irradiation. The lamp was left to warm up for at least 20 minutes prior to any photolysis.

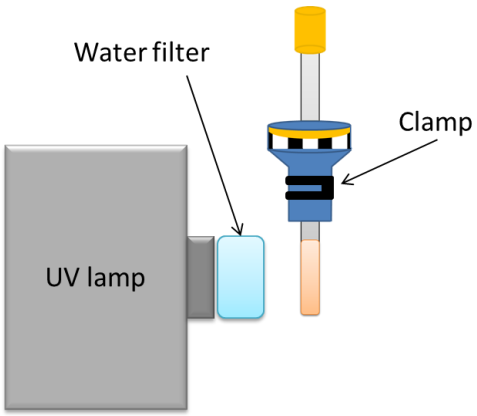

Figure 8.4: Schematic representation of the *ex-situ* irradiation set up.

8.3.2 *In-situ* photochemistry setup (laser)

The *in-situ* photochemistry setup in York is performed on a Bruker Avance widebore 600 MHz spectrometer using a BBO probe for data acquisition. The light source was a pulse Nd:YAG laser (Continuum Surelite II) fitted with a frequency tripling crystal (output wavelength 355 nm). Operating conditions were typically; flash lamp voltage 1.49 kV, in the internally triggered mode a 10 Hz repetition rate was used with a Q-switch delay increased from the standard to 320 µs yielding a laser power of 75 mW, In the externally triggered mode a Q-switch delay of

150 μs delivering a single laser pulse with an energy of 29.8 mJ.[87] . In internally triggered mode a purpose-written program was used to control the firing of the laser pulse. A warm up shot is triggered first before the fire shot, this sequence was repeat with a variable time delay in experiments with specified laser pulses. Following this the NMR pulse sequence is initiated after a set time delay (τ). This contained a 140 μs delay relating to the intrinsic time delay between sending the fire signal from the spectrometer and the laser firing. The precision of this delay between the laser and RF pulses is controlled by the 200 ns clock of the spectrometer.

The laser beam was directed to the base of the spectrometer onto an adjustable mirror which directed the laser beam up into the spectrometer onto a second fixed mirror held in a collar on the probe which allows the light to be directed through a hole in the probe and onto the side of the sample (Figure 8.5). The adjustable mirror underneath the spectrometer is to allow the fine-tuning of the laser alignment to be performed. There are two nylon rods attached the mirror amount which allows for the alignment to be optimised. The laser alignment is optimised using parahydrogen enhancements. An optically dilute sample of *cis*-[Ru(dppe)$_2$H$_2$], where dppe refers to 1,2-bis(diphenylphosphino)ethane, was prepared in C_6D_6. This was degassed by three cycles of freeze-pump-thaw and back filled with 3 bar of *p*-H_2. The sample was shaken and placed in the spectrometer. Using real time scanning (gs mode) with a pulse sequence modified to pulse the laser and a short d1 time ^{1}H spectra were acquired. These show the enhancements of the dihydride complex, the nylon rods were moved to find the position which gives the largest enhancement of this dihydride. This reflects more of the laser light being hitting the sample as a consequence of a better alignment of the laser. The sample was shaken and a record of this enhancement made to allow comparisons of the enhancements/alignment from one day to the next.

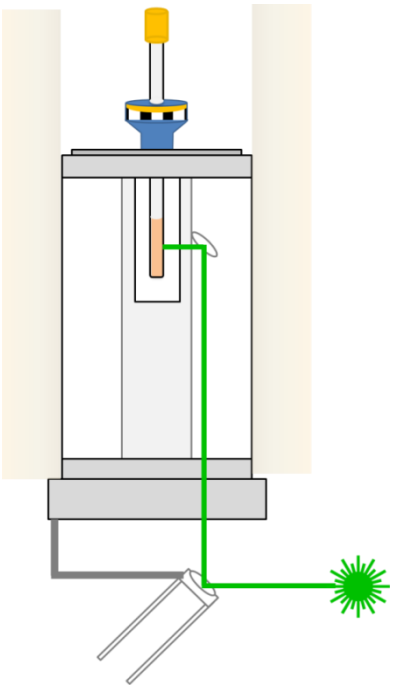

Figure 8.5: Schematic of the *in-situ* laser irradiation inside an NMR spectrometer.

8.3.3 *In-situ* photochemistry Setup (UV lamp)

One of the *in-situ* photochemistry set up in York uses Oriel 200 W Hg-Xe arc lamp which provides a source of broadband UV light. An adaptor was attached to the lamp to allow an ethanol liquid light guide cable to be connected to the lamp. This cable is used to direct the light inside the NMR spectrometer and on to a mirror held in a collar on the probe head. This mirror reflects the light through a hole in the probe head and onto the side of the NMR sample.

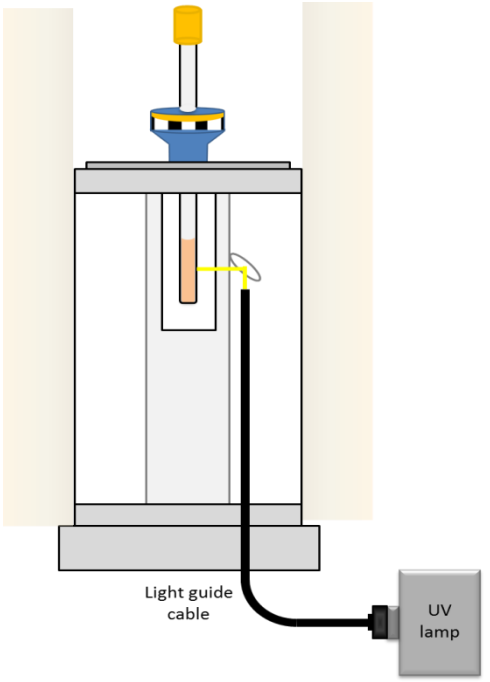

Figure 8.6: Schematic of the *in-situ* laser irradiation inside an NMR spectrometer.

8.4 Data processing

8.4.1 Determining concentrations by NMR

The concentrations of the starting materials and any products which formed following photolysis were determined using ^{1}H NMR spectroscopy. To use the proton spectra quantitatively they were acquired using a 30° pulse and a 30 second relaxation delay (d1) this was to allow complete relaxation of the magnetisation before the next pulse. The spectra were then integrated using defined integrals regions for each of the species and a reference peak. The reference peak allows comparison between the different spectra accounting for any variation between them. The residual protio solvent peak or an internal standard, ferrocene, were used. The following procedure was then used to convert these integrations into relative concentrations:

1. Divide the integrations by the number of protons to give Int_{1H}
2. Divide Int_{1H} by the integration for the reference peak (Int_{ref})

3. Divide each Int_{ref} by the sum of Int_{ref} at t=0 (prior to photolysis) and x 100 to give as a percentage of the initial rhodium content.
4. The errors in these measurements were estimated using the standard deviations during the equilibria for that approximate concentration
    - <5% conversion, a 20% error was assumed
    - 5-15% conversion, a 10% error was used
    - 15-25% conversion, a 5% error was used
    - >25% conversion, a 3% error was used

8.4.2 Determining equilibrium constants using Origin

The percent of each species relative to the initial rhodium content were plotted against the irradiation time in seconds. For the kinetic models which consists of two complexes in equilibrium as depicted in Figure 8.7, the concentration of the metal complexes were fitted to Equation (8.1) where k_{obs} is the relaxation constant for the equilibrium and is described by the expression $k_{obs} = k_1([M]+[L])+k_2([L']+[M'])$. The equilibrium constant for these reactions can be calculated using the equilibrium concentrations of each species in equilibrium using Equation (8.2). The experimentally determined k_{obs} and K_{eq} can be combined to give values of k_1 and k_2 using Equations (8.3) and (8.4).

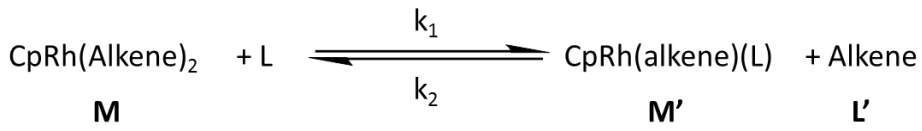

Figure 8.7: Generic Kinetic Model showing two metal complexes, M and M', in equilibrium through the substitution of ligands L and L'.

$$[M]_t = [M]_{eq} + ([M]_0 - [M]_{eq})e^{-k_{obs}t} \qquad (8.1)$$

$$K_{eq} = \frac{k_1}{k_2} = \frac{[M']_{eq}[L']_{eq}}{[M]_{eq}[L]_{eq}} \qquad (8.2)$$

$$k_1 = \frac{K.k_{obs}}{K([M]+[L])+[M']+[L']} \quad (8.3)$$

$$k_2 = \frac{k_{obs}}{K([M]+[L])+[M']+[L']} \quad (8.4)$$

8.4.3 Determining rate constants using Excel

The Excel simulation package uses a differential rate approach and its methodology will now be illustrated using a first order equilibrium between A and B (Figure 8.8). The concentrations of A and B were measured as percentages of the initial concentrations and tabulated in Excel with the total irradiation time in seconds. A series of simulated data is then obtained based on an appropriate kinetic model, according to the general Equation (8.5), where dt is the time increment(s), t is the time (s), $[A]_t$, is the concentration of A at time t (%), Σk_{lossA} is the sum of all rate constants which result in the loss of A and Σk_{gainA} is sum the rate constants which results in the gain of A and [Prod] are the concentrations of any products formed. For the model in Figure 8.8, the rate of formation of A is given by k_{BA} and loss of A by k_{AB}. The simulated data can therefore be calculated using Equations (8.6) and (8.7) with a time increment of 0.2 s. The Solver function in Excel changes the values of k_{AB} and k_{BA}, to minimise the sum of the squares of differences between the calculated and experimental data, for *n* experimental observations.

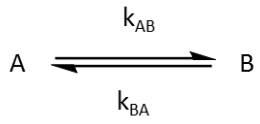

Figure 8.8: Generic kinetic model for a first order equilibrium.

$$[A]_t = [A]_{t-dt} - dt(\Sigma k_{lossA})[A]_{t-dt} + dt\Sigma(k_{gainA}[Prod])_{t-dt} \quad (8.5)$$

$$[A]_t = [A]_{t-0.2} - 0.2(k_{AB})([A]_{t-0.2}) + 0.2(k_{BA})([B]_{t-0.2}) \quad (8.6)$$

$$[B]_t = [B]_{t-0.2} - 0.2(k_{BA})([B]_{t-0.2}) + 0.2(k_{AB})([A]_{t-0.2}) \quad (8.7)$$

The errors in these measurements were determined using the jack-knife/bootstrap approach where each experimental point is removed in turn and the values of k_{AB} and k_{BA} are fitted using the Solver routine giving n – 1 observations. The error is calculated using the following procedure:

- Calculate the average values of k_{AB} and k_{BA} using the whole set of data
- Calculate the values of k_{AB} and k_{BA} for all the permutations using n – 1 observations
- Calculate the standard deviation, SD, for these values of k_{AB} and k_{BA}
- Calculate the standard error, SE, using the SD and number of points, n

$$\mathrm{SE} = \frac{\mathrm{SD}}{\sqrt{\mathrm{n}}}$$

- Calculate the 95% confidence interval , CI, using the SE and student t value

$$\mathrm{CI} = \mathrm{SE} \times \mathrm{t\ value}$$

8.4.4 Creating a 2D map

A blank 2D dataset was acquired using the *timestore* pulse sequence with the following parameters:

- The number of data points and sweep width of the NMR spectrum must be the 1D ^{1}H NMR spectrum
- The number of increments in the 2D data set must be greater than or equal to the number of 1D to be included
- The increment delay, IN_F, must correspond to the step size used when incrementing the pump probe delay

Having created the blank data set the ^{1}H NMR spectra were added to it using the command *fidtoser* and the following information added if the NMR spectra to be added were in sequential datasets. If this was not the case, *wser* was used to manual insert each individual 1D dataset into the appropriate slot of the 2D data set.

9 Appendix 1: Relaxation and Photochemical Kinetics

9.1 Introduction

Relaxation kinetics describes a process where the equilibrium position is perturbed by an external factor. The system adjusts accordingly and a second equilibrium is reached (Figure 9.1).[182] The most common routes for perturbation are by changing the temperature or the pressure of the system and this causes a jump in the concentration of one of the species in the equilibrium, hence why these are also known as temperature/pressure jump experiments. The system may also be perturbed by an increase in the concentration of a ligand, this is commonly seen in enzymatic systems, or, as is the case in this research, through the use of UV light. Regardless of the method used to perturb the system the analysis is the same. This has the advantage that, providing the kinetic model is known, the expression that determines the rate of relaxation and thus the rate constants for the reactions has already been solved and these results will now be exemplified. In this analysis, it is assumed that the perturbation is small allowing the simpler definitions of the relaxation kinetics to be used.[121-125] It should also be noted that with UV light there is a second perturbation of the system when the light is switched off. Some assumptions about these relative rates of the equilibria need to be made. Primarily, that the rate of the thermal equilibrium, once the light has been switched off, takes place on a much slower timescale than the photochemical equilibrium step and thus the photochemical equilibrium can be treated separately.

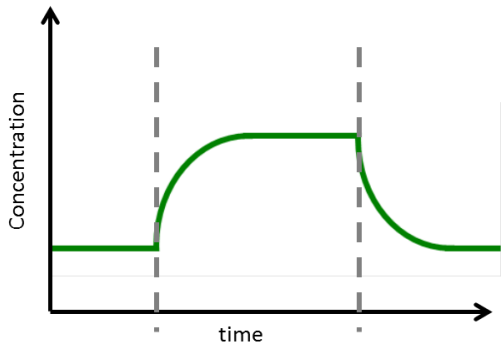

Figure 9.1: Schematic to demonstrate relaxation kinetics, the dashed lines signify the point at which the system is perturbed.

9.2 First Order Equilibrium

9.2.1 Thermal Reaction

The simplest system involves two species, often two isomers, in equilibrium with one another (Figure 9.2). The rate of the forward reaction, A going to B, is given by k_1 and the reverse reaction by k_{-1}. The rate equations for the A and B can be written as per Equations (9.1) and (9.2).

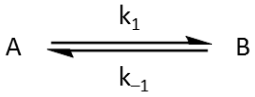

Figure 9.2: Kinetic Model for a 2 component, 1 step reversible reaction.

$$-\frac{d[A]}{dt} = k_1[A] - k_{-1}[B] \tag{9.1}$$

$$-\frac{d[B]}{dt} = -k_1[A] + k_{-1}[B] \tag{9.2}$$

Once the system is at equilibrium, both of these rate equations will equal zero and the two rate equations will also equal one another. This means that they can be combined to give expressions for the equilibrium constant, K_{eq}. As shown below, this can be expressed either, in terms of the rate constants for the two processes or by the concentrations of the species in equilibrium, Equation (9.3).[122]

$$k_1[A]_{eq} - k_{-1}[B]_{eq} = -k_1[A]_{eq} + k_{-1}[B]_{eq}$$

$$2k_1[A]_{eq} = 2k_{-1}[B]_{eq}$$

$$\boxed{K_{eq} = \frac{[B]_{eq}}{[A]_{eq}} = \frac{k_1}{k_{-1}}} \tag{9.3}$$

The kinetics of such a system can also be studied using an integrated rate approach and the integrated rate expressions (9.4) and (9.5) were obtained, following the perturbation of the system.[121]

$$[A] = [A]_{eq} + ([A]_0 - [A]_{eq})e^{-(k_1+k_{-1})t} \quad (9.4)$$

$$[B] = [B]_{eq} + ([B]_0 - [B]_{eq})e^{-(k_1+k_{-1})t} \quad (9.5)$$

These comply with the equation $y = a + be^{-kt}$ which can be readily modelled using the graphical packages such as Origin or Sigmaplot. This also means that there are two observable terms which relate to k_1 and k_{-1} and therefore these expressions can be combined in order to calculate the rate constants using Equations (9.6) and (9.7), where k_{obs} is defined by Equation (9.8).[124]

$$k_1 = \frac{k_{obs}K_{eq}}{K_{eq} + 1} \quad (9.6)$$

$$k_{-1} = \frac{k_{obs}}{K_{eq} + 1} \quad (9.7)$$

$$k_{obs} = k_1 + k_{-1} \quad (9.8)$$

Derivation of the Integrated Rate Expressions

The change in the concentrations, x, of A and B at any point in time compared to the equilibrium concentration can be described by Equations (9.9) and (9.10) these can be rearranged and used in Equation (9.1) to substitute for $[A]_t$ and $[B]_t$ to give Equation (9.11). At the new equilibrium position, the rate of change in A matches the rate of change in B, mathematically, this is described by Equation (9.13) and therefore the terms containing $[A]_{eq}$ and $[B]_{eq}$, in Equation (9.12) cancel one another out, leaving just $(k_1 + k_{-1})x$. This can then be integrated with respect to x to give Equation (9.14), substituting the x terms with Equation

(9.9) gives the rate equation (9.15) which is easily rearranged to give Equation (9.4). The same procedure can be used to obtain the rate expression for B.

$$x = [A]_t - [A]_{eq} \tag{9.9}$$

$$-x = [B]_t - [B]_{eq} \tag{9.10}$$

$$-\frac{d[A]}{dt} = k_1\big([A]_{eq} + x\big) - k_{-1}([B]_{eq} - x) \tag{9.11}$$

$$-\frac{d[A]}{dt} = -\frac{dx}{dt} = k_1[A]_{eq} + k_1 x - k_{-1}[B]_{eq} + k_{-1}x \tag{9.12}$$

$$k_1[A]_{eq} = k_{-1}[B]_{eq} \tag{9.13}$$

$$-\frac{dx}{dt} = k_1 x + k_{-1}x = (k_1 + k_{-1})x$$

$$-\ln\frac{x}{x_0} = (k_1 + k_{-1})t$$

$$x = x_0 e^{(-(k_1+k_{-1})t)} \tag{9.14}$$

$$[A] - [A]_{eq} = ([A]_0 - [A]_{eq})e^{(-(k_1+k_{-1})t)} \tag{9.15}$$

9.2.2 Photochemical reaction

The kinetics for a photochemical reaction requires a different approach. The concentrations of the photoactive species depend on the Beer-Lambert law (9.16) and the quantum yield, Φ, of the species. The rate equations for the changes in concentration are now given by the expressions in (9.17) and (9.18) based on the work by Hippler.[125] When these two isomers are in equilibrium the two expressions can be combined to give an expression begins to describe the equilibrium in Equation (9.19), note the I_0 terms cancel one another out

$$\log_{10}\frac{I_0}{I} = \varepsilon c l \tag{9.16}$$

$$-\frac{d[A]}{dt} = \Phi_A I_A - \Phi_B I_B = \Phi_A I_o(1 - e^{-\varepsilon_A[A]l}) - \Phi_B I_o(1 - e^{-\varepsilon_B[B]l}) \tag{9.17}$$

$$-\frac{d[B]}{dt} = \Phi_B I_B - \Phi_A I_A = \Phi_B I_o\left(1 - e^{-\varepsilon_B[B]l}\right) - \Phi_A I_o(1 - e^{-\varepsilon_A[A]l}) \quad (9.18)$$

At equilibrium: $\frac{d[A]}{dt} = \frac{d[B]}{dt}$

and $\Phi_A I_A = \Phi_B I_B$

$$\frac{(1 - e^{-\varepsilon_B[B]l})}{(1 - e^{-\varepsilon_A[A]l})} = \frac{\Phi_A}{\Phi_B} \quad (9.19)$$

We now consider the situation corresponding to low absorbance.

Low absorbance

If the sample is optically dilute, it has low absorbance and ε[A]l and ε[B]l are small and therefore the exponential term can be simplified since e^{-x} tends towards 1 – x. For isomers formed by different orientation of the vinylsilane, we also assume that ε_A and ε_B are equal to ε. This means that $e^{-\varepsilon[A]l}$ and $e^{-\varepsilon[B]l}$ tend towards 1 − ε[A]l and 1 − ε[B]l and these terms can be substituted into Equation (9.19) to give Equation (9.20). The expression for K_{eq} now resembles its thermal equivalent (Equation (9.3)).

$$\frac{(1 - 1 - (-\varepsilon[B]l))}{(1 - 1 - (-\varepsilon[A]l))} = \frac{\Phi_A}{\Phi_B}$$

$$\boxed{K_{eq} = \frac{[B]}{[A]} = \frac{\Phi_A}{\Phi_B}} \quad (9.20)$$

Making the same approximations and integrating between times 0 and t, we obtain the rate of loss of A and the rate of formation of B. Note to distinguish the equilibrium concentrations under photochemical conditions from the thermal situation previously described $[Y]_{PSS}$ is used in place of $[Y]_{eq}$ where PSS stands for photostationary state.

$$\frac{d[A]}{dt} = -\Phi_A I_o \varepsilon_A [A]_t l + \Phi_B I_o \varepsilon_B [B]_t l \quad (9.21)$$

$$\frac{d[B]}{dt} = -\Phi_B I_o \varepsilon_B [B]_t l + \Phi_A I_o \varepsilon_A [A]_t l \quad (9.22)$$

During the reaction, the concentrations of [A] and [B] change by x, where x is defined by the equations below:

$$x = [A]_t - [A]_{PSS} \tag{9.23}$$

$$-x = [B]_t - [B]_{PSS}$$

$$-\frac{d[A]}{dt} = -(\Phi_A I_o \varepsilon_A l)(x + [A]_{PSS}) + (\Phi_B I_o \varepsilon_B l)([B]_{PSS} - x) \tag{9.24}$$

$$-\frac{d[A]}{dt} = \frac{dx}{dt} = -x(\Phi_A I_o \varepsilon_A l + \Phi_B I_o \varepsilon_B l) - \Phi_A I_o \varepsilon_A [A]_{PSS} l + \Phi_B I_o \varepsilon_B [B]_{PSS} l \tag{9.25}$$

At equilibrium, a photostationary state is formed and the rate of the formed and back reactions are equal and x is zero. This can be substituted into Equation (9.25) giving an expression only in terms of x.

$$-\Phi_A I_o \varepsilon_A [A]_{PSS} l + \Phi_B I_o \varepsilon_B [B]_{PSS} l = 0$$

$$\frac{dx}{dt} = -x(\Phi_A I_o \varepsilon_A l + \Phi_B I_o \varepsilon_B l)$$

Integrate with respect to x

$$-\ln\frac{x}{x_0} = (\Phi_A I_o \varepsilon_A l + \Phi_B I_o \varepsilon_B l)t$$

$$x = x_0 e^{(-(\Phi_A I_o \varepsilon_A l + \Phi_B I_o \varepsilon_B l)t)}$$

Can now substitute x with Equation (9.23).

$$[A]_t = [A]_{PSS} + ([A]_0 - [A]_{PSS})e^{-k_{obs}t} \tag{9.26}$$

$$[B]_t = [B]_{PSS} + ([B]_0 - [B]_{PSS})e^{-k_{obs}t} \tag{9.27}$$

$$k_{obs} = I_o \varepsilon l(\Phi_A + \Phi_B)$$

The photoreaction is first order in $[A]_0 - [A]_{PSS}$and the apparent rate constant is

$$I_o \varepsilon l(\Phi_A + \Phi_B)$$

Determination of rate constants under photochemical conditions

Both k_{obs} and K_{eq} relate to the rates of the reaction and allowing expressions for Φ_A and Φ_B to be obtained and can relate the measured values of k_1 and k_2 to the photochemical properties of the reactants.

$$k_{obs} = I_o \varepsilon l(\Phi_A + \Phi_B)$$

$$K_{eq} = \frac{\Phi_A}{\Phi_B}$$

$$\Phi_A = \Phi_B K_{eq} \qquad \Phi_B = \frac{\Phi_A}{K_{eq}}$$

$$k_{obs} = I_o \varepsilon l(\Phi_A + \frac{\Phi_A}{K_{eq}})$$

$$\frac{K_{eq} k_{obs}}{I_0 \varepsilon l} = (\Phi_A K_{eq} + \Phi_A)$$

$$\boxed{\Phi_A = \frac{K_{eq} k_{obs}}{(K_{eq} + 1) I_0 \varepsilon l}}$$

$$k_{obs} = I_o \varepsilon l(\Phi_B K_{eq} + \Phi_B)$$

$$\frac{k_{obs}}{I_0 \varepsilon l} = \Phi_B (K_{eq} + 1)$$

$$\boxed{\Phi_B = \frac{k_{obs}}{(K_{eq} + 1) I_0 \varepsilon l}}$$

$$\boxed{k_1 = \Phi_A I_0 \varepsilon l} \qquad \boxed{k_{-1} = \Phi_B I_0 \varepsilon l}$$

Limitations

The exact quantum yields cannot be determined exactly from these measurements due to nature of the experiments. Firstly, the measurements were made using broadband UV light

which means a wide range of wavelengths are used and therefore individual processes cannot be separated out. The samples were irradiated within the NMR tube, since these are cylindrical the path length is not uniform across the sample and the solution experiences different degrees of irradiation depending on its location within the tube.

If the assumption of low absorbance is not true, this adds further limitations. The Beer-Lambert law assumes a linear dependence between the path length and the absorbance (Figure 9.3). If solution had high absorbance, the path length associated with 90% absorbance is shorter. Therefore the light irradiation a smaller proportion of the sample and reduces the reactive region of the sample resulting in longer reaction times.

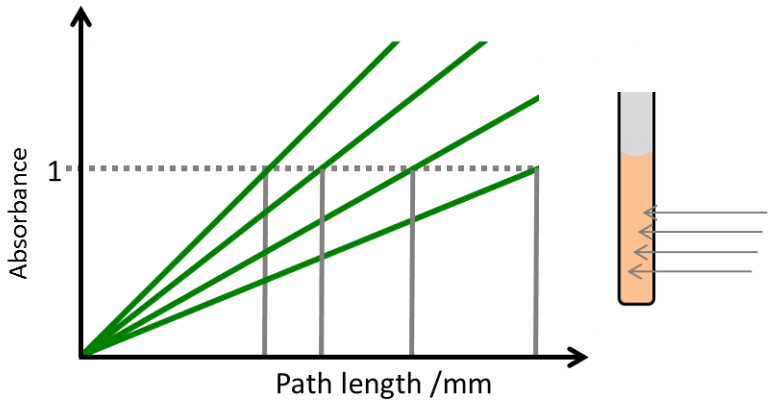

Figure 9.3: Schematic representation path length against absorbance and implication this has on absorbance in an NMR tube.

9.3 Bimolecular Second Order Equilibrium

9.3.1 Thermal relaxation kinetics

This approach can be readily extended to other kinetic models. The natural next step is to move to a second order equilibrium (Figure 9.2). Like the first model, this includes just one reversible step, this time however there are four species in equilibrium. This situation typically arises in substitution reactions. Each component of the rate equation is now bimolecular. They can however be treated in the same manner as the first model which gives a description of K_{eq} where it can be determined using the equilibrium concentrations of all four species in

equilibrium using the expression in Equation (4.10).[122] These rate equations can be converted into integrated expressions using the same approach as with first order system to give Equations (9.31) and (9.32) where k_{obs} is defined by Equation (9.33).[123]

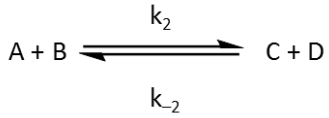

Figure 9.4: Kinetic Model for a four component bimolecular reversible reaction

$$-\frac{d[A]}{dt} = k_2[A][B] - k_{-2}[C][D] \tag{9.28}$$

$$-\frac{d[C]}{dt} = -k_2[A][B] + k_{-2}[C][D] \tag{9.29}$$

$$K_{eq} = \frac{[C]_{eq}[D]_{eq}}{[A]_{eq}[B]_{eq}} = \frac{k_2}{k_{-2}} \tag{9.30}$$

$$[A] = [A]_{eq} + ([A]_0 - [A]_{eq})e^{-k_{obs}t} \tag{9.31}$$

$$[C] = [C]_{eq} + ([C]_0 - [C]_{eq})e^{-k_{obs}t} \tag{9.32}$$

$$k_{obs} = k_2([A] + [B]) + k_{-2}([C] + [D]) \tag{9.33}$$

Derivation of Rate Equation

$$x = [A]_t - [A]_{eq}$$

$$[A]_t = [A]_{eq} - x \qquad [B]_t = [B]_{eq} - x$$

$$[C]_t = [C]_{eq} + x \qquad [C]_t = [C]_{eq} + x$$

$$-\frac{d[A]}{dt} = k_2[A][B] - k_{-2}[C][D]$$

$$-\frac{d[A]}{dt} = k_2([A]_{eq} - x)([B]_{eq} - x) - k_{-2}([C]_{eq} + x)([D]_{eq} + x)$$

$$= k_2[A]_{eq}[B]_{eq} - k_{-2}[C]_{eq}[D]_{eq} - x(k_2([A]_{eq} + [B]_{eq}) + k_{-2}([C]_{eq} + [D]_{eq}) + (k_2 - k_{-2})x^2$$

At Equilibrium $$-\frac{d[A]}{dt} = 0$$

$$\frac{dx}{dt} = x(k_2([A]_{eq} + [B]_{eq}) + k_{-2}([C]_{eq} + [D]_{eq}) + (k_2 - k_{-2})x^2$$

$$-\ln\frac{x}{x_0} = \left(k_2\left([A]_{eq} + [B]_{eq}\right) + k_{-2}\left([C]_{eq} + [D]_{eq}\right)\right)t$$

The x^2 term is neglected as it is assumed that if x is small, x^2 will be negligible in comparison to x.

Calculation of Rate Constants

In this scenario there are also two observable constants which are related to the values of k_3 and k_4 and therefore the observed rate constant and the equilibrium constant can be used to determine the rate constants k_2 and k_{-2} using Equations (9.34) and (9.35).[124]

$$k_2 = \frac{\mathrm{k_{obs}K_{eq}}}{\mathrm{K_{eq}}([A] + [B]) + [\mathrm{C}] + [\mathrm{D}]} \qquad (9.34)$$

$$k_{-2} = \frac{\mathrm{k_{obs}}}{\mathrm{K_{eq}}([A] + [B]) + [\mathrm{C}] + [\mathrm{D}]} \qquad (9.35)$$

9.3.2 Photochemical Kinetics

In terms of a photochemical reaction the net reaction is the same as the thermal reaction (Figure 9.5), however, for this analysis it needs to be broken down further (Figure 9.6). For the substitution to occur, photoinduced ligand lost must occur, creating a reactive intermediate which can react with the free ligand to form the product. The reaction rates can be written as Equations (9.36)-(9.37), which incorporates the Beer Lambert law, to determine the concentration of A followed by a thermal step.[125] Similarly, the rate of formation of the intermediate can be described. Using the steady state approximation, the concentration of the intermediate can be expressed in terms of the photochemical and thermal parameters (Equation (9.38)). The photochemical components of the intermediate have not been substituted with the Beer-Lambert law only for simplicity.

$$\mathrm{A + B} \underset{h\nu}{\overset{h\nu}{\rightleftharpoons}} \mathrm{C + D}$$

Figure 9.5: Net reaction for a four component bimolecular reversible photochemical reaction.

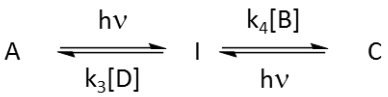

Figure 9.6: Kinetic Model for a four component bimolecular reversible photochemical reaction via an intermediate I.

$$-\frac{d[A]}{dt} = \Phi_A I_A - k_3[D][I] = \Phi_A I_o(1 - e^{-\varepsilon_A[A]l}) - k_5[D][I] \tag{9.36}$$

$$-\frac{d[C]}{dt} = \Phi_C I_C - k_4[B][I] = \Phi_C I_o(1 - e^{-\varepsilon_C[C]l}) - k_4[B][I] \tag{9.37}$$

$$-\frac{d[I]}{dt} = -\Phi_A I_A + k_3[D][I] - \Phi_C I_C + k_4[B][I] \simeq 0$$

$$k_3[D][I] + k_4[B][I] = \Phi_A I_A + \Phi_C I_C$$

$$[I] = \frac{\Phi_A I_A + \Phi_C I_C}{k_4[B] + k_3[D]} \tag{9.38}$$

This equation for [I] can be substituted into the rate equations.

$$-\frac{d[A]}{dt} = \Phi_A I_A - k_3[D]\left(\frac{\Phi_A I_A + \Phi_C I_C}{k_4[B] + k_3[D]}\right)$$

$$= \frac{\Phi_A I_A(k_4[B] + k_5[D]) - k_3[D](\Phi_A I_A + \Phi_C I_C)}{k_4[B] + k_3[D]}$$

$$= \frac{\Phi_A I_A k_4[B] + \Phi_A I_A k_3[D] - \Phi_A I_A k_3[D] - \Phi_C I_C k_3[D]}{k_4[B] + k_3[D]}$$

$$-\frac{d[A]}{dt} = \frac{k_4[B]\Phi_A I_A - k_3[D]\Phi_C I_C}{k_4[B] + k_3[D]}$$

$$-\frac{d[A]}{dt} = \frac{k_4[B]\Phi_A I_0(1 - e^{-\varepsilon_A[A]l}) - k_3[D]\Phi_C I_0(1 - e^{-\varepsilon_C[C]l})}{k_4[B] + k_3[D]} \tag{9.39}$$

$$-\frac{d[C]}{dt} = \Phi_C I_C - k_4[B]\left(\frac{\Phi_A I_A + \Phi_C I_C}{k_4[B] + k_3[D]]}\right)$$

$$= \frac{\Phi_C I_C(k_4[B] + k_4[D]) - k_4[B](\Phi_A I_A + \Phi_C I_C)}{k_4[B] + k_3[D]}$$

$$-\frac{d[C]}{dt} = \frac{k_3[D]\Phi_C I_C - k_4[B]\Phi_A I_A}{k_4[B] + k_3[D]]}$$

$$-\frac{d[C]}{dt} = \frac{k_3[D]\Phi_C I_0(1 - e^{\varepsilon_C[C]l}) - k_4[B]\Phi_A I_0(1 - e^{-\varepsilon_A[A]l})}{k_4[B] + k_3[D]} \tag{9.40}$$

Low Absorbance

By assuming that the sample is optically dilute, these rate expressions can be simplified. Since they will have low absorbance and therefore $\varepsilon_A[A]l$ and $\varepsilon_C[C]l$ are small and thus the exponential term can be simplified since e^{-x} tends towards $1 - x$. These terms can be substituted into Equations (9.39) and (9.40).

$$-\frac{d[A]}{dt} = \frac{k_4[B]\Phi_A I_0(1-(1-\varepsilon_A[A]l)) - k_3[D]\Phi_C I_0(1-(1-\varepsilon_C[C]l)}{k_4[B]+k_3[D]}$$

$$-\frac{d[A]}{dt} = \frac{k_4[B]\Phi_A I_0\varepsilon_A[A]l - k_3[D]\Phi_C I_0\varepsilon_C[C]l}{k_4[B]+k_3[D]} \quad (9.41)$$

$$-\frac{d[C]}{dt} = \frac{k_3[D]\Phi_C I_0\varepsilon_C[C]l - k_4[B]\Phi_A I_0\varepsilon_A[A]l}{k_4[B]+k_3[D]} \quad (9.42)$$

At the equilibrium position, the rate of change in A and the rate of change in C are equal and both equal zero. Equations (9.41) and (9.42) can be combined in order to give the equilibrium constant, K_{eq} (Equation (9.43)).

$$\frac{k_4[B]\Phi_A I_0\varepsilon_A[A]l - k_3[D]\Phi_C I_0\varepsilon_C[C]l}{k_4[B]+k_3[D]} = \frac{k_3[D]\Phi_C I_0\varepsilon_C[C]l - k_4[B]\Phi_A I_0\varepsilon_A[A]l}{k_4[B]+k_3[D]}$$

$$2k_4[B]\Phi_A I_0\varepsilon_A[A]l = 2k_3[D]\Phi_C I_0\varepsilon_C[C]l$$

$$\boxed{K_{eq} = \frac{\varepsilon_A\Phi_A k_4}{\varepsilon_C\Phi_C k_3} = \frac{[C][D]}{[A][B]}} \quad (9.43)$$

Integrated Rate Equations

The integrated rate equations can be determined using the differential rate expressions assuming the sample has low absorbance, (Equations (9.41) and (9.42)). If the change in

concentrations of each of the components is denoted by *x* the concentrations of A and C at time,t, are given below, where PSS stands for photostationary state and refers to an equilibrium from a photochemical reaction

$$[A]_t = [A]_{PSS} - x \qquad [C]_t = [C]_{PSS} + x$$

$$[B]_t = [B]_{PSS} - x \qquad [D]_t = [D]_{PSS} + x$$

$$a = \frac{\Phi_A \varepsilon_A I_0 l k_4}{k_4[B] + k_3[D]} \qquad c = \frac{\Phi_C \varepsilon_C I_0 l k_3}{k_4[B] + k_3[D]}$$

These can then be substituted into the rate expression, the photochemical properties are substituted with *a* and *c* for clarity.

$$-\frac{d[A]}{dt} = a[A][B] - c[C][D]$$

$$-\frac{d[A]}{dt} = a([A]_{PSS} - x)([B]_{PSS} - x) - c([C]_{PSS} + x)([D]_{PSS} + x)$$

$$= a[A]_{PSS}[B]_{PSS} - ax([A]_{PSS} + [B]_{PSS}) - c[C]_{PSS}[D]_{PSS} - cx([C]_{PSS} + [D]_{PSS}) + (a - c)x^2$$

At the equilibrium position, the rate of change in concentrations is zero and therefore offering a simplification to the rate expression. Furthermore, if is it assumed that the change in concentration, *x*, is small the x^2 terms would be negligible and thus can be ignored.

$$a[A]_{PSS}[B]_{PSS} - c[C]_{PSS}[D]_{PSS} = 0$$

The rate expression now is given by the following equation, which can be integrated with respect to x from t = 0 to t = t, resulting in Equation (9.44). Substituting *x* the concentrations of A and C gives the integrated rate equations for A and C as Equations (9.45) and (9.46) where k_{obs} is defined by Equation (9.47).

$$-\frac{d[A]}{dt} = \frac{dx}{dt} = -ax([A]_{PSS} + [B]_{PSS}) - cx([C]_{PSS} - [D]_{PSS})$$

$$-\int_0^t \frac{dx}{x} = \int_0^t a([A]_{PSS} + [B]_{PSS}) + c([C]_{PSS} - [D]_{PSS})\, dt$$

$$-\ln\frac{x}{x_0} = (a[A]_{PSS} + c[C]_{PSS})t \tag{9.44}$$

$$[A] = [A]_{PSS} + ([A]_0 - [A]_{PSS})e^{-k_{obs}t} \tag{9.45}$$

$$[C] = [C]_{PSS} + ([C]_0 - [C]_{PSS})e^{-k_{obs}t} \tag{9.46}$$

$$k_{obs} = \left(\frac{\Phi_A \varepsilon_A I_0 l k_4}{k_4[B] + k_3[D]}\right)([A] + [B]) + \left(\frac{\Phi_C \varepsilon_C I_0 l k_3}{k_4[B] + k_3[D]}\right)([C] + [D]) \tag{9.47}$$

Determination of rate constants under photochemical conditions

Both k_{obs} and K_{eq} relate to the rates of the reaction and allowing expressions for Φ_A and Φ_C to be obtained and can relate the measured values of k_2 and k_{-2} to the photochemical properties of the reactants.

$$K_{eq} = \frac{\varepsilon_A \Phi_A k_4}{\varepsilon_C \Phi_C k_3}$$

$$\varepsilon_A \Phi_A k_4 = \varepsilon_C \Phi_C k_3 K_{eq} \qquad \varepsilon_C \Phi_C k_3 = \frac{\varepsilon_A \Phi_A k_4}{K_{eq}}$$

$$k_{obs} = I_0 l(k_4 \Phi_A \varepsilon_A([A] + [B]) + \frac{\varepsilon_A \Phi_A k_4}{K_{eq}}([C] + [D]))$$

$$\frac{K_{eq} k_{obs}}{I_0 l} = \varepsilon_A \Phi_A k_4 (K_{eq}([A] + [B]) + [C] + [D])$$

$$\boxed{\Phi_A = \frac{K_{eq} k_{obs}(k_3[D] + k_4[B])}{I_0 l \varepsilon_A k_4 \big(K_{eq}([A] + [B]) + [C] + [D]\big)}}$$

$$k_{obs} = I_0 l(\varepsilon_C \Phi_C k_3 K_{eq}([A] + [B]) + k_3 \Phi_C \varepsilon_C([C] + [D]))$$

$$\frac{k_{obs}}{I_0 l} = \varepsilon_C \Phi_C k_3 (K_{eq}([A] + [B]) + [C] + [D])$$

$$\boxed{\Phi_C = \frac{k_{obs}(k_3[D] + k_4[B])}{I_0 l \varepsilon_C k_3 (K_{eq}([A] + [B]) + [C] + [D])}}$$

$$k_2 = \frac{\Phi_A I_0 l \varepsilon_A k_4}{k_3[D] + k_4[B]} \qquad k_{-2} = \frac{\Phi_C I_0 l \varepsilon_C k_3}{k_3[D] + k_4[B]}$$

9.4 First and Second Order Equilibrim

Similar observations can be made when one step in the equilibrium is first order and the other step is second order (Figure 9.7 and Figure 9.8).

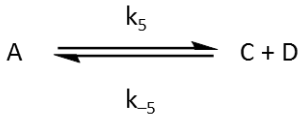

Figure 9.7: Net reaction for a 3 component reaction, first order in the forward direction and second order in the back reaction.

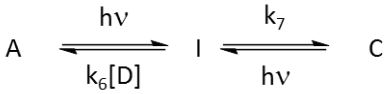

Figure 9.8: Kinetic model for the reversible photochemical reaction via an intermediate, I.

Thermal relaxation kinetics

Using the same analysis as described for the previous equilibrium the results for a mixed equilibrium under thermal control is given below.

$$-\frac{d[A]}{dt} = k_5[A] - k_{-5}[C][D] \tag{9.48}$$

$$-\frac{d[C]}{dt} = -k_5[A] + k_{-5}[C][D] \tag{9.49}$$

$$K_{eq} = \frac{[C]_{eq}[D]_{eq}}{[A]_{eq}} = \frac{k_5}{k_{-5}} \tag{9.50}$$

$$[A] = [A]_{eq} + ([A]_0 - [A]_{eq})e^{-k_{obs}t} \tag{9.51}$$

$$[C] = [C]_{eq} + ([C]_0 - [C]_{eq})e^{-k_{obs}t} \tag{9.52}$$

$$k_{obs} = k_5 + k_{-5}([C] + [D]) \tag{9.53}$$

Photochemical Kinetics

Under photochemical conditions the equilibrium is now described by the equations below.

$$-\frac{d[A]}{dt} = \frac{k_7 I_0(1 - e^{-\varepsilon_A[A]l}) - k_6[D]\Phi_C I_0(1 - e^{-\varepsilon_C[C]l})}{k_7 + k_6[D]} \qquad (9.54)$$

$$-\frac{d[C]}{dt} = \frac{k_6[D]\Phi_C I_0(1 - e^{\varepsilon_C[C]l}) - k_7 I_0(1 - e^{-\varepsilon_A[A]l})}{k_7 + k_6[D]} \qquad (9.55)$$

These equations can then be used to calculated the equilibrium constant (Equation (9.56)), this has assumed that the sample has low absorbance therefore $\varepsilon_A[A]l$ and $\varepsilon_C[C]l$ are small and thus the exponential term can be simplified since e^{-x} tends towards $1 - x$.

$$K_{eq} = \frac{\varepsilon_A \Phi_A k_7}{\varepsilon_C \Phi_C k_6} = \frac{[C][D]}{[A]} \qquad (9.56)$$

Under photochemical control, the integrated rate expressions still match Equations (9.51) and (9.52) however the equation for k_{obs} is now Equation (9.57).

$$k_{obs} = \left(\frac{\Phi_A \varepsilon_A I_0 l k_7}{k_6[D] + k_7}\right) + \left(\frac{\Phi_C \varepsilon_C I_0 l k_6}{k_6[D] + k_7}\right)([C] + [D]) \qquad (9.57)$$

The equations for K_{eq} and k_{obs} can be combined to calculate the rate constants k_5 and k_{-5} which are given by the equations below.

$$k_5 = \frac{\Phi_A I_0 l \varepsilon_A k_7}{k_6[D] + k_7}$$

$$k_{-5} = \frac{\Phi_C I_0 l \varepsilon_C k_6}{k_6[D] + k_7}$$

Complex Structures and Numbering

Chapter Two

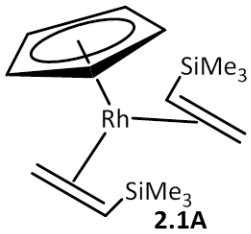

2.1A

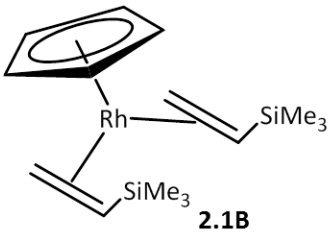

2.1B

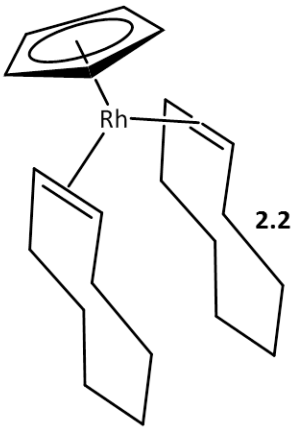

2.2

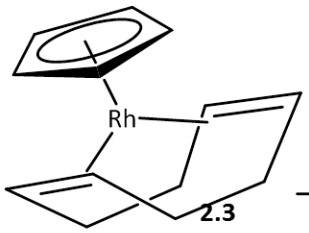

2.3

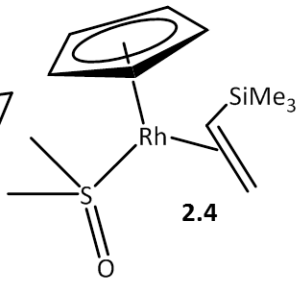

2.4

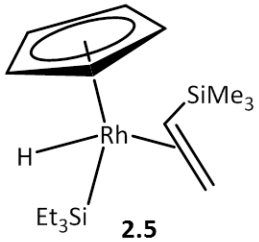

2.5

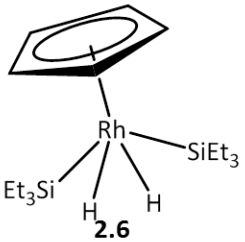

2.6

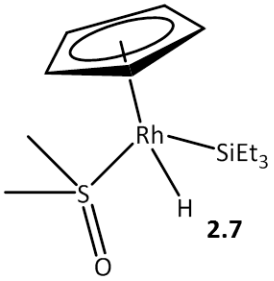

2.7

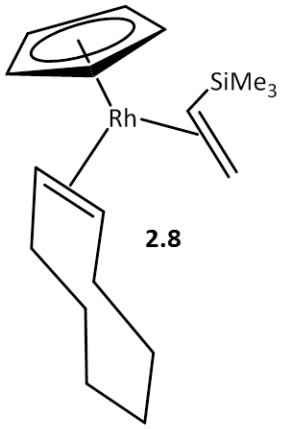

2.8

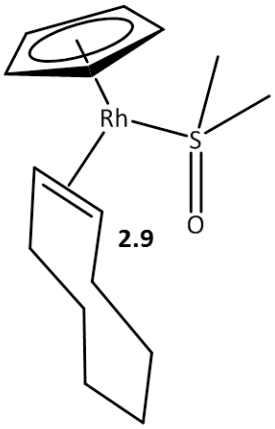

2.9

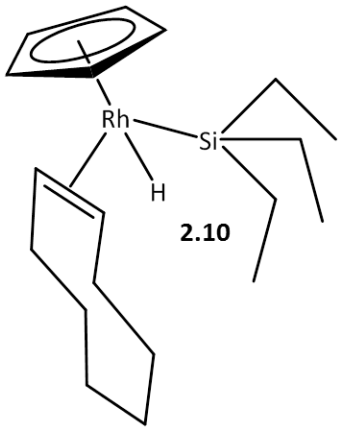

2.10

Chapter Three

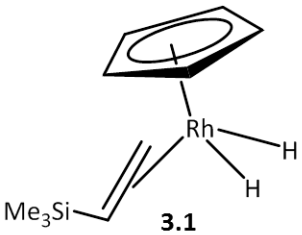

3.1

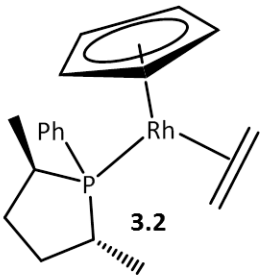

3.2

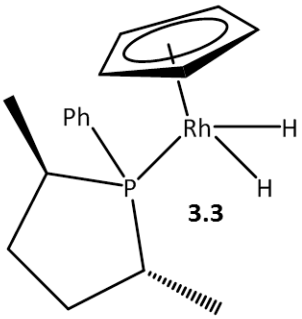

3.3

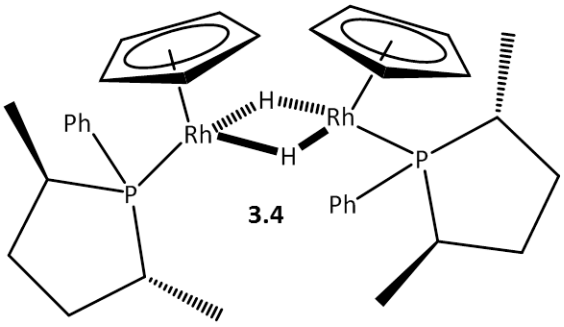

3.4

Chapter Four

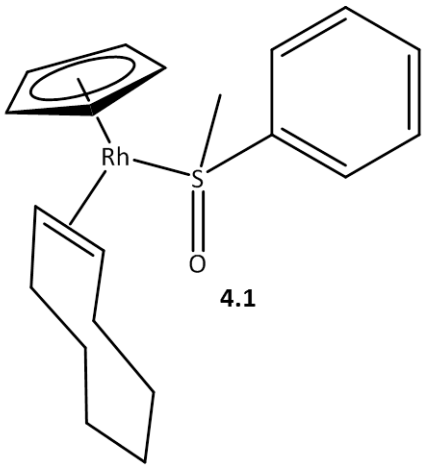

4.1

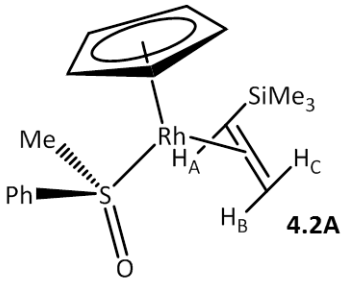

4.2A

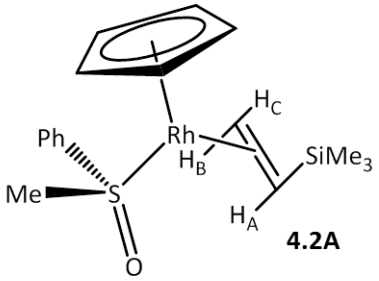

4.2A

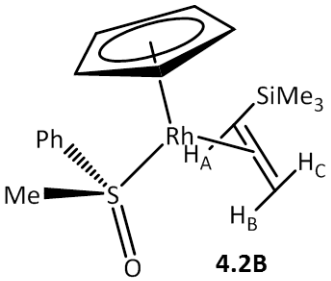

4.2B

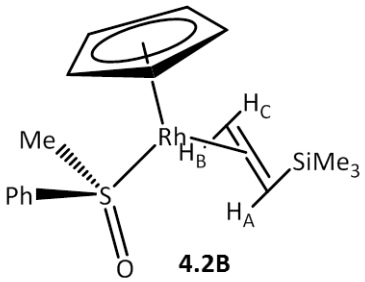

4.2B

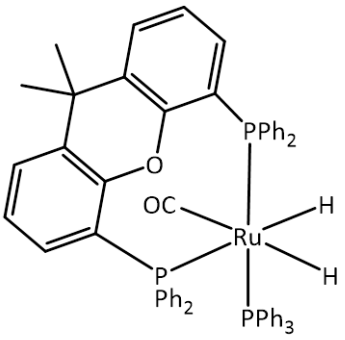

5.1

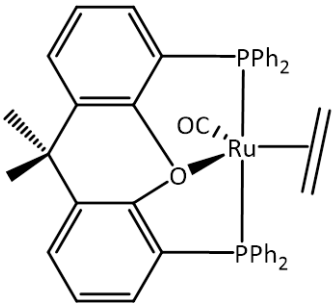

5.2

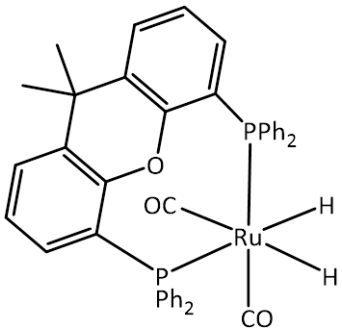

5.3

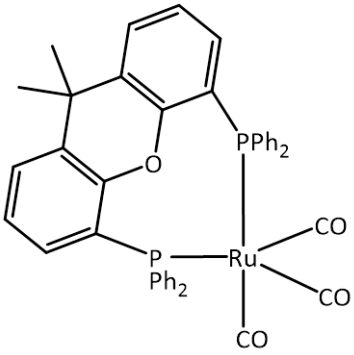

5.4

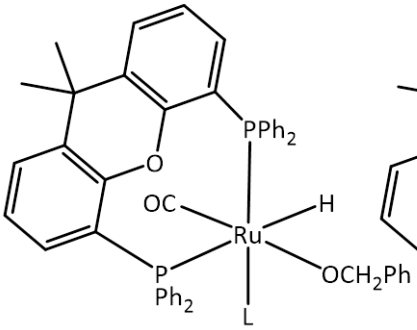

5.5

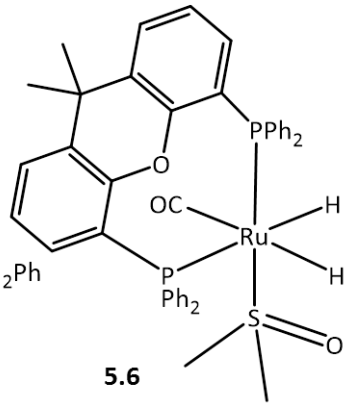

5.6

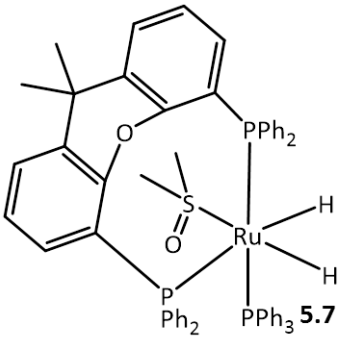

5.7

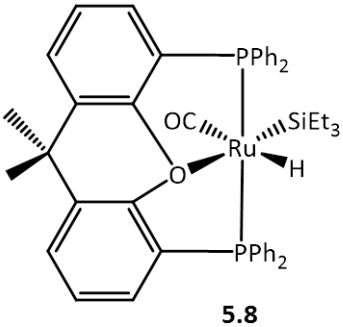

5.8

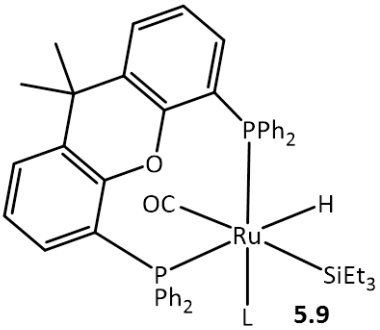

5.9

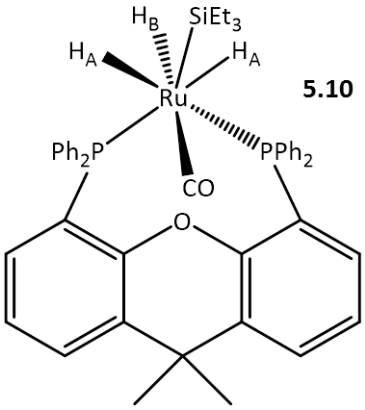

5.10

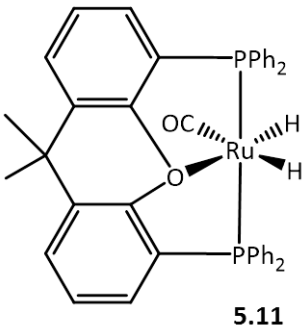

5.11

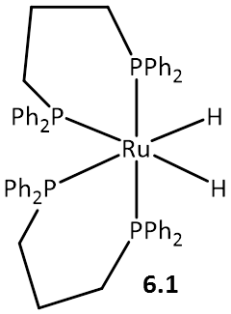

6.1

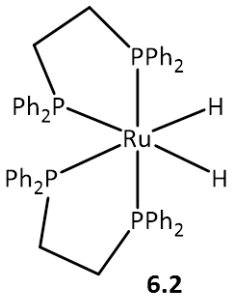

6.2

Abbreviations

1D	one-dimensional
2D	two-dimensional
Å	bond length, 10^{-10} m
δ	chemical shift /ppm
µL	microlitre
Ω	chemical shift
σ-CAM	σ-complex assisted metathesis
ψ	wavefunction
B_0	applied magnetic field
br	broad
COD	1,5- *cis*-*cis*-cyclooctadiene
COE	cyclooctene
COSY	correlation spectroscopy
Cp	cyclopentadienyl
Cp’	cyclopentadienyl derived ligand
Cp*	pentamethylcyclopentadienyl
cw	continuous wave
d	doublet
DCM	dichloromethane
depe	1,2-bis(diethylphosphino)ethane
dfepe	1,2-bis(bis(pentafluoroethyl)phosphino)ethane
DFT	density function theory
dm	decimetre, 0.1 m
dmpm	1,2-bis(dimethylphosphino)methane
DMSO	dimethylsulfoxide

dpae	1,2-bis(diphenylarsenio)ethane
DPE	Bis(2-diphenylphosphinophenyl)ether
dppe	1,2-bis(diphenylphosphino)ethane
dppp	1,3-bis(diphenylphosphino)propane
DQ	double quantum
DuPHOS	1,2-Bis[2,5-dimethylphospholano]benzene
Et	ethyl
etp	$PhP(CH_2CH_2PPh_2)_2$)
EXSY	exchange spectroscopy
FID	free induction decay
HBpin	pinacolborane
HEB	hexaethylbenzene
HMQC	heteronuclear multiple quantum correlation spectroscopy
Hz	Hertz
^{i}Pr	iso-propyl
IR	Infrared
J	coupling constant /Hz
K	Kelvin
K_{eq}	equilibrium constant
LIFDI	liquid injection field desorption ionisation
m	meta
M	bulk magnetisation
Me	methy
mg	milligram
MHz	megahertz
min	minutes

mJ	millijoule
mol	mole
ms	milliseconds
mW	milliwatt
Nd:YAG	neodymium-doped yttrium aluminium garnet
NMR	nuclear magnetic resonance
nOe	nuclear overhausser effect
NOESY	nuclear overhausser effect spectroscopy
o	ortho
OPSY	only parahydrogen spectroscopy
p	para
PASADENA	parahydrogen and synthesis allow dramatic enhanced nuclear alignment
p-H_2	parahydrogen
Ph	phenyl
PHIP	parahydrogen induced polarisation
P*Ph	(2R, 5R) 2,5 dimethyl, 1-phenyl phospholane
PP	a bidentate phosphine
PP_3	a tridentate phosphine
ppm	parts per million
PR_3	a monodentate phosphine
PSS	photostationary state
py	pyridine
RF	radio frequency
s	seconds
s	singlet
SABRE	signal amplication by reversible exchange

SD	standard deviation
SE	standard error
T	Tesla
T_1	longitudinal relaxation time
^{t}Bu	tert-butyl
THF	tetrahydrafuran
UV	ultraviolet
ZQ	zero quantum

References

1. R. Cramer and L. P. Seiwell, *J. Organomet. Chem.*, 1975, **92**, 245-252.
2. T. W. Bell, D. M. Haddleton, A. McCamley, M. G. Partridge, R. N. Perutz and H. Willner, *J. Am. Chem. Soc.*, 1990, **112**, 9212-9226.
3. S. T. Belt, S. B. Duckett, M. Helliwell and R. N. Perutz, *J. Chem. Soc., Chem. Commun.*, 1989, 928-930.
4. W. A. G. Graham and A. J. Oliver, *Inorg. Chem.*, 1971, **10**, 1165-1169.
5. M. V. Câmpian, J. L. Harris, N. Jasim, R. N. Perutz, T. B. Marder and A. C. Whitwood, *Organometallics*, 2006, **25**, 5093-5104.
6. M. V. Câmpian, E. Clot, O. Eisenstein, U. Helmstedt, N. Jasim, R. N. Perutz, A. C. Whitwood and D. Williamson, *J. Am. Chem. Soc.*, 2008, **130**, 4375-4385.
7. J. F. Hartwig, *Nature*, 2008, **455**, 314-322.
8. E. E. Kwan and S. G. Huang, *Eur. J. Org. Chem.*, 2008, **2008**, 2671-2688.
9. D. G. Gusev, *Angew. Chem., Int. Ed. Engl.*, 2012, **51**, 12930-12931.
10. W. F. Vranken, *Prog. Nucl. Magn. Reson. Spectrosc.*, 2014, **82**, 27-38.
11. P. Atkins and J. De Paula, *Physical Chemistry*, Oxford University Press, 2006.
12. J. H. Ardenkjaer-Larsen, *J. Magn. Reson.*, 2016, **264**, 3-12.
13. M. Levitt, *Spin Dynamics*, 2nd edn., John Wiley & Sons Ltd, 2008.
14. R. A. Green, R. W. Adams, S. B. Duckett, R. E. Mewis, D. C. Williamson and G. G. R. Green, *Prog. Nucl. Magn. Reson. Spectrosc.*, 2012, **67**, 1-48.
15. O. Torres, B. Procacci, M. E. Halse, R. W. Adams, D. Blazina, S. B. Duckett, B. Eguillor, R. A. Green, R. N. Perutz and D. C. Williamson, *J. Am. Chem. Soc.*, 2014, **136**, 10124-10131.
16. N. D. Bhaskar, W. Happer and T. McClelland, *Phys. Rev. Lett.*, 1982, **49**, 25-28.
17. T. G. Walker and W. Happer, *Rev. Mod. Phys.* , 1997, **69**, 629-642.
18. M. S. Albert, G. D. Cates, B. Driehuys, W. Happer, B. Saam, C. S. Springer and A. Wishnia, *Nature*, 1994, **370**, 199-201.
19. H. Middleton, R. D. Black, B. Saam, G. D. Cates, G. P. Cofer, R. Guenther, W. Happer, L. W. Hedlund, G. Alan Johnson, K. Juvan and J. Swartz, *Magn. Reson. Med*, 1995, **33**, 271-275.
20. A. Abragam and M. Goldman, *Rep. Prog. Phys.*, 1978, **41**, 395.
21. A. Abragam and W. G. Proctor, *Phys. Rev.*, 1958, **109**, 1441-1458.
22. C. D. Jeffries, *Phys. Rev.*, 1957, **106**, 164-165.
23. J. H. Ardenkjær-Larsen, B. Fridlund, A. Gram, G. Hansson, L. Hansson, M. H. Lerche, R. Servin, M. Thaning and K. Golman, *Proc. Natl. Acad. Sci. U S A*, 2003, **100**, 10158-10163.
24. C. R. Bowers and D. P. Weitekamp, *Phys. Rev. Lett.*, 1986, **57**, 2645-2648.
25. C. R. Bowers and D. P. Weitekamp, *J. Am. Chem. Soc.*, 1987, **109**, 5541-5542.
26. J. A. Osborn, F. H. Jardine, J. F. Young and G. Wilkinson, *Journal of the Chemical Society A: Inorganic, Physical, Theoretical*, 1966, 1711-1732.
27. T. C. Eisenschmid, R. U. Kirss, P. P. Deutsch, S. I. Hommeltoft, R. Eisenberg, J. Bargon, R. G. Lawler and A. L. Balch, *J. Am. Chem. Soc.*, 1987, **109**, 8089-8091.
28. J. Natterer and J. Bargon, *Prog. Nucl. Magn. Reson. Spectrosc.*, 1997, **31**, 293-315.
29. Simon B. Duckett and D. Blazina, *Eur. J. Inorg. Chem.*, 2003, **2003**, 2901-2912.
30. S. B. Duckett and N. J. Wood, *Coord. Chem. Rev.*, 2008, **252**, 2278-2291.
31. R. W. Adams, J. A. Aguilar, K. D. Atkinson, M. J. Cowley, P. I. P. Elliott, S. B. Duckett, G. G. R. Green, I. G. Khazal, J. López-Serrano and D. C. Williamson, *Science*, 2009, **323**, 1708-1711.
32. J. Keeler, Wiley, 2nd edn., 2011.
33. W. Tang and X. Zhang, *Chem. Rev. (Washington, DC, U. S.)*, 2003, **103**, 3029-3070.

34. J. Pospech, I. Fleischer, R. Franke, S. Buchholz and M. Beller, *Angew. Chem., Int. Ed. Engl.*, 2013, **52**, 2852-2872.
35. J. Y. Corey and J. Braddock-Wilking, *Chem. Rev. (Washington, DC, U. S.)*, 1999, **99**, 175-292.
36. R. Noyori and S. Hashiguchi, *Acc. Chem. Res.*, 1997, **30**, 97-102.
37. G. J. Kubas, *Chem. Rev. (Washington, DC, U. S.)*, 2007, **107**, 4152-4205.
38. P. G. Jessop and R. H. Morris, *Coord. Chem. Rev.*, 1992, **121**, 155-284.
39. R. H. Morris, *Can. J. Chem.*, 1996, **74**, 1907-1915.
40. H. Fong, M.-E. Moret, Y. Lee and J. C. Peters, *Organometallics*, 2013, **32**, 3053-3062.
41. R. N. Perutz and S. Sabo-Etienne, *Angew. Chem., Int. Ed. Engl.*, 2007, **46**, 2578-2592.
42. Q. Zhang, H.-Z. Yu, Y.-T. Li, L. Liu, Y. Huang and Y. Fu, *Dalton Trans.*, 2013, **42**, 4175-4184.
43. D. Devarajan and D. H. Ess, *Inorg. Chem.*, 2012, **51**, 6367-6375.
44. G. J. Kubas, R. R. Ryan, B. I. Swanson, P. J. Vergamini and H. J. Wasserman, *J. Am. Chem. Soc.*, 1984, **106**, 451-452.
45. R. H. Crabtree, *Chem. Rev. (Washington, DC, U. S.)*, 2016, **116**, 8750-8769.
46. G. J. Kubas, *J. Organomet. Chem.*, 2001, **635**, 37-68.
47. M. J. S. Dewar., *Bull. Soc. Chim. Fr.*, 1951, **18**, C79.
48. J. Chatt and L. A. Duncanson, *Journal of the Chemical Society (Resumed)*, 1953, 2939-2947.
49. W. D. Jones, *Acc. Chem. Res.*, 2003, **36**, 140-146.
50. J. Y. Corey, *Chem. Rev. (Washington, DC, U. S.)*, 2011, **111**, 863-1071.
51. G. Alcaraz, M. Grellier and S. Sabo-Etienne, *Acc. Chem. Res.*, 2009, **42**, 1640-1649.
52. J. Kubas Gregory, *Acc. Chem. Res.*, 1988, **21**, 120-128.
53. D. M. Heinekey and W. J. Oldham, *Chem. Rev. (Washington, DC, U. S.)*, 1993, **93**, 913-926.
54. G. S. McGrady and G. Guilera, *Chem. Soc. Rev.*, 2003, **32**, 383-392.
55. R. N. Perutz and B. Procacci, *Chem. Rev. (Washington, DC, U. S.)*, 2016, **116**, 8506-8544.
56. S. B. Duckett, D. M. Haddleton, S. A. Jackson, R. N. Perutz, M. Poliakoff and R. K. Upmacis, *Organometallics*, 1988, **7**, 1526-1532.
57. S. T. Belt, S. B. Duckett, D. M. Haddleton and R. N. Perutz, *Organometallics*, 1989, **8**, 748-759.
58. R. N. Perutz, O. Torres and A. Vlček Jr, in *Comprehensive Inorganic Chemistry II (Second Edition)*, ed. K. Poeppelmeier, Elsevier, Amsterdam, 2013, pp. 229-253.
59. M. Wrighton, *Chem. Rev. (Washington, DC, U. S.)*, 1974, **74**, 401-430.
60. A. H. Zewail, *Angew. Chem., Int. Ed. Engl.*, 2000, **39**, 2586-2631.
61. E. T. J. Nibbering, H. Fidder and E. Pines, *Annu. Rev. Phys. Chem.*, 2005, **56**, 337-367.
62. J. M. Butler, M. W. George, J. R. Schoonover, D. M. Dattelbaum and T. J. Meyer, *Coord. Chem. Rev.*, 2007, **251**, 492-514.
63. G. E. Ball, in *Spectroscopic Properties of Inorganic and Organometallic Compounds: Techniques, Materials and Applications, Volume 41*, The Royal Society of Chemistry, 2010, vol. 41, pp. 262-287.
64. S. Geftakis and G. E. Ball, *J. Am. Chem. Soc.*, 1998, **120**, 9953-9954.
65. A. Mills and C. O'Rourke, *The Journal of Organic Chemistry*, 2015, **80**, 10342-10345.
66. J. A. Calladine, O. Torres, M. Anstey, G. E. Ball, R. G. Bergman, J. Curley, S. B. Duckett, M. W. George, A. I. Gilson, D. J. Lawes, R. N. Perutz, X.-Z. Sun and K. P. C. Vollhardt, *Chem. Sci.* , 2010, **1**, 622-630.
67. K. M. Tait, J. A. Parkinson, S. P. Bates, W. J. Ebenezer and A. C. Jones, *Journal of Photochemistry and Photobiology A: Chemistry*, 2003, **154**, 179-188.
68. K. M. Tait, J. A. Parkinson, D. I. Gibson, P. R. Richardson, W. J. Ebenezer, M. G. Hutchings and A. C. Jones, *Photochem. Photobiol. Sci.*, 2007, **6**, 1010-1018.

69. N. A. Wazzan, P. R. Richardson and A. C. Jones, *Photochem. Photobiol. Sci.*, 2010, **9**, 968-974.
70. A. Fihey, A. Perrier, W. R. Browne and D. Jacquemin, *Chem. Soc. Rev.*, 2015, **44**, 3719-3759.
71. L. Schweighauser, D. Haussinger, M. Neuburger and H. A. Wegner, *Org. Biomol. Chem.*, 2014, **12**, 3371-3379.
72. P. Müller, B. Schröder, J. A. Parkinson, N. A. Kratochwil, R. A. Coxall, A. Parkin, S. Parsons and P. J. Sadler, *Angew. Chem., Int. Ed. Engl.*, 2003, **42**, 335-339.
73. C. Feldmeier, H. Bartling, E. Riedle and R. M. Gschwind, *J. Magn. Reson.*, 2013, **232**, 39-44.
74. C. Godard, P. Callaghan, J. L. Cunningham, S. B. Duckett, J. A. B. Lohman and R. N. Perutz, *Chem. Commun. (Cambridge, U. K.)*, 2002, 2836-2837.
75. G. E. Ball, C. M. Brookes, A. J. Cowan, T. A. Darwish, M. W. George, H. K. Kawanami, P. Portius and J. P. Rourke, *Proc. Natl. Acad. Sci. U S A*, 2007, **104**, 6927-6932.
76. S. J. Pridmore, P. A. Slatford and J. M. J. Williams, *Tetrahedron Lett.*, 2007, **48**, 5111-5114.
77. H. M. Yau, A. I. McKay, H. Hesse, R. Xu, M. He, C. E. Holt and G. E. Ball, *J. Am. Chem. Soc.*, 2016, **138**, 281-288.
78. R. D. Young, A. F. Hill, W. Hillier and G. E. Ball, *J. Am. Chem. Soc.*, 2011, **133**, 13806-13809.
79. D. M. Haddleton, A. McCamley and R. N. Perutz, *J. Am. Chem. Soc.*, 1988, **110**, 1810-1817.
80. O. Torres, J. A. Calladine, S. B. Duckett, M. W. George and R. N. Perutz, *Chem. Sci.* , 2015, **6**, 418-424.
81. B. Eguillor, P. J. Caldwell, M. C. R. Cockett, S. B. Duckett, R. O. John, J. M. Lynam, C. J. Sleigh and I. Wilson, *J. Am. Chem. Soc.*, 2012, **134**, 18257-18265.
82. D. Blazina, S. B. Duckett, T. K. Halstead, C. M. Kozak, R. J. K. Taylor, M. S. Anwar, J. A. Jones and H. A. Carteret, *Magn. Reson. Chem.*, 2005, **43**, 200-208.
83. D. Schott, C. J. Sleigh, J. P. Lowe, S. B. Duckett, R. J. Mawby and M. G. Partridge, *Inorg. Chem.*, 2002, **41**, 2960-2970.
84. D. Schott, P. Callaghan, J. Dunne, S. B. Duckett, C. Godard, J. M. Goicoechea, J. N. Harvey, J. P. Lowe, R. J. Mawby, G. Muller, R. N. Perutz, R. Poli and M. K. Whittlesey, *Dalton Trans.*, 2004, 3218-3224.
85. D. Blazina, J. P. Dunne, S. Aiken, S. B. Duckett, C. Elkington, J. E. McGrady, R. Poli, S. J. Walton, M. S. Anwar, J. A. Jones and H. A. Carteret, *Dalton Trans.*, 2006, 2072-2080.
86. J. P. Dunne, D. Blazina, S. Aiken, H. A. Carteret, S. B. Duckett, J. A. Jones, R. Poli and A. C. Whitwood, *Dalton Trans.*, 2004, 3616-3628.
87. B. Procacci, P. M. Aguiar, M. E. Halse, R. N. Perutz and S. B. Duckett, *Chem. Sci.* , 2016.
88. P. B. Chock and J. Halpern, *J. Am. Chem. Soc.*, 1966, **88**, 3511-3514.
89. L. Vaska and M. F. Werneke, *Ann. N. Y. Acad. Sci.*, 1971, **172**, 546-562.
90. L. Cronin, M. C. Nicasio, R. N. Perutz, R. G. Peters, D. M. Roddick and M. K. Whittlesey, *J. Am. Chem. Soc.*, 1995, **117**, 10047-10054.
91. M. C. Nicasio, R. N. Perutz and P. H. Walton, *Organometallics*, 1997, **16**, 1410-1417.
92. C. Hall, W. D. Jones, R. J. Mawby, R. Osman, R. N. Perutz and M. K. Whittlesey, *J. Am. Chem. Soc.*, 1992, **114**, 7425-7435.
93. P. L. Callaghan, R. Fernandez-Pacheco, N. Jasim, S. Lachaize, T. B. Marder, R. N. Perutz, E. Rivalta and S. Sabo-Etienne, *Chem. Commun. (Cambridge, U. K.)*, 2004, 242-243.
94. M. V. Câmpian, R. N. Perutz, B. Procacci, R. J. Thatcher, O. Torres and A. C. Whitwood, *J. Am. Chem. Soc.*, 2012, **134**, 3480-3497.
95. V. Montiel-Palma, R. N. Perutz, M. W. George, O. S. Jina and S. Sabo-Etienne, *Chem. Commun. (Cambridge, U. K.)*, 2000, 1175-1176.

96. R. Osman, D. I. Pattison, R. N. Perutz, C. Bianchini, J. A. Casares and M. Peruzzini, *J. Am. Chem. Soc.*, 1997, **119**, 8459-8473.
97. M. Colombo, M. W. George, J. N. Moore, D. I. Pattison, R. N. Perutz, I. G. Virrels and T.-Q. Ye, *Journal of the Chemical Society, Dalton Transactions*, 1997, 2857-2860.
98. V. Montiel-Palma, D. I. Pattison, R. N. Perutz and C. Turner, *Organometallics*, 2004, **23**, 4034-4039.
99. K. A. M. Ampt, S. Burling, S. M. A. Donald, S. Douglas, S. B. Duckett, S. A. Macgregor, R. N. Perutz and M. K. Whittlesey, *J. Am. Chem. Soc.*, 2006, **128**, 7452-7453.
100. D. M. Haddleton and R. N. Perutz, *J. Chem. Soc., Chem. Commun.*, 1985, 1372-1374.
101. R. Cramer, *J. Am. Chem. Soc.*, 1964, **86**, 217-222.
102. R. Cramer, *J. Am. Chem. Soc.*, 1972, **94**, 5681-5685.
103. C. P. Lenges, P. S. White and M. Brookhart, *J. Am. Chem. Soc.*, 1999, **121**, 4385-4396.
104. W. D. D. Jones, Robert P. Jr.; Feher, Frank J.; Hessell, Edward T., *Nouveau journal de chimie*, 1989, **13**, 725-736.
105. C. P. Lenges and M. Brookhart, *J. Am. Chem. Soc.*, 1999, **121**, 6616-6623.
106. M. M. Diaz-Requejo, D. DiSalvo and M. Brookhart, *J. Am. Chem. Soc.*, 2003, **125**, 2038-2039.
107. A. H. Roy, C. P. Lenges and M. Brookhart, *J. Am. Chem. Soc.*, 2007, **129**, 2082-2093.
108. A. D. Bolig, T. W. Lyons, D. T. DiSalvo and M. Brookhart, *Polyhedron*, 2016, **103, Part A**, 51-57.
109. S. T. Belt, D. M. Haddleton, R. N. Perutz, B. P. H. Smith and A. J. Dixon, *J. Chem. Soc., Chem. Commun.*, 1987, 1347-1349.
110. S. B. Duckett and R. N. Perutz, *J. Chem. Soc., Chem. Commun.*, 1991, 28-31.
111. K. A. M. Ampt, S. B. Duckett and R. N. Perutz, *Dalton Trans.*, 2004, 3331-3337.
112. C. J. Sexton, J. Lopez-Serrano, A. Lledos and S. B. Duckett, *Chem. Commun. (Cambridge, U. K.)*, 2008, 4834-4836.
113. S. B. Duckett and R. N. Perutz, *Organometallics*, 1992, **11**, 90-98.
114. R. Cramer, J. A. McCleverty and J. Bray, in *Inorg. Synth.*, John Wiley & Sons, Inc., 2007, pp. 14-18.
115. P. Błażejewska-Chadyniak, M. Kubicki, H. Maciejewski and B. Marciniec, *Inorg. Chim. Acta*, 2003, **350**, 603-608.
116. E. Hauptman, S. Sabo-Etienne, P. S. White, M. Brookhart, J. M. Garner, P. J. Fagan and J. C. Calabrese, *J. Am. Chem. Soc.*, 1994, **116**, 8038-8060.
117. A. van der Ent, A. L. Onderdelinden and R. A. Schunn, in *Inorg. Synth.*, John Wiley & Sons, Inc., 2007, pp. 92-95.
118. G. Giordano, R. H. Crabtree, R. M. Heintz, D. Forster and D. E. Morris, in *Inorg. Synth.*, John Wiley & Sons, Inc., 2007, pp. 218-220.
119. F. Cicogna, B. Gaddi, G. Ingrosso, M. Marcaccio, F. Marchetti, D. Paolucci, F. Paolucci, C. Pinzino and R. Viglione, *Inorg. Chim. Acta*, 2004, **357**, 2915-2932.
120. M. J. Minch, *Concepts in Magnetic Resonance*, 1994, **6**, 41-56.
121. J. A. Santaballa, H. Maskill and M. Canle L, in *The Investigation of Organic Reactions and Their Mechanisms*, Blackwell Publishing Ltd, 2007, pp. 79-103.
122. R. G. Wilkins, in *Kinetics and Mechanism of Reactions of Transition Metal Complexes*, Wiley-VCH Verlag GmbH & Co. KGaA, 2003, pp. 1-64.
123. C. F. Bernasconi, in *Relaxation Kinetics*, Academic Press, 1976, pp. 11-19.
124. J. A. Swinehart, *J. Chem. Educ.*, 1967, **44**, 524.
125. M. Hippler, *J. Chem. Educ.*, 2003, **80**, 1074.
126. E. Alessio, *Chem. Rev. (Washington, DC, U. S.)*, 2004, **104**, 4203-4242.
127. M. Calligaris, *Coord. Chem. Rev.*, 2004, **248**, 351-375.
128. F. A. Cotton, E. V. Dikarev, M. A. Petrukhina and S.-E. Stiriba, *Inorg. Chem.*, 2000, **39**, 1748-1754.

129. A. Abbasi, M. Y. Skripkin, L. Eriksson and N. Torapava, *Dalton Trans.*, 2011, **40**, 1111-1118.
130. R. Dorta, H. Rozenberg and D. Milstein, *Chem. Commun. (Cambridge, U. K.)*, 2002, 710-711.
131. B. R. James and R. H. Morris, *Can. J. Chem.*, 1980, **58**, 399-408.
132. G. A. H. J. D. Fotheringham, A. J. Lindsay and T. A. Stephenson, *J. Chem. Res., Synop.*, 1986, 82.
133. J. L. Cunningham and S. B. Duckett, *Dalton Trans.*, 2005, 744-759.
134. S. F. Vyboishchikov and G. I. Nikonov, *Organometallics*, 2007, **26**, 4160-4169.
135. G. R. Fulmer, A. J. M. Miller, N. H. Sherden, H. E. Gottlieb, A. Nudelman, B. M. Stoltz, J. E. Bercaw and K. I. Goldberg, *Organometallics*, 2010, **29**, 2176-2179.
136. C. J. Sexton, *D. Phil. Thesis*, 2008, University of York.
137. W. D. Jones and F. J. Feher, *J. Am. Chem. Soc.*, 1984, **106**, 1650-1663.
138. S. N. Heaton, M. G. Partridge, R. N. Perutz, S. J. Parsons and F. Zimmermann, *Journal of the Chemical Society, Dalton Transactions*, 1998, 2515-2520.
139. Y. Suzuki, J. Wakatsuki, M. Tsubaki and M. Sato, *Tetrahedron*, 2013, **69**, 9690-9700.
140. M. J. Burk, J. E. Feaster and R. L. Harlow, *Tetrahedron: Asymmetry*, 1991, **2**, 569-592.
141. S. T. Belt, L. Dong, S. B. Duckett, W. D. Jones, M. G. Partridge and R. N. Perutz, *J. Chem. Soc., Chem. Commun.*, 1991, 266-269.
142. C. F. Tormena, J. D. Vilcachagua, V. Karcher, R. Rittner and R. H. Contreras, *Magn. Reson. Chem.*, 2007, **45**, 590-594.
143. H. Pellissier, *Tetrahedron*, 2006, **62**, 5559-5601.
144. J. W. Faller and P. P. Fontaine, *J. Organomet. Chem.*, 2006, **691**, 5798-5803.
145. B. K. T. Batagoda, P. I. Djurovich, S. Bräse and M. E. Thompson, *Polyhedron*, 2016, **116**, 182-188.
146. T. Katayama, K. Onitsuka and S. Takahashi, *J. Organomet. Chem.*, 2006, **691**, 2245-2256.
147. U. Knof and A. von Zelewsky, *Angew. Chem., Int. Ed. Engl.*, 1999, **38**, 302-322.
148. J.-L. Pierre, *Coord. Chem. Rev.*, 1998, **178–180, Part 2**, 1183-1192.
149. H. Amouri and M. Gruselle, in *Chirality in Transition Metal Chemistry*, John Wiley & Sons, Ltd, 2009, pp. 7-64.
150. R. S. Cahn, C. Ingold and V. Prelog, *Angew. Chem., Int. Ed. Engl.*, 1966, **5**, 385-415.
151. V. Prelog and G. Helmchen, *Angew. Chem., Int. Ed. Engl.*, 1982, **21**, 567-583.
152. M.-N. Birkholz, Z. Freixa and P. W. N. M. van Leeuwen, *Chem. Soc. Rev.*, 2009, **38**, 1099-1118.
153. P. C. J. Kamer, P. W. N. M. van Leeuwen and J. N. H. Reek, *Acc. Chem. Res.*, 2001, **34**, 895-904.
154. P. A. Slatford, M. K. Whittlesey and J. M. J. Williams, *Tetrahedron Lett.*, 2006, **47**, 6787-6789.
155. S. J. Pridmore, P. A. Slatford, J. E. Taylor, M. K. Whittlesey and J. M. J. Williams, *Tetrahedron*, 2009, **65**, 8981-8986.
156. S. J. Pridmore, P. A. Slatford, A. Daniel, M. K. Whittlesey and J. M. J. Williams, *Tetrahedron Lett.*, 2007, **48**, 5115-5120.
157. N. Anand, N. A. Owston, A. J. Parker, P. A. Slatford and J. M. J. Williams, *Tetrahedron Lett.*, 2007, **48**, 7761-7763.
158. A. E. W. Ledger, P. A. Slatford, J. P. Lowe, M. F. Mahon, M. K. Whittlesey and J. M. J. Williams, *Dalton Trans.*, 2009, 716-722.
159. G. Petöcz, Z. Berente, T. Kégl and L. Kollár, *J. Organomet. Chem.*, 2004, **689**, 1188-1193.
160. A. Kaltzoglou, T. F. Fässler and P. Aslanidis, *J. Coord. Chem.*, 2008, **61**, 1774-1781.

161. A. N. Kharat, A. Bakhoda and B. T. Jahromi, *Inorg. Chem. Commun.*, 2011, **14**, 1161-1164.
162. A. E. W. Ledger, A. Moreno, C. E. Ellul, M. F. Mahon, P. S. Pregosin, M. K. Whittlesey and J. M. J. Williams, *Inorg. Chem.*, 2010, **49**, 7244-7256.
163. J. Alós, M. A. Esteruelas, M. Oliván, E. Oñate and P. Puylaert, *Organometallics*, 2015, **34**, 4908-4921.
164. A. Wu, B. O. Patrick, E. Chung and B. R. James, *Dalton Trans.*, 2012, **41**, 11093-11106.
165. H. Samouei and V. V. Grushin, *Organometallics*, 2013, **32**, 4440-4443.
166. D. Pingen, M. Lutz and D. Vogt, *Organometallics*, 2014, **33**, 1623-1629.
167. D. Pingen, T. Lebl, M. Lutz, G. S. Nichol, P. C. J. Kamer and D. Vogt, *Organometallics*, 2014, **33**, 2798-2805.
168. V. Bakhmutov, T. Buergi, P. Burger, U. Ruppli and H. Berke, *Organometallics*, 1994, **13**, 4203-4213.
169. G. E. Ball and B. E. Mann, *J. Chem. Soc., Chem. Commun.*, 1992, 561-563.
170. C. Soubra, Y. Oishi, T. A. Albright and H. Fujimoto, *Inorg. Chem.*, 2001, **40**, 620-627.
171. H. Günther, *Angew. Chem., Int. Ed. Engl.*, 1972, **11**, 861-874.
172. M. Möhlen, C. E. F. Rickard, W. R. Roper, D. M. Salter and L. J. Wright, *J. Organomet. Chem.*, 2000, **593–594**, 458-464.
173. A. Wu, B. O. Patrick and B. R. James, *Inorganic Chemistry Communications*, 2012, **24**, 11-15.
174. M. O. Albers, T. V. Ashworth, H. E. Oosthuizen, E. Singleton, J. S. Merola and R. T. Kacmarcik, in *Inorg. Synth.*, John Wiley & Sons, Inc., 2007, pp. 68-77.
175. S. P. Nolan, T. R. Belderrain and R. H. Grubbs, *Organometallics*, 1997, **16**, 5569-5571.
176. J. J. Hore Peter, Wimperis Stephen, *NMR: The Toolkit*, Oxford University Press, 2000.
177. J. A. Aguilar, P. I. P. Elliott, J. Lopez-Serrano, R. W. Adams and S. B. Duckett, *Chem. Commun. (Cambridge, U. K.)*, 2007, 1183-1185.
178. J. A. Aguilar, R. W. Adams, S. B. Duckett, G. G. R. Green and R. Kandiah, *J. Magn. Reson.*, 2011, **208**, 49-57.
179. T. Komuro, T. Arai, K. Kikuchi and H. Tobita, *Organometallics*, 2015, **34**, 1211-1217.
180. L. M. Guard, A. E. W. Ledger, S. P. Reade, C. E. Ellul, M. F. Mahon and M. K. Whittlesey, *J. Organomet. Chem.*, 2011, **696**, 780-786.
181. R. W. Harkness and W. E. Deming, *J. Am. Chem. Soc.*, 1932, **54**, 2850-2852.
182. C. F. Bernasconi, in *Relaxation Kinetics*, Academic Press, 1976, pp. 3-10.